Heat and Mass Transport in Tubular Packed Bed Reactors at Reacting and Non-Reacting Conditions

Bert Koning

2002

Ph.D. thesis
University of Twente

Twente University **Press**

Also available in print:
http://www.tup.utwente.nl/catalogue/book/index.jsp?isbn=903651813x

HEAT AND MASS TRANSPORT IN TUBULAR PACKED BED REACTORS AT REACTING AND NON-REACTING CONDITIONS

EXPERIMENTS AND MODELS

The research reported in this thesis was funded by the Dutch Organization for Scientific Research (NWO).

Twente University **Press**

Publisher: Twente University Press, P.O. Box 217, 7500 AE Enschede, the Netherlands
www.tup.utwente.nl

ISBN 903651813x

HEAT AND MASS TRANSPORT IN TUBULAR PACKED BED REACTORS AT REACTING AND NON-REACTING CONDITIONS

EXPERIMENTS AND MODELS

PROEFSCHRIFT

ter verkrijging van
de graad van doctor aan de Universiteit Twente,
op gezag van de rector magnificus,
prof. dr. F.A. van Vught,
volgens besluit van het College voor Promoties
in het openbaar te verdedigen
op donderdag 24 oktober 2002 te 15.00 uur

door

Gijsbertus Wilhelmus Koning

geboren op 1 januari 1973
te Wehl

Dit proefschrift is goedgekeurd door de promotor

prof. dr. ir. W.P.M. van Swaaij

en de assistent-promotor

dr. A.E. Kronberg

Contents

General Introduction

Tubular packed bed reactors with heat exchange through the wall are used in industry to carry out chemical reactions that have large heat effects. Such reactions may be exothermic, e.g. (partial) oxidation or hydrogenation, or endothermic, e.g. steam reforming. Industrial multi-tubular packed bed reactors consist of a large number of parallel tubes that are placed inside a cooling- or heating jacket, as shown Fig. 1. Gaseous reactants flow through these tubes, which contain packed beds of catalyst particles. Outside of the tubes is the heating or cooling

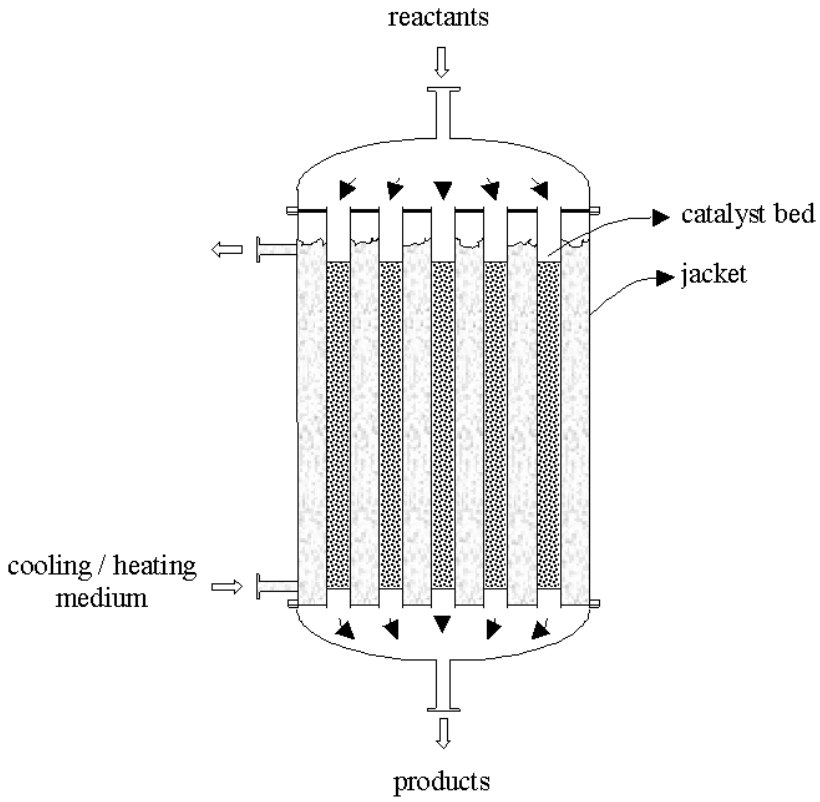

Fig. 1 Tubular packed bed reactor.

medium, which can be water, steam, oil or a molten salt. Boiling water or steam is often preferred as heat transfer medium for exothermic and endothermic reactions respectively. The advantage of these media is the high heat transfer coefficient, which is caused by the phase transitions that occur at the outer surface of the tubes, and the fact that it is relatively easy to have a constant temperature over the entire cooling jacket. Compared to other types of packed bed reactors, the diameter of the individual reactor tubes of a tubular reactor is small, which allows for effective heat transfer because of the high ratio of the heat transfer surface and the reactor volume.

Usually, the reaction rate - and thus the heat production rate - is an exponential function of temperature. If the reaction is exothermic and no cooling is applied, the reactor temperature will increase very rapidly along the length of the reactor, which may result in damaging of the catalyst and the reactor itself, or in the initiation of undesired parallel- or consecutive reactions. In such an adiabatic packed bed reactor, the conversion or the reactant inlet concentrations should therefore be kept small. If heat is removed via the wall, the production rate can be increased without sacrificing selectivity or risking damage to the reactor and the catalyst. If the reaction is endothermic, it is not self-accelerating. If no heat is supplied to the reactants, the temperature of the bed will decrease in the direction of fluid flow until it becomes too low for the reaction to proceed. In this case, the purpose of intermediate addition of heat is to increase conversion. In the remainder of this section, it will be assumed that the reaction is exothermic, since, in that case, the reaction conditions in a tubular packed bed reactor are more sensitive to the operating parameters.

The design of a tubular packed bed reactor is always a compromise between selectivity, yield and investment- and operating costs. For most reaction systems, maximum selectivity and yield can be obtained if the temperature changes over the reactor volume and inside the catalyst particles are small. Such requirements would result in the design of a large reactor with a huge number of very narrow tubes. At the same time, the flow rate should be high to maximize the heat transfer rate and to minimize the conversion of the reactants per pass. It is evident that such reactor will be not economic. The reactor itself and the downstream process equipment will be costly, whilst the energy consumption by the recycle compressor will be very large.

In practice, the temperature of the bed is allowed to increase. The maximum allowable temperature is either limited by the minimum desired selectivity or by the temperature above which so-called ‘runaway’ occurs, which will be discussed later in this section.

Fig. 2 shows a temperature field that is typical for a wall-cooled tubular reactor. In axial direction, heat is transported mainly by convection; heat conduction in this direction is only of minor importance at conditions as applied in industry. In radial direction, heat is transported inside the packing through a complex process, which is usually characterized by the effective radial thermal conductivity $\lambda_{e,r}$. Near the wall, a temperature jump occurs, which is generally described by a wall heat transfer coefficient α_w. Together with the temperature gradients, radial and axial concentration gradients will develop. However, concentration differences in radial direction are usually smaller and of less importance than radial temperature differences.

From the inlet, the temperature starts to increase until the rates of heat removal and heat production become equal. Downstream from this position, the reaction rate –and therefore the temperature- decreases due to a decrease of the concentrations of the reactants. The position at which the maximum temperature occurs is referred to as the ‘hot spot’ of the reactor.

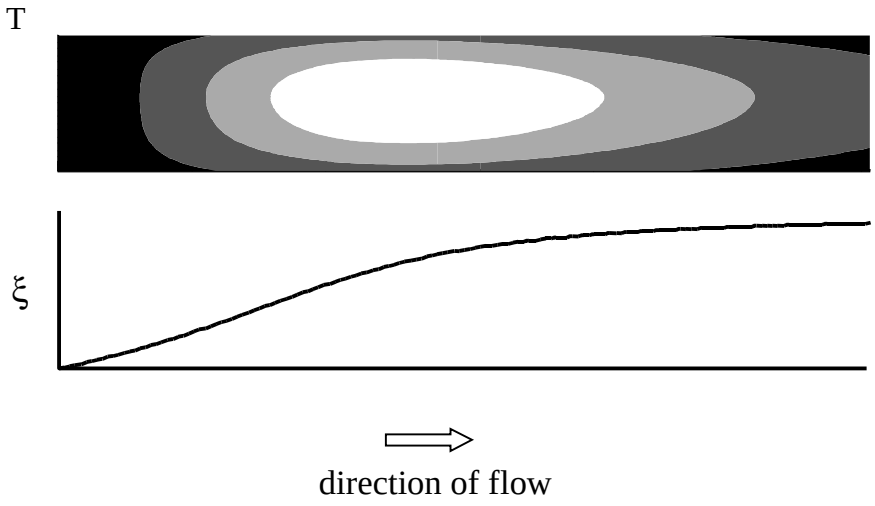

Fig. 2 Two-dimensional temperature field and conversion in case of an exothermic reaction. The lighter the color, the higher the temperature.

If, at certain conditions, the rate of heat production is not equalized by the rate of heat removal, the temperature of the fluid will rapidly increase until almost all reactants are consumed. Such a rapid temperature increase is the most simple and common definition of runaway. When operating close to runaway, the reactor behavior is very sensitive to the operating conditions. Well known are the examples in the usual textbooks, demonstrating that a minute change of the inlet temperature may result in an increase of the hot spot temperature of tenths of degrees, or even in runaway.

To maximize yield and minimize the size of the reactor, wall-cooled tubular reactors are usually operated at conditions that are not too far from runaway. A precise knowledge of the heat transport phenomena inside the catalyst bed and inside the cooling jacket is therefore of the utmost importance.

In this thesis, attention is paid on the modeling of heat and mass transfer inside the tubular catalyst bed. A proper reactor model should enable the design of a tubular packed-bed reactor on the basis of separately measured reaction kinetics and heat transfer parameters. Despite the efforts that have been made over the past 50 years, industrial tubular reactors are designed after numerous expensive and time-consuming pilot scale experiments. The predictions of the performance of this type of reactors is still unreliable. This is rather conspicuous, since scaling-up mainly involves an increase of the number parallel tubes, whilst their diameter and the size of the catalyst pellets are restricted to relatively small ranges.

The main part of this work, which is a continuation of earlier work at the Twente University (*Wijngaarden, 1988, Borkink, 1991, Borman, 1993, Schouten, 1995*), is devoted to the resolution of the observed discrepancy between the heat transfer parameters obtained from experiments performed under reacting and non-reacting conditions. This is done on the basis of experimental data obtained in a pilot-scale wall-cooled tubular packed bed reactor over a

wide range of operating conditions, including elevated pressures. The kinetics of the model reaction, i.e. CO oxidation over a copper oxide catalyst has been measured separately in kinetic reactors.

Chapter 1 of this thesis is an introduction to the modeling of wall-cooled tubular packed bed reactors. In this chapter, existing one- and two-dimensional reactor models will be discussed, as well as the underlying physical phenomena that are responsible for heat and mass transfer in packed beds. A selection of literature correlations for the effective heat and mass transport parameters is presented, of which some are used later in the experimental study. Finally, possible reasons for the uncertainty of the heat transfer parameters and for the discrepancy between literature correlations are discussed qualitatively.

In chapter 2, the experiments are discussed that were performed to determine the intrinsic and the apparent kinetics of the model reaction. The intrinsic reaction kinetics of CO oxidation over the used copper oxide catalyst was studied in an integral reactor, using finely crushed catalyst. The apparent reaction rate measured using the actual catalyst particles, which is a function of the intrinsic kinetics and of the heat and mass transport properties of the catalyst pellets, was measured in a kinetic reactor with internal recycle.

The results of the experimental investigation of heat transfer in the pilot-scale wall cooled tubular reactor under non-reacting and reacting conditions are discussed in chapter 3. Experiments were performed over a wide range of reactor pressures and temperatures, reactant inlet concentrations and flow rates. In this chapter, it is demonstrated that the effective heat transfer parameters obtained from experiments at reacting and non-reacting conditions are the same if a radial distribution of the porosity and of the axial fluid velocity are taken into account.

In chapter 4, an extensive set of measured temperature profiles in radial and angular direction is used to interpret heat transport inside packed beds in terms of fluid elements with different temperatures moving at different velocities. The spread in temperatures measured in angular direction, which is a result of this chaotic movement of fluid elements, is subsequently used to distinguish between a film resistance to heat transfer near the wall and an apparent resistance, which is caused by radial mixing of the fluid elements moving towards and from the wall. The results of this investigation support the wave model, which has been proposed by *Kronberg and Westerterp, 1999* as an alternative to the standard dispersion model.

One-dimensional reactor models of tubular packed bed reactors are often applied to minimize the calculation time when studying reactor dynamics, when optimizing kinetic parameters or if the reactor model is part of the process control software of an industrial plant. The most important drawback of the standard one-dimensional models is the use of the radial average

temperature to calculate the reaction rate. One-dimensional models do exist, which take into account the radial temperature distribution, such as the ‘α-model’ of *Hagan, Herskowitz and Pirkles, 1988.* These models, however, require solving of an implicit equations at each grid point in axial direction. In chapter 5, a new one-dimensional model is proposed as alternative to this model. The advantages of this ‘δ-model’ are that it has a wider range of applicability and that it has the same form as the conventional 1-dimensional model, which makes programming of it far easier. It is further demonstrated that, at conditions not too close to runaway, the new model performs better than the α-model.

Summary

Many different models for wall-cooled tubular reactors have been developed over the past 50 years, ranging from a simple one-dimensional homogeneous plug-flow model to more complex ones, such as the two-dimensional heterogeneous, axially dispersed plug-flow model. The parameters for heat and mass transport in these models lump different physical transport mechanisms of heat and mass, occurring at different scales, into simple overall coefficients. In the models, the driving forces for transport of heat and mass, which may actually vary strongly due to the heterogeneity of the packed bed, are averaged values. Many empirical correlations for the transport coefficients have been proposed, which may differ widely. This is probably due to the sensitivity of the parameters to experimental errors, the use of different transport model concepts and to a poor understanding of the influence of the geometry of the catalyst particles and the packing. A difference between the values of the effective transport parameters obtained at reacting and non-reacting conditions, has been reported in literature. This is an important subject of the present investigation (see Chapter 3). The wave model (*Kronberg and Westerterp, 1999*) avoids some of the drawbacks of the conventional Fickian and Fourier-type dispersion models. It will be used in this thesis to describe some detailed experiments on radial transport under non-reacting conditions. In principle, computational fluid dynamics modeling could contribute greatly to improvement of the understanding of cooled tubular reactors. The models that are currently developed (*Bey and Eigenberger, 1977, Logtenberg and Dixon, 1998*) generate many new insights, but due to the complex geometry of packed beds and the complex flow patterns inside it, these models are not (yet) suited for reactor design.

The heterogeneously catalyzed oxidation of carbon monoxide in air was used as a model reaction system for the investigation of heat and mass transport in a pilot-scale wall-cooled tubular reactor (see Chapter 3). In Chapter 2, the investigation of the kinetics of this reaction is described. The used catalyst consisted of 29 wt% copper oxide on porous γ-alumina in the form of cylinders with a diameter of 5.5 mm and an average height of 11.2 mm. The reaction kinetics were studied over a wide range of temperature and pressure. The reactor feed contained a constant mass fraction of water, which was necessary to avoid a change of the activity over time. The intrinsic reaction rate was measured using an integral reactor, which contained a bed of catalyst fragments with a diameter of 0.2 mm, diluted with silicium carbide particles of the same size. The measured reaction rate was described using an Eley-Rideal type of expression. In an internal-recycle reactor, the reaction rate was measured using intact catalyst particles. The reaction rates measured in this reactor were influenced by intra-particle mass transport, which was taken into account by using a new, analytical

approximation of the effectiveness factor. After parameter optimization, the average difference between the measured and the predicted carbon monoxide conversion was 4%.

In a pilot-scale wall-cooled tubular reactor with a length of 1 m and a diameter of 53 mm, heat transfer experiments were performed at reacting and non-reacting conditions. The oxidation of carbon monoxide in air over the catalyst described in the previous section was used as a model reaction system. Experiments were performed at inlet- and wall temperatures between 156 and 200 °C and reactor pressures of 3, 5.9 and 8 bara. The gas load was varied between values corresponding to 200< Re <1400 and the CO inlet concentration was between 0.1 and 1.5 vol%. A two-dimensional pseudo-heterogeneous reactor model was used as a basic model to predict the temperature and concentration profiles that were measured inside the catalyst packing. When using the heat transport parameters measured at non-reacting conditions and the separately measured reaction kinetics, the basic model gave a fair description of the temperature profiles measured at reacting conditions. At high flow rates, however, the effective heat transport parameters, obtained at reacting conditions, were smaller than the values obtained at non-reacting conditions. Optimization of the reaction rate on the basis of the measured conversion did not eliminate this difference, but only reduced the scatter. It was found that a radial distribution of the bed porosity and, as a result of this, of the axial fluid velocity has to be taken into account in order to reconcile the heat transfer parameters derived from experiments at reacting and non-reacting conditions.

In two reactors with different diameters, detailed temperature profiles were measured over packed beds of 14 mm glass spheres and the cylindrical catalyst that was used in the pilot-scale wall-cooled tubular reactor. The wave model, which has been recently developed at the University of Twente, was successfully applied to interpret the spread in the measured temperatures around the angulary averaged temperature. In this model, heat transport is not driven directly by the radial and axial temperature gradients, but is a result of movement and mixing of fluid elements with different temperatures and velocities.
By using the measured temperature spread, the wall heat transfer coefficient in the two-dimensional reactor model could be divided into a film resistance to heat transfer at the wall and an apparent resistance, which is caused by the presence of fluid elements with different temperatures. The experiments showed that the film resistance accounts for more than 80% of the total resistance to heat transfer at the wall at Re> 500.

The major drawback of one-dimensional models, which are often used if the available calculation time is limited, is the fact that the reaction rate is calculated using the radially averaged temperature. The difference between this reaction rate and the radially averaged reaction rate increases with increasing temperature difference over the radius of the reactor and with increasing activation energy of reaction. Improved one-dimensional models, such as the α-model model' (*Hagan, Herskowitz and Pirkles, 1988*), are available, which contain an

analytical approximation of the radial temperature profile to improve the prediction of the average reaction rate. However, application of these models involves solving of implicit equations. A new model is proposed as alternative to the existing one-dimensional models. This ‘δ-model’ has the same form as the conventional one-dimensional model, which means that it contains only explicit functions. It is demonstrated that, at conditions not too close to runaway, the new model performs better than the well-known α-model.

Samenvatting

Gedurende de laatste 50 jaar is een grote verscheidenheid aan modellen ontwikkeld voor de beschrijving van wandgekoelde buisreactoren, variërend van eenvoudige eendimensionale, homogene propstroom-modellen tot de meer complexe tweedimensionale, heterogene modellen met axiale en radiale dispersie van warmte en massa. De meest recente modellen zijn gebaseerd op Computational Fluid Dynamics. Deze dragen weliswaar bij aan een beter begrip van gekoelde buisreactoren, maar zijn nog niet geschikt voor het ontwerp van reactoren. In de momenteel toegepaste modellen worden eenvoudige correlaties voor effectieve transportparameters gebruikt voor de beschrijving van een complex systeem, waarin warmte- en stoftransport plaatsvindt op verschillende schaalniveaus. Voor de berekening van de effectieve transport parameters is een groot aantal correlaties beschikbaar, die onderling sterk kunnen verschillen. Dit is te wijten aan de sterke gevoeligheid van de parameters voor experimentele fouten, het gebruik van verschillende transportmodellen en aan de onzekerheid over de invloed van de reactor- en katalysatorgeometrie. Hiernaast zijn een aantal aannamen in de afleiding van de standaard dispersie modellen op zijn minst twijfelachtig. Zo worden de gemiddelde concentratie- en temperatuurgradiënten beschouwd als de drijvende kracht voor massa- en warmtetransport. In realiteit vertonen deze gradiënten sterke lokale variaties door het heterogeen karakter van het gepakt bed. Tenslotte is in de literatuur gerapporteerd dat de waarden van de effectieve warmtetransport parameters afhankelijk kunnen zijn van het al dan niet optreden van chemische reactie. Deze invloed van chemische reactie op de warmtetransport parameters is het belangrijkste onderwerp in het onderhavige proefschrift. Om dit te kunnen bestuderen zijn warmtetransport metingen met en zonder reactie verricht in een pilot-scale wandgekoelde buisreactor. De in de reactormodellen gebruikte reactiekinetiek werd gemeten in afzonderlijke kinetiek-reactoren.

De heterogeen gekatalyseerde oxidatie van koolmonoxide in lucht over een cilindervormige katalysator, bestaande uit CuO op γ-alumina, is gebruikt als modelreactie. In Hoofdstuk 2 wordt het onderzoek naar de kinetiek van deze reactie beschreven. De reactiesnelheid is gemeten over een groot bereik van temperaturen (100 tot 240 °C) en reactordrukken (2 tot 9 bara). De fractie water in de reactorvoeding werd constant gehouden, hetgeen nodig was om te voorkomen dat de activiteit van de katalysator sterk veranderde gedurende het gebruik ervan. De intrinsieke reactiesnelheid is gemeten in een zogenaamde integraal reactor, waarin een gemalen katalysator (0.2 mm), verdund met inerte siliciumcarbide deeltjes van dezelfde afmeting werd gebruikt. Daarnaast zijn conversiesnelheden gemeten in een reactor met interne recycle, gebruikmakend van de oorspronkelijke katalysatordeeltjes (diameter=5.5 mm, hoogte= 11.2 mm). Een Eley-Rideal reactiemechanisme bleek geschikt voor de beschrijving van de gemeten reactiekinetiek, waarbij de metingen in de recycle reactor zijn

gecorrigeerd voor interne stoftransport limitering. Voor deze correctie is gebruik gemaakt van een nieuwe, analytische uitdrukking voor de effectiveness factor.

In hoofdstuk 3 worden vervolgens de metingen beschreven waarin de bovengenoemde reactie is uitgevoerd in een wandgekoelde buisreactor met een lengte van 1 m en een diameter van 53 mm. In deze reactor zijn eveneens warmtetransport metingen uitgevoerd zonder reactie. De experimenten werden uitgevoerd bij diverse wand- en inlaattemperaturen (156 tot 200 °C), CO ingangsconcentraties (0.1 tot 1.5 vol%) en reactordrukken (3 tot 8 bara). De gassnelheid werd gevarieerd tussen waarden die corresponderen met 200< Re <1400. Een tweedimensionaal, heterogeen reactor model is gebruikt als basismodel voor de voorspelling van de in de reactor gemeten temperatuur- en concentratieprofielen.
Wanneer gebruik werd gemaakt van de warmtetransportparameters, bepaald zonder chemische reactie, en de afzonderlijk gemeten reactiekinetiek, gaf dit basismodel een redelijk goede voorspelling van de gemeten conversies en temperatuurprofielen. Echter, in het geval van experimenten bij hoge gassnelheden waren de effectieve warmtetransport parameters tijdens reactie systematisch lager dan de waarden die werden gemeten bij afwezigheid van reactie. Na correctie van de reactiesnelheid, op basis van de gemeten CO conversies, bleef dit verschil bestaan, hoewel de spreiding in de waarden, gemeten onder reagerende condities, afnam. Een goede overeenkomst tussen de warmtetransport parameters, gemeten met en zonder reactie, werd verkregen wanneer rekening werd gehouden met de radiale verdeling van de porositeit van het katalysatorbed en de variatie in de axiale gassnelheid welke hierdoor ontstaat.

In twee reactoren met verschillende diameters zijn gedetailleerde temperatuurprofielen gemeten boven pakkingen van glasbolletjes en van de katalysator die eveneens werd gebruikt in de pilot-scale wandgekoelde buisreactor. Deze experimenten worden beschreven in hoofdstuk 4. De gemeten temperatuurspreiding in angulaire richting kon goed voorspeld door het wave model, dat is ontwikkeld door *Kronberg and Westerterp, 1999*. In dit model wordt verondersteld dat de warmte- of massaflux het resultaat zijn van menging van gasstromen met verschillende temperaturen en concentraties, die zich min of meer chaotisch tussen de deeltjes door bewegen. De tot nu toe gebruikte standaard dispersie modellen, waarin wordt aangenomen dat de fluxen evenredig toenemen met de temperatuur- of concentratiegradiënten, zijn niet in staat deze temperatuurspreiding te voorspellen of verklaren.
Door gebruik te maken van de gemeten temperatuurspreiding in angulaire richting kon de totale weerstand tegen warmtetransport tussen de pakking en de reactorwand worden gesplitst in een filmweerstand en een schijnbare weerstand, die ontstaat door het middelen van de temperaturen van de gaspakketjes die naar de wand toe en van de wand af bewegen. Op basis van de experimenten kon worden geconcludeerd dat, bij waarden van Re groter dan 500, de

belangrijkste weerstand tegen warmtetransport tussen de pakking en de wand wordt gevormd door de filmweerstand.

Een groot nadeel van eendimensionale reactormodellen is dat de reactiesnelheid wordt berekend op basis van de gemiddelde temperatuur over de doorsnede van de reactor. Het verschil tussen de zo berekende waarde en de eigenlijke gemiddelde reactiesnelheid is afhankelijk van de activeringsenergie van de reactie en neemt toe met het verschil tussen de temperatuur in het centrum van het bed en de temperatuur nabij de wand. Verbeterde versies van het eendimensionale model zijn beschikbaar, zoals het α-model, waarin een analytische benadering van het radiale temperatuurprofiel wordt gebruikt om de gemiddelde reactiesnelheid nauwkeuriger te benaderen (*Hagan, Herskowitz and Pirkles, 1988*). Deze verbeterde eendimensionale modellen hebben echter als nadeel dat impliciete vergelijkingen dienen te worden opgelost. In Hoofdstuk 5 wordt een eendimensionaal model geïntroduceerd dat dit nadeel niet heeft. Dit 'δ-model' heeft dezelfde vorm als het conventionele eendimensionale model en bevat uitsluitend expliciete vergelijkingen. Bij condities niet te dicht bij runaway komt het δ-model beter overeen met de oplossing van het tweedimensionale model dan het α-model. Dichtbij runaway kan elk van de eendimensionale modellen de exacte oplossing het dichtst benaderen, afhankelijk van de operatiecondities.

Chapter 1

Introduction to Modeling of Wall-Cooled Tubular Packed Bed Reactors

ABSTRACT

In this chapter, the most common models of wall-cooled tubular packed bed reactors are presented, which were also used in the present investigation. The currently applied models are semi-empirical and contain effective transport parameters in which heat- and mass transport processes at different scales are lumped. Correlations for the effective transport parameters, measured at non-reacting conditions, may show a large spread. In addition to this, it has been reported that the values of the effective heat transport parameters obtained form experiments at reacting conditions may be different from those obtained from experiments without reaction. A qualitative explanation is given for the spread in heat- and mass transport parameters by considering the heterogeneity of the system and the sensitivity of the transport parameters to the used experimental procedure.

1.1 Introduction

Models used for the description of packed bed reactors are chosen depending on the desired accuracy, the required computational efforts and the available information on the packed bed. Systematic surveys are given by *Hlavacek and Votruba, 1977* and *Lemcoff et al., 1990*. For the simulation of steady-state reactor behavior at conditions not too close to runaway, a one-dimensional pseudo-homogeneous plug-flow model generally is sufficient, whilst for a detailed design of a tubular reactor two-dimensional heterogeneous reactor models with axial mass and heat dispersion are usually applied. The effective heat- and mass transfer parameters are not only a function of the physical properties of the applied catalyst and the gas phase, but are also determined by the flow conditions, the reactor (tube) size and, more important, they depend on the selected reactor model. Any model is valid within a certain range of operating conditions, depending on the extent to which it simplifies reality. The commonly used models are described in the well known textbooks, see e.g. *Froment and Bischof, 1979* and *Westerterp et al., 1984*.

Recently, attention is paid to fluid dynamics modeling of packed bed reactors in order to gain more insight in the fluid flow and the heat- and mass transfer processes that also occur at

scales smaller than the particle diameter (B*ey and Eigenberger, 1997*, Logtenberg *and Dixon, 1998 Logtenberg et al., 1999*). Ultimately, this may much improve modeling, but up to now, these processes are still described by lumped parameters.

The goal of the present work is to investigate how chemical reaction can influence the values of the effective heat- and mass transfer parameters in different models. Experimental data are available that suggest that such dependency exists, see e.g. *Hall and Smith, 1949*, *Hoffman, 1979*, *Schwedock et al., 1989* and *Schouten et al., 1994*. This does not mean that a reaction occurring at or in the catalyst is suspected to alter the true transport mechanisms. However, the occurrence of a fast chemical reaction at the surface of the catalyst may lead to steep temperature and concentration gradients. At these conditions, shortcomings due to oversimplification and parameter lumping may become manifest.

In this chapter, the mechanisms of heat and mass transfer in packed beds are discussed, together with the reactor models that are most frequently applied. After this, available literature correlations of the effective heat transport parameters in these models are compared. Possible explanations are given for the differences between the various correlations and the discrepancy between the heat transport parameters obtained at reacting and non-reacting conditions. Finally, the wave model is briefly discussed.

1.2 Mechanisms for heat and mass transport

In all existing two-dimensional models of tubular reactors, axial symmetry is assumed, which is allowed if the described reactor is carefully packed to avoid variation of the porosity in angular direction. In a two-dimensional reactor model, the packed bed is mostly divided into a core zone and a wall zone. As is illustrated in Fig. 1.1 for the case of an exothermic reaction, the temperature profiles in these zones are very different. A typical temperature profile in the core zone of the packing is parabolically shaped. In the wall zone, the temperature shows a sharp decrease. In the models, the heat flux at the wall is proportional to the difference between the wall temperature and the fluid temperature inside the bed close to the wall:

$$j_H = \alpha_w \left(T_{r=R_t} - T_w \right) \tag{1.1}$$

The proportionality coefficient α_w is called the wall heat transfer coefficient. Since wall generally is impermeable, the radial mass flux is zero at the wall. Inside the packing, the radial heat flux, j_H, is mostly calculated using Fourier's law for heat conduction, which is well known for the description if heat flow in solids and stagnant fluids. Analogously, the radial mass flux, j_M, is calculated using Fick's law for molecular diffusion:

$$j_H = -\lambda_e \frac{\partial T}{\partial x} \quad ; \quad j_M = -D_e \frac{\partial c}{\partial x}, \tag{1.2}$$

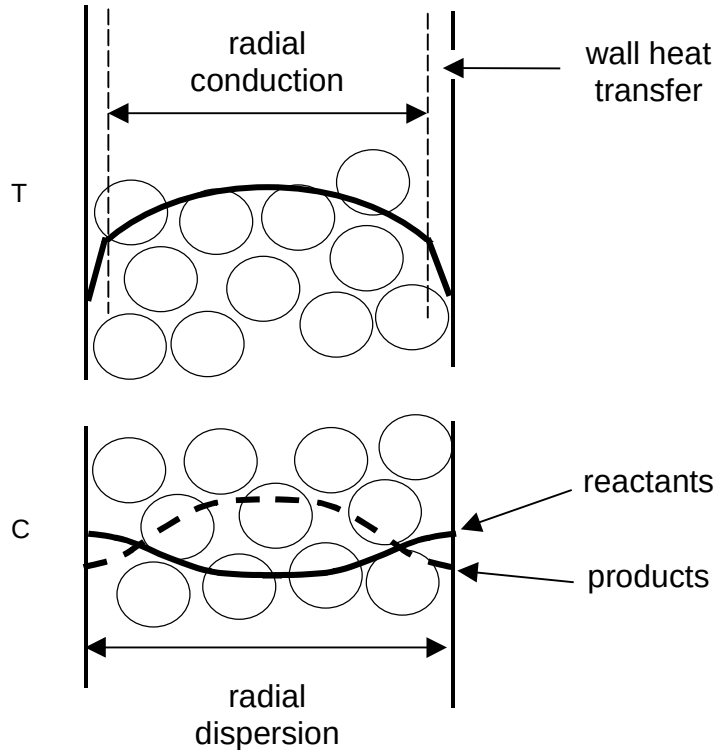

Fig. 1.1 Typical radial temperature and concentration profiles.

In packed beds, dispersion of heat and mass are mainly caused by fluid convection and mixing. The molecular diffusion- coefficient and thermal conductivity of the two-phase medium are therefore replaced by effective values D_e and λ_e, which are determined by the combination of the physical properties of these substances, the operating conditions and the reactor (tube) and catalyst geometry. As many as 8 different mechanisms for heat and mass transport can be distinguished (e.g. *Lemcoff et al. 1990, Westerterp et al. 1984*):

Independent of fluid velocity:

1.1. Conduction/diffusion through the solid
1.2. Conduction through the solid-solid contact points
1.3. Heat transfer by radiation between the surfaces of particles
1.4. Diffusion and conduction within the fluid

Depending on fluid velocity:

2.1. Convection by the fluid in axial direction
2.2. Axial and transverse mixing of the fluid
2.3. Fluid-solid heat- and mass transfer
2.4. Diffusion and conduction through the fluid film near the solid-solid contact point

Variation of the fluid density over the bed may lead to free convection, which causes additional dispersion of heat and mass in axial and radial direction *(Benneker et al., 1996*). Transport of heat and mass occurs in both phases both in parallel and in series.
The bulk of the fluid flows axially and causes convective transport (2.1) in this direction. In the reactor models, this transport is accounted for by convection terms $-u\,\partial c/\partial z$ and $-u\rho_f c_{p,f}\,\partial T/\partial z$ in the mass- and heat balance respectively. Inside the packing, fluid elements chaotically move between the particles (see Fig. 1.2), which causes additional heat and mass transport in radial and axial direction (2.2). Mixing of the fluid elements occurs due to turbulence and molecular diffusion and conduction. At high fluid flow rates, which are typical for industrial packed bed reactors, this transport additional to the overall convective transport is referred to as 'dispersion' of heat and mass.

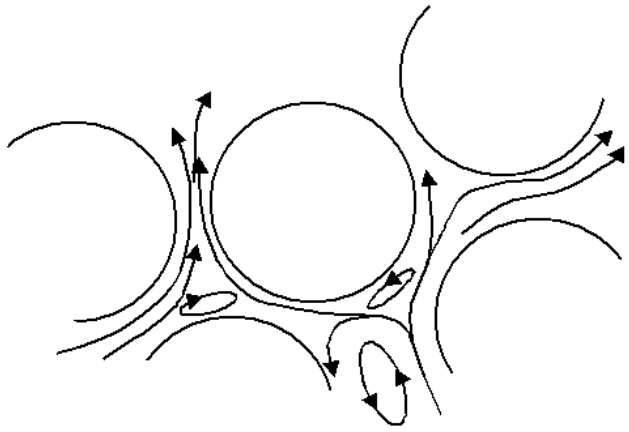

Fig. 1.2 Mixing of fluid elements between particles.

If the temperature and/or concentration at the surface of the particle differs from its value in the fluid phase, mass and/or heat exchange between the fluid and the particles will occur (1.2). The heat- or mass flux is calculated as the product of a mass transfer coefficient k_g or a heat transfer coefficient α_p and the concentration or temperature difference between the phases:

$$j_H = \alpha_p \left(T_f - T_s^i \right) \tag{1.3}$$

$$j_M = k_g \left(c_f - c_s^i \right) \tag{1.4}$$

α_p and k_g actually are averaged values over the surface of the particles, as are the driving forces. Due to variation of the temperature over the surface of the pellets and the occurrence of chemical reaction inside the solid, temperature and concentration profiles will exist within the particles, as is shown schematically in Fig. 1.3. Inside a catalyst particle, the temperature will increase towards the center of the particle if the reaction is exothermic. At the same time reactants are consumed and products are formed, which leads to concentration gradients.
If the temperature and the concentration inside the catalyst particle are known, it is possible to calculate the reaction rate over the volume of the particle. Since it would require a large computational effort to perform these calculations for the entire catalyst bed, simplifications are usually made. With a typical thermal conductivity of porous catalyst particles of 0.5–2 W m^{-1} K^{-1}, the temperature variation over a catalyst particle is usually small, so that it can be assumed constant when calculating the reaction rate over the volume of the particle. Most often, intra-particle concentration gradients are not negligible at conditions applied in industry.

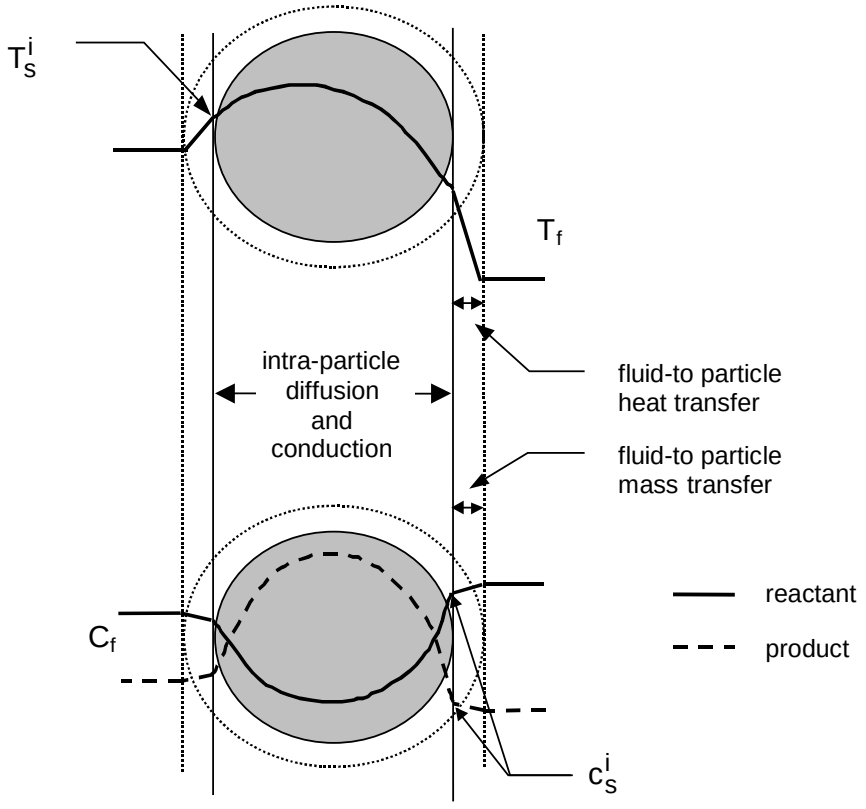

Fig. 1.3 Temperature and concentration profiles over the particles and the surrounding fluid film in case of an exothermic reaction in a cooled packed-bed reactor.

The minimum size of the catalyst particles is determined by the heat transfer properties of the bed and by the allowable pressure drop over the reactor. Both the effective radial heat transfer coefficient and the wall heat transfer coefficient, which are amongst the most important design characteristics, decrease with decreasing particle size. The maximum size of the particles is determined by the degree of utilization of the catalysts' active material. With increasing particle diameter, the reaction rate per unit volume of catalyst will decrease due to a decrease of the reactant concentrations towards the particle's center. One can partly get around this problem by using catalysts with a higher specific surface area as, for instance, raschig rings, trilobes or honey-comb like structures. If the active material of the catalyst is rather expensive, or if consecutive reactions should be avoided, a shell-type catalyst may be used.
The degree of utilization of the catalyst is characterized by the 'effectiveness factor', which is defined as the ratio of the average reaction rate over the particle and the reaction rate at the temperature and concentrations at the catalysts' surface:

$$\eta = \frac{\frac{1}{V_p}\int_{V_p} R(\mathbf{c},T)\,dV_p}{R(\mathbf{c}_s,T_s)} \tag{1.5}$$

Equation (1.5) is not applicable to all types of chemical reactions, see *Wijngaarden et al., 1999*. Generally, the effectiveness factor is smaller than one. Values of η larger than one can be found for e.g. a Langmuir-Hinshelwood type of expression for the reaction rate, if one or more of the reactants inhibits reaction by adsorbing at and blocking of active sites. Intra-particle heat transfer limitation can also cause η to be larger than unity if the effect of the internal temperature rise outweighs the effect of decreasing reactant concentrations.
For most types of reaction rate expressions, exact solution of the mass balance equations over the particle is not necessary. Analytical approximations, based on the intrinsic reaction rate, the catalysts' shape and the intra-particle transport properties are easier to handle and will give an estimate with a high enough accuracy compared to that of the input parameters and the available models. An analytical expression for the particle effectiveness factor, used in this investigation, will be discussed in Appendix B.

The contribution of mass transport through the porous particles to the overall radial and axial mass transport generally is negligible. The contribution of heat conduction through the solid can be significant, depending on its thermal conductivity and the fluid velocity. If the fluid temperature varies around the particles, temperature gradients over the particles will develop. Between two adjacent particles, heat is transferred by means of direct heat exchange and by heat transfer through the fluid around the contact area between the particles, as is shown in Fig. 1.4. Not shown in this figure is heat transfer by radiation between the surfaces of

particles, which is strongly dependent on the temperature of the bed. This path for heat transfer will not be discussed here, since it only plays a significant role at a temperature above 400 °C (*Vortmeyer, 1974*), which is well above the maximum temperature occurring during the experimental investigations in this work.

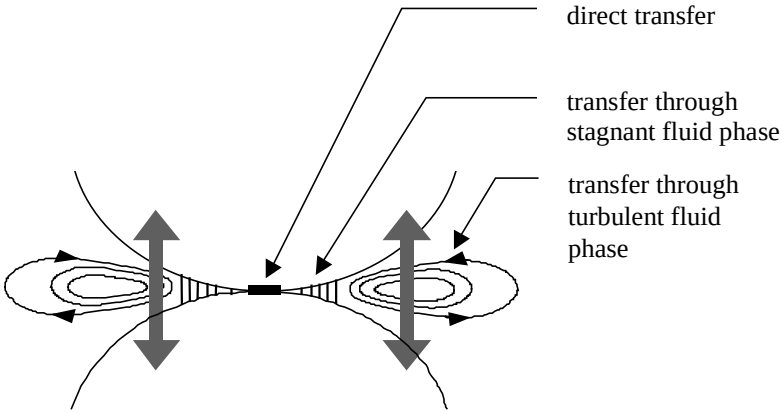

Fig. 1.4 Heat transfer near a solid-solid contact.

Up to a small distance from the surface of the particles, the fluid can be regarded as more or less stagnant and heat transport occurs through molecular conduction (*Lund et al. 1999*). Further from the interface, the heat transfer rate will no longer be independent of the fluid velocity (*Singer and Wilhelm, 1950*). Estimation of the direct heat exchange between two particles is rather difficult. In principle, the size of the contact area can only be calculated for very smooth spherical particles with a known elasticity modulus. Even then, calculation of the gravity-induced forces between the individual particles is not obvious in case of long, narrow beds. Catalyst particles are not smooth and usually not spherical. The contact area will depend on the orientation and the roughness of the particles, as well as on the surface deformation that occurs during the packing of the catalyst bed. As a result, the contact area between the particles is generally not known (*Eigenberger 1972*).

There is no principle difference between the mechanisms for heat transport near the reactor wall and those inside the packing, except for the fact that, besides with the catalyst, the fluid now also exchanges heat with a ‘flat’ surface, which usually has a constant, uniform temperature. The earliest models of wall-cooled tubular reactors (e.g. *Damköhler,1938 G., Singer and Wilhelm, 1950*) do not contain an additional resistance to heat transfer near the wall. These models performed satisfactory in case of small fluid velocities, when the fluid temperature gradually approaches the wall temperature. At higher flow rates, a temperature drop is observed near the reactor wall, which was attributed to a change in the effective radial thermal conductivity in this region. Near the wall, the porosity is higher than that in the center of the bed, causing a change of the effective mixing length for heat and mass dispersion and

an increase of the axial fluid velocity. The resistance to heat transfer near the wall is a function of the effective radial thermal conductivity in this region and a true 'film' resistance near the wall. For practical use, a wall heat transfer coefficient α_w was introduced to predict the steep temperature change near the wall, which is still generally used. Recently, it has been argued that the use of a film-resistance to heat transfer is artificial and should be avoided by using an effective thermal conductivity that is a function of the radial position (*Kuo and Tien, 1989, Winterberg and Tsotsas 2000 a,b*). One reason for this is the large spread in empirical correlations for the wall heat transfer coefficients obtained over the years by different authors. Although the radial dependence of the effective radial thermal conductivity is very complex, since it is determined by the distribution of the porosity and the axial fluid velocity, temperature fields calculated using such a model are similar to those predicted by the α_w model using an 'arbitrary' set of literature correlations for the effective heat transfer parameters.

1.3 Reactor models

Over the years, reactor models have been developed with different levels of sophistication. Firstly, one-dimensional models can be distinguished from two-dimensional models. In a one-dimensional model, radial variations of concentration and temperature are not considered, but some averaged values over the cross section over the bed are used. The heat exchange rate between the fluid and the wall is assumed to be proportional to the difference between the average bed temperature and the wall temperature. For the simple case of no resistance to solid-to-fluid heat and mass transfer, the heat and mass balance of the **homogeneous one-dimensional model** are given by eq. (1.6) and (1.7):

Heat balance

$$(\varepsilon\rho_f c_{p,f} + (1-\varepsilon)\rho_s c_{p,s})\frac{\partial \overline{T}}{\partial t} = -u_0\rho_f c_{p,f}\frac{\partial \overline{T}}{\partial z} + \frac{\partial}{\partial z}\left(\lambda_{e,ax}\frac{\partial \overline{T}}{\partial z}\right) - \frac{4U}{D_t}\left(\overline{T} - T_w\right) + \sum_{i=1}^{n}\left(-\Delta H_r^i\right)\eta_i R_i\left(\overline{\mathbf{c}},\overline{T}\right) \tag{1.6}$$

Mass balance component j

$$\varepsilon\frac{\partial \overline{c^j}}{\partial t} = -u_0\frac{\partial \overline{c^j}}{\partial z} + \frac{\partial}{\partial z}\left(D_{e,ax}\frac{\partial \overline{c^j}}{\partial z}\right) - \sum_{i=1}^{n}\nu_i^j\eta_i R_i\left(\overline{\mathbf{c}},\overline{T}\right) \tag{1.7}$$

In equations (1.6) and (1.7), ε is the bed porosity, ΔH_r^i is the heat of reaction i and ν_i^j is the stoichiometric coefficient of component j in reaction i. The subscripts f and s refer to the fluid

and the solid phase respectively. The concentrations of individual components are denoted as c^j, whilst **c** is a vector representing the concentrations of all species involved.
The one-dimensional model is not very suitable for detailed modeling, but is it useful when studying the dynamic behavior of the reactor or when estimating reactor dimensions if precise information on the reaction kinetics and catalyst shape and size is lacking, since the computational effort is small. The overall heat transfer coefficient is not truly constant over the entire length of the reactor, but is a function of the axial position, or rather of the shape of the developing radial temperature profile (*Westerink et al., 1993*). Lumping of the effective radial thermal conductivity and the wall heat transfer coefficient into U results in a fair approximation of the rate of heat removal through the wall if the shape of the radial temperature profile does not change along the reactor, but fails in case of a developing temperature profile. More important is the use of the radial average temperature to calculate the reaction rate. Since the reaction rate is not a linear function of temperature, but usually increases exponentially with temperature, the reaction rate at the radial average temperature will be smaller than the radial average reaction rate:

$$R\left(\overline{T}\right) \le \overline{R\left(T\right)} \tag{1.8}$$

The difference between the predictions of the one-dimensional and two-dimensional models therefore increases with increasing difference between the temperature at the centerline of the reactor and the temperature near the wall and with increasing overall activation energy.
Improvement of the one-dimensional model is possible if the radial temperature distribution is taken into account when calculating the reaction rate. This was done by *Hagan et al., 1988*, who used a reaction rate-average temperature in their model instead of the average temperature. The correction of the reaction rate that was actually made appeared as a correction-factor α in the overall heat transfer coefficient. The one-dimensional model will be discussed further in Chapter 5, where a new, improved one-dimensional model is proposed.

Two-dimensional reactor models can be divided into three categories. In the most simple form, the temperatures of the fluid and the solid are assumed to be the same the effective radial and axial thermal conductivity and wall heat transfer coefficients lump all the heat- and mass transfer processes occurring in the individual phases. This model is generally referred to as the 'Two-Dimensional Pseudo-Homogeneous Plug-Flow Model'. Sometimes, axial dispersion is considered. If the temperature and/or concentration difference between the phases are significant, the 'Pseudo-Heterogeneous Model', which partly recognizes the systems' two-phase nature, is more suitable. The effective transport parameters in this model still lump the heat transport in both phases, whilst the reaction rate is calculated using the temperature of the solid phase and the concentrations inside the particles. This model has been adopted by *Westerterp et al., 1984*. The temperature and concentrations in both phases

are calculated by solving the following heat and mass balance equations for the **Two-Dimensional Pseudo-Heterogeneous Model**:

Heat balance

Fluid phase:

$$\varepsilon\rho_f c_{p,f}\frac{\partial T_f}{\partial t} = -u_0\rho_f c_{p,f}\frac{\partial T_f}{\partial z} + \frac{\partial}{\partial z}\left(\lambda_{e,ax}\frac{\partial T_f}{\partial z}\right) + \frac{1}{r}\frac{\partial}{\partial r}\left(\lambda_{e,r} r\frac{\partial T_f}{\partial r}\right) + a\alpha_p\left(T_s - T_f\right) \tag{1.9}$$

Solid phase:

$$(1\text{-}\varepsilon)\rho_s c_{p,s}\frac{\partial T_s}{\partial t} = -a\alpha_p\left(T_s - T_f\right) + \sum_{i=1}^{n}\left(-\Delta H_r^i\right)\eta_i R_i\left(\mathbf{c}_s, T_s\right) \tag{1.10}$$

Mass balance component j

Fluid phase:

$$\varepsilon\frac{\partial c_f^j}{\partial t} = -u_0\frac{\partial c_f^j}{\partial z} + \frac{\partial}{\partial z}\left(D_{e,ax}^j\frac{\partial c_f^j}{\partial z}\right) + \frac{1}{r}\frac{\partial}{\partial r}\left(D_{e,r}^j r\frac{\partial c_f^j}{\partial r}\right) + ak_g\left(c_s^j - c_f^j\right) \tag{1.11}$$

Solid phase:

$$(1\text{-}\varepsilon)\frac{\partial c_s^j}{\partial t} = -ak_g\left(c_s^j - c_f^j\right) - \sum_{i=1}^{n}\nu_i^j\eta_i R_i\left(\mathbf{c}_s, T_s\right) \tag{1.12}$$

Here, α_p and k_g are the particle-to-fluid heat and mass transfer coefficients and a is the specific external surface area of the solid per unit reactor volume. The following boundary conditions are applied at the center of the reactor tube and the wall:

$$r = 0: \qquad \frac{\partial c_f^j}{\partial r} = 0 \quad ; \quad \frac{\partial T_f}{\partial r} = 0 \tag{1.13}$$

$$r = R_t: \qquad \frac{\partial c_f^j}{\partial r} = 0 \quad ; \quad -\lambda_{e,r}\frac{\partial T_f}{\partial r} = \alpha_w\left(T_f - T_w\right) \tag{1.14}$$

The true boundary conditions at the inlet and outlet, in case of axial dispersion of heat and mass, should express continuity of concentration and temperature and of mass and heat fluxes. This requires consideration of concentration and temperature before and after the

reactor, which is difficult to implement. Therefore, many different approximate boundary conditions have been proposed from which the most important ones are:

$$z = 0: \quad u_0 c_f^j - D_{e,ax}^j \frac{\partial c_f^j}{\partial z} = u_0 c_0^j \quad ; \quad u_0 \rho_f c_{p,f} T_f - \lambda_{e,ax} \frac{\partial T_f}{\partial z} = u_0 \rho_f c_{p,f} T_0 \tag{1.15}$$

$$z = L: \quad \frac{\partial c_f}{\partial z} = 0 \quad ; \quad \frac{\partial T_f}{\partial z} = 0 \tag{1.16}$$

The subscript '0' is used to refer to a property of reactor feed. These boundary conditions are similar to those proposed by *Danckwerts, 1953* for the one-dimensional model and express continuity of mass and heat flux at z=0 and z=L at steady state. The problem of the definition of the boundary conditions is eliminated if axial dispersion is not considered:

$$z = 0: \quad c_f^j = c_0^j \quad ; \quad T_f = T_0 \tag{1.17}$$

When assuming that the effective diffusivity and conductivity are constant, the following dimensionless numbers and variables can be defined:

$$\Theta = \frac{T - T_0}{|\Delta T_{ad}|^{max}} \quad \text{or:} \quad \Theta = \frac{T\text{-}T_w}{T_0 - T_w} \quad \text{(no reaction)}$$

$$|\Delta T_{ad}|^{max} = \frac{|\Delta H_r|^{max} c_0^*}{\rho_f c_{p,f}} \quad , \quad C^j = \frac{c^j}{c_0^j}$$

$$x = \frac{z}{R_t} \quad , \quad y = \frac{r}{R_t}$$

$$Pe_{h,r} = \frac{u_0 \rho_f c_{p,f} R_t}{\lambda_{e,r}} \quad , \quad Pe_{h,ax} = \frac{u_0 \rho_f c_{p,f} R_t}{\lambda_{e,ax}} \tag{1.18}$$

$$Pe_{m,r}^j = \frac{u_0 R_t}{D_{e,r}^j} \quad , \quad Pe_{m,ax}^j = \frac{u_0 R_t}{D_{e,ax}^j}$$

$$Bi = \frac{\alpha_w R_t}{\lambda_{e,r}} \quad , \quad St_h = \frac{a \alpha_p R_t}{u_0 \rho_f c_{p,f}} \quad , \quad St_m^j = \frac{a k_g^j R_t}{u_0}$$

$$\mathrm{Da} = \frac{R_t}{u_0 c_0} R\left(\mathbf{C}_{0,}\Theta_0\right) \ , \qquad \Re\left(\mathbf{C}_s,\Theta_s\right) = \frac{R\left(\mathbf{C}_s,\Theta_s\right)}{R\left(\mathbf{C}_0,\Theta_0\right)}$$

$$R\left(\mathbf{C},\Theta\right) = \sum_{i=1}^{n} \nu_i^j \eta_i R_i\left(\mathbf{C},\Theta\right)$$

The Damkohler number Da is defined using one of the species involved in the reaction as key component. The temperature can be made dimensionless using any reference temperature or temperature difference. In case of a single reaction, it is convenient to use the adiabatic temperature rise. If the inlet temperature is equal to the wall temperature, the dimensionless temperature will then be between 0 and 1. In this example with multiple reactions, the maximum possible temperature rise is used as reference temperature. This temperature rise is a function of the maximum amount of heat that is released when converting all key component c_0^*.
In the Peclet numbers PE for heat and mass transfer, the tube radius R_t is used as the characteristic length, which follows from the used definition of the dimensionless coordinates. This definition of the Peclet number differs from the one generally used in literature, in which the real characteristic size for mixing is used and which will be referred to as 'Pe'.

Using the above dimensionless numbers and variables, the heat and mass balances of the **pseudo-heterogeneous model** in case of steady state (derivatives with respect to time are zero) can be written as:

Heat balance

Fluid phase:

$$\frac{\partial \Theta_f}{\partial x} = \frac{1}{PE_{h,r}} \frac{1}{y} \frac{\partial}{\partial y}\left(y \frac{\partial \Theta_f}{\partial y} \right) + \frac{1}{PE_{h,ax}} \frac{\partial^2 \Theta_f}{\partial x^2} + St_h\left(\Theta_s - \Theta_f\right) \tag{1.19}$$

Solid phase

$$St_h\left(\Theta_s - \Theta_f\right) - Da\,\Re\left(\mathbf{C}_s,\Theta_s\right) = 0 \tag{1.20}$$

Mass balance

Fluid phase

$$\frac{\partial C_f^j}{\partial x} = \frac{1}{PE_{m,r}^j} \frac{1}{y} \frac{\partial}{\partial y}\left(y \frac{\partial C_f^j}{\partial y} \right) + \frac{1}{PE_{m,ax}^j} \frac{\partial^2 C_f^j}{\partial x^2} + St_m^j\left(C_s^j - C_f^j\right) \tag{1.21}$$

Solid phase:

$$\mathrm{St}_m^j\left(C_s^j - C_f^j\right) + \mathrm{Da}\Re\left(\mathbf{C}_s, \Theta_s\right) = 0 \tag{1.22}$$

with the dimensionless boundary conditions:

$$x = 0: \qquad C_f^j - C_{in}^j = \frac{1}{\mathrm{PE}_{m,ax}}\frac{\partial C_f^j}{\partial x} \qquad \Theta_f - \Theta_{in} = \frac{1}{\mathrm{PE}_{h,ax}}\frac{\partial \Theta_f}{\partial x} \tag{1.23}$$

$$x = \frac{L_t}{R_t}: \qquad \frac{\partial C_f^j}{\partial x} = 0 \qquad -\frac{\partial \Theta_f^j}{\partial x} = 0 \tag{1.24}$$

$$y = 0: \qquad \frac{\partial C_f^j}{\partial y} = 0 \qquad -\frac{\partial \Theta_f^j}{\partial y} = 0 \tag{1.25}$$

$$y = 1: \qquad \frac{\partial C_f^j}{\partial y} = 0 \qquad -\frac{\partial \Theta_f^j}{\partial y} = \mathrm{Bi}\left(\Theta_f^j - \Theta_w\right) \tag{1.26}$$

The presented model differs from the heterogeneous models in which heat transfer through the solid- and the fluid phase are considered separately, see e.g. *Hein et al. 1995, Azevedo et al. 1990* and *Lemcov et al. 1990*. Such approach is rather questionable, because the contact areas between the particles are very small compared to the particle size (*Tsotsas and Schlünder, 1990*) and heat and mass transfer via direct heat exchange between adjacent particles is negligible. Moreover, accounting for the heat transfer through the solid phase leads to a great inconvenience, because this requires additional parameters. Therefore, such models are not considered in this work. The main route via which heat is transferred from one particle to the other is through the fluid phase, as discussed earlier in this chapter. At the wall, heat exchange between the solid and the fluid will also be dominated by transfer through the fluid phase rather than by direct heat exchange between the particles and the wall. From physical point of view, it is therefore not legitimate to separate heat transfer in both phases. Methods to estimate the influence the contribution of solid phase heat conduction into the effective thermal conductivity are well know, e.g. the model of *Bauer and Schlünder 1978 a*.
As mentioned earlier, heat and mass dispersion in axial direction are often neglected. Usually, these terms do not influence the model results in case of long beds, whereas using them greatly increases the computational time.
A radial distribution of the axial fluid velocity can be assumed and, in relation to this, the effective heat transfer parameters can vary over the reactor (*Borkink and Westerterp, 1994*,

Vortmeyer and Haidegger, 1991). In that case the term 'Plug Flow' does no longer apply to the model.
The heat and mass balances of the models used in this work were solved numerically, using the method of finite differences. When possible, the solution of the numerical model was checked by comparison with analytical solutions.

1.4 Correlations for effective transport parameters

In this section, a number of well-known correlations for the effective heat- and mass transfer parameters will be discussed. It is not an objective to make a complete literature overview When examining the relevant literature, one will notice the huge amount of re-evaluations compared to the amount of original experimental data published. Amongst the reviews are those by *Kunii and Smith, 1957, Hennecke and Schlünder, 1973*(α_w), *Hlavacek and Vortruba, 1977, Li and Finlayson, 1977, Bauer and Schlünder, 1978, Specchia et al., 1980, Kulkarnu and Doraiswamy, 1980, Pereira Duarte et al., 1984, Tsotsas and Martin, 1987, Stanckiewicz, 1989, De Azevedo et al., 1990* and *Lemcoff et al., 1990*. Experimental data were provided by *de Wasch and Froment, 1972, Borkink and Westerterp, 1992* and *Martin and Nilles, 1993*.

1.4.1 Radial thermal conductivity

The effective radial thermal conductivity, $\lambda_{e,r}$, in the pseudo-homogeneous and -heterogeneous reactor model lumps all flow-dependent and flow-independent heat transfer mechanisms that contribute to radial heat transfer. Correlations for $\lambda_{e,r}$ usually have the following form:

$$\lambda_{e,r} = \lambda_r^0 + \lambda_r^f , \tag{1.27}$$

in which λ_r^f is the effective thermal conductivity due to fluid convection and λ_r^0 is the effective thermal conductivity due to molecular conduction in the fluid and the solid phase. From experiments it was found that λ_r^f is proportional to the fluid velocity and the particle size:

$$\lambda_r^f = k u_0 d_p^e \tag{1.28}$$

In case of non-spherical particles, the effective particle diameter d_p^e is usually calculated as the diameter of a sphere that has the same external surface area or volume. In this work, the

volume-equivalent particle diameter d_p^v is used. For a cylinder with a diameter d and a height h, this is:

$$d_p^v = d\left(\frac{3}{2}\frac{h}{d}\right)^{\frac{1}{3}} \tag{1.29}$$

Correlation (1.27) is usually presented in dimensionless form using a molecular Peclet number (*Agnew and Potter 1970, Olbrich and Potter 1972*):

$$Pe_h^0 = \frac{u_0 \rho_f c_{p,f} d_p^v}{\lambda_f} = RePr\,, \tag{1.30}$$

so that:

$$\frac{\lambda_{e,r}}{\lambda_f} = \frac{\lambda_r^0}{\lambda_f} + \frac{Pe_h^0}{Pe_{h,r}^\infty}\,, \tag{1.31}$$

in which $Pe_{h,r}^\infty$ is equal to Pe_r^f at sufficiently high fluid velocity:

$$u \to \infty \qquad Pe_r^\infty = Pe_{h,r}^f = \frac{u_0 \rho_f c_{p,f} d_p^v}{\lambda_r^f} \tag{1.32}$$

For infinitely wide beds, the theoretical value of $Pe_{h,r}^\infty$ is 8. As the number of particles on the tube diameter, or aspect ratio,

$$N = \frac{D_t}{d_p^v} \tag{1.33}$$

decreases, the value of $Pe_{h,r}^\infty$ increases, which is attributed to an increased porosity near the wall. With decreasing aspect ratio, the importance of the porosity distribution becomes more important. *Bauer and Schlünder, 1978a* give the following correlation for the dependence of $Pe_{h,r}^\infty$ on the aspect ratio, which is the same as the correlation that was found by *Schlünder et al. 1966* for radial mass transport:

$$Pe_{h,r}^\infty = 8\left[2 - \left(1 - \frac{2}{N}\right)^2\right] \tag{1.34}$$

A similar quadratic dependence on the aspect ration has been reported by *Fahien and Smith, 1955* for the dependence of the Peclet number for radial mass transfer in packings of spherical particles:

$$Pe_{m,r}^{\infty} = C\left(1+\frac{19.4}{N^2}\right) \tag{1.35}$$

with C between 8 and 12. Eq. (1.35) was adopted by *Specchia et al. 1980,* who used experimental data obtained using packings of spheres, cylinders and Raschig rings to obtain:

$$C = 8.65\frac{d_p^v}{d_p^a} \tag{1.36}$$

When applying eq. (1.36), the aspect ratio must be defined as

$$N = \frac{D_t}{d_p^a} \tag{1.37}$$

In equations (1.36) and (1.37), $d_p{}^a$ is the equivalent diameter of a sphere with the same surface area as the particles inside the bed. In case of cylindrical particles:

$$d_p^a = d\sqrt{\frac{1}{2}+\frac{h}{d}} \tag{1.38}$$

The term λ_r^0, in eq. (1.27) lumps the contributions of molecular heat conduction in the solid and the fluid phase and heat radiation between the particles. It is generally assumed that λ_r^0 is independent of the fluid velocity, though extrapolation of the experimentally obtained values of $\lambda_{e,r}$ to u=0 do not always give the expected values of λ_r^0 (*Specchia et al., 1980, Dixon, 1988*).

The best known correlations for $\lambda_r{}^0$ were developed by *Yagi and Kunii, 1957, Smith, 1960, Zehner and Schlünder, 1970* and *Bauer and Schlünder, 1978 b*. The correlation proposed by Yagi and Kunii lumps conduction through the solid and the fluid, as well as heat radiation:

$$\frac{\lambda_r^0}{\lambda_f} = \varepsilon\left(1+\beta\alpha_{rv}\frac{d_p}{\lambda_f}\right)+\frac{\beta(1-\varepsilon)}{\left[\left(\frac{1}{\varphi}+\frac{d_p(\alpha_{rs}+\alpha_{ss})}{\lambda_f}\right)^{-1}+\gamma\frac{\lambda_f}{\lambda_s}\right]} \tag{1.39}$$

Here ε is the average bed porosity. α_{rv} and α_{rs} are the effective heat transfer coefficients for heat exchange between the solid surfaces and the voids due to radiation and α_{ss} encompasses direct heat transfer through the solid-solid contact points. β, γ and φ are geometrical parameters. The advantage of this model is its simplicity when heat transfer due to radiation and direct particle-to-particle heat transfer may be neglected:

$$\frac{\lambda_r^0}{\lambda_f} = \varepsilon + \frac{\beta(1-\varepsilon)}{\left[\varphi + \gamma\frac{\lambda_f}{\lambda_s}\right]} \tag{1.40}$$

The values of the geometrical parameters may be estimated theoretically, or can be obtained from experiments. For all packings, β should be between 0.9 and 1. Kunii and Smith used γ=2/3. In the later article by Yagi and Kunii (*Yagi and Kunii, 1959*), γ=1 was used for packings of spheres and cylinders (h=d). The value of φ is calculated as:

$$\varphi = \varphi_2 + (\varphi_1 - \varphi_2)\frac{\varepsilon - 0.26}{0.216} \qquad ; \qquad 0.26 \le \varepsilon \le 0.476$$

$$\varphi_1 = \frac{1}{2}\frac{\frac{2}{3}\left(\frac{\kappa-1}{\kappa}\right)^2}{\ln\left(\kappa - 0.58(\kappa-1)\right) - 0.42\frac{\kappa-1}{\kappa}} \; ; \varphi_2 = \frac{1}{2}\frac{\frac{1}{4\sqrt{3}}\left(\frac{\kappa-1}{\kappa}\right)^2}{\ln\left(\kappa - 0.925(\kappa-1)\right) - 0.075\frac{\kappa-1}{\kappa}} \tag{1.41}$$

where κ is the ratio of the thermal conductivities of the solid and the fluid. *Bauer and Schlünder, 1978b* calculated the effective thermal conductivity of packings of different particle shape and size. After omitting the contributions of heat radiation, direct particle-to particle heat transfer and the influence of the system pressure, the following expression for the effective stagnant thermal conductivity was obtained:

$$\frac{\lambda_r^0}{\lambda_f} = \left(1-\sqrt{1-\varepsilon}\right) + \frac{2\sqrt{1-\varepsilon}}{1-B\kappa^{-1}}\left[\frac{B\left(1-\kappa^{-1}\right)}{\left(1-B\kappa^{-1}\right)^2}\ln\left(\frac{\kappa}{B}\right) - \frac{B-1}{1-B\kappa^{-1}} - \frac{B+1}{2}\right] \tag{1.42}$$

$$B = C_f\left(\frac{1-\varepsilon}{\varepsilon}\right)^{1.11} \; ; C_f = 1.25 \text{ (sphere), } 2.5 \text{ (cylinder) or } 2.5\left(1+\left(\frac{d_i}{d_p}\right)\right) \text{ (rings)}$$

Fig. 1.5 shows the values of λ_r^0 according to (1.40) and (1.42), together with the correlation of *Specchia et al., 1980*, who optimized the parameter φ in the model of Kunii and Smith to fit experimental data of different investigators. In gas-solid systems, direct experimental validation of correlations for λ_r^0 is difficult due to the occurrence free convection caused by the presence of temperature gradients. In this work, λ_r^0 is calculated according to eq. (1.42), which is the most used and best validated correlation. At the experimental conditions used in this work, , the differences between the correlations are small.

Dixon and Cresswell, 1979 considered the full heterogeneous reactor model in which heat transfer in both phases is separated. By comparing this model to the pseudo-homogeneous one, they obtained the following expression for the effective overall radial thermal conductivity to be used in the pseudo-homogeneous model:

$$\lambda_{e,r} = \lambda_r^f + \lambda_r^0\left(1+\frac{8\lambda_r^f}{\alpha_w^f D_t}\right)\left[1+\frac{\frac{16}{3}\lambda_r^0\left(\frac{1}{\alpha_w^s d_p}+\frac{0.1}{\alpha_p}\right)}{(1-\varepsilon)\left(\frac{D_t}{d_p}\right)^2}\right]^{-1} \tag{1.43}$$

Except in the work of *Dixon and Cresswell, 1979*, all correlations for $\lambda_{e,r}$, except that of assume that the effective radial thermal conductivity is proportional to the fluid velocity. The proportionality coefficients can be very different (see Chapter 3). This is due to the fact that individual correlations are mostly based on experimental data obtained for a small range of reactor- and particle sizes, using particles that are more or less ideally shaped. Since the values of the heat transfer parameters depend on the experimental procedure and the calculation method, it is difficult to combine the results of different investigators. Most

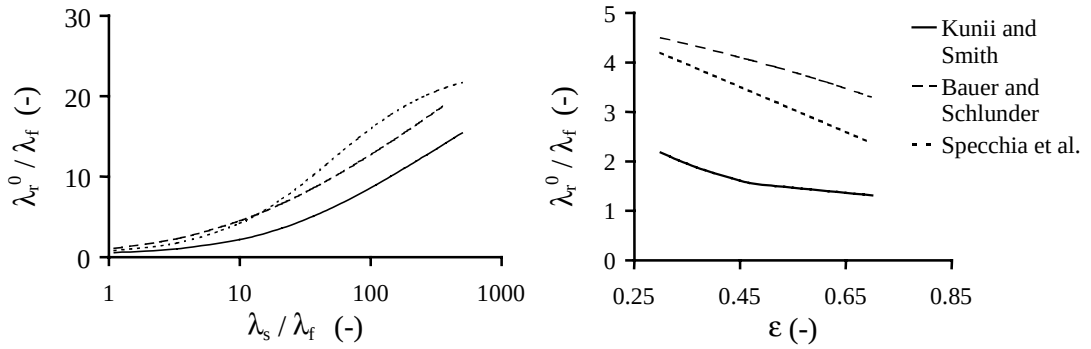

Fig. 1.5 Effective thermal conductivity of a packing with stagnant fluid, according to different models. Left: as function of ratio λ_s/λ_f at ε=0.4. Right: as function of porosity for λ_s/λ_f=10 (as for catalyst used in this investigation).

correlations were derived for heat transfer in packings of spheres and packings of cylinders with a height-to-diameter ratio close to one. If, as in this work, the height-to-diameter ratio of the catalyst cylinders is larger, correlations are likely to fail to precisely predict the effective radial thermal conductivity. The relationships between $\lambda_{e,r}$ and the fluid velocity that are used in this work were derived from our own experimental data.

1.4.2 Axial thermal conductivity

As in the case of the effective radial thermal conductivity, the effective axial thermal conductivity in the pseudo-homogeneous and pseudo-heterogeneous model is generally described as the sum of a static contribution λ_{ax}^{0} and a dynamic contribution:

$$\lambda_{e,ax} = \lambda_{ax}^{0} + \lambda_{ax}^{f} \tag{1.44}$$

The flow-independent part of the effective axial thermal is identical to that of the effective radial thermal conductivity. The determination of the effective axial thermal conductivity from experimental data obtained in wall-cooled or wall-heated tubular reactors is rather difficult and imprecise, as will be discussed in paragraph 1.5. If no chemical reaction takes place, the sensitivity of the steady-state temperature profiles towards the axial heat dispersion coefficient is usually small. Correlations for the effective axial thermal conductivity are therefore either obtained by measuring back-propagation of heat against the direction of fluid flow (see e.g. *Votruba et al., 1972*), or by applying a (periodic) variation to the inlet temperature. *Votruba et al., 1972* obtained the following empirical correlation for the Peclet number for heat dispersion in axial direction for packings of spheres and rings of different materials:

$$\frac{1}{Pe_{h,ax}} = \frac{\lambda_{e,ax}}{u_0 \rho_f c_{p,f} d_p^v} = \frac{\lambda_{ax}^{0}}{\lambda_f}\left(Pe_h^0\right)^{-1} + \frac{14.5}{d_p\left(1 + C\left(RePr\right)^{-1}\right)} \qquad (Re<1000) \tag{1.45}$$

In this equation, C is a constant depending on the properties of the solid and of the aspect ratio and has a value between 0 and 5. At turbulent conditions (Re>100), axial mixing of mass in the fluid phases can be approximated as the resulting effect of mixing in a cascade of L/d_p ideal mixers. In this case, the limiting value of the fluid phase Peclet number $Pe_{m,ax}^{\infty}$ should be equal to 2 (*Westerterp et al. 1984*). Since axial heat dispersion in the fluid phases is considered to be analogous to that of mass, this limiting value is also generally used for $Pe_{h,ax}^{\infty}$.

Similar to the derivation of the effective radial thermal conductivity in the pseudo-homogeneous and –heterogeneous model, *Dixon and Cresswell, 1979* obtained the following relationship for the effective axial thermal conductivity:

$$\lambda_{e,ax} = \lambda_{ax}^{f} + \lambda_{ax}^{0}\left[1+\frac{\frac{16}{3}\lambda_{ax}^{0}\left(\frac{1}{\alpha_w^s d_p^v}+\frac{0.1}{\alpha_p}\right)}{(1-\varepsilon)\left(\frac{D_t}{d_p^v}\right)^2}\right]^{-1} \tag{1.46}$$

In this work, axial dispersion is generally not included in the used reactor models. If it is used, Pe_{ax} is set equal to 2.

1.4.3 Wall heat transfer coefficient

As in case of the effective radial and axial thermal conductivity, the wall heat transfer coefficient is commonly defined as the sum of a flow-dependent and a flow-independent heat transfer coefficient:

$$\alpha_w = \alpha_w^0 + \alpha_w^f \tag{1.47}$$

In correlations, α_w is usually expressed in the form of a dimensionless Nusselt number Nu:

$$Nu_w = \frac{\alpha_w d_p^v}{\lambda_f} \tag{1.48}$$

Expressions for the contributions of convection usually have the form:

$$Nu_w^f = \frac{\alpha_w^f d_p^v}{\lambda_f} = C \quad Re^{n_1} Pr^{n_2}, \tag{1.49}$$

in which C is a constant depending on the aspect ratio. Some empirical correlations that are frequently referred to are given below:

Li and Finlayson, 1977:

$$\begin{aligned} &\text{Cylinders*:} \quad Nu_w = 0.16\ Re^{0.93} \quad ; \quad 20 < Re < 800 \quad ; \quad 5 < N < 20 \\ &\text{Spheres:} \quad\ Nu_w = 0.17\ Re^{0.79} \quad ; \quad 20 < Re < 7600 \quad ; \quad 3 < N < 20 \end{aligned} \tag{1.50}$$

* $d_p = 6V_p/A_p$

Dixon and Paterson, 1978:

$$Nu_W = 11.46\ N^{-0.5} Pr\left(0.11\ Re + 20.64\right) Re^{-0.262}$$

$$35 < Re < 500 \ ; \ 5 < N < 12 \tag{1.51}$$

Martin and Nilles, 1993:

$$Nu_w^f = 0.19\ Re^{0.75} Pr^{-0.42}, \tag{1.52}$$

with (using data of *Borkink, 1991*):

$$Nu_w^0 = \frac{\alpha_w^0 d_p^v}{\lambda_f} = \left(1.3 + \frac{5}{N}\frac{\lambda_{e,r}}{\lambda_f}\right) \tag{1.53}$$

Many more correlations are available in literature and experimental data on the wall heat transfer differ quite markedly (e.g. *Hennecke and Schlünder 1973, Tsotsas and Schlünder 1990, Cybulski et al. 1997*). *Lemcoff et al. 1990* give an overview of the correlations proposed by 13 different investigators, who report orders with respect to Re between 0.45 and 1.

Attempts were made to provide some theoretical background for the experimental correlations for the wall heat transfer coefficient.
Specchia et al., 1979 predicted the flow-independent contribution to the wall heat transfer coefficient by applying the approach of *Kunii and Smith, 1960* used to estimate the value of λ_r^0 (1.41):

$$\frac{\alpha_w^0 d_p^v}{\lambda_f} = 2\varepsilon + \frac{1-\varepsilon}{\frac{\lambda_f}{\lambda_s}\gamma_w + \varphi_w} \tag{1.54}$$

Eq. (1.54) was derived assuming that the wall zone has a width of half a particle diameter ($\gamma_w = \gamma/2$). Stagnant heat conduction occurs in parallel through a fraction ε of the surface of

the wall that is not covered by particles and through a fraction (1-ε) that is covered. The heat flux through the latter fraction of the surface is calculated according to a series-configuration of the particles and the fluid. γ_w and φ_w depend on the geometry of the contact between the wall and the surface of the particles. φ_w is the characteristic distance between the wall and the surface of the particles and depends on the aspect ratio of the bed. The authors obtained the following correlation for φ_w using experimental data:

$$\varphi_w = 0.0024N^{1.58} \tag{1.55}$$

For the convective contribution, only an empirical correlations were used:

$$\begin{aligned} \frac{\alpha_w^f d_p^v}{\lambda_f} &= 0.0835Re^{0.91} \quad 10 \le Re \le 1200 \\ \frac{\alpha_w^f d_p^v}{\lambda_f} &= 1.23Re^{0.53} \quad 1200 \le Re \le 10000 \end{aligned} \tag{1.56}$$

Hennecke and Schlünder, 1973 simultaneously measured the heat and mass transfer coefficients at the tube wall for different types of packing by evaporation of water through the wall. They proposed the following correlation for the wall Nusselt number, based on literature and their own data:

$$Nu_w = \frac{\alpha_w d_p^a}{\lambda_f} = \frac{Nu_p + C_a \pi \left(\frac{\lambda_{e,r}}{\lambda_f} - 1 \right)(1-K) + Nu_r}{1 + \frac{L/D_t}{Pe_p} c_d} \tag{1.57}$$

with:

$$\begin{aligned} K &= \frac{1}{Nu_p} \quad \text{(spheres)} \quad ; \quad K = \frac{1}{Nu_p^{0.5}} \quad \text{(cylinders. h=d)} \\ K &= \frac{1.5}{Nu_p^{0.33}} \quad \text{(cylinders, h=2d, Raschig rings)} \end{aligned} \tag{1.58}$$

Nu_r in eq. (1.57) accounts for radiation between the wall and the particles. To describe the observed length dependency of α_w and $\lambda_{e,r}$, a term L/D_t was introduced. Nu_p stands for the contribution of convective heat transport, which is proportional to that along a flat surface

with a length d_p^a (area-equivalent diameter of a sphere), multiplied by a constant C_b which accounts for the increase of the heat transfer rate due to the presence of the particles:

$$Nu_p = \frac{C_b}{Pr^{1/6}} \sqrt[4]{0.194 Pe_p^2 + 0.34 \cdot 10^{-4} Pr^{-2/3} Pe_p^3} \tag{1.59}$$

with:

$$Pe_p = \sqrt{\left(\frac{u_w d_p^a \left(\rho c_p\right)_f}{\lambda_f} \right)^2 + C_c} \qquad ; \qquad u_w = \frac{\overline{u_0}}{\varepsilon} \frac{K + \left(P+2\right)/2}{K+1} \tag{1.60}$$

Near the wall, the axial fluid velocity, u_w, is higher than at the core of the bed and is calculated from an analytical expression given by *Schwartz and Smith 1953*. By using this velocity, the authors claim to partially resolve the discrepancy between the values of α_w obtained by different investigators. The thickness of the zone over which the temperature drop occurs is much smaller than the particle diameter and much smaller than half the particle diameter, which was used by *Yagi and Kunii, 1959*. Despite its complexity, the model is to a fair extent empirical.

It is disputed whether α_w depends on the axial position and experimental evidence often attributed to experimental errors (measurement of temperature profiles above the packing instead of inside the bed, temperature gradients along the wall and incorrect inlet temperature profile.

The influence of the velocity profile on both $\lambda_{e,r}$ and α_w was investigated by *Tsotsas and Schlünder, 1990*, who question the validity of the α_w-model in case of low Re numbers. The authors state that only at large molecular Peclet numbers Pe_h^0, the assumption of a temperature drop at the wall can be justified. They calculate the velocity profile within the packing from a porosity distribution using the extended Brinkman-equation and estimate the thickness of the stagnant fluid layer at the wall to be:

$$\frac{\delta_{stag}}{d_p} = \left(\frac{1.75\left(1-\varepsilon\right)}{\varepsilon^3} Re \right)^{-1/2}, \tag{1.61}$$

so that, with $\alpha_w = \lambda_f / \delta_{stag}$:

$$Nu_w = \frac{\alpha_w d_p}{\lambda_f} = \left(\frac{1.75\left(1-\varepsilon\right)}{\varepsilon^3} Re \right)^{\frac{1}{2}} \tag{1.62}$$

Eq. (1.62) gives values of Nu_w that are up to 10 times lager than those according to the empirical correlations of *Hennecke and Schlünder, 1972,* and *Specchia et al., 1980*.

In the approach of *Dixon and Cresswell, 1979*, the effective wall heat transfer coefficient is closely related to the effective thermal conductivity. The full expression of the wall heat transfer coefficient is rather extensive and contains parameters as the fluid-to-particle heat transfer coefficient and a solid-Biot number $Bi_s = \alpha_w^s R_t / \lambda_r^0$:

$$Nu_w = \frac{8\beta}{N} + Nu_w^f \left(1 + \beta \frac{Pe_r^f}{Pe_h^0}\right);$$

$$\beta = \frac{\lambda_r^0/\lambda_f}{\frac{8}{N_s} + \frac{Bi_s + 4}{Bi_s}} \;;\; N_s = \frac{1.5(1-\varepsilon)N^2}{\frac{\lambda_r^0}{\lambda_f}\left(\frac{1}{Nu_p} + \frac{0.1}{\lambda_s/\lambda_f}\right)} \tag{1.63}$$

Instead of this correlation, the authors recommend to correlate the wall heat transfer coefficient to the effective radial thermal conductivity of the bed in terms of the Biot number:

$$Bi = \frac{\alpha_w R_t}{\lambda_{e,r}} = 1.5 \; N \; Re^{-0.25} \tag{1.64}$$

The use of correlations of α_w in terms of the Biot number is to be preferred to the commonly used expressions for the wall Nusselt number. In reactor models, α_w is used only in combination with $\lambda_{e,r}$, as in the Biot number. Unfortunately, too few correlations for Biot are available. In Chapter 3, correlations for α_w, taken from literature, are compared to the results of the experiments of this investigation. In the present work, none of the correlations in the literature were applied. It was only assumed that α_w increases with the fluid flow rate according to a power function of Re.

1.4.4 Fluid-to-particle heat and mass transfer

In this section, correlations for the effective mass and heat transfer coefficients between the solid particles and the fluid will be discussed, which were used in the reactor models to calculate the temperature and the concentrations at the surface of the solids. Literature data on particle-to-fluid heat and mass transfer are rather consistent at values of Re larger than 500. At low Reynolds numbers, large differences can be observed, which are caused by flow maldistribution (wall channeling), axial dispersion or incorrect prediction of the radial concentration profile (*Rexwinkel et al., 1997*). Since, in many cases, the mechanisms of heat

and mass transfer are similar, the Chilton-Colburn analogy (*Westerterp et al., 1984*) is often used:

$$\mathrm{Nu} = \mathrm{Sh}\left(\frac{\mathrm{Pr}}{\mathrm{Sc}}\right)^{\frac{1}{3}} \tag{1.65}$$

At low Re, direct or indirect heat transfer between particles has to be taken into account when calculating the particle Nusselt number. As a result, empirical correlations for heat transfer between particles and fluid may differ from mass transfer correlations. *Thoenes and Kramers, 1958* determined mass transfer coefficients in packed beds of spheres with flowing liquid and gas. A distinction is made between laminar, turbulent and stagnant contributions, which appear in this order:

$$\mathrm{Sh} = \left(1.26\mathrm{Re}^{1/3}\mathrm{Sc}^{1/3}\right) + \left(0.054\mathrm{Re}^{0.8}\mathrm{Sc}^{0.4}\right) + 0.8\mathrm{Re}^{0.2} \tag{1.66}$$

The weak dependence on Re of the stagnant term is explained as an increasing penetration of 'quiet corners' between the particles.

Most reliable seem to be the correlations by *Gnielinski, 1982*. He made a thorough investigation of available literature data on gas and liquid heat and mass transfer in packed beds of spheres, cylinders, Raschig rings and other shapes and obtained the following correlation:

$$\mathrm{Sh_p} = \mathrm{Nu_p} = \mathrm{f_a}\,\mathrm{Nu_{sp}} \;\; ; \;\; \mathrm{Nu_{sp}} = 2 + \sqrt{\mathrm{Nu_{lam}^2} + \mathrm{Nu_{turb}^2}}$$

$$\mathrm{Nu_{lam}} = 0.664\mathrm{Pr}^{1/3}\left(\mathrm{Re}/\varepsilon\right)^{1/2} \quad ; \quad \mathrm{Nu_{turb}} = \frac{0.037\left(\mathrm{Re}/\varepsilon\right)^{0.8}\,\mathrm{Pr}}{1 + 2.443\left(\mathrm{Re}/\varepsilon\right)^{-0.1}\left(\mathrm{Pr}^{2/3} - 1\right)} \tag{1.67}$$

In the above equation, the effective diameter for particle heat and mass transfer is $\mathrm{d_p^a}$, the area-equivalent diameter of a sphere. Compared to single particles, the heat and mass transfer coefficients in a packed bed are higher by a factor $\mathrm{f_a}$, which is 1.6 for spheres and cylinders at $\mathrm{Pe_h^0} > 500$. *Martin, 1978* showed that the eq. (1.67) also holds for smaller values of $\mathrm{Pe_h^0}$, provided that the radial distribution in the axial fluid velocity is taken into account. In Fig. 1.6, some well known correlations for Sh and Nu are compared. In this work, that of Gnielinski will be used, which was derived using the most extensive set of experimental data. For the derivation of this correlation, literature data were carefully re-examined to exclude the possible influence of wall channeling.

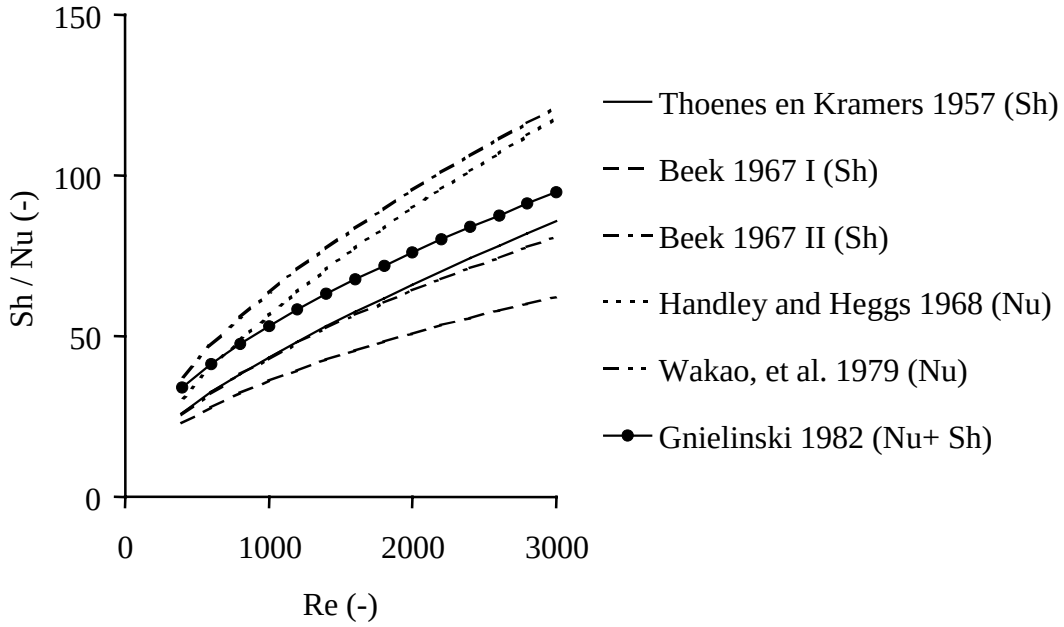

Fig. 1.6 Comparison of Nu and Sh correlations by *Thoenes and Kramers, 1957*: 100<Re<3500; *Beek, 1967*, taken from *Westerterp et al., 1983*, I: 5<Re<500; II: 50<Re<2000; *Handley and Heggs, 1968*, taken from *Dixon and Cresswell, 1979*: Re>100, N>8; *Wakao et al., 1979; Gnielinski, 1982*: $500<Re<2\cdot10^4$.

1.4.5 Axial and radial dispersion of mass

Dispersion of mass is analogous to dispersion of heat if the transport through the solid phase is negligible. In case of liquids, the contribution of molecular diffusion is negligible at Re>1. In gases, the molecular diffusivity is larger by several orders of magnitude, so that the effective diffusivity is determined by convective mixing (dispersion) and molecular diffusion. In literature, much attention is paid to the investigation of mass dispersion in axial direction at low Reynolds numbers. At Re larger than 300-400, correlations for axial dispersion in beds with a large aspect ration agree quite well. At lower aspect ratios, as are typical for tubular reactors, axial and radial dispersion coefficients are influenced by the radial distribution of the porosity and the axial fluid velocity. Gunn (*Gunn, 1969, 1987*), interprets axial dispersion as the result of mass exchange between fluid streams with different axial velocities. The author states that this physical interpretation conflicts with the use of a mass balance equation of the parabolic type to calculate the concentration distribution inside a packed bed. In case of point-injection of tracer in a packed bed, such a model predicts a large mass flux against the direction of flow because of the extreme concentration gradients near the injection point. This predicted back-propagation of mass cannot be observed experimentally (*Hiby, 1963* and *Benneker et al., 2002*). *Westerterp et al., 1995* developed a new, hyperbolic model, which is

in accordance with the physical nature of axial dispersion in packed beds. This model will be discussed in section 1.7.
As discussed in section 1.4.2, axial dispersion of heat is usually not significant compared to heat transport by convection an radial dispersion. The same holds true for axial mass dispersion. If axial dispersion is used, the mostly recommended value of $Pe_{m,ax}=2$ will be used. The flow-dependent part of the Peclet number for radial mass dispersion will be taken equal to that for radial heat transfer. The flow-independent part of the radial mass dispersion coefficient is calculated as:

$$D_r^0 = \frac{\varepsilon}{\tau} D_m , \tag{1.68}$$

in which ε and τ are the porosity and tortuosity of the bed and D_m is the molecular diffusion coefficient.

1.5 Uncertainty in heat transport parameters

The main reasons for the differences between the values of $\lambda_{e,r}$, $\lambda_{e,ax}$ and α_w obtained by different investigators are the strong correlation amongst these parameters (*Tsang et al., 1976, Borkink et al., 1993*), experimental errors and the non-uniform structure of the bed.
As Bi tends to increase at lower fluid velocities, the sensitivity of the models' prediction with respect to Bi decreases to become almost negligible at Biot ≈10. Small experimental errors will then lead to a large uncertainty of the observed Biot number.

Many sources of experimental errors can be identified, which can significantly influence the distribution of the total resistance to heat transfer over $\lambda_{e,r}$, $\lambda_{e,ax}$ and α_w. Heat transfer limitation in the cooling or heating jacket, together with conduction through the wall in axial direction, can cause the wall temperature to change over the length and/ or cause a non-uniform temperature distribution at the inlet of the reactor. Furthermore, the number of thermocouples used to measured the radial temperature profiles and their positions may affect the outcome. To minimize the correlation between α_w and $\lambda_{e,r}$, the temperature should be measured as close to the wall as possible. However, the minimum distance between the thermocouples and the wall is often taken rather large to avoid bending of the thermocouples of the temperature probe when the temperature probe is inserted into the reactor.
The relationship between the derived values for α_w and $\lambda_{e,r}$ is strongly dependent on the temperatures measured closest to wall, where the largest temperature gradients occur. Exactly here the risk of experimental errors is largest. Very often, radial temperature profiles are not measured inside the bed, but above it, to avoid disturbing of the packing. These temperature profiles do not necessarily represent the temperature profile inside the bed. Moreover, mixing

of the fluid after the bed can change the derived values of $\lambda_{e,r}$ and $\alpha_{w,}$ since the height of the packing is not constant, but, by its nature, varies over approximately 0.5-1 particle diameter.
When performing heat transfer experiments without chemical reaction, it is rather difficult to control the boundary conditions. Temperature gradients inside the reactor wall will easily develop. In most experiments, a 'calming zone' before the test section is used to smoothen the inlet temperature and to avoid a change of the distribution of the axial fluid velocity. At the interface between the calming section and the reactor, the wall temperature can hardly be forced to be a step function. Even in case of boiling liquid or condensing fluid as heating or cooling agent, problems will arise at the connection of two sections due to heat conduction through the wall and poor heat transfer at the bottom and top of the cooling and heating jackets. The uncertainty in the boundary conditions is one of the reasons why measurement of heat dispersion in axial direction is almost impossible in practice, as was pointed out by *Dixon, 1988*, who stated that the axial thermal conductivity was used merely as a fitting parameters to compensate for the non-uniformity of the wall temperature. *Borkink 1991* recommends to neglect axial dispersion of heat at Re>50, since he did not observe any improvement of his model, provided that a measured inlet temperature distribution was used in the boundary condition.
A length-dependency of the radial heat transport coefficient has been reported by different investigators (*Borkink, 1991, Dixon, 1985a and b, De Wasch and Froment, 1972, Li and Finlayson, 1977, Martin and Nilles, 1993, Winterberg et al, 2000 a, b*). Different causes for this length-dependency have been mentioned in literature, such as the neglecting of a non-uniform wall temperature (Dixon) or inlet temperature (Borkink). Heat conduction along the thermocouples and their support can also cause an apparent length dependency of the effective radial thermal conductivity (see Appendix F).

Because the division of the resistance to radial heat transfer over α_w and $\lambda_{e,r}$ is subject to experimental errors and to the interpretation of the measured temperature fields, one should avoid combination of correlations obtained by different investigators. This statement is supported by the fact that the overall heat transfer coefficient in the one-dimensional model, in which the effective radial thermal conductivity and wall heat transfer coefficient are lumped, exhibits much less variation when comparing the results of different investigators.

1.6 Discrepancy between heat transfer coefficients measured with and without reaction

Different authors (*Hall and Smith, 1949, Hoffman, 1979, Schwedock et al. 1989, Schouten et al. 1994*) have reported a discrepancy between the effective heat transfer parameters obtained from experiments with and without chemical reaction. This discrepancy can have difference

causes, as, for instance, errors in the heat transfer measurements with and without reaction, errors in the kinetics used as input for the model, or the use of an inappropriate reactor model. Kinetic experiments are usually performed in reactors in which conditions are very different from those in a tubular reactor. When calculating the reaction rates from measured conversions, usually corrections have to made to account for the intra- and extra-particle heat and mass transport limitations. The latter may be uncertain or may vary over the reactor. When using differential packed bed-type reactors for kinetic measurements, it is far from easy to avoid a temperature increase over the reactor due to the large heat of reaction. Aging of the catalyst caused by heating and exposure to the feed might be different. In situ pretreatment of the catalyst in order to increase the reaction rate and / or selectivity can be performed at better controlled conditions in a kinetic reactor than in a full scale tubular reactor, in which temperature and concentration gradients are more difficult to avoid.

A model that is often used for the calculation of the radial and axial temperature profiles is the pseudo-heterogeneous model with axial and radial dispersion superimposed on plug flow in axial direction, as described in section 1.3. In this model, the heat and mass dispersion fluxes are calculated according to Fick's law for mass dispersion and Fourier's law for heat conduction. The application of these laws to packed bed reactors is questionable. In the kinetic theory of gases, for instance, the use of these laws is only allowed if the distance is larger than 500 times the mean free path of the molecules. In tubular packed bed reactors, in which the effective mixing length d_p replaces the mean free path, the aspect ratio is usually smaller than 10.

Even on a macroscopic scale, radial temperature and concentration profiles in the packing are not smooth, like in the case of molecular conduction and diffusion in stagnant media, but show large oscillations in radial and angular direction. The effective heat transfer parameters measured at reacting conditions may be different from the values measured at non-reacting conditions, since the reaction rate at the angulary averaged temperature is different from the angulary averaged reaction rate.

The non-uniformity of the packed bed may cause the local particle-to-fluid heat and mass transfer coefficients to be different from the predicted values, so that the temperature of the particles can differ from the predictions of the pseudo-heterogeneous model (see Fig. 1.7).

For reasons discussed in section 1.5, the division of the total resistance to heat transfer between α_w and $\lambda_{e,r}$ is subject to experimental errors and to the interpretation of the experimental data. In case of no reaction, the reactor model is often not sensitive to the combination of the heat transfer parameters, as long as the overall heat transfer coefficient U remains constant. This sensitivity increases if a chemical reaction is performed, which is due to the non-linear dependence of the reaction rate on temperature. A change of the estimated temperature near the reactor wall affects the calculated reaction rate over a relatively large fraction of the cross-sectional area.

The effective heat transfer parameters depend on the radial distribution of the porosity and the axial fluid velocity. The importance of such distributions was indicated by, for instance, *Giese et al., 1998, Vortmeyer and Schuster, 1983, Vortmeyer, 1987, Bey and Eigenberger, 1996, Stephenson and Stewart, 1986, Borkink et al., 1992, White and Tien, 1987, Lesage et al. 1999* and *Legawiec and Ziólkowski, 1995.*

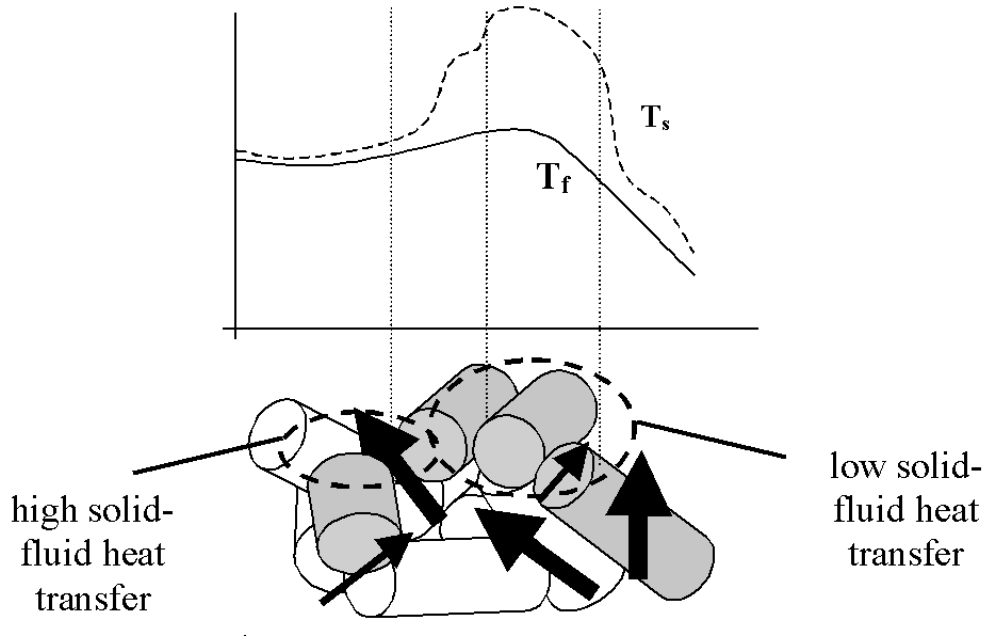

Fig. 1.7 Influence of the flow pattern and fluid-to particle heat transfer on the developing radial solid and fluid temperature profile

Measurement of the velocity distribution at the bed exit might not be entirely reliable, since the velocity profiles rapidly changes when the fluid leaves the packing (*Kalthoff and Vortmeyer, 1979, Cybulski et al., 1997*). Measurement of the fluid velocity within the packing is rather difficult and may give values that depend on the position of the measuring probe relative to the particles and on possible disturbance of the bed by the probe. The radial velocity distribution can be estimated from the porosity distribution and the total pressure drop over the bed. The pressure drop is calculated using the Brinkman or Ergun equation, which were derived to describe the pressure drop in beds with a high aspect ratio, in which wall channeling is not important. Application of these correlations to beds with an aspect ratio less than 10 is not very realistic, since the fluid velocity may double over a distance less than a particle diameter. Investigators disagree on the boundary conditions at the wall that should be applied to the velocity profile. It is not very clear how to define the velocity. Within the packing, both magnitude and direction of the velocity vary locally on a scale less than a particle diameter. Correlations for the velocity distribution based on the average value are therefore more or less empirical.

1.7 Other types of reactor models

In recent years, new models have been developed for the description of wall-cooled packed bed reactors, such as fluid-dynamics models and the wave model (*Westerterp et al., 1995a and b*). Though the standard dispersion model, discussed in the previous part of this chapter, gives satisfactory results for most packed bed problems, it does have one major shortcoming. Since the model is of the parabolic type, it predicts an infinite speed of propagation of a signal. From physical point of view, this is incorrect. Experimental data are available that demonstrate that the two-dimensional standard dispersion model with axial dispersion is unable to accurately describe tracer propagation in a packed bed (*Hiby, 1963, Benneker et al., 2002*). Due to the parabolic nature of the model, it predicts propagation of mass against the direction of fluid flow, which contradicts these experiments. At not too low fluid velocities, mainly fluid convection is responsible for dispersion of heat and mass. This was recognized by *Stewart, 1965*, who proposed a model of a hyperbolic type, although without explanation of its meaning and its derivation.

In Chapter 4, the heat transport parameters will be discussed in the framework of the wave model, which is a hyperbolic model that was derived using a non-equilibrium approach: the heat and mass flux are not directly caused by the temperature and concentration gradients, but are the net result of migration of fluid elements with different temperatures, concentrations and fluctuation velocities. The speed at which a signal propagates is determined by the fluctuation velocities and is therefore limited.

The wave model will not be discussed here in detail. The reader is referred to the literature on this subject, see e.g. *Kronberg and Westerterp, 1999*.

1.8 Conclusions

Many different reactor models for wall-cooled tubular reactors have been developed over the past 50 years, ranging from simple one-dimensional homogeneous plug-flow models to more complex ones like the two-dimensional pseudo-heterogeneous dispersed plug-flow model which was adopted for the main purpose of this thesis.

The parameters for heat and mass transport used in the models are still lumping parameters. They lump different physical transport mechanisms of heat and mass, occurring at different scales, into simple overall coefficients.

In the models, the driving forces for transport of heat and mass, which may actually vary strongly due to the heterogeneity of the packed bed, are averaged values. Many empirical correlations for the transport coefficients have been presented, which may differ widely in the case of important parameters, such as the effective radial thermal conductivity and the wall heat transfer coefficient. This is probably due to the sensitivity of the parameters to

experimental errors, the use of different transport model concepts and to a poor understanding of the influence of the particle and the packing geometry.
Different values for the effective transport parameters at reacting and non-reacting conditions have been reported in the literature. This is an important subject of the present investigation (Chapter 3).

The wave model (*Westerterp et al., 1995*) avoids some of the less satisfactory aspects of the dispersion-type of models. It will be used in this thesis to describe some detailed experiments on radial transport under non-reacting conditions.
In principle, computational fluid dynamics modeling could contribute greatly to improving of the understanding of cooled tubular reactors. The models that are currently developed (*Bey and Eigenberger, 1977*, *Logtenberg and Dixon, 1998*) generate many new insights, but due to the complex geometry of packed beds and the complex flow patterns inside it, these models are not (yet) suited for reactor design.

Notation

A_p	particle surface area	m^2
a	specific are of solid	$m^2\ m^{-3}$
c	concentration	mole m^{-3}
C	dimensionless concentration	-
c_p	heat capacity	$J\ kg^{-1}K^{-1}$
$D_{e,r}$	effective radial diffusion coefficient	m^2s^{-1}
D_m^j	molecular diffusion coefficient component j	$m^2\ s^{-1}$
D_t	reactor diameter	m
d	diameter of cylindrical particle	m
d_p	particle diameter	m
d_p^a	diameter of sphere with equal surface area	m
d_p^v	diameter of sphere with equal volume	m
F	ratio of effective mixing length and particle diameter	-
h	height of cylindrical particle	m
ΔH_r	reaction enthalpy	J $mole^{-1}$
j_H	heat flux	W m^{-2}
$j_{h,r}$	radial heat flux	W m^{-2}
$j_{h,z}$	axial heat flux	W m^{-2}
j_M	mass flux	mole $m^{-2}s^{-1}$
$j_{m,r}$	radial mass flux	mole $m^{-2}s^{-1}$
$j_{m,z}$	axial mass flux	mole $m^{-2}s^{-1}$
k	constant	-
k_g	particle-to-fluid mass transfer coefficient	m s^{-1}
L_t	bed length	m^3
N	aspect ratio	D_t/d_p^v
N_s	number of transfer units heat tr. through solid phase	-
$Pe_{h,r}^{\infty}$	Peclet radial. heat tr. for fully developed turb. flow	-
$Pe_{h,ax}^{\infty}$	Peclet axial heat tr. for fully developed turb. flow	-
R	reaction rate	mole kg^{-1} s^{-1}
r	radial coordinate	m
T	temperature	K
ΔT_{ad}	adiabatic temperature rise	K
t	time	s
U	overall heat transfer coefficient	W m^{-2} K^{-1}
u_0	superficial velocity	m s^{-1}
u_{ax}	asymmetry of axial fluctuation velocity	m s^{-1}
V_p	particle volume	m^3
x	spatial coordinate / dimensionless axial coordinate	m / -
x_f	mixing length for dispersion inside packing	m
y	dimensionless radial coordinate	-

z	axial coordinate	m
x	dimensionless axial coordinate	z/R_t
y	dimensionless radial coordinate	r/R_t

Greek

α_p	particle-to-fluid heat transfer coefficient	W $m^{-2}K^{-1}$
α_{rs}	heat tr. coeff. for radiation betw. solids surf.	W m^{-2} K^{-1}
α_{rv}	heat tr. coeff. for radiation betw. solids and voids	W m^{-2} K^{-1}
α_s	heat tr. coeff. through particle contact	W $m^{-2}K^{-1}$
α_{ss}	heat tr. coeff. for direct solid-solid heat transfer	W $m^{-2}K^{-1}$
α_w	wall heat transfer coefficient	W $m^{-2}K^{-1}$
α_w^0	flow-independent contr. to α_w	W $m^{-2}K^{-1}$
α_w^f	flow-dependent contr. to α_w	W $m^{-2}K^{-1}$
α_w^s	wall heat transfer coefficient solid phase	W m^{-1} K^{-1}
β	geometrical parameter	-
	constant	-
δ_{stag}	thickness stagnant fluid layer at wall	m
ε	bed porosity	-
ε_m	surface emissivity	-
γ	geometrical parameter	-
γ_w	geometrical parameter particles at wall	-
η	viscosity	Pa s
η_i	effectiveness factor	-
φ	geometrical parameter	-
φ_w	geometrical parameter particles at wall	-
κ	ratio of thermal conductivity of solid and fluid	-
λ	thermal conductivity	W $m^{-1}K^{-1}$
$\lambda_{e,r}$	effective radial thermal conductivity	W $m^{-1}K^{-1}$
λ_r^f	flow-dependent contr. to $\lambda_{e,r}$	W $m^{-1}K^{-1}$
λ_r^0	flow-independent contr. to $\lambda_{e,r}$	W $m^{-1}K^{-1}$
$\lambda_{e,ax}$	effective axial thermal conductivity	W $m^{-1}K^{-1}$
λ_{ax}^f	flow-dependent contr. to $\lambda_{e,ax}$	W $m^{-1}K^{-1}$
λ_{ax}^0	flow-independent contr. to $\lambda_{e,ax}$	W m^{-1} K^{-1}
$\lambda_{radiative}$	thermal conductivity due to radiation	W $m^{-1}K^{-1}$
ν_i^j	stoichiometric constant component j in reaction i	-
Θ	dimensionless temperature with reaction:	$\Theta = (T - T_0)/\Delta T_{ad}$
	without reaction:	$\Theta = (T\text{-}T_w)/(T_0 - T_w)$
ρ	density	kg m^{-3}

τ	bed tortuosity	-
	relaxation time	s

Dimensionless groups and variables:

Bi	Biot number	$\frac{\alpha_w R_t}{\lambda_{e,r}}$
Da	Damkohler number	$\frac{R_t}{u_0 c_0} R(c_0, T_0)$
Nu_p	Particle Nusselt number	$\frac{\alpha_p d_p^v}{\lambda_f}$ *
Nu_r	wall-Nusselt number for heat tr. through radiation	-
Nu_w	wall Nusselt number	$\frac{\alpha_w d_p^v}{\lambda_f}$
Nu_w^f	flow-dependent contr. to wall Nusselt number	$\frac{\alpha_w^f d_p^v}{\lambda_f}$
Pe_h^0	fluid Peclet number for heat transfer	$\frac{u_0 \rho_f c_{p,f} d_p^v}{\lambda_f}$
$PE_{h,ax}$	Peclet number for axial heat conduction (model)	$\frac{u_0 \rho_f c_{p,f} R_t}{\lambda_{e,ax}}$
$PE_{h,r}$	Peclet number for radial heat conduction (model)	$\frac{u_0 \rho_f c_{p,f} R_t}{\lambda_{e,r}}$
$Pe_{h,ax}$	Peclet number for axial heat conduction	$\frac{u_0 \rho_f c_{p,f} d_p^v}{\lambda_{e,ax}}$
$Pe_{h,r}$	Peclet number for radial heat conduction	$\frac{u_0 \rho_f c_{p,f} d_p^v}{\lambda_{e,r}}$
$PE_{m,ax}$	Peclet number for axial mass dispersion (model)	$\frac{u_0 R_t}{D_{e,ax}}$
$PE_{m,r}$	Peclet number for radial mass dispersion (model)	$\frac{u_0 R_t}{D_{e,r}}$
$Pe_{m,ax}$	Peclet number for axial mass dispersion	$\frac{u_0 d_p^v}{D_{e,ax}}$
$Pe_{m,r}$	Peclet number for radial mass dispersion	$\frac{u_0 d_p^v}{D_{e,r}}$
Pr	Prandtl number	$Pr = \frac{\eta_f c_{p,f}}{\lambda_f}$
Re	Reynolds number	$Re = \frac{u_0 \rho_f d_p^v}{\eta_f}$
$\Re$	dimensionless reaction rate	$\Re(c,T) = \frac{R(c,T)}{R(c_0,T_0)}$

Sc	Schmidt number	$Sc=\frac{\eta_f}{\rho_f D_m^j}$
Sh	Sherwood number	$Sh=\frac{k_g^j d_p^v}{D_m^j}$
St_h	Stanton number for particle-to-fluid heat transfer	$St_h=\frac{a\alpha_p R_t}{u_0 \rho_f c_{p,f}}$
St_m	Stanton number for particle-to-fluid mass transfer	$St_h=\frac{a k_g^j R_t}{u_0}$

Subscripts

0	value at reactor inlet
ax	axial
e	effective
equil	equilibrium
f	fluid phase
H	heat
i	reaction number
	value at particle surface
j	component number
lam	laminar
M	mass
r	radial
s	solid phase
turb	turbulent

Chapter 2

Kinetics of CO oxidation in air over CuO/γ-alumina

ABSTRACT

The heterogeneously catalyzed oxidation of carbon monoxide in air was used as a model reaction system for the investigation of heat and mass transport in a pilot-scale wall-cooled tubular reactor (see Chapter 3). The used catalyst consisted of 29 wt% copper oxide on porous γ-alumina in the form of cylinders with a diameter of 5.5 mm and an average height of 11.2 mm. The reaction kinetics were studied over a wide range of temperature and pressure. The reactor feed contained a constant mass fraction of water, which was necessary to avoid a change of the activity over time. The intrinsic reaction rate was measured in an integral reactor, which contained a bed of catalyst fragments with a diameter of 0.2 mm, diluted with silicium carbide particles of the same size. The measured reaction rate was described using a Eley-Rideal type of expression. In an internal-recycle reactor, the reaction rate was measured using intact catalyst cylinders. The reaction rates measured in this reactor were influenced by intra-particle mass transport, which was taken into account by using a new, analytical approximation of the effectiveness factor. After parameter optimization, the average difference between the measured and the predicted carbon monoxide conversion was 4%.

2.1 Introduction

The kinetics of carbon monoxide oxidation in air over a CuO/γ-alumina catalyst, used as a model system in the heat and mass transfer measurements in the wall-cooled tubular reactor, was studied in two different types of kinetic reactors. The first reactor, the so-called 'BoBo' reactor is an internal recycle reactor and was utilized for the measurement of the overall reaction rate of the applied catalyst. The intrinsic reaction kinetics were studied using an integral reactor. This reactor contained a packed bed that consisted of a mixture of crushed catalyst particles and silicium carbide particles with the same diameter. The size of the catalyst fragments was small enough to avoid intra-particle heat and mass transfer limitations.

Initially, the use of a noble metal catalyst was considered, since such catalysts are known to be very active in the oxidation of CO. However, for application as a model system in the study of heat and mass transfer in a wall cooled tubular reactor they are not well suitable, since strong adsorption of carbon monoxide leads to multiplicity of steady state and oscillatory behavior, as is described in numerous papers. Initially, experiments were

performed using a shell catalyst of Pd on γ-alumina. These experiments confirmed the occurrence of multiple steady states and periodic oscillations, which are the result of the sorption behavior of carbon monoxide and oxygen and the occurrence of heat- and mass transfer limitations. In the lower steady state, the catalyst surface is occupied almost entirely by carbon monoxide, preventing the adsorption of oxygen. Transition from the lower steady state to the higher steady state occurs if active sites are freed for oxygen adsorption, either by a decrease of the carbon monoxide concentration or by an increase in temperature. Strong hysteresis occurs due to mass transport limitations, which delay the reoccupation of the active sites by carbon monoxide. For this particular catalyst, the reaction rate at the lower steady state was found to be too low to generate a sufficient temperature rise at the experimental conditions used in the wall-cooled tubular reactor. At the upper steady state, the reaction rate measured in the kinetic reactors was determined by mass transport limitations, rather than by the reaction kinetics. In the pilot scale wall-cooled tubular reactor, operated at typical conditions, the high reaction rate would lead to complete conversion of the carbon monoxide at a distance of a few particle diameters from the inlet. Moreover, the state of each particle cannot be predicted in the region of multiplicity.

As has been demonstrated by *Annamalai et al.* for CO oxidation over a Pd/γ-alumina catalyst, temperature gradients of more than 100 °C can exist within a single particle. The temperature differences on the scale of a particle diameter will be of the same magnitude as the radial temperature differences, making the application of any known reactor model impossible.

Oxides of non-noble metals as (in order of activity according to *Severino, 1983*) copper, cobalt, iron, manganese, nickel, chromium and vanadium are known to catalyze CO oxidation according to a redox mechanism and to have a lower activity, making them more suitable for our purposes. Of the catalysts listed above, copper oxide is the most active in the oxidation of carbon monoxide and also the best studied one. The catalyst used in this investigation is ICT-12-6, produced by 'Katalizator Company' in Novosibirsk, Russia. This catalyst is a mixture of 29 wt% copper oxide and γ-alumina in the form of an extrudate. Its properties are given in Table 2.1. This catalyst was especially designed for CO oxidation at low temperature and was prepared by mixing pre-sintered γ-alumina and copper oxide. The size of the CuO-clusters is

Table 2.1 Catalyst properties

Property	Value
Copper oxide content	29 wt%
Shape	cylinder
Color	Green with small, black speckles
Particle height	10-13 mm, average 11.4 mm
Particle diameter	5.5 mm
Particle density	1319 kg m^{-3}
Porosity ε	63 % [1)]

[1)] mercury porosimetry, see appendix A

not uniform and varies between 3 and 60 μm approximately, as was determined by examination of a particle cross-section under an optical microscope.

The particle porosity of 63% was determined by mercury intrusion experiments (see Appendix A). The pore size distribution is broad and ranges from 10 nm to 10 μm. Pores with a diameter smaller than 100 nm account for half the pore volume. A strong hysteresis was observed when comparing intrusion and extrusion curves. About 30% of the pores was not emptied after reducing the pressure to atmospheric, indicating the presence of bottle-necks (*Webb et al., 1977*). Such pore structure can be expected in an extrudate of powder with a non-uniform particle size distribution.

Permeation experiments were performed, in which helium was passed to a slice of catalyst with a thickness of 2 mm at temperatures between 50 and 200 °C and pressures between 1 and 6 bars. (see Appendix A). If the pores were assumed to be in parallel, the observed permeation flux could be described rather well using a tortuosity of 1.25. The measured permeation fluxes corresponded to the values for a porous solid with an effective pore diameter of 190 nm and a ratio ε/τ=0.27. This effective pore diameter for viscous flow is four times larger than the average pore diameter measured by mercury intrusion. The contribution of Knudsen diffusion to the overall diffusion rate was rather small, despite the large volume fraction of very small pores.

On the basis of the mercury intrusion and helium permeation experiments, it was concluded that the effective diffusivity inside the catalyst particles is determined by molecular diffusion in the larger pores, which were formed during extrusion of the starting material. The smaller pores of the bi-disperse structure do not contribute to the effective diffusivity of the reactants inside the catalyst particles.

2.2 Copper-based catalysts for CO oxidation

Different mechanisms have been suggested for the oxidation of carbon monoxide over copper oxide containing catalysts on supports as alumina, silica, zirconium, zeolites and titanium oxide. Despite the fact that the mechanisms of CO oxidation over these catalysts are still not clear, they are often applied as model systems in experiments (e.g. transient response studies (*Dekker et al., (1994) (I) and (II), Subbotin et al.,* (1993)).

Catalysts with only copper as active component are not often used in industrial processes. Another metal is usually added to stabilize the catalyst. Chromium oxide is mostly used in combination with copper oxide. Chromium itself does catalyze carbon monoxide oxidation, but its contribution to the overall activity of the catalyst is generally small, depending on the concentration of both components. Chromium is assumed to protect the catalyst against sintering, to limit reduction of the catalyst in a reducing atmosphere (*Yao and Fang 1975, Laine et al., 1990*) and to promote favorable coordination of the copper atoms within the support matrix. The activity of supported copper-based catalyst depends on the metal oxide

concentration, the type of support, the oxidation state of the metal, the dispersion of the metal oxide within the support matrix and, what is important, on the history of the catalyst.

According to *Severino et al., 1998*, the specific nature of the active sites is still not known. Copper can be present as a separate CuO phase, a 'surface Cu-Al_2O_3 spinel' and as a bulk $CuAl_2O_4$ spinel. The concentrations of these phases are determined by the composition of the catalyst and the preparation method. The oxidation state of the copper depends on the reaction conditions and the local phase structure. Copper can be present as metallic copper, Cu^+ and Cu^{2+}. According to *Dekker et al., 1992* and *Deen et al., 1976*, the system Cu^+-Cu^{2+} is the most important redox couple in a net oxidizing atmosphere. *Severino et al 1998* and *Agudo et al., 1992* found that Cu^+ and metallic copper are the main active sites for CO oxidation. According to the latter authors, all three valences are present under oxidizing conditions at a temperature of 400 °C. *Jernigan et al., 1994* measured the activity of the different copper species and found a decrease in activity with increasing oxidation state.

Cu/γ-alumina catalysts are prepared either by impregnation of the alumina support, followed by drying and calcination, or by mixing of pre-sintered copper oxide and alumina. *Agudo et al., 1992* and *Severino et al., 1998* state that finely dispersed copper, such as $CuAl_2O_4$ (spinel) is more active than CuO particles present at the surface of the pores The difference in activity is attributed to the increase in the surface concentration of Cu^0 and Cu^+. Reversible deactivation by water is explained by a rearrangement of the copper atoms, leading to the formation of CuO particles. *Severino et al., 1983* found that the copper in a CuO/Al_2O_3 has an optimum activity if the copper content is approximately 6 %. This is close to the concentration necessary to convert all of alumina into a copper aluminate. At higher metal loadings, CuO crystals are assumed to block the more active aluminate surface. If the spinel form is the most active form of copper, it is to be expected that catalysts prepared by impregnation are superior to those prepared by mixing of the pre-sintered components. This agrees well with the findings of *Yao and Kummer 1977*, who made a comparative study of catalysts prepared by both methods. They observed a large increase in activity for the mixed oxide (α-alumina) catalysts after a thermal treatment at 700 °C, whilst the activity of the impregnated catalyst did not change noticeably. If γ-alumina was used as a support, treatment at high temperature increased the spreading of copper and with this the activity in CO oxidation, but also caused sintering of the catalyst which decreased the activity. The authors found that the activity of the mixed oxide catalyst after treatment at high temperature is comparable to that of the catalyst prepared by impregnation.

In order to obtain reproducible catalytic activity, CuO/γ-alumina catalysts generally are subjected to elevated temperatures in an oxidizing atmosphere, followed by reduction by He or CO and re-oxidation by oxygen. During the heating of the catalyst, water that absorbed during exposure of the catalyst to ambient air will be removed, possibly causing a change in the dispersion state of copper. At the same time, organic and sulfurous contaminants will be removed by oxidation. A reduction/oxidation cycle has been reported to enhance activity by

re-distribution of the copper, leading to a change in the distribution of copper (*Severino et al., 1985, Mardanova et al., 1996*).

Kinetic models used for the description of the rate of oxidation of CO greatly differ in form and complexity. Expressions vary from a simple Arrhenius-type with a first order with respect to CO to models distinguishing over 10 steps, involving adsorption, diffusion and reaction.

For practical use, the reaction rates are usually simplified to an Arrhenius-type of equation that is valid in the region of the used operating conditions. A limited overview of kinetic investigations on CO oxidation over copper oxide is given in Table 2.2.

In an oxygen-rich environment, the apparent order with respect to oxygen is generally zero. Reported orders in CO are positive and increase to unity at high temperatures. The order in CO_2 is negative at low temperatures and decreases to zero with increasing temperature. Both the Eley-Rideal (ER) mechanism, according to which gas phase CO reacts with adsorbed oxygen, as the Langmuir-Hinshelwood (LH) mechanism have been proposed. Some models

Table 2.2 Selected kinetic investigations on CO-oxidation over copper-based catalysts: Apparent orders and activation energy; zero order in oxygen.

Catalyst	order CO	order CO_2	E_a kJ mole^{-1}	T °C	P bara	CO, (CO_2) v%	Ref.
CuO, 2mm pellets	0.3-0.8	<0	73-106	150-200	atm[1)]	0-0.12 and 0-10	Thomas et al., 1969
CuO	0.7 1	<0 0	92 <13 [4)]	150-200 200-500	atm[1)]		Yao and Fang., 1975 [3)]
17 wt% CuO/Al_2O_3	1	-	60	62-146	0.03-0.22	0-10	Kakhniashvili et al., 1989
3 wt% CuO/Al_2O_3	1	-	30	53-235	idem	idem	idem
1 wt% CuO/Al_2O_3	1	-	35	90-176	idem	idem	idem
0.5 wt% CuO/Al_2O_3	1	-	33	90-201	idem	idem	idem
CuO/Al_2O_3, 3.4 mm spheres	0.94	-0.48	127	120-142	atm[1)]	0-10 (0-10)	Eckert et al. 1973
CuO/Al_2O_3, 3.4 mm spheres	1	0	96	130-190	atm	0-4	Hlavaček et al. 1974
10 wt% CuO/γ-Al_2O_3, 4.2 mm cylinders	0.7	-	56	136-183	atm	0.3-6.65	Baumann et al., 1990
CuO/SiO_2	1	-	87	130-300	atm[1)]	1.7[2)]	Hoffman, 1979
10 wt% CuO/SiO_2	≤ 1	-	62	220-280	atm	0.1-8	Prokopowicz et al., 1988

[1)] value not mentioned, atmospheric pressure assumed

[2)] maximum concentration in the figures

[3)] order in water of –0.1 at 250<T<500 and <-0.3 at 150<T<200 reported

[4)] probably due to diffusion limitation

include different states of adsorbed oxygen and carbon monoxide. According to *Prokopowicz et al., 1987* and *Subbotin et al., 1993,* CO is adsorbed in reasonable amounts, but this adorbed CO does not take part in the reaction. *Dekker et al 1994* uses a kinetic model in which the reaction rate is dominated by reaction according to the ER mechanism if the catalyst is fully oxidized. When the catalyst is reduced, the LH reaction of adsorbed CO becomes dominant.

Oxygen can be present as a relatively weakly bonded species at the catalyst surface or as lattice oxygen in the CuO-γ-alumina spinel (*Dekker et al., 1994, Subbotin et al., 1995).* The second type of oxygen is assumed to react mainly with adsorbed CO. At low temperatures CO_2 can inhibit the reaction by occupying active sites. The reaction of CO with surface oxygen is reported to form a complex (carbonate) of which the dissociation can become rate-limiting at low temperatures. *Thomas et al., 1969* have studied the influence of carbon dioxide on the oxidation rate of CO in air at temperatures up to 130 °C and found that CO_2 slows down the reaction, increases the effective order in CO and increases the apparent activation energy.

Little is known about the influence of water on the reaction rate. *Yao and Fang* found an order < -0.3 at temperatures between 150 and 200 °C and –0.1 for temperatures between 200 and 500 °C. According to *Gmelin 1961*, CuO and water form a blue hydroxide ($Cu(OH)_2$). When heating this hydroxide, adsorbed water is removed, after which the hydroxide slowly dissociates to form CuO. In the course of this dissociation, the color changes from blue to dark brown via green. Dissociation of the hydroxide generally starts around 100 °C, depending on the preparation method. Complete de-watering to CuO requires temperatures higher than 220 °C.

The catalyst used in this investigation is green, which suggests that at least part of the copper is present as a hydroxide. Heating of a small sample of catalyst (15 g) during 24 hours in a miniature oven flushed with dry air at 400 °C did not lead to a color change. This was also the case for a larger amount (1.5 kg) of catalyst that was calcined in a tubular oven at 550 °C for 40 hours. This catalyst was present as a packed bed that was flushed with 4 l min^{-1} of dry (<18 ppm) air. The greenish color of the catalyst does not disappear when it is heated over a flame until it is red hot, although the surface becomes a bit darker. When exposed to air containing carbon monoxide (99.9 % purity), supplied directly from a gas cylinder, the color of the catalyst slowly changed from green to dark brown. In the BoBo reactor, this discoloration was accompanied by the formation of a rust-like deposition that covered the inside of the entire reactor. The discoloration was only observed at the surface of the catalyst, so that it cannot be attributed to the formation of pure CuO, which is brown. After the carbon monoxide was heated before it entered the reactor, no discoloration was observed anymore. This led to the conclusion that decomposition of iron carbonyls present in the fresh CO was responsible for this color change.

2.3 Experimental

2.3.1 Catalyst pre-treatment

The results of the kinetic measurements were to be used for the modeling of temperature and concentration profiles measured in a much larger wall-cooled packed bed reactor. The pre-treatment of the catalyst should therefore be such that it can be performed using a large batch (1.5 kg) of catalyst. Catalyst pre-treatment as described in literature involves thermal treatment, most often followed by subsequent reduction and oxidation. Prolonged heating of the catalyst in air or nitrogen will remove all adsorbed water and, at higher temperatures, causes a (re-) dispersion of the active material in the support matrix. A batch of 2 kg of fresh catalyst, used in both the kinetic reactors and in the wall-cooled tubular reactor, was heated for ±40 hours at 550 °C in a tubular oven which was flushed with dry (< 18 ppm water) air. It was assumed that any dispersion of the copper over the alumina, reported by Yao and Kummer 1977, would occur during treatment at this temperature, which is well above the maximum temperature of 290 °C during the further experiments. For several reasons, the catalyst was not subjected to a reduction/oxidation cycle. The first reason is that it is almost impossible to have uniform conditions for the whole batch of catalyst, especially during the oxidation cycle. Experiments in the wall-cooled tubular reactor showed that this highly exothermic and fast reaction causes a temperature front to move through the reactor. High temperature and concentration differences occurred within the packing. Secondly, it is not possible to take a sample from this treated catalyst for kinetic measurements without exposing it to air. Water can change the nature and distribution of the active sites, possibly canceling the effect of the reduction/oxidation cycle.

2.3.2 Experimental set-up

A flow scheme of the set-up used for the kinetics investigations is shown in Fig. 2.1. Nitrogen (99,999 %) was supplied from a liquid nitrogen storage. Carbon monoxide and carbon dioxide (99.9%) were supplied from cylinders. The carbon monoxide was passed through a packed bed with a length of 15 cm, which consisted of 0.2 mm silicium carbide particles. This bed was heated at 250 ^{0}C to remove iron-carbonyls that were present in the CO. Air was supplied from the set-up of wall-cooled tubular reactor. Ambient air was compressed, cooled and passed through two coalescing filters for water and oil removal before it entered a self-regenerating desiccant dryer (Domminick Hunter Pneudri Midi). After drying, the air was passed through a carbon filter with a height 1 m (2.6 mm Norit RB3, dried in vacuum at 250 ^{0}C). The residence time of the air in this filter was approximately 10 seconds. During later experiments, air with a constant humidity was used. In that case, the desiccant was removed from the dryer. The air humidity was kept constant at ± 1200 ppm by

cooling the air coming from the compressor in a heat exchanger. The excess of water was condensed and removed in the coalescing filters. When using the desiccant air dryer, the water content of the air, measured using an optical dew point hygrometer (Panametrics), was below the minimum of the measuring range of 18 ppm.

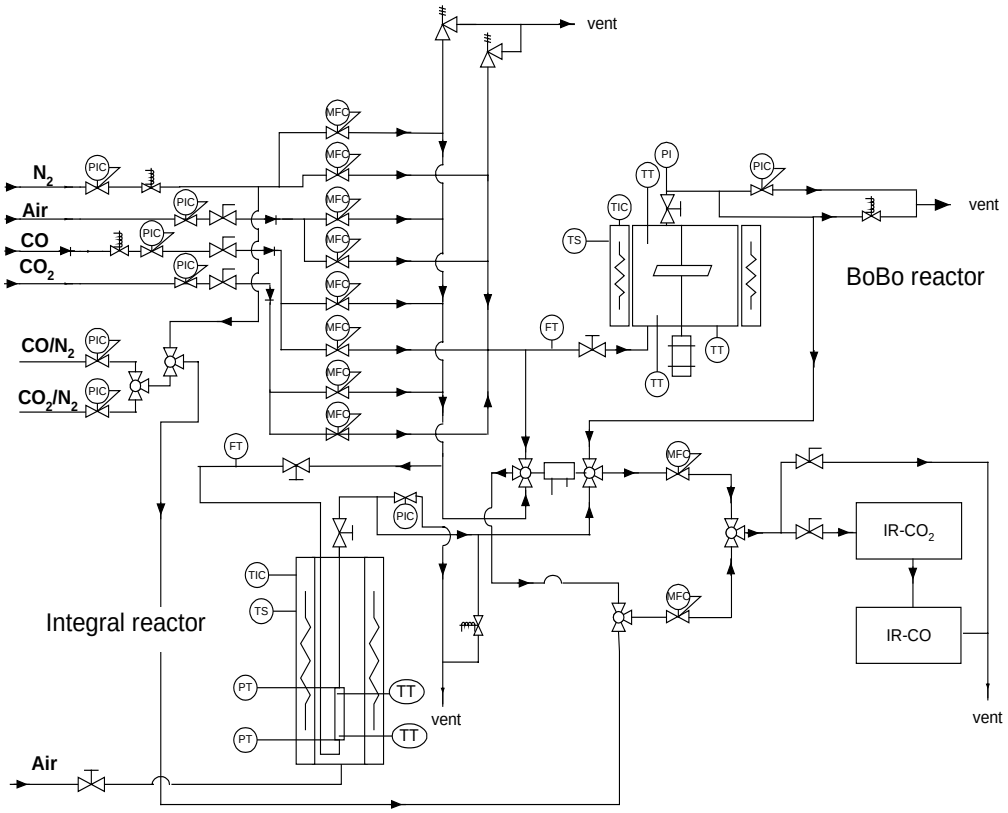

Fig. 2.1 Flow scheme of the kinetic set-up

The used BoBo and integral reactor had separate feed sections. The oxygen concentration could be varied between 0 and 21 vol% by varying the ratio of air and nitrogen. All gas flows were controlled by electronic mass flow controllers (Brooks). After mixing of the different feed streams, the total flow rate was measured again. The reactor pressures were set using electronic back pressure controllers (Bronkhorst Hi-Tec). Two Maihak UNOR 610 infrared analyzers continuously measured the carbon monoxide and dioxide concentrations before or after the reactors. The analyzers were calibrated regularly using calibration gas mixtures (Praxair, 1% accuracy). The setup was fully automated. A Hewlett Packard data acquisition unit, coupled to a PC, was used for data collection, controlling of all process conditions and for safeguarding of the set-up. The CO concentration inside the reactor could be kept at a desired set point by variation of the CO inlet concentration using a feedback controller. Series of up to a few hundred experiments could be performed automatically. After loading the reactor with fresh catalyst, it was slowly heated whilst adding a constant flow of air. This was

done to avoid a change in activity due to adsorption of water during the experiments (see paragraph 2.4.2). For the same reason, experiments were started 6 hours after changing the reactor pressure and / or temperature.

Concentration setpoints were changed if, after some minimum time interval, the CO_2 concentration in the effluent was constant. The minimum time interval was the sum of the 'dead time' of the analysis system and the time necessary to assure that the reactor is at steady state. In case of the BoBo reactor, experiments were started after minimum 7.5 times the residence time. After that, the concentration in the reactor effluent should deviate less than 0.5 % from the final outlet concentration.

Together with water, the desiccant dryer removed CO_2 from the air. At low air loads, CO_2 removal was complete, whilst a breakthrough of CO_2 was observed at high air loads (a large quantity of air was used in the setup of the wall-cooled tubular reactor). To correct for the changing CO_2 concentration in the reactor feed, the concentration was measured in between the experiments.

2.3.3 Reactors: BoBo reactor

The BoBo reactor, developed within our research group (*Borman et al.,, 1994)*, was used for the investigation of the overall kinetics. Compared to other types of internal recycle reactors with gas circulation achieved by means of an impeller (*Carberry 1964, Berty 1974*), gas-solid heat and mass transfer rates are significantly higher. The main dimensions of the reactor are given in table 2.3.

Table 2.3 Properties of BoBo reactor

Property	**Dimension or value**
Reactor volume	3.3. liters
Height	16 cm
Width	18 cm
Impeller diameter	13 cm
Max. pressure	10 bar
Max. temperature	300 °C
Max. flow rate	
air	5000 ml min^{-1}
nitrogen	3000 ml min^{-1}
CO	100 ml min^{-1}
CO_2	100 ml min^{-1}

In the reactor, shown in Fig. 2.2, the catalyst can be placed either in the blades of an axial impeller, or pinned on a rack just below the impeller, which can rotate at speeds up to 5500 rpm. The impeller is magnetically driven by an electric motor; the magnets and the bearings are water-cooled. During experiments, rotational speeds up to 3000 rpm were used. At the center of the reactor, the gas is pushed downwards by the impeller. It flows upward along the wall, which is kept at a constant temperature by an electrical oven. If the particles are put between gausses in the impeller blades, the flow pattern inside the reactor causes a large velocity difference between the particles and the gas. If the particles are mounted on the rack, the velocity is smaller, but in those experiments the temperatures of the catalyst can be measured. In this configuration, the temperatures of the

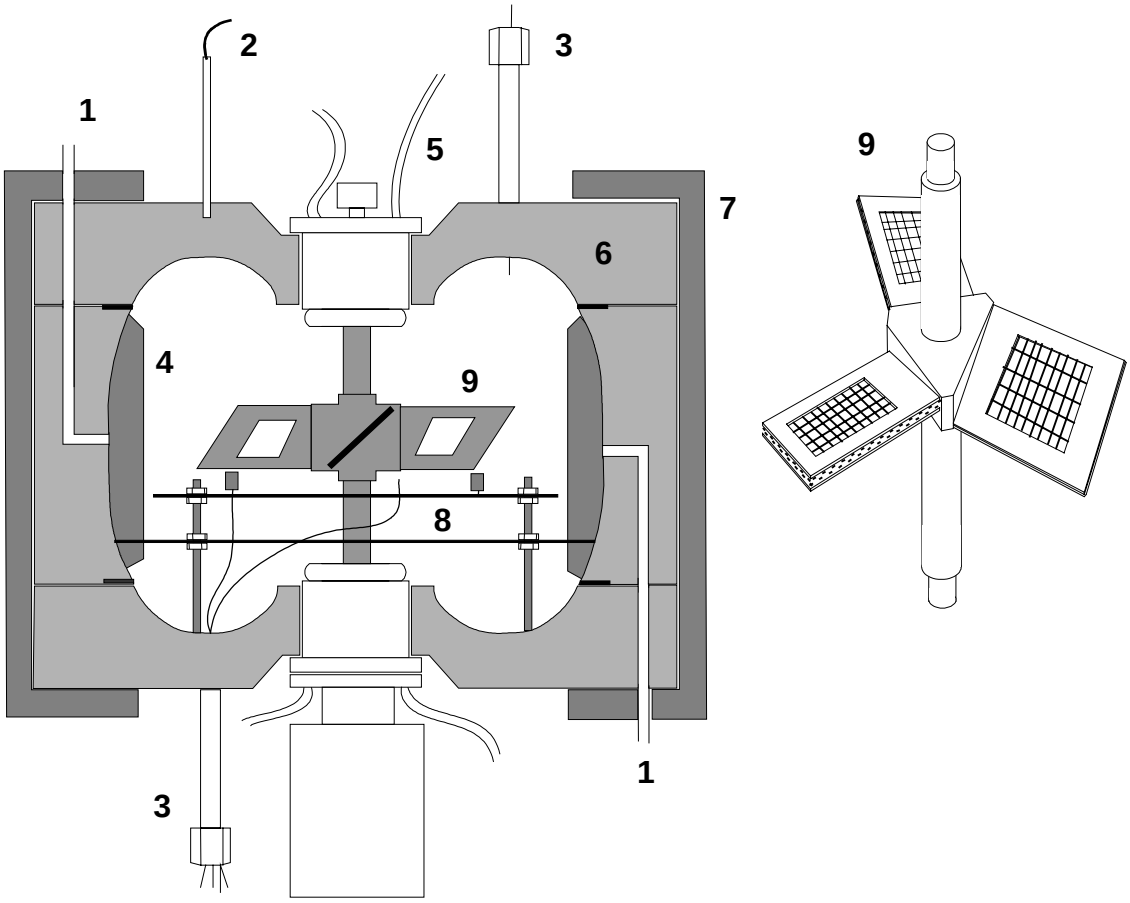

Fig. 2.2 Scheme of the BoBo reactor. 1: gas inlet/outlet, 2: TC wall temperature, 3: TC gas/cat. temperature, 4: baffle (4x), 5: cooling water in/out, 6: reactor wall, 7: bronze jacket, 8: cat. support rack, 9: impeller. The reactor and its internals are constructed of stainless steel 316.

particles and the gas were measured at the same distance from the impeller. To be able to fix the particles on the rack, 0.5 mm holes were drilled in them. Two particles were put on top of 0.5 mm thermocouples (type K, Eurotherm), the remaining (maximum 30) were stuck on stainless steel pins protruding from the rack. The distance between the particles and the impeller was approximately 3 mm.

A relationship between the mass transfer rate to the particles rotating with the impeller and the speed of the impeller was determined experimentally by *Borman 1994*, who obtained the following correlation for the particle Sherwood number:

$$Sh = 0.3 + 0.07\ Re_{rp}^{0.76}\ Sc^{0.54} \qquad (2.1)$$

where:

$$Re_{rp} = \frac{2\pi R_p \omega \rho_f d_p^v}{\eta_f} \tag{2.2}$$

In the definition of the Reynolds number used here, the gas velocity has been replaced by the tangential velocity of the rotating particle $2\pi\omega R_p$, where ω is the rotational speed of the impeller and R_p the distance between the particle and the axis of the impeller. The effective particle size is the diameter of a sphere of equal volume.
The mass transfer coefficient for a stationary particle on a thermocouple below the impeller was found to be two times smaller than that for the rotating particles. When treating the experiments during which the particles were fixed on the rack below the impeller, the occurrence of external heat and mass transfer limitation could be checked by using the measured differences between the temperatures of two catalyst particles and the temperatures measured by two bare thermocouples at the same distance from the axis of the impeller:

$$Nu = \frac{\rho_p \Delta H_r R(c,T) d_p}{a_p (T_p - T_f) \lambda_f} \tag{2.3}$$

where ρ_p is the particle density, a_p is the specific area of the catalyst particle and λ_g is the thermal conductivity of the gas. R(c,T) is the reaction.
The mass transfer coefficient can be calculated using the analogy proposed by Chilton and Colburn:

$$Sh = Nu \ \ Le^{1/3} \tag{2.4}$$

The degree of mixing inside the reactor is determined by the recycle ratio:

$$R_{rec.} = \frac{Q_d + Q_f}{Q_f}, \tag{2.5}$$

where Q_f is the feed rate and Q_d is the discharge rate, given by:

$$Q_d = N_Q \omega D_{imp}^3 \tag{2.6}$$

In equation (2.6), ω is the rotational speed of the impeller, D_{imp} the impeller diameter in m and N_Q a pumping coefficient that has a value of ± 0.4 according to *Perry and Green, 1997.*

$R_{rec.}$ is the average number of times that a fluid element moves through the impeller and over the catalyst particles before it leaves the reactor. At a feed rate of 5 liters per minute and a rotational speed of the impeller of 3000 rpm, the recycle ratio is approximately 500, which allows for high conversions until external concentration gradients over the particles become of importance. For power-law type kinetics, *Borman, 1993* gives the following correlation to calculate the ratio between the observed and the real reaction rate, f ,as function of the internal recycle ratio:

$$f = \frac{1}{1+\Xi}\left[1-\frac{1}{2}n\varsigma_b+\frac{\alpha\beta}{R_{rec}-1}-\frac{\alpha\beta}{\varsigma_b\left(R_{rec}-1\right)^2}\ln\left(1+\zeta\left(R_{rec}-1\right)\right)\right]$$

$$\Xi=\left(1+\alpha\beta\frac{\zeta}{R_{rec}}\right)\left(1-\zeta_b\right)^n-1 \qquad (2.7)$$

$$\zeta_b=\left(\frac{1-\zeta}{\zeta}R_{rec}+1\right)^{-1}$$

In (2.7), n is the apparent reaction order, ζ the total conversion of the key reactant, ζ_b the conversion per pass and Ξ the ratio of the reaction rates at conditions before and after the catalyst layer. $\alpha=\Delta T_{ad}/T_f$ and $\beta=E_a/(RT_f)$ are the dimensionless temperature and activation energy. Both the temperature and concentration change over the catalyst bed, which in our case consisted of 1 'layer' of catalyst pellets, are taken into account in the calculation of f. If the influence of the temperature difference over the bed is neglected, the above equation is very close to the better known criterion of *Wedel and Villadsen 1983.* A more general criterion than eq. (2.7) is given by *Wijngaarden et al.,, 1999*. When the catalyst rack is placed inside the reactor, the flow will be somewhat impaired. However, even if the recylce ratio is taken 5 times smaller than the value according to eq. (2.5), the influence of temperature and concentration gradients along the particle will be less than 1% for a high value of E_a of 100 kJ $mole^{-1}$ and a reaction order of 2.

For the catalyst particles described in the first paragraph of this chapter, intra-particle diffusion limitations occur at conditions as used in the pilot-scale wall-cooled tubular reactor. These diffusion limitations were accounted for through the use of a particle effectiveness factor, which is a function of the effective diffusion coefficients of the reacting species inside the catalyst and the used expression for the intrinsic reaction kinetics. The effectiveness factor was calculated using an analytical approximation of which the derivation is given in Appendix B and is defined as the ratio of the reaction rate the conditions at the surface of the particle and the average reaction rate over the particle volume :

$$\eta = \frac{R\left(C_s^i, T_s^i\right)}{\frac{1}{V_p}\int_{V_p} R\left(C_s, T_s\right) dV} \tag{2.8}$$

To check whether internal transport limitation occurs, the following simple criterion, derived by *Stewart et al., 1969* can be used:

$$\frac{\rho_p R\left(c,T\right) {r_p}^2}{C_i D_{eff}} < \frac{1}{n} \tag{2.9}$$

r_p is the particle radius and C_i and D_{eff} are the surface concentration and the effective intraparticle diffusion coefficient of the reacting species. Since the oxidation of carbon monoxide is highly exothermic, temperature gradients can occur within the catalyst particles, depending on the thermal conductivity of the catalyst material., For a spherical catalyst particle in which a reaction occurs that is described using an effective rate expression of the Arrhenius type, the following criterion has been derived by *Anderson 1963* to check if the overall reaction rate is significantly influenced by the temperature profile existing within the particle:

$$\frac{\left|\Delta H_r\right| \rho_p R\left(c,T\right) r_p^2}{\lambda_p T_s} < 0.75 \frac{R T_i}{E_a} \tag{2.10}$$

in which λ_s is the effective thermal conductivity of the particle, T_i is the surface temperature of the particle, R is the gas constant and E_a is the apparent activation energy of the reaction.
For the catalyst used in this investigation, r_p was replaced by the radius of a sphere with the same volume as the particles. Equation (2.10) does not consider internal concentration gradients. At condition at which the overall reaction rate is severely limited by mass transport, temperature differences within the particle will be smaller than assumed in eq. (2.10) since the distance over which the heat of reaction has to be transported is smaller. It is possible to give a more accurate prediction of the importance of intra-particle heat and mass transfer limitations by using the analytical expression for the effectiveness factor in appendix B and expressing the temperature is function of the concentration.

2.3.4 Reactors: Integral reactor

In order to study the reaction kinetics in absence of intra-particle temperature and concentration gradients, experiments were performed in an integral reactor using crushed catalyst particles with a diameter of 0.2 mm. The integral reactor was a stainless steel tube with a length of 14 cm, an internal diameter of 8 mm and a wall thickness of 1 mm. The reactor was kept at a constant temperature by placing it in a fluidized bed, surrounded by an oven. A scheme of the reactor is shown in Fig. 2.3. The catalyst, diluted with SiC particles, was put between porous glass discs covered with glass wool. Two thermocouples (type K, 1.5 mm, ThermoElectric) protruded into the bed over a distance of approximately 2 mm. To the top and bottom of the reactor, two pressure transmitters were connected via 1 mm capillaries. The feed entered the reactor at the bottom through a 1 mm stainless steel capillary which was coiled up to create enough surface area to heat the feed to the temperature of the fluidized bed. Most of the reactor effluent passed through the back pressure controller, the rest was sent to the infrared analyzers.

On the basis of heat transfer experiments using a stainless steel sphere placed inside the fluidized bed, it was concluded that heat transfer limitation between the wall of the reactor and the fluidized bed could be neglected. At not too high conversions, the temperature along the length of the reactor does not have a maximum. In that case, the difference between the

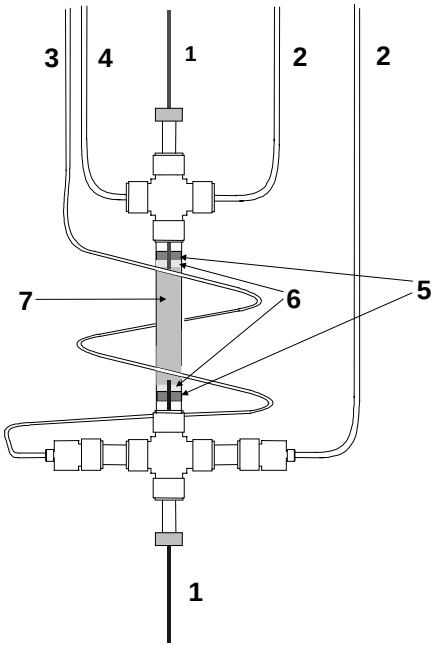

1: thermocouples, 1.5 mm
2: capillary to pressure transmitter
3: feed
4: effluent
5: porous glass disks
6: glass wool
7: catalyst bed

Table 2.4 Properties of the integral reactor

Property	Value
Volume	8 ml
Height	14 cm
Width	8 mm
max. pressure	10 bara
max. temperature	240 °C
max. flow rate	
air	3000 ml min^{-1}
nitrogen	3000 ml min^{-1}
CO	100 ml min^{-1}
CO_2	100 ml min^{-1}

Fig. 2.3 Scheme of the integral reactor.

temperature at the centerline of the reactor and the temperature of the wall is smaller than the measured temperature difference between the inlet and the outlet of the reactor.. At conversions larger than about 40%, the temperature at the centerline will have a maximum, which can be calculated using the reactor model for the calculation of the temperature and concentration fields inside the pilot-scale wall-cooled tubular reactor (Chapter 3).
Temperature and concentration differences between the catalyst particles and the gas were calculated using the correlations given by *Gnielinski, 1982*:

$$\mathrm{Nu} = \mathrm{f_a}\left(2+\sqrt{\mathrm{Nu_{lam}^2}+\mathrm{Nu_{turb}^2}}\right) \tag{2.11}$$

$$\mathrm{Nu_{lam}} = 0.664\mathrm{Pr}^{1/3}\mathrm{Re}^{1/2} \tag{2.12}$$

$$\mathrm{Nu_{turb}} = \frac{0.037\mathrm{Re}^{0.8}\mathrm{Pr}}{1+2.443\mathrm{Re}^{-0.1}\left(\mathrm{Pr}^{2/3}-1\right)} \tag{2.13}$$

In equations (2.12) and (2.13), Re is calculated using the interstitial gas velocity. The factor f_a in eq. 2.10 accounts for the difference between the Nusselt number for a particle in a packed bed and that for a single particle and has a value of 1.6. The Sherwood number can be calculated using the Chilton-Colburn analogy (eq. (2.4)). The effect of axial dispersion was assumed to be negligible, since number of particles over the length of the reactor was more than 500. At low reactor pressures, the pressure drop over the reactor was significant (up to 18% at 2 bara). When treating the experimental data, a linear decrease in pressure over the reactor was assumed.

2.3.5 Treatment of experimental data

In case of the BoBo reactor, in which intact catalyst particles are used, the overall reaction rate is determined by the intrinsic reaction kinetics and internal heat- and mass transport limitation. The effect of internal diffusion limitation was accounted for through a particle effectiveness factor which can be calculated either numerically or analytically (Appendix B). The kinetic parameters were calculated by minimizing the difference between the measured and the calculated CO conversion:

$$F = \sum_{n} \left(\frac{\zeta_m - \zeta_c}{\zeta_m} \right)^2 \quad ; \quad \zeta = \frac{[CO]_{in} - [CO]_{out}}{[CO]_{in}} \tag{2.14}$$

where ζ_m and ζ_c are the measured and the calculated conversions. The conversion was calculated by integration of the following mass balance over the reactor length using a fourth order Runge-Kutta procedure:

$$\frac{dc_i}{dz} = \frac{\rho_{cat}}{u_0} \nu_i R(c,T,P) \tag{2.15}$$

In (2.15), c_i is the component concentration, ν_i is the stoichiometric coefficient, ρ_{cat} is the density of catalyst in kg m^{-3} and u_0 is the gas velocity at the average reactor temperature and pressure. Since the concentrations of all components involved in the reaction can be expressed as function of the local CO concentration, only one mass balance had to be solved. The change of the fluid density along the length of the reactor due to the pressure drop was accounted for. It was assumed that the pressure decreased linearly.
The kinetic parameters were optimized using the Downhill-Simplex method (*Press and Teukolsky, 1986),* incorporated in a program written in Pascal.

2.4 Experimental results

2.4.1 Iron Carbonyls

Initially, carbon monoxide was not passed through the carbonyl filter described in paragraph 2.4. After some time, it was observed that the color of the catalyst in the BoBo reactor changed from bright green to almost black. At the same time, a brown, rust-like deposition was found on the reactor wall. In previous measurements this discoloration did not appear, except for some light brown spots that were hardly visible. The discoloration of the catalyst occurred only at the surface, indicating that it should be some sort of deposit. The activity of the catalyst was not affected noticeably. The most likely cause for the discoloration is the presence of iron carbonyl in the CO, which was taken from an iron cylinder. Iron carbonyls are stable at low temperature and decompose when heated. After installing a small filter in the CO supply, in which the CO was heated at ± 250 °C, no color change of the catalyst was observed anymore. *Werner 1994* and *Annamalai et al., 1999* report the use of such a 'carbonyl filter', but many authors do not.

2.4.2 Deactivation of the catalyst by water

As mentioned in paragraph 2.2, the activity of a copper oxide catalyst is decreased by the presence of water in the reaction mixture. The change of activity was first observed in the pilot-scale wall-cooled tubular reactor, described in Chapter 3 of this thesis. The used air was initially dried in a desiccant dryer and contained less than 18 ppm of water. After filling the pilot-scale wall-cooled tubular reactor with fresh catalyst, the reactor was heated to a temperature of 200 °C for at least 12 hours. After that, experiments were performed, during which the temperature of the bed did not exceed 200 °C. It was observed that the catalyst activity slowly changed over a period of several weeks, as is shown in Fig. 2.4.

An increase of the reaction rate was observed after performing experiments at higher wall- and inlet temperatures (d). The lowest conversion was measured after cooling down the reactor to 30 °C during one week. During this whole period, the reactor was flushed with the dried air.

Since water is known to decrease the reaction rate of CO oxidation over copper oxide catalysts, tests were made in which it was deliberately added to the feed of the wall-cooled tubular reactor by pumping a very small amount into the air pre-heater.

In Fig. 2.5, the change in activity after addition of water is shown. Addition of 9 g/hour water to the reactor feed was started at t= 2.5 h. The water concentration shown in the figure was measured in the reactor effluent. The increase of the measured water concentration was

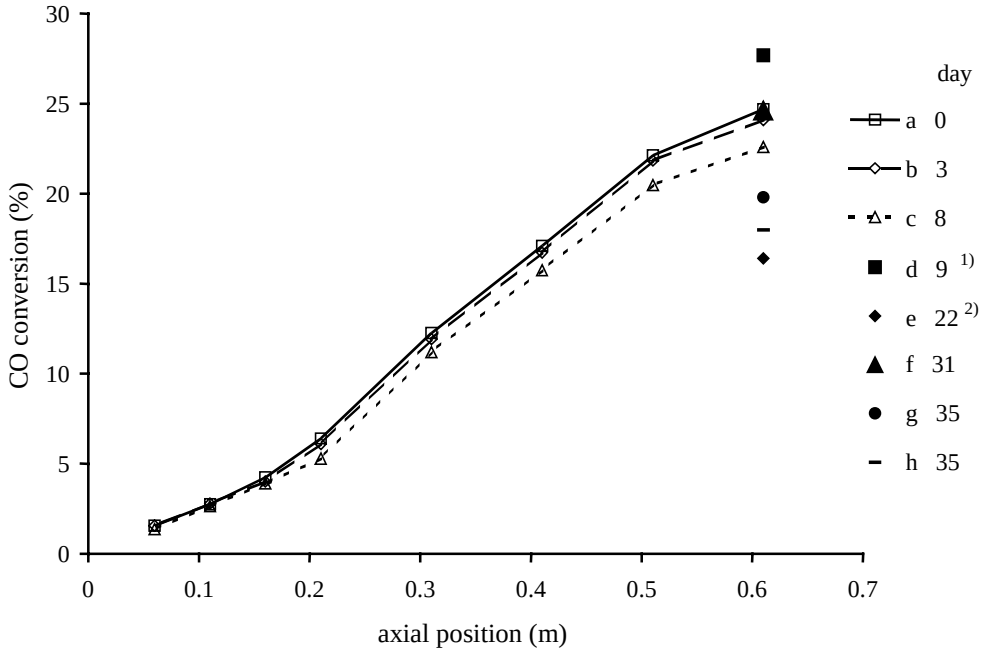

Fig. 2.4 Change of the CO conversion in the pilot-scale wall-cooled tubular reactor over a period of one month; conditions: $T_{inlet}=T_{wall}=102$ °C, P=3.5 bara, $CO_{inlet}=1$ v% and $u_0=1.2$ m s^{-1}.

1) $T_{inlet}=T_{wall}=156$ °C

2) $T_{inlet}=T_{wall}=30$ °C

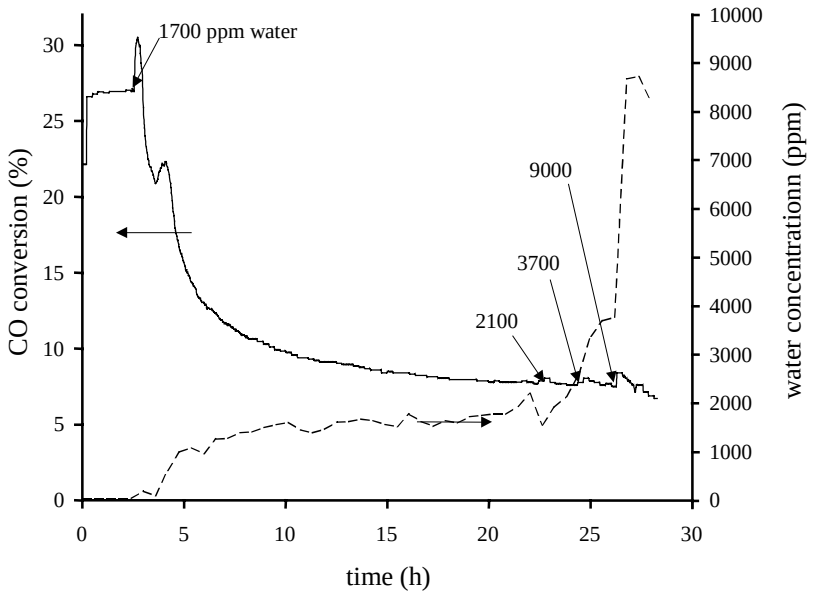

Fig. 2.5 Change of the CO conversion in the wall-cooled tubular reactor at 0.6 m from the reactor inlet after addition of water to the feed. CO_{in}= 1 v%, T_{inlet}=T_{wall}= 140 °C, P.3.8 bara, u_0=0.4 m s^{-1}.

delayed with respect to the change of the water flow rate because, initially, all water was adsorbed. As soon as the first water droplet entered the system, a fast increase in conversion was observed. The increase was only temporary and is attributed to so called 'wrong way behavior': The catalyst near the inlet is very rapidly deactivated after contact with water, causing an increase in the CO concentration further from the inlet. Here, the temperature of the catalyst has not been affected yet, so that the reaction rate is temporarily higher. The temperature in this part of the reactor therefore increases until colder gas coming from the first part of the bed causes the catalyst temperature to decrease to a value that is lower than before the addition of water. This behavior can only be observed if the water is adsorbed very rapidly, causing a concentration front moving through the reactor. The conversion decrease continued for approximately 24 hours. After that time, the water concentration was increased a several times, but the effect on the reaction rate was far less than initially.

The influence of water was also studied in the integral reactor. In Fig. 2.7, it is shown that, in this reactor, deactivation occurred much faster than in the pilot-scale wall-cooled tubular reactor.

After the addition of water was stopped, the catalyst activity very slowly increased again. This process took more than 24 hours in the integral reactor at 190 °C and more than 3 days in the pilot-scale reactor at 140 °C. After 3 days, the conversion in the pilot-scale reactor was approximately 75% of the initial value. When the catalyst was again heated at ± 200 °C for 3 days, the conversion at 140 °C was higher than the original one, and could be increased further by exposing the catalyst to temperatures higher than 200 °C.

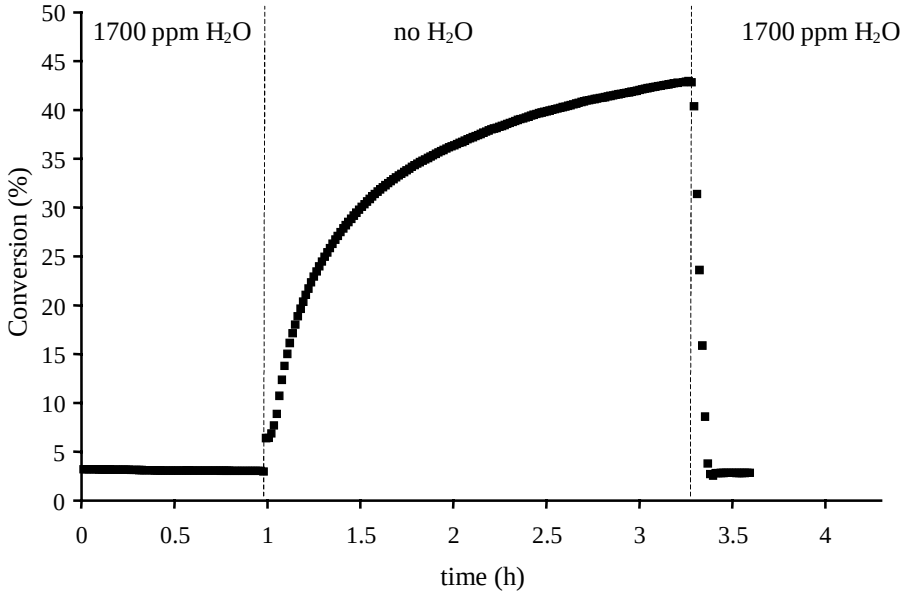

Fig. 2.6 Change of the CO conversion in integral reactor when switching between dry air and air containing 1700 ppm of water. CO_{inlet}=1 v%, T = 190 °C, P=5 bara, u=0.2 m s^{-1}, m_{cat}=0.47 g, bed height=10 cm.

We can conclude that water is a very powerful inhibitor for carbon monoxide oxidation over the used CuO/γ-alumina catalyst and that the decrease in activity is most likely caused by reversible adsorption at the active sites of the catalyst. It was decided to operate the reactor using a constant fraction of water of 1200 ppm. This was achieved by condensing a part of the water in the air feed in a heat exchanger, as was described in paragraph 2.3. A concentration higher than 1200 ppm would inconvenient, since the necessary water should be available in the ambient air at all weather conditions. Concentrations smaller than 1200 ppm require such a low temperature of the coolant (glycol) in the heat exchanger that the system would become clogged with ice.

2.4.3 Kinetics measured in the integral reactor

The experiments with air containing 1200 ppm water were performed at T= 130 - 230 ^{0}C, P= 2 - 9 bara, CO_{in}= 0.1 -1.2 vol% $CO_{2,in}$= 0 - 1 vol%.
The gas velocity was varied between 0.15 and 0.65 $Nm^3m^{-2}s^{-1}$ to study the influence of external heat and mass transfer limitations on the observed reaction rate. At the same conditions, conversions were measured using dry (<18 ppm water) air. The mixture of inert material and catalyst was prepared by mixing both in a glass cylinder, followed by violent shaking, until the mixture appeared homogeneous. After that, it was poured into the reactor. The mass fraction of catalyst was approximately 3 percent.

By applying eqs. 10-12 it was found that the maximum difference between the concentration at the catalyst surface and the concentration in the fluid concentration was less than 1% for all experiments. The temperature difference between the catalyst and the bulk was less than 1 ^{0}C at the maximum reactor temperature of 230 ^{0}C. At a constant mass flow of the feed, the pressure drop over the reactor increased when lowering the reactor pressure. At the highest flow rate, the measured pressure drop was less than 0.25 bar for experiments at pressures of 4 bara and higher and was maximum 0.4 bar at the lowest reactor pressure of 2 bara. The maximum measured temperature difference over the reactor was 7 ^{0}C at the maximum reactor temperature of 230 °C. At reactor temperatures up to 200 °C, the temperature difference was less than 3 ^{0}C. For the catalyst particles with a diameter of 0.2 mm, the effectiveness factor according to the model described in appendix B was always larger than 95% (ε/τ=0.05). When using dry (<18 ppm water) air, no influence of the reactor pressure on the reaction rate was observed. If the air contained a fixed fraction of water, the reaction rate decreased with the total pressure, which is attributed to the adsorption of water. This is confirmed by an experiment in which the water concentration in the feed was varied at constant total pressure by changing the temperature of the condenser in the air supply. The effective order with respect to the water concentration is approximately –0.6.

If the influence of the partial pressure of water is not included in the reaction rate equation, intra-particle transport limitation should be responsible of the decrease of the reaction rate with increasing reactor pressure. In that case, however, the effective diffusion coefficient of CO should be irrealistically small.

Different kinetic models were tested for the description of the experimental data, varying from power law-type to Langmuir-Hinshelwood-type of reaction rate expression. A fair agreement between calculated and measured conversions was obtained when applying the model proposed by *Dekker et al., 1992* to which adsorption of water on active sites was

Table 2.4 Steps involved in the reaction*

			rate constant
$O_2 + 2 \otimes$	$\rightarrow$	$2\ O\text{-}\otimes$	k_1
$CO + O\text{-}\otimes$	$\rightarrow$	$CO_2\text{-}\otimes$	k_3
$CO\text{-}\otimes + \otimes$	$\rightarrow$	$CO\text{-}\otimes$	K_4
$CO\text{-}\otimes + O\text{-}\otimes$	$\rightarrow$	$CO_2\text{-}\otimes + \otimes$	k_5
$CO_2 + \otimes$	$\leftrightarrow$	$CO_2\text{-}\otimes$	k_6/k_{-6}
$CO_2 + O\text{-}\otimes$	$\leftrightarrow$	$CO_3\text{-}\otimes$	K_7
$H_2O + O\text{-}\otimes$	$\leftrightarrow$	$H_2O\text{-}O\text{-}\otimes$	K_8

* numbered as in *Dekker et al., 1992*

added (see eq. (2.16)). It is assumed that the adsorption and reaction steps, listen in Table 2.4, occur on identical active sites, denoted as ⊗.

In the last step, the blocking of an active site by water is denoted as 'H_2O-O-⊗'. The true nature of the adsorbed species is not known. Water may be present as an adsorbed species, but it is likely that unstable –OH groups are formed at the catalyst surface that do participate in the reaction with carbon monoxide.

If it is assumed that oxidation of the active sites is very fast (zeroth order in oxygen) and that CO only reacts from the gas phase, the reaction rate can expressed as (*Dekker et al., 1992*):

$$R = \frac{k_3\ [CO]}{1+\frac{k_3}{k_{-6}}[CO]+K_7[CO_2]+K_8[H_2O]} \tag{2.16}$$

$$k_j = k_{0,j}\ \exp\left(\frac{-E_a}{RT}\right)\ ;\ K_j = K_{0,j}\exp\left(\frac{-\Delta H_{ads}}{RT}\right) \tag{2.17}$$

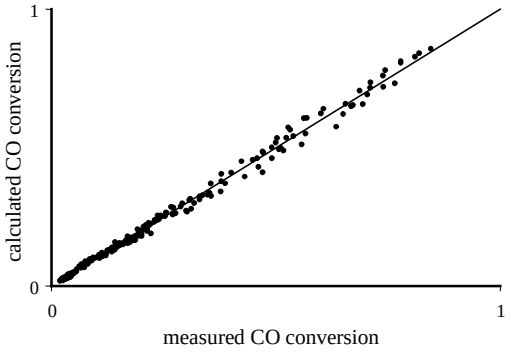

Table 2.5 Kinetics according to eq. (2.17)

$k_{0,3}$	$1.12\cdot10^6$	$kg^{-1}s^{-1}$
Ea_3	68	kJ $mole^{-1}$
$k_{0,3}/k_{0,-6}$	$1.8\cdot10^3$	$kg^{-1}s^{-1}$
Ea_{-6}-Ea_3	-29	kJ $mole^{-1}$
$K_{0,7}$	$2.6\cdot10^3$	$kg^{-1}s^{-1}$
ΔH_7	-28	kJ $mole^{-1}$
$K_{0,8}$	$7.1\cdot10^3$	$kg^{-1}s^{-1}$
ΔH_8	-33	kJ $mole^{-1}$

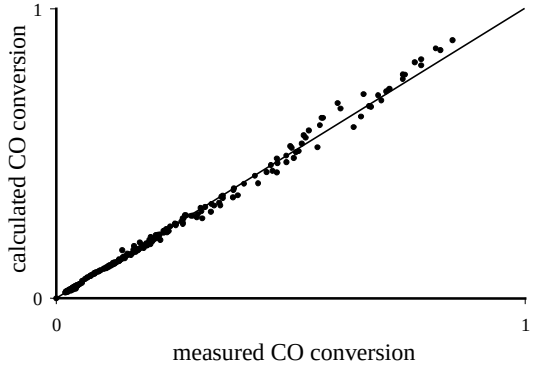

Table 2.6 Power law kinetics

k_0	$70\cdot10^6$	$mole^{1-\Sigma n_1}\ kg^{-1}s^{-1}$
Ea	99	kJ $mole^{-1}$
n_{CO}	0.8	-
n_{CO2}	-0.15	-
n_{water}	-0.5	-

Fig. 2.7 Parity plots of the reaction rate of CO oxidation over 0.2 mm catalyst particles in the integral reactor according to different rate expressions. 130<T<230 °C, 2<P<9 bara, 0.1<CO_{inlet}<1.2 vol%, 0<$CO_{2,inlet}$<1 vol%, 0.15<u_0<0.65 $Nm^3m^{-2}s^{-1}$. The feed contained a constant mass fraction of water of 1200 ppm.

CO is assumed to react from the gas phase according to the Eley-Rideal mechanism. A distinction is made between CO_2 which is adsorbed from the gas and CO_2 that is present as a result of reaction of CO with adsorbed oxygen. The presence of different species of CO_2 cannot be verified on the basis of our steady-state experiments. The first graph in Fig. 2.7 is a parity plot of the conversion calculated according to this expression and the measured conversion.

None of the terms in eq. (2.16) can be omitted. k_3/k_{-6} [CO] accounts for the effective order in CO being smaller than one, K_7 [CO_2] accounts for the negative influence of CO_2 on the overall reaction rate, as was observed during experiments in which the gas velocity was changed and experiments during which extra CO_2 was added to the reactor feed.

The dependence of the effective orders with respect to CO_2 and water on temperature is not very strong, as can be concluded from the activation energy Ea_{-6}-Ea_3 and the adsorption enthalpies of CO_2 and water ΔH_7 and ΔH_8 in table 2.5.

As can be seen in Fig. 2.8, the reaction rates measured at different CO_2 concentrations are described equally well by the expression (2.16) or a power law rate expression:

$$R = k_0 e^{-\frac{E_a}{RT}} [CO]^{n1} [CO_2]^{n2} [H_2O]^{n3} \qquad (2.18)$$

However, such power law expression has several drawbacks. It does not take into account the physical phenomena that cause the overall orders to differ from unity. As a result, the reaction rate becomes infinite if one of the concentrations goes to zero. This makes it very

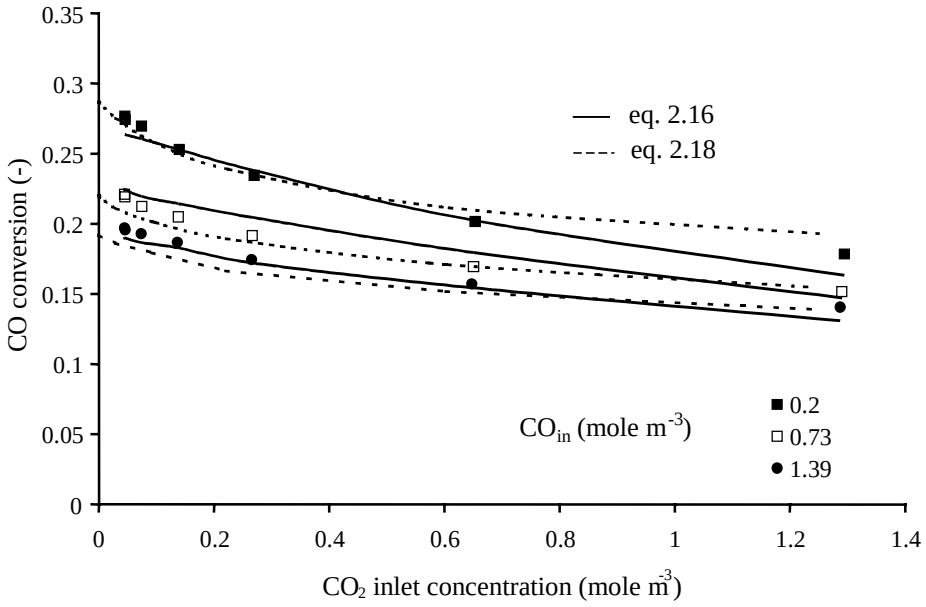

Fig. 2.8 Influence of the CO_2 inlet concentration on the observed (dots) and modeled (lines) reaction rate at different CO inlet concentrations at T= 210 °C, P= 5 bara, and u_0= 0.65 $Nm^3\ m^{-2}\ s^{-1}$.

difficult to apply the power law expression in the analytical and numerical models that are used to calculate temperature and concentration fields inside the catalyst pellets and in the pilot-scale wall-cooled tubular reactor.

2.4.4 Kinetics measured in the BoBo reactor

As in case the of the experiments performed in the integral reactor, the experimental data obtained at a constant water fraction of 1200 ppm will be considered here. In the BoBo reactor, experiments were performed at reactor pressures of 2.2, 3.7, 5.7 and 8.2 bara at temperatures between 117 and 225 °C. The CO and CO_2 concentration inside the reactor was varied between 0.05 and 1 and between 0.04 and 1.4 vol% respectively. The gas load was varied between 90 and 180 Nl h^{-1}. During the experiments presented here, the catalyst particles were mounted on the rack just below the impeller instead of inside the impeller blades, which is shown in Fig. 2.2. As was observed during the experiments using the integral reactor, the presence of 1200 ppm water in the air feed reduced the reaction rate by a factor of four.

Fig. 2.9 is a parity plot of the predicted and the measured reaction rates in the BoBo reactor at the conditions given above. The reaction rate was calculated using the kinetic parameters in Table 2.5, which were obtained from the experiments performed using the integral reactor.

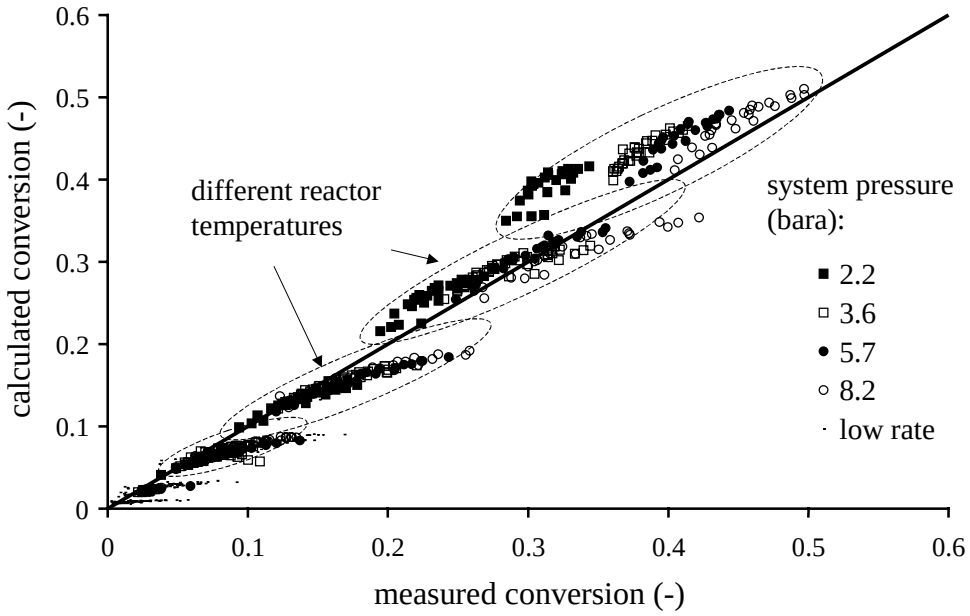

Fig. 2.9 Calculated vs measured conversion for experiments in BoBo reactor at different system pressures at a gas load of 0.65 N m^3 m^{-2} s^{-1} and 117<T_{cat}<225 °C, 0.05<CO<1 vol%, 0<CO_2<1.4 vol%. The reaction rate calculated using intrinsic kinetics measured in integral reactor, together with intra- and extra-particle mass transfer limitations. Experiment at which the CO_2 concentration in the effluent was less than 0.02 vol% are shown in the series 'low rate'.The effectiveness factor, η, was between 0.4 and 1.

In the case of the catalyst particles used in the BoBo reactor, which are significantly larger than the crushed catalyst used in the integral reactor, the reaction rate was influenced by both intra- and extra-particle diffusion limitation of CO and CO_2. The influence of intra-particle mass transfer limitation was accounted for by the particle effectiveness factor,η , which was calculated from the analytical approximation described in Appendix B. The value of In the analytical expression for the effectiveness factor, the intra-particle diffusivity of CO_2 was taken equal to the effective diffusivity of CO. Since the apparent order of the reaction rate towards CO_2 is small, this assumption does not change the calculated effectiveness factor by more than 3%, as was concluded after numerical calculation of the concentration profiles of CO and CO_2 over the volume of a particle. The effective intra-particle diffusivities were estimated from the measured catalyst pore size distribution and the pore tortuosity obtained from permeability experiments (see Appendix A). It was found that intra-particle transport is governed mainly by molecular diffusion and not by Knudsen diffusion. The concentrations of CO and CO_2 at the surface of the catalyst particles were calculated from the measured difference between the temperature and the temperature at the center of a catalyst particle. If the temperature is assumed constant over the particle, the Nusselt number for particle-to-fluid heat transfer can be calculated as (eq. (2.3)):

$$\mathrm{Nu} = \frac{\rho_p \Delta H_r R(c,T) d_p}{a_p (T_p - T_g) \lambda_g}$$

where R(c,T) is the measured reaction rate. The dependence of the particle Nusselt number on the Reynolds number can be described quite well using the following expression:

$$\mathrm{Nu} = 0.35\mathrm{Re}^{0.5} \qquad (2.19)$$

This correlation is close to the heat-transfer equivalent of the Sherwood number for the stationary particles, which, according to *Borman, 1994*, is half the value for the rotating particles according to eq. (2.1) (see Fig. 2.10). In the work of Borman, the distance between the stationary particle and the impeller was larger than the distance used in this investigation. Therefore, additional mass transfer experiments were done using camphor particles of the same size and shape as the catalyst particles. These experiments were performed using air at ambient temperature and pressure. The obtained values of Sh agree with the findings of Borman. When calculating the reaction rates for the catalyst in the BoBo reactor, the concentrations at the surface of the catalyst pellets were corrected for external mass transport limitation using eq. (2.19), assuming that $\mathrm{Sh}=\mathrm{Nu}\cdot\mathrm{Le}^{1/3}$. Since the effective reaction order with respect to CO is smaller than one, the relative concentration drop at the surface of the catalyst, $([CO]_f-[CO]_s)/[CO]_f$, increases with decreasing CO concentration in the fluid bulk, $[CO]_f$. This is because the derivative of the reaction rate with respect to CO decreases with

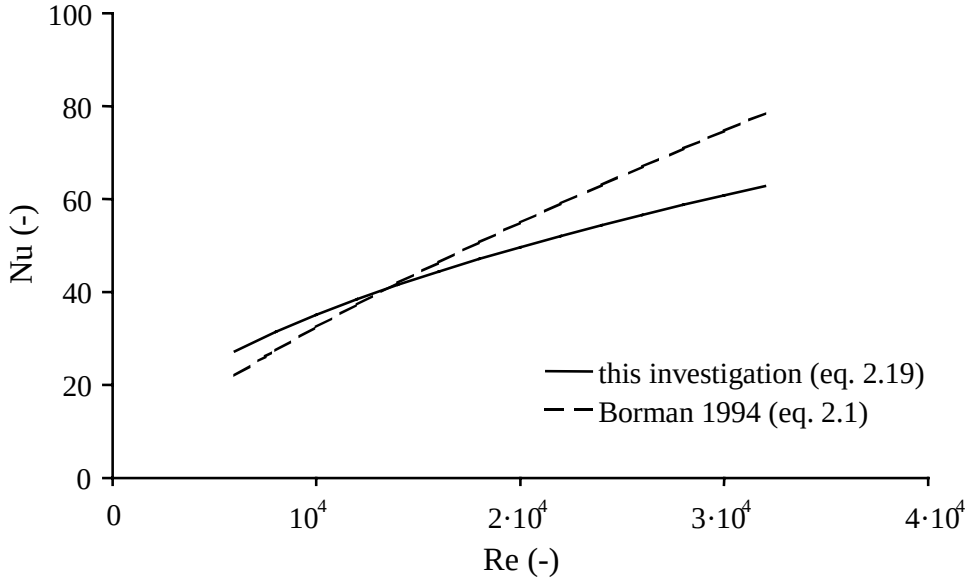

Fig. 2.10 Nusselt number as function of the particle Reynolds number for stationary particles below the impeller of the BoBo reactor. Solid line: calculated from the measured reaction rate and temperature difference between the center of the catalyst particles and the fluid; dashed line: based on mass transfer experiments of *Borman, 1994*.

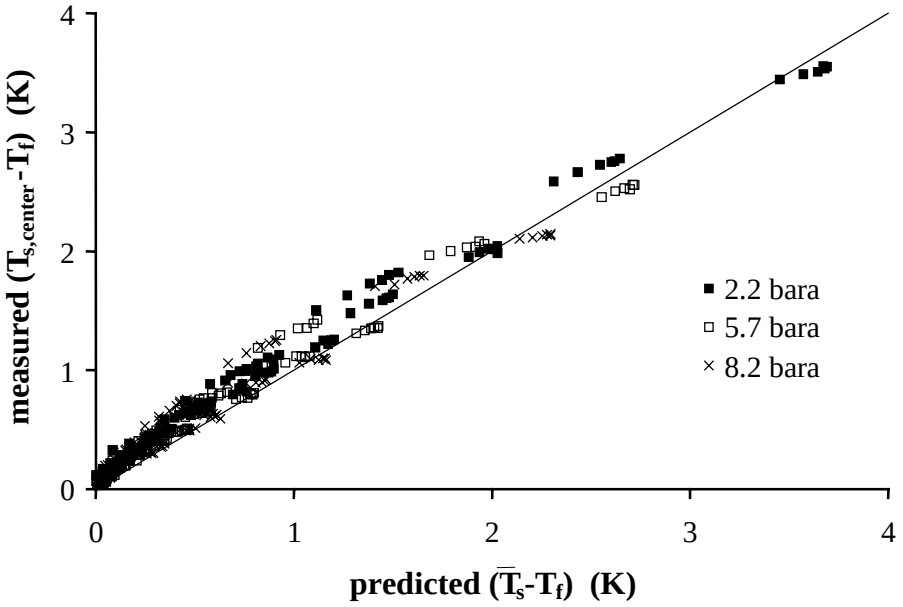

Fig. 2.11 Measured temperature difference between the fluid and the center of the catalyst versus the predicted temperature difference between the fluid and the average catalyst temperature for experiments shown in Fig. 2.9.

increasing CO concentration, whilst the concentration difference is a linear function of the reaction rate. The predicted relative concentration difference has a maximum of 8% at the highest reactor pressure and the smallest CO concentration.

The effect of intra-particle temperature gradients can become important at high reaction rates and a high apparent activation energy of the reaction. Application of the criterion of Anderson (*Anderson, 1963*):

$$\frac{|\Delta H_r|\rho_p R(c,T) r_p^2}{\lambda_p T_s} \Big/ 0.75\frac{RT_s}{E_a} < 1 \qquad (2.20)$$

to the reaction rates used in Fig. 2.9 indicates that the reaction rate should be influenced by intra-particle heat transfer limitation. The maximum value of the left hand side of eq. (2.20) exceeds the value of 3.

However, the occurrence of intra-particle mass transport limitation reduces the temperature increase inside the particles. In figure Fig. 2.11, the measured temperature difference between the center of the catalyst particles and the fluid is compared to the temperature difference that is predicted when the temperature of the catalyst is assumed to be uniform. If the reaction rate would be influenced by intra-particle heat transport limitation, the measured temperature difference would be higher than predicted and it would increase with increasing reaction rate. The trend shown in Fig. 2.11 is opposite from this, so that it seems safe to assume a uniform temperature of the catalyst.

In the derivation of the criterion (2.20), concentration gradients inside the particles were neglected. With increasing reaction rate, the concentrations of the reactants decrease towards

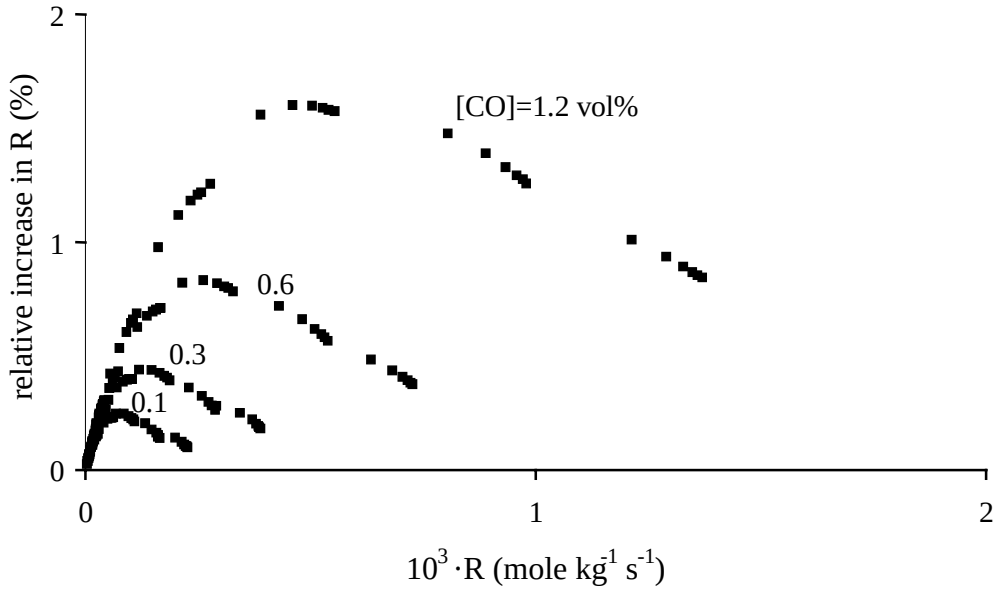

Fig. 2.12 Predicted relative increase of the reaction rate due to intra-particle heat transfer limitation as function of the reaction rate. The reaction was calculated using the kinetic parameters obtained from experiments in the integral reactor. For this graph, the reaction conditions of all experiments performed at a reactor pressure of 5.7 bara were used. λ_p=0.25 (see appendix C); effective diffusivities of CO and CO_2 as calculated in Appendix A.

the center of the particle and eventually the reaction takes place mainly in a zone near the surface of the particle. The distance over which the evolved heat has to be transferred to the surface decreases, so that the real temperature difference over the particle is smaller than in case of a uniform concentration. This is the case here. Fig. 2.12 shows the predicted increase of the average reaction rate inside a catalyst particle due to heat transport limitation if intra-particle mass transfer limitation is taken into account. The two-dimensional heat- and mass balance equations for the cylindrical catalyst pellet were solved numerically. The reaction rate was calculated according to eq. (2.17), using the parameters obtained from the experiments in the integral reactor (Table 2.5). An average value of the effective thermal conductivity of the catalyst of 0.25 W m^{-1} K^{-1} was used (see Appendix C)

The increase of the reaction rate has a maximum. Initially, it increases due to an increase of the temperature inside the pellet. At a certain moment, the temperature near the center of the particle starts to decrease due to mass transport limitation. The maximum increase of the reaction rate depends on the concentration at the surface of the particle and on the reaction kinetics and was less than 2% for all experiments that are considered in this work.

As shown in Fig. 2.9, the reaction rates calculated from experiments in the BoBo reactor do not perfectly agree with the intrinsic kinetics that were obtained from the experiments in the integral reactor. The apparent activation energy of the reaction, which is determined by the intrinsic kinetics and the intra-particle mass transport, seems to be too high, as a result of which the reaction rates at the higher temperatures are overestimated. The apparent order with respect to CO for the experiments performed in the BoBo reactor is higher than the value derived from the experiments in the integral reactor. This change of the apparent order causes the slope of the data sets measured at different temperatures to deviate from unity. The difference between the measured and the calculated conversions can be due to errors in the intrinsic kinetics or to an uncertainty of the intra-particle diffusivity. It should be realized that the actual internal geometry of the catalyst has been simplified in the model. To improve the prediction of the reaction rate, the parameters of the reaction rate equation (2.16) were optimized.
Fig. 2.13 shows the parity plots after optimization. Experiments at different pressures, during which the CO_2 concentrations in the reactor effluent were below 0.02 vol%, are labeled as 'low rate' and were neglected in the optimization procedure because of insufficient accuracy of infrared analyzers. These points are shown in the graphs,, however, since they agree well with the remaining data. The apparent activation energy of the reaction was calculated by fitting:

$$R = k\, e^{\frac{-E_{a,apparent}}{RT_S}} \qquad (2.21)$$

to the overall reaction rate. This overall reaction rate was calculated as the product of the particle effectiveness factor and the intrinsic reaction rate according to eq. (2.16). $E_{a,apparent}$ was calculated usssuming concentrations of CO and CO_2 of 0.5 vol% at the surface of the particles.

Optimization of only the frequency factors significantly reduces the difference between the calculated and measured reaction rates, but does not make the trends in Fig. 2.9 disappear completely. A better agreement between the experiments and the kinetic model is obtained when fitting all parameters in the reaction rate expression. In that case, a large change of the activation energies and adsorption enthalpies occurs, which may not be true or realistic values. Since the kinetic parameters in the rate expression (2.16) already show a strong correlation, it is difficult to make a distinction between the Eley-Rideal mechanism, which was used here, and a Langmuir-Hinshelwood mechanism, in which CO reacts from the

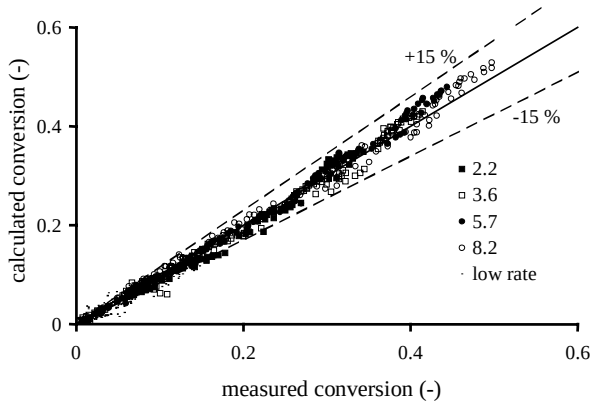

Frequency factors optimized

Table 2.7

$k_{0,3}$	$0.30 \cdot 10^{6}$	$kg^{-1}s^{-1}$
Ea_3	68	kJ $mole^{-1}$
$k_{0,3}/k_{0,-6}$	$0.54 \cdot 10^{-3}$	$kg^{-1}s^{-1}$
Ea_{-6}-Ea_3	-29	kJ $mole^{-1}$
$K_{0,7}$	$1.0 \cdot 10^{-3}$	$kg^{-1}s^{-1}$
ΔH_7	-28	kJ $mole^{-1}$
$K_{0,8}$	$0.56 \cdot 10^{-3}$	$kg^{-1}s^{-1}$
ΔH_8	-33	kJ $mole^{-1}$
E_a apparent	55	kJ $mole^{-1}$
Average error	7 %	

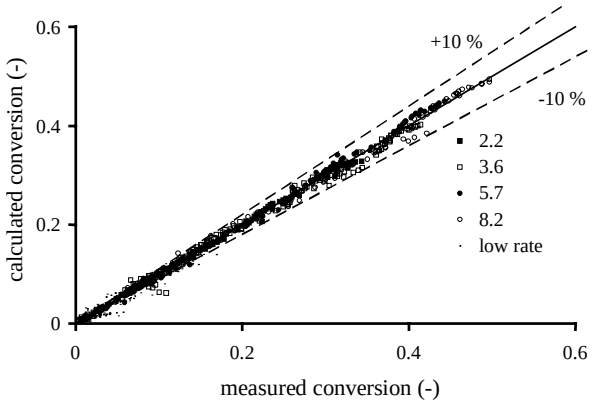

All parameters optimized

Table 2.8

$k_{0,3}$	43	$kg^{-1}s^{-1}$
Ea_3	33	kJ $mole^{-1}$
$k_{0,3}/k_{0,-6}$	$6.3 \cdot 10^{-6}$	$kg^{-1}s^{-1}$
Ea_{-6}-Ea_3	-49	kJ $mole^{-1}$
$K_{0,7}$	$2.0 \cdot 10^{-9}$	$kg^{-1}s^{-1}$
ΔH_7	-79	kJ $mole^{-1}$
$K_{0,8}$	$1.2 \cdot 10^{-6}$	$kg^{-1}s^{-1}$
ΔH_8	-60	kJ $mole^{-1}$
E_a apparent	50	kJ $mole^{-1}$
Average error	4 %	

Fig. 2.13 Parity plots of the reaction rate of CO oxidation over intact catalyst particles after optimization of the frequency factors only and after optimization of all kinetic constants. The intrinsic reaction rate has the form of equation (2.16) and intra-particle diffusion limitations were accounted for by the use of an effectiveness factor (see Appendix B), which was between 0.4 and 1.

adsorbed state.

Because the denominator of eq. (2.16) was usually much larger than 1, the activation energy of the reaction, $E_{a,3}$ is strongly correlated to the adsorption enthalpies. Despite the large differences in the activation energies and adsorption enthalpies, the overall dependence of the reaction rate on temperature is rather similar for the different sets of kinetic parameters, as is shown in Fig. 2.14. After optimization of only the frequency factors to the experiments in the BoBo, the overall dependence of the intrinsic reaction rate is almost identical to the one that was measured in the integral reactor. If the activation energies and the adsorption enthalpies are optimized as well, the intrinsic reaction rate becomes lower than was measured in the integral. Most likely, this is due to overestimation of the particle effectiveness factor. The dependence of the reaction rate on the concentrations of CO and CO_2 are also very similar for the three sets of parameters used in Fig. 2.14.

Because of the complex pore structure, the values of the effective diffusivity are rough estimations. Changing the effective intra-particle diffusivities of CO and CO_2 did not give better results. If the pore tortuosity was included as an extra parameter in the fitting procedure, unrealistic values were obtained.

In the remaining of this thesis, the reaction rate was calculated using the parameters given in table 2.8 in Fig. 2.13, which resulted after optimization of all parameters. This was done because only the overall reaction rate is important in the models that were used for the description of the experiments in the pilot-scale wall-cooled tubular reactor (see Chapter 3). Since the kinetic experiments were performed within the same range of operating conditions

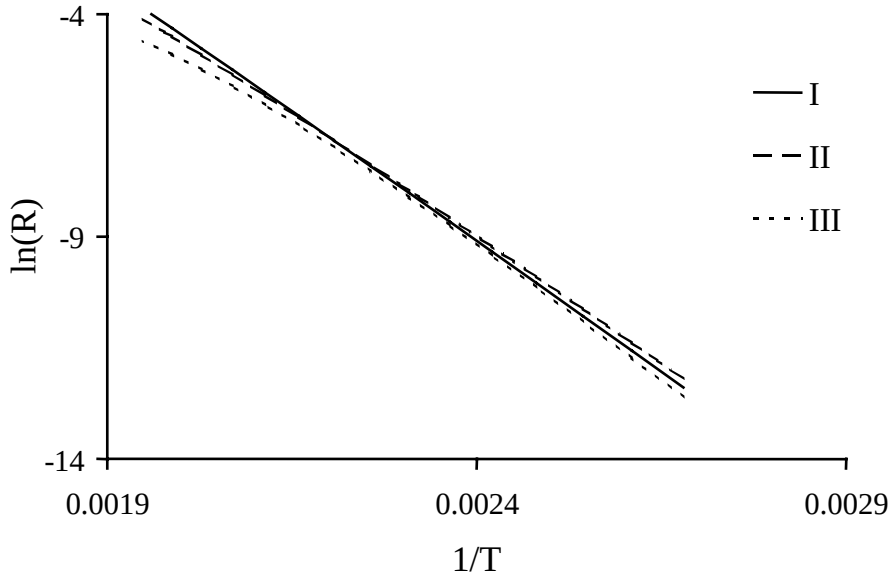

Fig. 2.14 Temperature dependence of the intrinsic reaction rate according to eq. (2.16) at P=5 bara, [CO]=1 vol%, [CO_2]=1 vol% and [H_2O]=1200 ppm. I: parameters optimized for the integral reactor; II: as I, but after optimization of the frequency factors to the experiments in the BoBo reactor (Table 2.7); III: after optimization of all reaction rate constants to the experiments in the BoBo reactor (Table 2.8).

as were used in the pilot-scale reactor, no errors were introduced by extrapolation of the reaction rate.

2.5 Conclusions

The reaction rate of CO oxidation in air over cylindrical catalyst pellets consisting of 29 wt% CuO on γ-alumina was measured over a broad range of temperatures, pressures and concentrations. It was found that the catalyst activity was sensitive to very small amounts of water, present in the feed. Reproducible experiments could be obtained only if the feed contained a constant mass fraction of water, which is assumed to be adsorbed reversibly on the active sites. Intrinsic reaction kinetics were measured in an integral reactor, containing a bed of crushed catalyst, diluted with silicium carbide.

When using these kinetics, the conversions measured in the BoBo reactor using the original (unbroken) catalyst particles could be predicted rather well if fluid-to-particle and intra-particle mass transfer limitations were taken into account.

The kinetic parameters to be used in the models of the pilot-scale wall-cooled tubular reactor were optimized to fit the experiments in the BoBo reactor. The maximum difference between the predicted and the measured reaction rates is approximately 10 %, whilst the average error is less than 4%.

Notation

a_p	specific surface area	$m^2\ m^{-3}$
a_j, b_j	kinetic constants after linearization reaction rate to T	-
C	concentration	mole m^{-3}
c_p	heat capacity	J $kg^{-1}K^{-1}$
D	diffusion coefficient	$m^{-1}\ s^{-1}$
D_{eff}	effective diffusivity	$m^{-1}\ s^{-1}$
D_{imp}	impeller diameter	m
d_p	particle diameter	m
E_a	(apparent) activation energy	J $mole^{-1}$
f	ratio between observed and real reaction rate	-
f_α	ratio heat and mass tr coeff. packed bed/ single particle	-
ΔH_{ads}	adsorption enthalpy	J $mole^{-1}$
k_0	frequency factor	$mole(^{1-x)}m^{3x}kg^{-1}s^{-1}$
K_0	adsorption equilibrium constant	$kg^{-1}\ s^{-1}$
k_g	particle-to-fluid mass transfer coefficient	m s^{-1}
N_Q	pumping coefficient	-
n	(apparent) reaction order	-
P	pressure	Pa
Q_D	impeller discharge rate	$m^3\ s^{-1}$
Q_f	feed rate	$m^3\ s^{-1}$
r_p	particle radius	m
R_p	distance between particle and impeller axis	m
R_{rec}	recylce ratio	-
R (c,T)	reaction rate	mole $kg^{-1}s^{-1}$
T	temperature	K
T^*	reference temperature	K
u_0	superficial fluid velocity	m s^{-1}
z	axial coordinate	m

Greek

α	dimensionless temperature	-
α_p	particle-to-fluid heat transfer coefficient	W $m^{-2}K^{-1}$
β	dimensionless activation energy	-
ε	porosity	-
λ	thermal conductivity	W $m^{-1}K^{-1}$
η	dynamic viscosity	Pa s
ν	stoichiometry coefficient	-
τ	pore tortuosity	-
ω	rotation frequency	s^{-1}

ρ	density	kg m^{-3}
ρ_{cat}	catalyst concentration	kg catalyst m^{-3}
Ξ	ratio reaction rate before and after catalyst sample	-
ζ, ζ_b	total conversion, resp. conversion per pass	-

Dimensionless groups

Le	Lewis number	$\frac{\lambda_f}{\rho_f c_{p,f} D}$
Nu	Nusselt number	$\frac{\alpha_p d_p}{\lambda_f}$
Pr	Prandtl number	$\frac{\eta_f c_{p,f}}{\lambda_f}$
Re	particle Reynolds number	$\frac{u_0 \rho_f d_p}{\eta_f}$
Re_{rp}	Reynolds number of rotating particle	$\frac{2\pi r_p \omega \rho_f d_p}{\eta_f}$
Sh	Sherwood number	$\frac{k_g d_p}{D}$

Subscripts

c	calculated
f	fluid
i	at surface of pellet
	index number reaction components
j	index number rate constants
in	at reactor inlet
lam	laminar
m	measured
out	at reactor outlet
p	particle
s	solid
turb	turbulent

Chapter 3

Heat transfer with and without reaction in a pilot-scale wall-cooled tubular reactor

ABSTRACT

In a pilot-scale wall-cooled tubular reactor with a length of 1 m and a diameter of 53 mm, heat transfer experiments were performed at reacting and non-reacting conditions. The oxidation of carbon monoxide in air over cylindrical catalyst pellets with a diameter of 5.5 mm and a height of 11.2 mm, consisting of CuO on γ-alumina, was used as a model reaction system. Experiments were performed at inlet- and wall temperatures between 156 and 200 °C and reactor pressures of 3, 5.9 and 8 bara. The gas load was varied between values corresponding to 200< Re <1400 and the CO inlet concentration was between 0.1 and 1.5 vol%. A two-dimensional pseudo-heterogeneous reactor model was used as a basic model to predict the temperature and concentration profiles that were measured inside the catalyst packing. When using the heat transport parameters measured at non-reacting conditions and the separately measured reaction kinetics, the basic model gave a fair description of the temperature profiles measured at reacting conditions. At high flow rates, however, the effective heat transport parameters, obtained at reacting conditions, were smaller than the values obtained at non-reacting conditions. Optimization of the reaction rate on the basis of the measured conversion did not make this difference disappear. It was found that a radial distribution of the bed porosity and, which is a result of this, of the axial fluid velocity has to be taken into account in order to obtain agreement between the heat transfer parameters derived from experiments at reacting and non-reacting conditions.

3.1 Introduction

For a proper design of a wall-cooled tubular reactor, an accurate knowledge of the heat transport properties of the catalyst bed is required. Especially at conditions close to runaway, the reactor behavior is very sensitive towards these propoperties.. Nowadays, most cooled tubular reactors are not designed on the basis of kinetic data and model calculations, but on the basis of experiments carried out using single tubes in pilot scale reactors, at conditions close to those of the industrial process. Previous studies of heat transport phenomena in wall-cooled tubular reactors have shown a discrepancy between the effective radial conductivities

of the catalyst bed measured with and without reaction (*Hall and Smith, 1949, Hoffman, 1979, Schwedock and Windes, 1989, Schouten et al., 1994*). Schwedock observed that, at reacting conditions, the effective radial thermal conductivity was about 50 % higher than at non-reacting conditions. In their work, *Schouten et al., 1994*, used partial oxidation of ethylene to ethylene oxide over a silver/γ-alumina catalyst as a model reaction. The main disadvantages of this reaction system are the complicated kinetics, caused by the occurrence of complete combustion of ethylene as a parallel reaction, the large number of reactants and a slow deactivation of the catalyst. This investigation is a continuation of their work, using a more simple reaction system. The oxidation of carbon monoxide to carbon dioxide over a copper oxide catalyst, supported on γ-alumina, has been chosen as model reaction. An advantage of this reaction is its large enthalpy of reaction of 283 kJ $mole^{-1}$, which causes a large temperature increase at a small change of the composition of the gas mixture. The kinetics of this reaction were studied separately using an integral and an internal-recycle reactor (see Chapter 2).
The experiments were performed at Re between 200 and 1400, reactor pressures of 3, 5.9 and 8 bara, wall temperatures of 156, 180 and 200 °C and CO inlet concentrations ranging from 0.1 to 1.5 vol%. A two-dimensional pseudo-heterogeneous reactor model was used for calculation of the temperature and concentration profiles inside the packing.

3.2 Experimental

3.2.1 Setup

The experimental setup used for the study of packed-bed heat transfer is shown in Figures 3.1 to 3.3. The setup was used in the previous work of Borman and Schouten (*Borman, 1993*, *Schouten, 1995*). The main changes of the setup were the addition of the air supply- and conditioning system, the use of a vibrator to be able to repack the catalyst bed in situ, and the full automation of the setup, including a gas sample system. The feed distributor was replaced to obtain a uniform velocity distribution and a smoother temperature profile at the reactor inlet.
The heart of the setup is a tubular reactor with a length of 1.5 m and an inner diameter of 53.1 mm. This reactor tube was surrounded by a cooling jacket with an internal diameter of 83 mm. Boiling water was used as a heat transfer medium since this gives the highest possible heat transfer coefficient, provided that the bed is cooled at the wall.
To avoid poor heat transfer if the feed inlet temperature was lower than the wall temperature, in which case the water locally stopped boiling, the water was circulated through the cooling jacket using a magnetically coupled centrifugal pump (HMD). The water velocity, as calculated from the pressure difference over the pump, was 0.5 m s^{-1}. At this flow rate, the heat transfer coefficient at the cooling side was approximately 4 kW m^{-2} K^{-1} if the water was

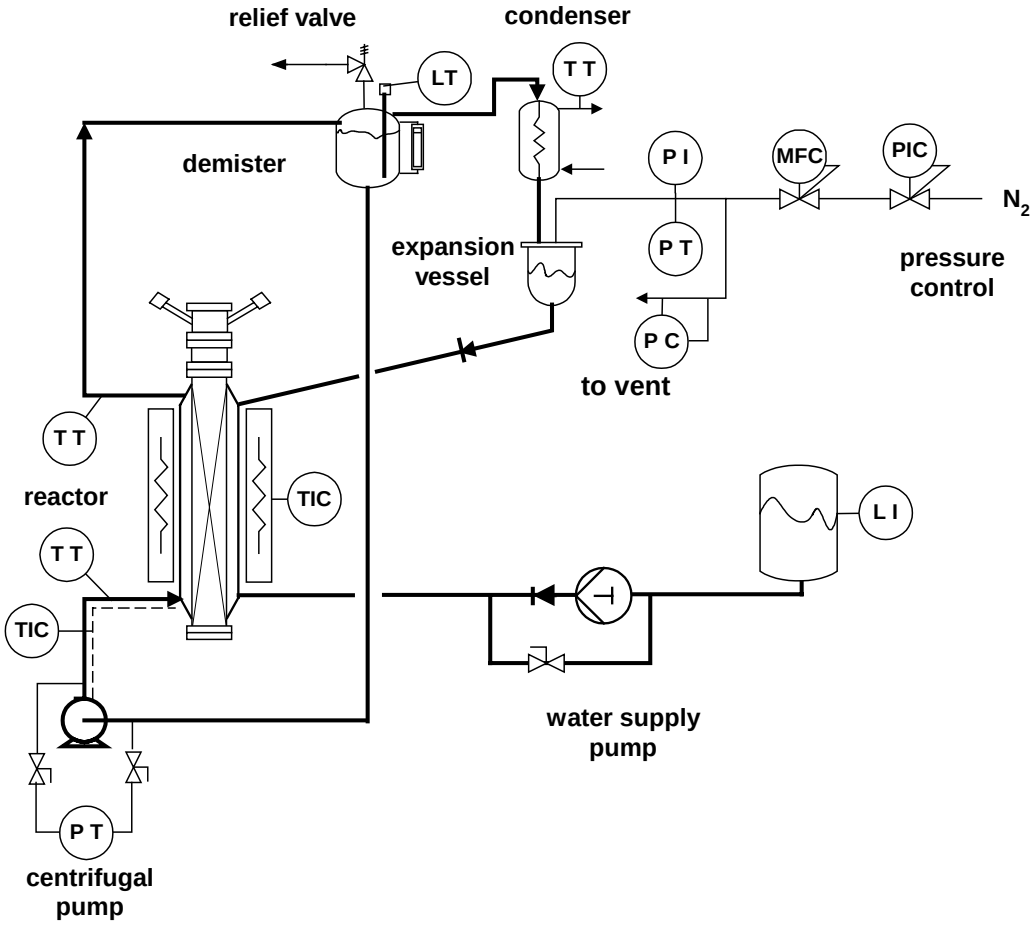

Fig. 3.1 Scheme of cooling circuit. Symbols: TT: temperature transmitter; TIC: temperature controller; PT: pressure transm.; PC: back pressure controller; PIC: pressure reducing valve; LT: level transm.; LI: level indicator.

not boiling, which is over 10 times as large as the maximum measured fluid-to wall heat transfer coefficient inside the bed. In case of boiling water, the heat transfer coefficient was several times larger.

Water and steam coming from the cooling jacket were led to a demister, in which steam and water were separated. The demister was positioned 3 meters above the circulation pump to create a pressure head, which should reduce cavitation. Since the temperature of the water inside the pump was very close to boiling point, however, cavitation did occur, which lead to fast wear of the pump's bearings. The steam coming from the demister was condensed and flowed to an expansion vessel before it was returned to the cooling system. The pressure –and therefore the temperature- of the cooling system was adjusted by supplying nitrogen to this expansion vessel. In order to minimize pressure fluctuations in the cooling water circuit, a small amount of nitrogen of approximately 5 Nl min^{-1} was supplied continuously, which left the system via a mechanical back pressure controller. In this way, the coolant temperature at the reactor inlet could be kept constant within 0.3 K. The water level in the demister was monitored continuously. This was necessary, since water could leave the system in case of

loss of nitrogen pressure. The cooling water was heated by a 6 kW electrical oven surrounding the reactor, and by a 1 kW electrical tracing around the pipe, connecting the circulation pump to the reactor. The entire setup was insulated with glass wool to minimize the temperature differences within the cooling system.

Fig. 3.2 shows the gas supply section of the pilot scale setup. Air was supplied by a compressor (Hydrovane) with a maximum capacity of 700 Nl min^{-1} at a pressure of 12 bara. Initially, this air was dried in a self-regenerating desiccant dryer (Dominick Hunter) to contain less than 18 ppm of water. Since the remaining traces of water water gradually decreased the catalyst activity (see Chapter 2), it was decided to use air with a constant water concentration of 1200 ppm. This was achieved by cooling the air after the compressor, using a heat exchanger. Ethylene glycol, supplied from a cryostat unit, was used as cooling medium. To obtain a constant temperature of the air leaving the heat exchanger, the temperature of the glycol was varied, depending on the air demand. Excess water, together with a small amount of oil coming from the compressor, was removed in two coalescing filters (Dominick Hunter OIL-X AO and AA).
After leaving the –now empty- desiccant dryer, the air was passed through a carbon bed to remove organic contaminants. This filter consisted of three parallel tubes with a length of 1 m

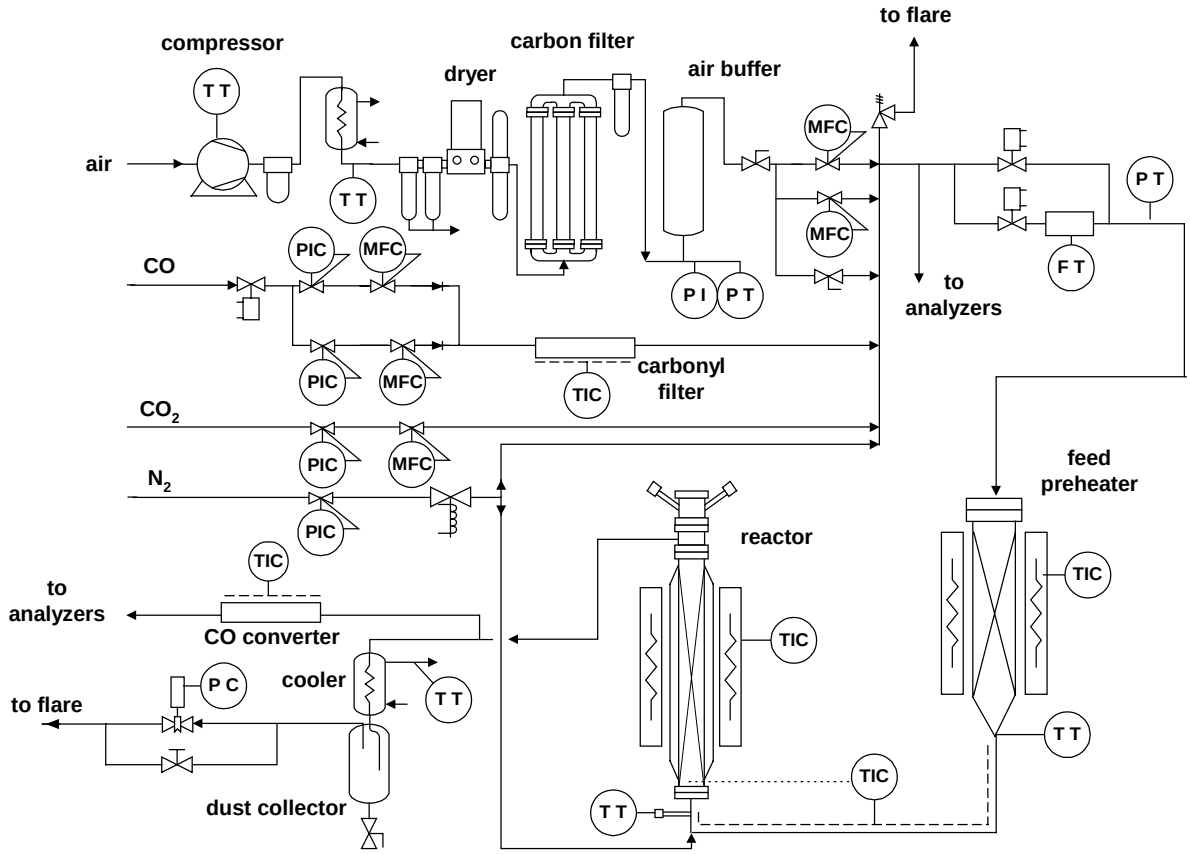

Fig. 3.2 Scheme of the gas supply system

and a diameter of 55 mm. The tubes were filled with 25 l of 2.6 mm Norit RB3 active carbon that was heated in vacuum at 260 °C prior to its use. The residence time of the air in this filter was approximately 10 seconds. After this filter, carbon dust was removed in an odor filter (Dominick Hunter OIL-X AC). Pressure-fluctuations were damped by a 50 l buffer vessel. The air was supplied to the feed section using electronic mass flow controllers; one with a capacity of 600 Nl min^{-1} (Bronckhorst Hi Tec) and one with a maximum capacity of 100 Nl min^{-1} (Brooks).

CO and CO_2 (Praxair, 99.9 %) were taken from gas cylinders. CO_2 was added directly to the air via an electronic mass flow controller (Brooks). CO was supplied via two electronic mass flow controllers (Brooks) and was passed through a carbonyl filter before entering the system. The carbonyl filter consisted of a stainless steel tube with a diameter of 8 mm and a length of 20 cm, filled with 0.2 mm silicium carbide particles. The filter was heated at 250 °C by an electrical tracing to make any iron carbonyls, that were present in the CO taken from the cylinder, deposit on the SiC. Without this filter, a brown, rust-like deposition covered the surface of the catalyst near the reactor inlet. In case of an emergency shut-down, the feed section and the reactor were flushed with nitrogen (Praxair, 99.999 %) by opening two electronic valves. After mixing of the feed gases, the total flow rate was measured by a propeller-anemometer (Hoentsch). A preheater was used to heat the feed till a temperature that was approximately 10 °C below the desired inlet temperature. This heater was tube with a length of 1 m and a diameter of 6 cm, filled with 2 cm alumina spheres. The wall of the tube was heated at a maximum temperature of 400 °C by the electrical, tubular oven that surrounded it. The feed was heated further by an electrical tracing around the pipe that connected the preheater to the reactor. The temperature of this tracing was controlled by an Eurotherm temperature controller that measured the temperature at the center of the gas distributor inside the reactor, which is shown in Fig. 3.3. The hot reactor effluent was cooled in a heat exchanger, after which dust was removed in a dust collector. An electronic back pressure controller was used to keep the reactor at a constant pressure. The pressure that was measured 400 mm from the reactor inlet was used as input for the PID controller (Eurotherm), which steered the back pressure controller. Part of the reactor effluent was passed through a CO converter, which was a catalyst bed that was heated at 200 °C. At this temperature, all CO remaining in the reactor effluent was converted to CO_2, allowing indirect measurement of the CO concentration in the feed of the reactor. The inlet concentration that was measured in this way was much more accurate than the value that could be calculated from the flows through the mass flow controllers, which depended on the reactor pressure. The maximum relative error in the CO inlet concentration was approximately 3 %. The CO_2 inlet concentration was measured by taking a sample directly after mixing the reactor feed. This concentration slightly oscillated if water was removed in the desiccant dryer, in which most CO_2 was adsorbed as well.

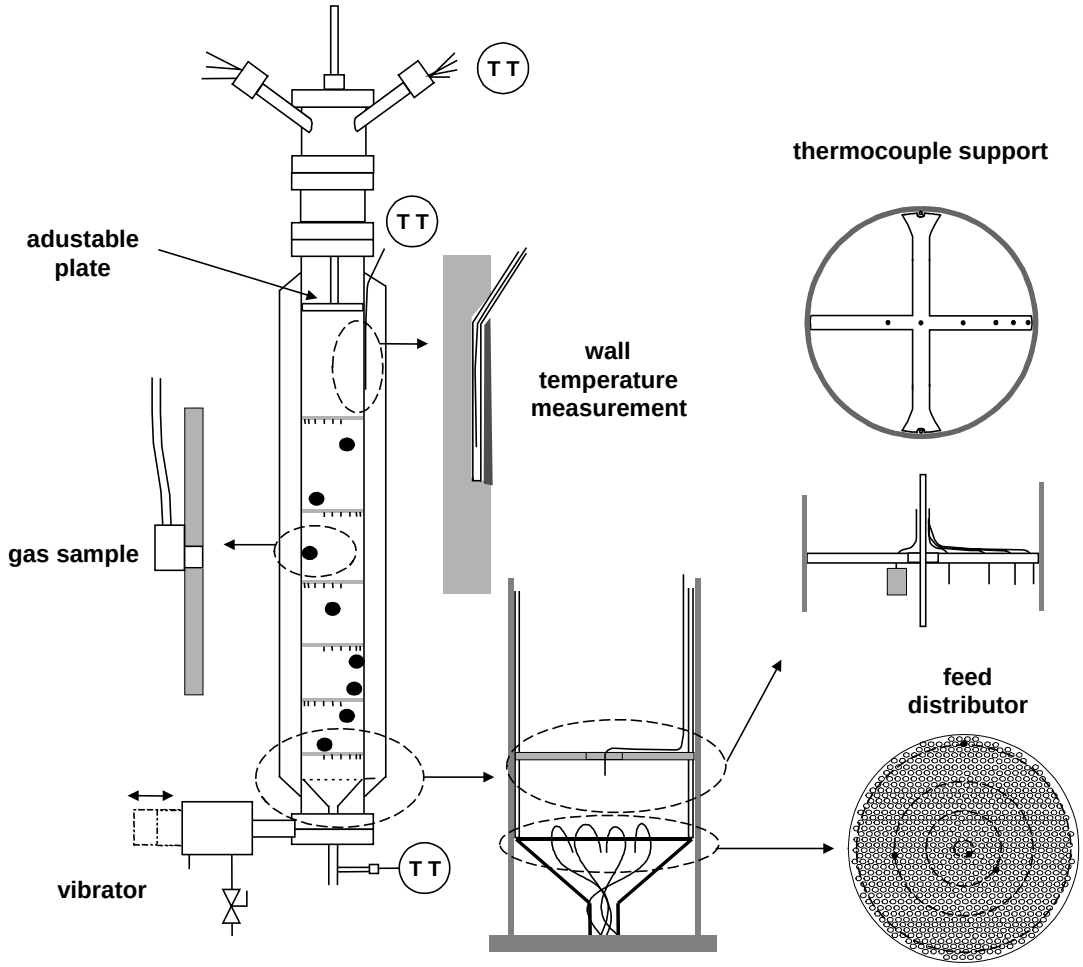

Fig. 3.3 Pilot scale wall-cooled tubular reactor

The wall-cooled tubular reactor is shown in more detail in Fig. 3.3. The entering feed was distributed over the cross section of the reactor by means of a stainless steel funnel, which was covered with a perforated metal disc. The top of the funnel was approximately 3 cm above the bottom of the cooling jacket. The funnel, with a total height of 10 cm, did not directly touch the reactor wall. At several radial positions, the inlet temperature was measured by 0.5 mm thermocouples, inserted through the holes in the distributor plate.
Inside the packing, radial temperature profiles were measured using a 'thermocouple ladder'. This ladder consisted of crosses of PEEK (Poly-Ether-Ether-Keton) which has a low thermal conductivity and resists temperatures up to 290 °C. The crosses had the same diameter as the reactor. In Appendix F, it is calculated that heat conduction along the PEEK crosses does not influence the temperatures of the tips of the thermocouples. Two arms of crosses were connected to vertical steel rods with a diameter of 1.5 mm. The two other arms of the crosses contained a total of 32 thermocouples with a diameter of 0.5 mm. The distance between the tips of the thermocouples and the crosses was 5 mm. The wires of the thermocouples were

bundled and fixed to two the steel rods. After assembly and precise measurement of the axial and radial positions of the thermocouples, the ladder was lowered into the empty reactor.
At four axial positions, the wall temperature was measured by 0.5 mm thermocouples that were inserted into steel capillaries that ran through the cooling jacket. The capillaries were welded into slits in the outside of the reactor wall to make sure that the wall temperature, and not the coolant temperature, was measured. At eight axial positions, a gas sample could be withdrawn at the wall of the reactor through capillaries that also went through the cooling jacket. A set of solenoid valves was used to automatically switch between the different sample positions and calibration gas mixtures. The samples were sent to a Mayhak UNOR infrared CO_2 analyzer (0-3 v%) and a Servomex infrared CO analyzer (0-8 v%), which were connected in series. The flow rate to the infrared analyzers was set at 500 Nml min^{-1}, which is less than 1% of the total feed rate at the minimum fluid velocity during all experiments. This flow rate was a compromise between possible disturbance of the velocity profile within the bed and the response time of the analyzers. The analyzers were calibrated using a mixture of CO or CO_2 in N_2 (Praxair, certified accuracy of 1 %). The water concentration in the last gas sample, relative to the feed inlet, was measured by an optical dew point hygrometer (Panametrics).
A pneumatically driven vibrator was connected to the flange at the bottom of the reactor to vibrate the reactor when repacking the catalyst bed.
The setup described above was fully automated, which allowed continuous operation. Data collection, safeguarding and control of the setup were done using a Hewlett Packard Data Acquisition Unit, connected to a PC. The control software was written in Hewlett Packard HPVEE. At 3 second intervals all input and output variables, 90 in total, were collected and sent.

3.2.2 Experimental procedure

The reactor was loaded with approximately 1.5 kg of catalyst, which had been calcined for 30 hrs at 550 °C in a tubular oven, flushed with air (see also Chapter 2). The loading was either done by carefully filling the reactor with few particles at a time, whilst constantly beating the reactor with a rubber hammer, or by quick filling of the reactor, followed by repacking by means of fluidization. The second method was applied later during the investigation, to be able to study the distribution of the catalyst activity by repacking of the bed, without exposing the catalyst to the ambient air. As discussed in Chapter 2, the catalyst activity was not constant when using air that contained only a few ppms of water. Adsorption of water caused the activity to depend on the axial position and on the temperature history of the catalyst. In order to overcome this problem, air with a constant mass fraction of water was used during the experiments that were used in this work.

After filling the reactor, a perforated disk was pushed on top of the bed to prevent particles being blown out of the reactor. After loading of the reactor with fresh catalyst, the wall temperature was increased till 200 °C and the reactor was flushed with air for at least 12 hours before performing measurements.

In case of heat transfer experiments without reaction, the difference between the temperatures of the feed and the wall temperature was 30 to 50 °C. After changing the operating conditions, the readings of a thermocouple at the centerline of the reactor, close the end of the bed were used to check whether steady state operation was attained. The necessary time was determined by the dynamics of the heating equipment and the cooling system, rather than by the dynamics of the packed bed itself. When the slope of the measured bed temperature versus time was zero, a steady-state temperature profile was recorded.

In case of experiments with reaction, the inlet temperature was set equal to the wall temperature. After setting the temperature, the feed rate and the pressure, scheduled experiments at various CO inlet concentrations were performed automatically by the control software. The CO inlet concentration was calculated from the difference between the CO_2 concentrations in the sample that was passed through the CO converter and the sample that was taken from the feed. The CO concentrations measured by the CO infrared analyzer were used as a backup and to verify if the time intervals, applied when switching between the samples were not too short. The response time of the CO analyzer was much less than that of the CO_2 analyzer. At too short switching intervals, the sum of the CO and the CO_2

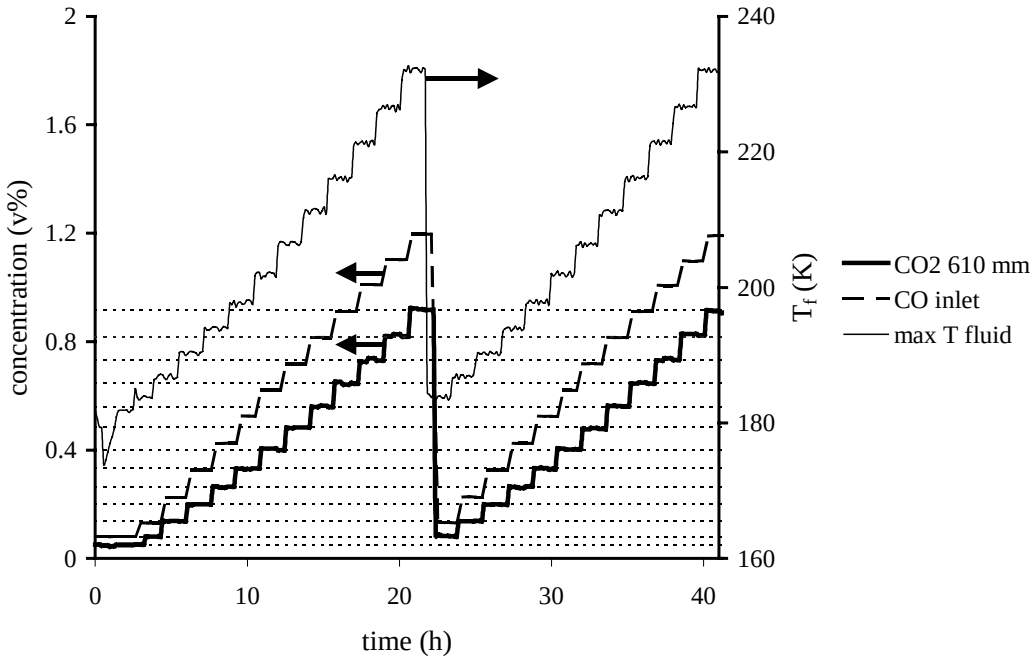

Fig. 3.4 Maximum temperature, CO inlet concentration and CO_2 concentration at 610 mm from the reactor inlet as function of time. $T_{inlet}=T_{wall}=178$ °C, P=3.8 bara, G=3.55 kg m^{-2} s^{-1}. The used air contained 1200 ppm of water. Dashed lines are drawn through CO_2 concentrations measured at the same inlet concentration.

concentrations were not constant along the length of the reactor. The partial pressure of water was proportional to the reactor pressure, since it was present as a constant mass fraction. If the inlet and wall temperature or the pressure were changed, experiments were started after a period of at least 12 hours. During this time, the adsorption equilibrium of water could be established. After that experiments at different CO concentrations were exactly reproducible, as is shown in Fig. 3.4.

This figure shows the CO_2 concentration close to the end of the reactor and the maximum temperature measured at the centerline of the reactor when the CO inlet concentration was increased twice from 0.1 to 1.2 vol% in steps of 0.1 vol%. No change of the catalyst activity was observed over the period of 40 hours, although the bed temperature and the concentrations were changed considerably.

Steady-state temperature and concentration profiles were recorded approximately 1 hour after changing the concentration or gas velocity. The duration of each experiment was determined by the time necessary for analyzing the 10 gas samples and not by the reactor's response time. The samples were analyzed successively at 100 s intervals, which was done three times during each experiment. The concentration profiles were considered to be reliable if the values measured during the second and the third cycle were identical. The withdrawal of the gas samples caused small fluctuations of the temperatures inside the packing of only a few tenths of a centigrade.

3.2.3 Treatment of experimental data

Different reactor models were compared and their accuracy in describing the measured temperature and concentration profiles was evaluated. In case of cold flow experiments, this is relatively straightforward. During these tests, temperature profiles inside the packed bed were created by introducing a feed with a higher temperature than the wall temperature. The difference between the measured and the predicted fluid temperatures, which had to be minimized, was well defined. For the temperature and concentration profiles obtained during experiments with chemical reaction, the 'target function' was more ambiguous. Due to the occurrence of a maximum temperature in axial direction, the minimum difference between the measured and calculated temperature profile does not necessarily coincide with the best choice of model and parameters, as is shown in Fig. 3.5.

Two models, for instance a homogeneous and a pseudo-heterogeneous model, can predict temperature profiles, which equally deviate from the measured profiles in terms of the quantitative difference between experiments and model. A choice between the models can only be made by comparing the measured and the calculated temperatures more carefully. In this example, the homogeneous model cannot predict the temperature profile near the inlet of the reactor. There, the temperature at the centerline of the reactor is insensitive to the radial heat transfer parameters, since the fluid did not yet 'sense' the presence of the reactor wall.

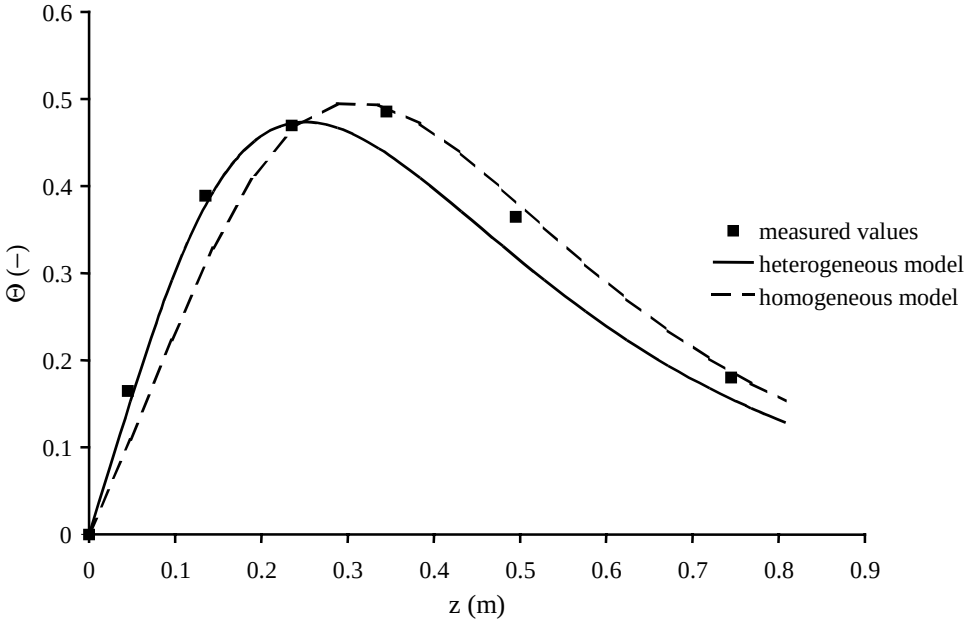

Fig. 3.5 Example of two models giving the same difference between the measured and the calculated temperatures at the centerline of the reactor.

The temperature in this region can only be described if the heat production rate is increased. This happens if particle-to-fluid heat transfer limitation is taken into account, as is done in a pseudo-heterogeneous model. The reaction rate according to this model is higher, because of the increased temperature of the catalyst. In this example, the pseudo-heterogeneous model would be preferable, since the neglecting of the temperature difference between the catalyst and the fluid is not justified.

When optimizing model parameters to have the best agreement between the model and the experimental data, the following target function for the fluid temperature was minimized:

$$F = \sum_{i=1}^{n_\Theta} \frac{1}{n_\Theta} \frac{\left(\Theta_{exp} - \Theta_{mod}\right)^2}{\left(\Theta_{exp,r=0} - \Theta_{exp,r=R_t}\right)} \tag{3.1}$$

in which n_Θ is the number of temperatures recorded per experiment. It was chosen not to use the reciprocal value of Θ_{exp} as weight factor, because Θ_{exp} was close to zero if the temperature was measured near the reactor wall. In case of reaction, the target function can be extended to include the difference between the measured and the calculated temperatures of the solid phase and the measured axial concentration profile. Due to the heterogeneity of the packing, measured temperature profiles can never be smooth. The local temperatures deviate from the angulary averaged temperature with a maximum difference that depends of the local radial and axial temperature gradients and the size of the catalyst particles (see Chapter 4). Measurement of this angulary averaged temperature profile is not possible in our setup. In that case temperatures should be measured at three different angular positions at

least, which would require a temperature probe that causes too much disturbance of the packing. Moreover, a reduction of the number temperature measurements in axial and radial direction in favor of an increase of the number of angular positions would increase the correlation between the effective radial thermal conductivity and the wall heat transfer coefficient. Due to the inevitable uncertainty in the local temperatures and the limited number of thermocouples used, the observed heat transfer parameters will show variations after repacking of the catalyst bed.

When regarding measuring of temperature profiles after repacking of the catalyst bed as being equivalent to taking temperature measurement at different angular positions, the accuracy of the heat transfer parameters can be improved by fitting them to a set of experiments at different flow rates, measured using different packings. In that case, the target function (3.1) becomes:

$$F = \sum_{i=1}^{n_{exp}} \sum_{j=1}^{n_\theta} \frac{\left(\Theta_{exp} - \Theta_{mod}\right)^2}{n_{exp} n_\Theta} \tag{3.2}$$

Since the number of thermocouples is limited, it can happen that, for instance, in some packings, the majority of the temperatures measured near the reactor wall are higher than the angular average temperature. This would result in lower values of the effective radial thermal conductivity, $\lambda_{e,r}$, and higher values of the wall heat transfer coefficient, α_w, compared to their actual values. The risk of such accidental errors in the heat transport parameters is reduced if they are calculated using data obtained using multiple packings.

3.2.4 Packing of catalyst bed

The reproducibility of the packing of the catalyst bed by repeated fluidization and settling was studied by measuring the pressure drop over the bed and its porosity. If the bed was packed by slowly adding small amounts of particles at a time, the bed porosity was between 0.41 and 0.42.

A glass tube with the same inner diameter as the pilot-scale tubular reactor was used to investigate whether it is possible to repack the reactor by fluidization of the catalyst particles. A similar ladder as the one used in the pilot scale reactor, but without thermocouples, was inserted in the glass tube. At atmospheric pressure, the catalyst particles started to vibrate at a superficial gas velocity of approximately 2 m s^{-1}. When increasing the flow rate, the particles at the top of the packing started to move in axial and radial direction. From 2.7 m $^{s-1}$, the catalyst bed became fully fluidized. When decreasing the air flow rate, fluidization stopped at a smaller flow rate of approximately 2.1 m s^{-1}. This hysteresis behavior of the minimum fluidization velocity is attributed to forces acting between the particles, the thermocouple ladder and the wall.

The mixing of the catalyst bed was studied by placing dyed catalyst particles on top of a bed with a height of 60 cm, which was fluidized at a superficial fluid velocity of 2.4 m s^{-1}. After roughly 3 minutes, the dyed particles that were visible through the wall were distributed homogeneously over the length of the bed.

To be able to obtain a constant bed porosity after fluidization, it was found necessary to vibrate the reactor whilst decreasing the air flow. Without this vibration, which was induced by means of a pneumatic vibrator, gaps in the packing appeared not only near the crosses of the thermocouple ladder, but in between them as well.

The structure of the packing was found to be influenced by the rate at which the air velocity was decreased. When slowly decreasing the air velocity, the particles at the bottom of the reactor started to settle in their position before the entire bed collapsed. Whilst settling, groups of particles close to the wall became orientated in parallel to each other, with their sides against the glass wall. This is shown in Fig. 3.6. After settling of the bed, the porosity was significantly lower than when the air supply was stopped abruptly. In that case, the bed porosity of 0.41 ± 1% was close to the values measured after filling the glass tube particle by particle (0.42). The bed structure also exhibited a similar randomness as when the reactor was filled manually. On the basis of these observations, it was decided to repack the catalyst bed in the pilot-scale by abruptly stopping the air supply after fluidization. Due to the pressure drop over the piping after the reactor outlet, the minimum pressure inside this reactor was higher than in the glass tube. To ensure that the catalyst was properly mixed, the air load was repeatedly varied between the minimum and maximum gas load of 660 Nl min^{-1}. This was doen for approximately 15 minutes, during which period the reactor was vibrated. The bed

A Fluid velocity slowly decreased B Fluid velocity abruptly stopped

Fig. 3.6 Orientation of the particles depending on the rate at which the fluid velocity is decreased.

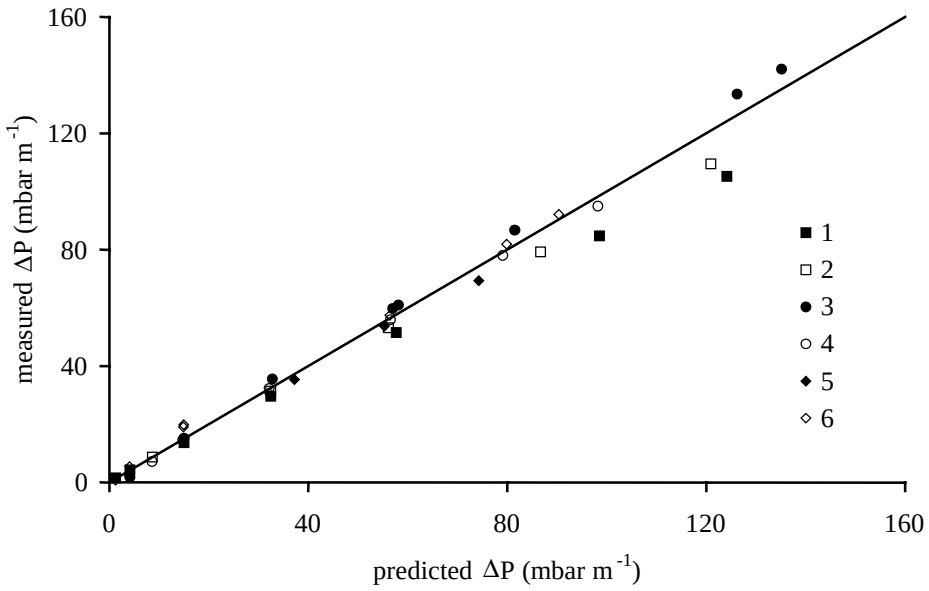

Fig. 3.7 Measured vs. predicted pressure drop after repeated repacking of the catalyst bed in the pilot-scale wall-cooled tubular reactor. Pressure drop predicted according to eq. (3.3) with A= 190 and B=1.45. Pressure drop measured during heat transfer experiments at an air load between 0.4 and 5.3 kg m^{-2} s^{-1}. The physical properties of the air were calculated for the average reactor temperature.

porosity was measured by lowering a perforated plate onto the bed. An average porosity of 0.425 ± 0.06 was obtained when repacking the bed 7 times.

The structure of the catalyst beds can be compared on the basis of the measured pressure drop. Fig. 3.7 shows the pressure drop per meter versus the pressure drop predicted according to the Ergun equation:

$$\frac{\partial p}{\partial z} = -f_1 u_0 - f_2 u_0^2$$

$$f_1 = A\frac{(1-\varepsilon)^2}{\varepsilon^3}\frac{\eta_f}{\left(d_p^v\right)^2} \qquad ; \qquad f_2 = B\frac{1-\varepsilon}{\varepsilon^3}\ \frac{\rho_f}{d_p^v} \tag{3.3}$$

Parameters A and B in eq. (3.3) are 150 and 1.75 in case of a very high tube-to-particle diameter ratio. At small ratios, their values are different, since the porosity and the fluid velocity are not uniform over the bed cross section. A and B were fitted to the measured pressure drop to obtain A=190 and B=1.45. The pressure drops over the different beds agree reasonably well.

3.2.5 Inlet- and wall temperature profile

In case of experiments with reaction, during which the inlet temperature was equal to the wall temperature, the inlet temperature profiles were rather uniform. When measuring the effective heat transport parameters without reaction, the inlet temperature was higher than the wall temperature. During these experiments, it was not possible to obtain a uniform temperature profile in the feed if the flow rate was small. Heat transfer between the wall and the feed distributor caused the temperature near the wall to be lower than at the center. Therefore, the measured inlet temperature profile, which had the shape of a parabola, was used as boundary condition at the reactor inlet.

Due to heat loss from the piping to the surroundings, the temperature of the water that entered the cooling jacket was a little (less than 1 K) below boiling point. Within the cooling jacket, the fluid did start to boil, as could be observed from the temperature rise of the cooling water in the steam condenser. In case of heat transfer experiments without reaction, during which the air was cooled at the wall, the wall temperature did not change more than 0.8 K over the length of the reactor, as is shown in Fig. 3.8. With increasing heat supply from the air flowing through the bed, the temperature difference over the wall decreased, to eventually become zero at the maximum air flow rate. In case of experiments with reaction, the wall temperature increased in axial direction, depending on the heat flux through the wall. The maximum temperature difference measured over the reactor length was approximately 1.5 K The increase of the coolant temperature over the cooling jacket was proportional to the heat production according to the CO conversion, as is shown in Fig. 3.9.

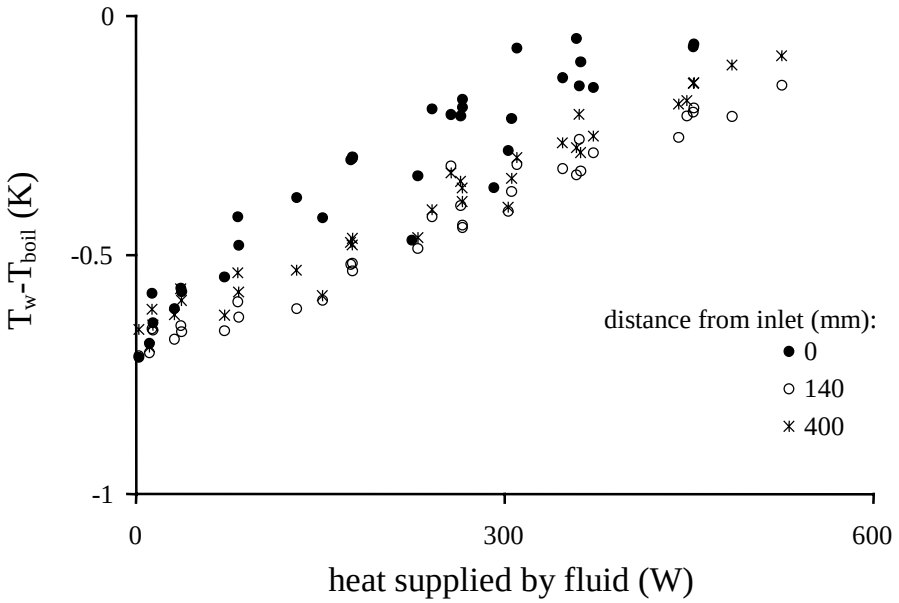

Fig. 3.8 Deviation of the wall temperature at different axial positions as function of the heat supplied by the hot reactor feed.

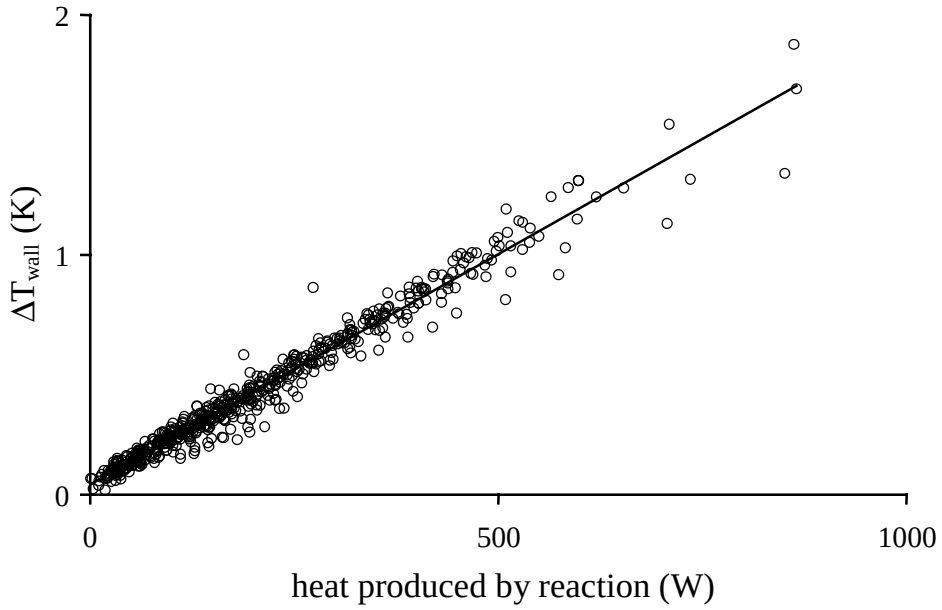

Fig. 3.9 Difference between the wall temperatures measured at 900 and at 0 mm from the feed inlet as function of the total amount of heat produced by chemical reaction.

In Figures 3.8 to 3.10, the latent heat of the reactor effluent was neglected. The slope of the graph in fig. Fig. 3.9 corresponds to a coolant flow rate of 4.4 m^3, which is close to the value of 4 m^3 h^{-1} that was calculated from the pressure difference over the cooling water circulation pump. In the reactor models, the measured wall temperature profiles were used as boundary condition. Since the wall temperature changed more or less linearly, the local wall temperature was calculated by linear interpolation between the measured values.
The used thermocouples were taken from a single batch, which had been deliberately aged at

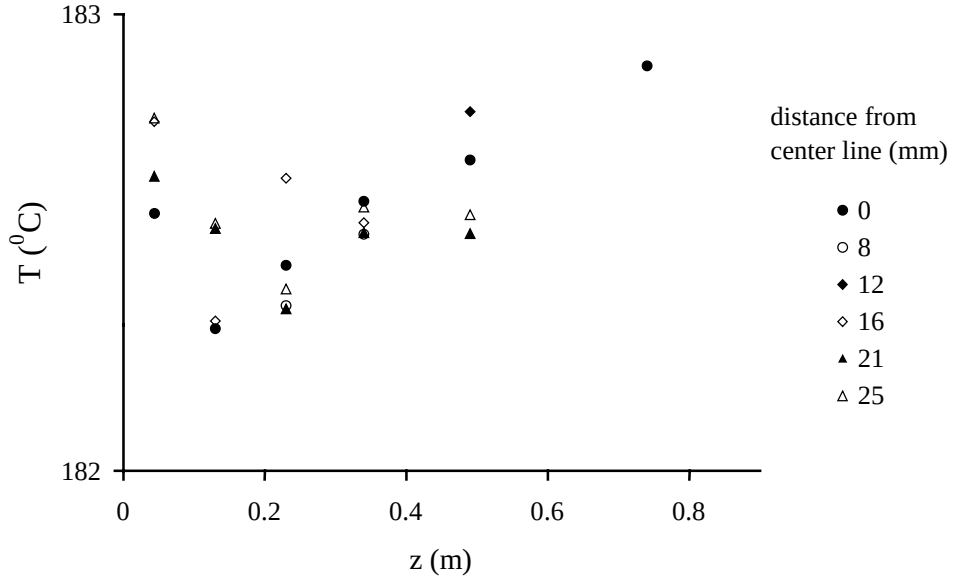

Fig. 3.10 Temperature profile measured without reaction at $T_{in}=T_w$.

a temperature of 350 °C to avoid any drift during the experiments. The difference between the temperatures measured inside the packing at equal wall- and inlet temperature and zero CO inlet concentration were very small, as is shown in Fig. 3.10. The temperature differences within the bed, which were mainly caused by the increase of the cooling water temperature, were less than 0.6 K.

3.3 Heat transfer without reaction

3.3.1 Introduction

In this paragraph, the effective heat transfer parameters, measured for different packings, will be discussed, as well as their accuracy. The packings used in the pilot-scale wall-cooled tubular reactor were the CuO/γ-alumina catalyst that was used in the experiments with chemical reaction, inert alumina pellets, a catalyst consisting of pure copper chromite and a copper chromite/γ-alumina catalyst in the shape of Raschig rings (see Table 3.1) . Experiments were performed at different reactor pressures and wall- and inlet temperatures, at air loads ranging from 0.4 to 5.7 kg m^{-2} s^{-1}. The effective radial heat transport parameters $\lambda_{e,r}$ and α_w were calculated using the two-dimensional model presented in Chapter 1, in which heat dispersion in axial direction was neglected.

Table 3.1 Packings used in heat transfer experiments without reaction

packing	h (mm)	d (mm)	wall thickness (mm)	ε (-)
CuO/γ-alumina	11.2	5.5	-	0.42
copper chromite	4.7	4.9	-	0.35
alumina	6.5	5	-	0.4
copper chromite (rings)	8	8	2	0.48 [1)]

[1)] assuming solid cylinders

3.3.2 Experimental results

Heat conduction in axial direction can be neglected at the conditions used in our experiments, in which Re is larger than 40. This was tested by including axial dispersion in the two-dimensional (homogeneous) reactor model as, (*Bauer and Schlünder 1978a*):

$$\frac{\lambda_{ax}^{f}}{\lambda_f} = \frac{Pe_h^0}{Pe_{h,ax}^{\infty}} \tag{3.4}$$

Assuming $Pe_{h,ax}^{\infty}$=2, the calculated change of $\lambda_{e,r}$ and α_w was less than 1% for experiments at Re<500 and less than 0.5% for experiments at Re>500. The overall heat transfer coefficient, calculated as (*Dixon, 1996*)

$$\frac{1}{U} = \frac{1}{\alpha_w} + \frac{R_t}{3\lambda_{e,r}} \frac{Bi+3}{Bi+4} \tag{3.5}$$

was lowered by half a percent in average. The difference between the measured and calculated temperatures, according to the target function (3.1), did not decrease appreciably. At the used experimental conditions, apparent axial dispersion of heat and mass due to free convection can be neglected, as was checked using the criterion derived in *Benneker, 1997*.

Heat transfer experiments were performed for 10 different packings of the CuO/γ-alumina catalyst. The particles have a diameter of 5.5 mm and a an average height of 11.2 mm. Two times, this packing was created by filling the reactor manually and eight times by fluidization Fig. 3.11 and Fig. 3.12 show the effective heat transfer parameters $\lambda_{e,r}$ and α_w in the two-dimensional homogeneous plug flow model using all the data for the CuO/γ-alumina cylinders. The experiments were performed at different system pressures and wall- and inlet temperatures. Three different series of experiments are distinguished here. In between each series of experiments the thermocouple ladder was re-assembled. Series 1 contains the experiments that were performed after manually filling the reactor. Series 2 and 3 contain experiments using 6 and 3 packings created by fluidization. All parameters are plotted as function of the fluid Peclet number Pe_h^0. This dimensionless group is commonly used in correlations for the effective thermal conductivity, which have the following form (see Chapter 1):

$$\lambda_{e,r} = \lambda_r^0 + \lambda_r^f \tag{3.6}$$

$$\frac{\lambda_r^f}{\lambda_f} = \frac{Pe_h^0}{Pe_{h,r}^{\infty}} \quad ; \qquad Pe_h^0 = \frac{u_0 \rho_f c_{p,f} d_p^v}{\lambda_f} \tag{3.7}$$

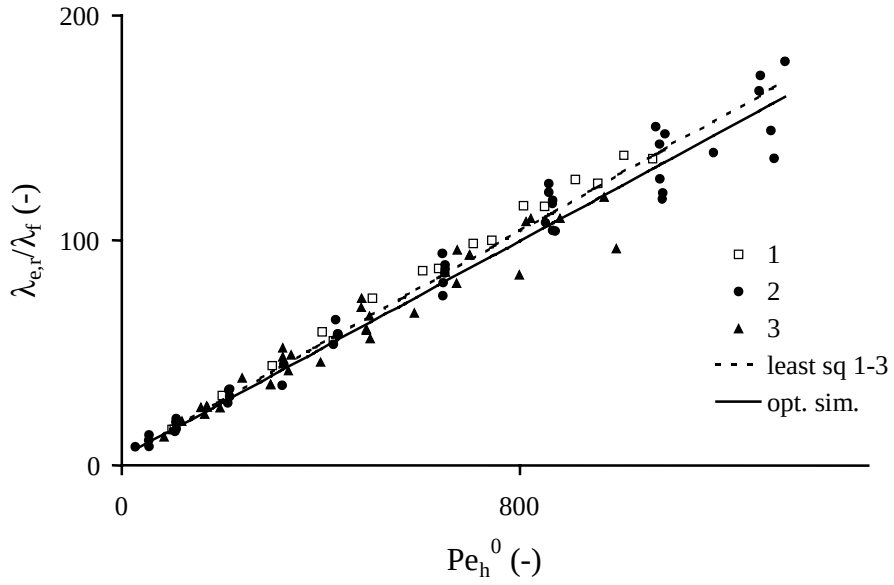

Fig. 3.11 Effective radial thermal conductivity as function of the fluid Peclet number. Series 1: reactor filled manually (two times); series 2: 6 times repacked by fluidization; series 3: three times repacked by fluidization. Thermocouple ladder rebuilt between series. Least sq.: least-squares fit of all values. Opt. sim: correlations (3.6)-(3.9) optimized to all experiments.

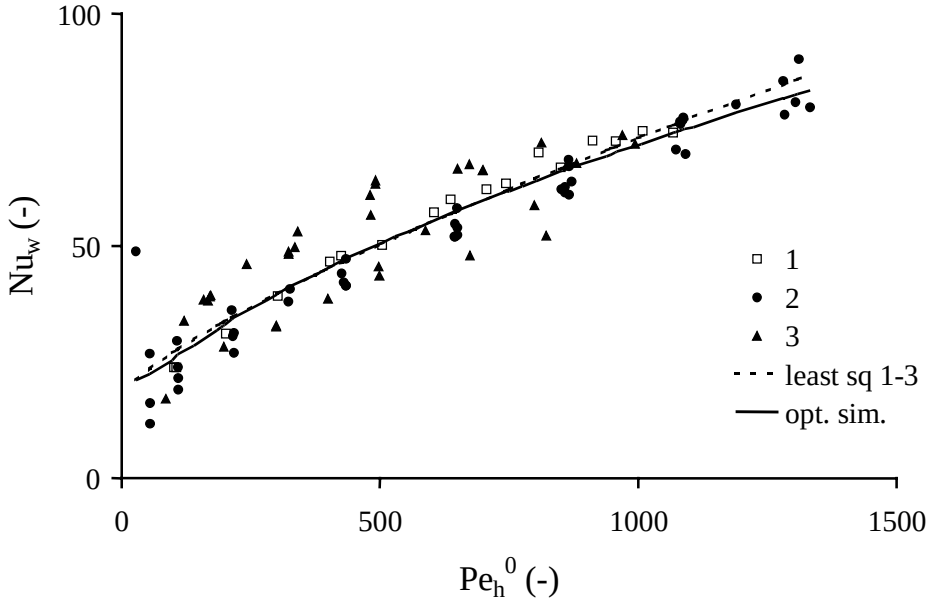

Fig. 3.12 Wall Nusselt number as function of the fluid Peclet number. α_w, in the form of Bi (eq. (3.9)), was optimized together with $\lambda_{e,r}$.

λ_r^0 is the flow-independent contribution, which, according to to *Bauer and Schlünder, 1978b*, is equal to:

$$\frac{\lambda_r^0}{\lambda_f} = \left(1-\sqrt{1-\varepsilon}\right) + \frac{2\sqrt{1-\varepsilon}}{1-B\kappa^{-1}}\left[\frac{B\left(1-\kappa^{-1}\right)}{\left(1-B\kappa^{-1}\right)^2}\ln\left(\frac{\kappa}{B}\right) - \frac{B-1}{1-B\kappa^{-1}} - \frac{B+1}{2}\right] \tag{3.8}$$

$$B = C_f\left(\frac{1-\varepsilon}{\varepsilon}\right)^{1.11}$$

In equation (3.8), κ is the ratio if the thermal conductivity of the solid and fluid and C_f is a shape factor, which, according to the authors, is 2.5 for cylinders and 1.75 for spheres.
The wall heat transfer coefficient was expressed in the form of the Biot number:

$$Bi = \frac{\alpha_w R_t}{\lambda_{e,r}} = C_1 Re^{C_2} \tag{3.9}$$

The solid lines in Fig. 3.11 and Fig. 3.12 show the values of the heat transfer parameters if $Pe_{h,r}^{\infty}$, C_f, C_1 and C_2 in eqs. (3.6)-(3.9) were optimized using all experiments.
A considerable spread occurs in the heat transfer parameter that were obtained from the individual temperature profiles at different flow rates, which is due to the correlation of $\lambda_{e,r}$ and α_w. The relative spread in the wall Nusselt number increases with decreasing fluid velocity, since the sensitivity of the model towards α_w si small at high values of the Biot number. The contours in the graphs in Fig. 3.14 represent the combinations of Bi and Pe_r giving the same difference between the measured and calculated the predicted temperatures.

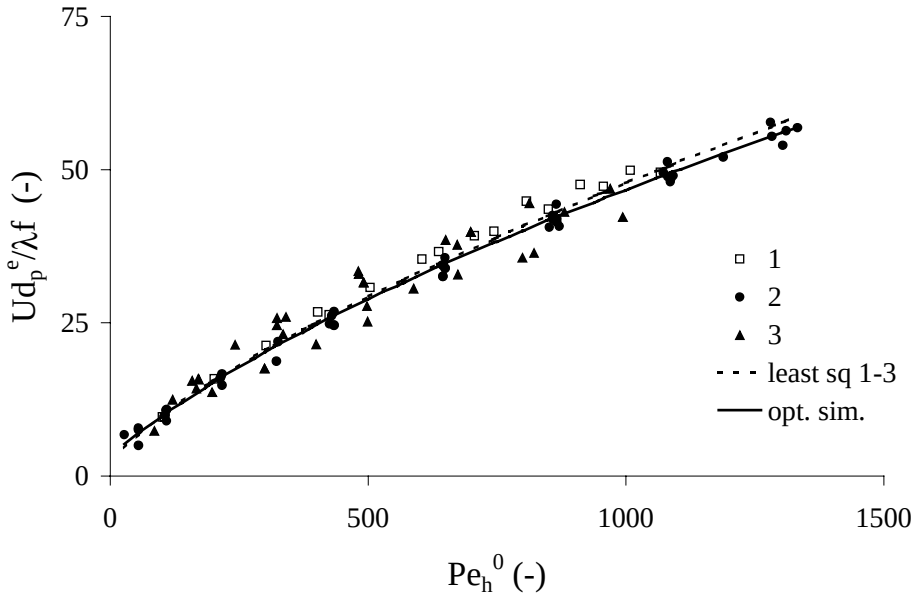

Fig. 3.13 Overall heat transfer coefficient calculated from $\lambda_{e,r}$ and α_w shown in Fig. 3.11 and Fig. 3.12.

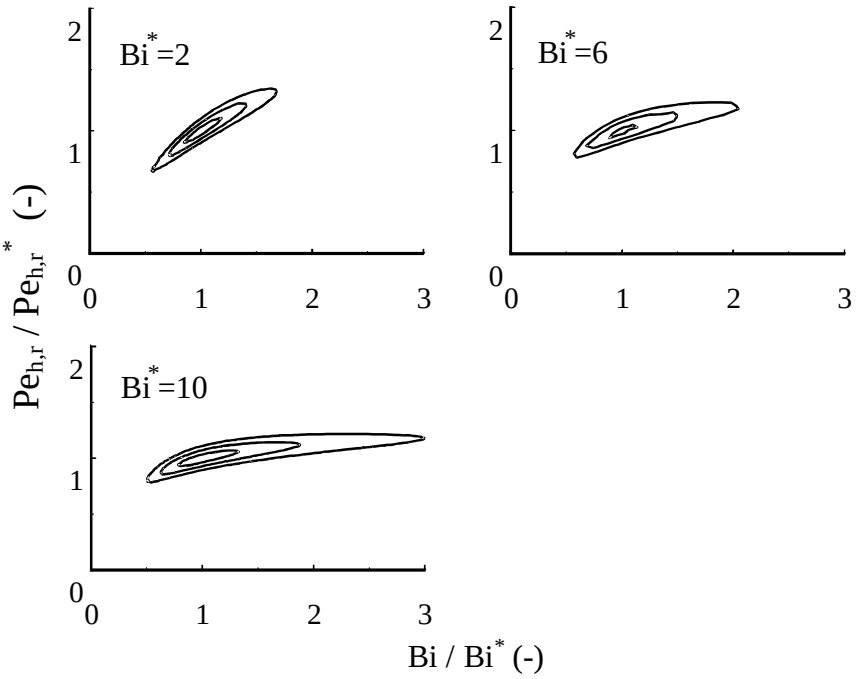

Fig. 3.14 Correlation between $Pe_{h,r}$ and Bi. F is the difference between the calculated temperatures Θ_{modl} and the temperature profile calculated for $Pe_{h,r}= Pe^{*}_{h,r}$ and $Bi=Bi^{*}$.

The diagrams were calculated for a configuration of thermocouples as was used in the actual experiments. Adding extra thermocouples closer to the wall would make the contours contract along the Bi axis, but this is impossible in the used setup. Fig. 3.13 shows the overall heat transfer coefficient, calculated according to eq. (3.5). The spread in the values of U is much less than in those of $\lambda_{e,r}$ and α_w, which indicates that the spread in the two parameters is caused by the correlation between them. This assumption is supported by the fact that the different averages, shown as dashed and solid lines in Fig. 3.11 and Fig. 3.12, are close to each other. If Bi is large, as is the case for low flow rates, errors in the temperatures measured near the wall will cause a much large change of α_w than of $\lambda_{e,r}$: the correlation of α_w and $\lambda_{e,r}$ is non-linear (see Fig. 3.14). If the heat transfer parameters in some of the packings would systematically differ from the true values, the averages of $\lambda_{e,r}$ and α_w, obtained using the individual steady state measurements, would be different from the average values according to eqs. (3.7) and (3.9).

The observed spread in the parameters is not larger than can be expected. In Chapter 4, experiments are described in which temperature profiles were measured at different angular positions above packings of the same catalyst. The number of angular positions was large enough to obtain an accurate value of the angulary averaged temperature. These experiments are referred to as 'cold flow' experiments. A radial temperature profile in the PSR is similar to the temperature profile in the cold flow setup that is measured at only one single angular position. Fig. 3.15 shows the values of the heat transfer parameters when the temperature profiles at each angular position were considered as separate steady-state experiments. In that

case, the spread in the values is comparable to ($\lambda_{e,r}$) or even larger than (α_w) the spread in the parameters obtained from the experiments in the pilot-scale tubular packed bed reactor.
In the remaining of this chapter, the effective heat transfer parameters obtained by optimization of correlations (3.6)-(3.9) to all experimental data will be used, because these are considered as most reliable.

The flow-independent thermal conductivity, calculated using eq. (3.8), agrees very well with the experimental data. The difference between the experimental value and the prediction of *Bauer and Schlünder, 1978b* was found to be less than 2 %.

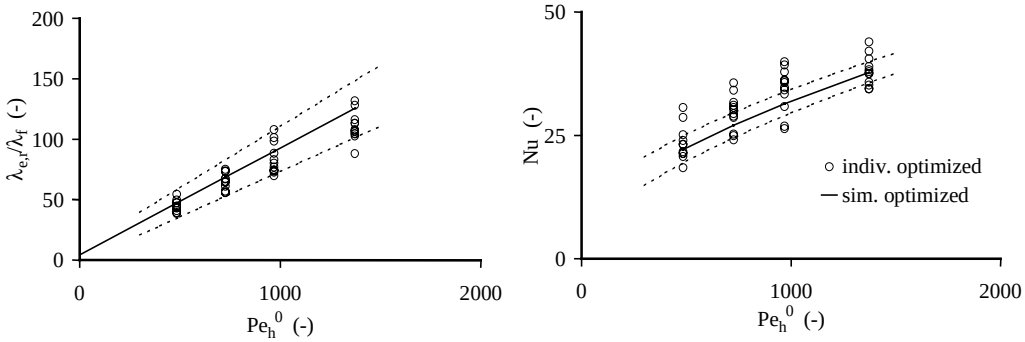

Fig. 3.15 Effective radial thermal conductivity and wall Nusselt number calculated from temperature profiles measured at different angular positions above a packing of the same catalyst particles as in Fig. 3.12. The used experimental setup is discussed in Chapter 4. The spread in the data obtained using the pilot-scale wall cooled tubular reactor is shown as dashed lines.

3.3.3 Length dependency of heat transfer parameters

Several authors (e.g. *Borkink, 1991, Dixon, 1985a and b, De Wasch and Froment, 1972, Li and Finlayson, 1977, Martin and Nilles, 1993, Winterberg et al, 2000 a, b*) observed a length-dependency of the effective heat transfer parameters. This dependency was attributed to experimental problems, such as an unknown wall- or inlet temperature profile, or to errors in the used model, such as neglecting of a radial distribution of the porosity and the axial fluid velocity. If this is true, the largest change of the parameters should be observed near the entrance of the reactor.
In this work, the dependence of the heat transfer parameters on the axial position was examined by either neglecting temperature profiles close to the inlet or by considering only a certain section of the reactor, using a measured radial temperature profile as 'inlet' profile. The latter method was applied to the experimental data for all packings of the CuO/γ-alumina catalyst. The temperature profile at some distance from the inlet was described by the following equation:

$$\Theta = c_1 + c_2\left(1 - r^{c_3}\right) \tag{3.10}$$

The parameters c_1-c_3 were optimized to fit eq. (3.10) to the measured temperature profile. Far from the inlet c_3 is approximately 2. Closer to the inlet, the value of c_3 increases to become infinite at z=0.

The values of the heat transfer parameters do not decrease systematically with increasing axial position, as can be seen in Fig. 3.16. The effective radial thermal conductivity and the overall heat transfer coefficient, obtained when starting from the temperature profile measured at 44 mm from the inlet, practically coincide with the values obtained when using all measured temperatures. At small fluid velocities, the wall heat transfer coefficient, shown here in the form of a wall Nusselt number, decreased a little. At these conditions, the model results are rather insensitive with respect to this parameter. When using temperature profiles further from the inlet as boundary condition at z=0, the parameters tend to deviate more, but do not show an obvious trend. The differences are attributed to a decrease of the accuracy, caused by the small number of temperatures used were used as input for the optimization procedure.

The experiments with other packings (see Table 3.1) were treated in the same way as those with the copper oxide catalyst. The thermal conductivity of these solids was not measured independently and was therefore included as an extra fit-parameter in the optimization procedure. After optimization, the values of $\lambda_{e,r}$ and α_w differed less than a factor two from the conductivity of the CuO catalyst. This is not much, considering the weak sensitivity of the

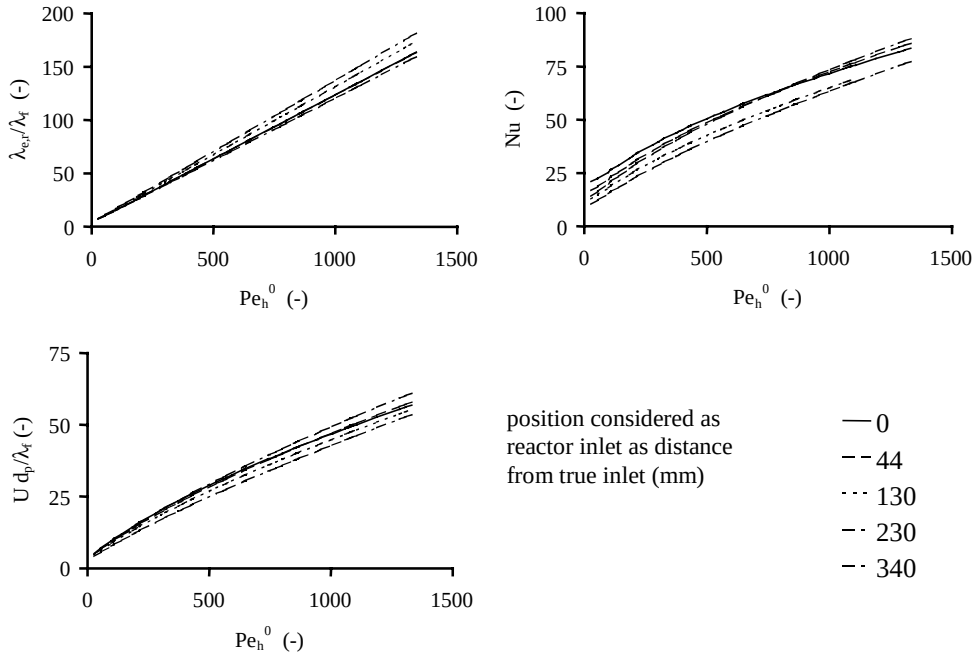

Fig. 3.16 Change of the heat transfer parameters when increasing the axial position that is considered as 'reactor inlet'.

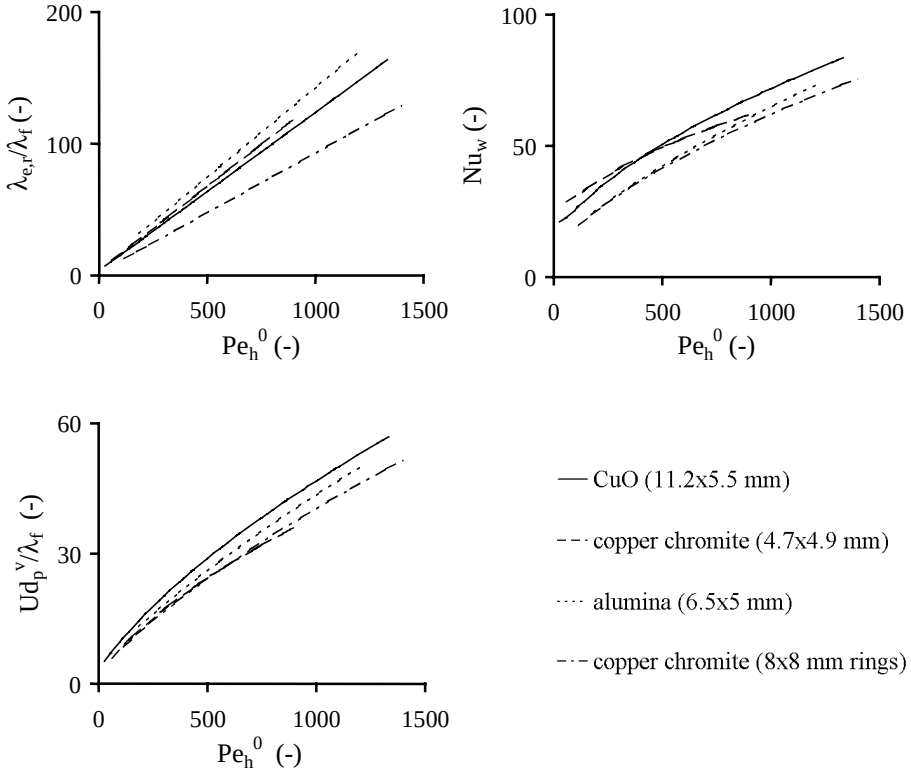

Fig. 3.17 Heat transfer parameters obtained for different packings.

model to this parameters at the small flow rates that were applied. The heat transfer parameters in the two-dimensional homogenous plug-flow model are shown in the Fig. 3.17. The first two packings are rather similar to that of the CuO/γ-alumina catalyst, except for the fact that the ratio of the length and the diameter of the particles is smaller. It is therefore not surprising that the effective heat transfer parameters for these packings are close to the values for the CuO catalyst. The effective radial thermal conductivity decreases a little with increasing particle size, which is consistent with literature.

In Figures 3.18 and 3.19, the effective heat transfer parameters obtained for the packings of the CuO catalyst are compared to literature correlations and to data that were obtained for conditions (aspect ratio, cylindrical particles of low thermal conductivity) close to those of this investigation. The values of $\lambda_{e,r}$ are close to the correlations of Bauer and Schlünder and Dixon. Better agreement between our data and the literature correlations cannot be expected, since the ratio of the height and the diameter of the particles (≈2) is different from that of the cylinders generally used in heat transfer investigations, which is close to one. Comparison of the wall heat transfer coefficient to literature correlations is difficult, due to the huge spread in the literature values, of which only a few are shown in Fig. 3.19. Our data agree best with the correlation of Dixon and the values obtained by Borkink and Westerterp for a bed of alumina cylinders.

From the comparison with literature data, it can be concluded that, for a detailed reactor design, the use of literature correlations for the heat transport parameters cannot be advised.

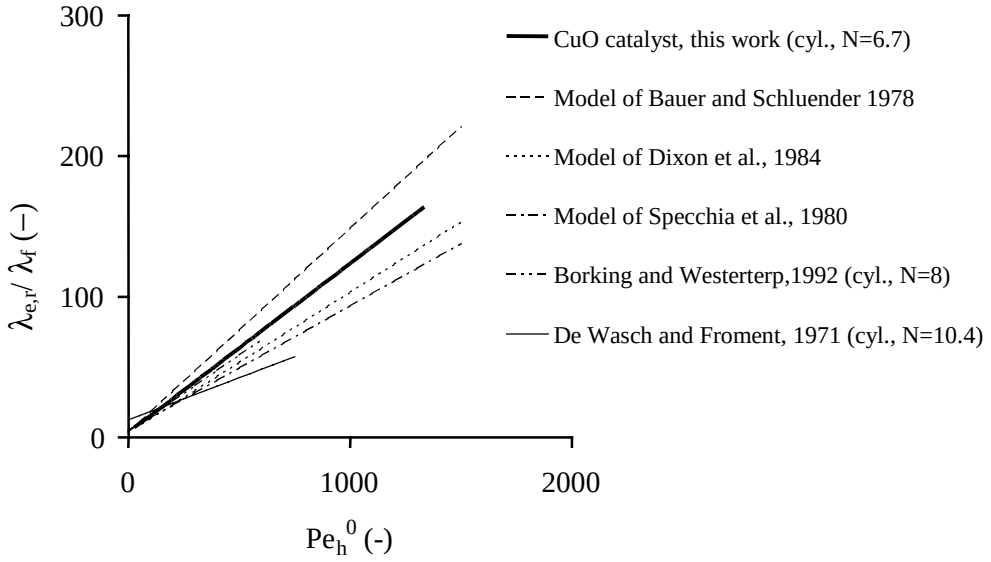

Fig. 3.18 Comparison of the effective radial thermal conductivity of the packing of CuO catalyst with literature correlations and data.

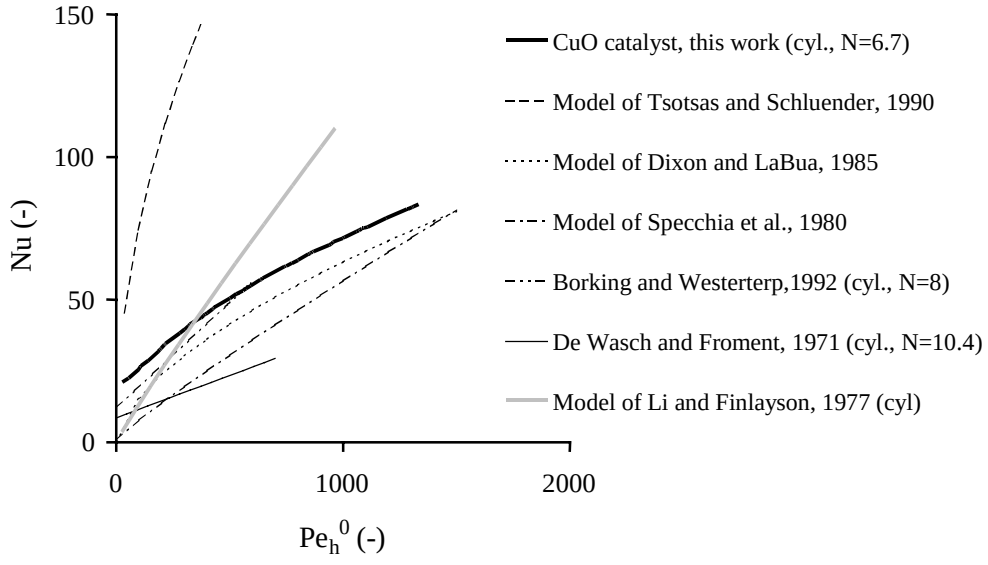

Fig. 3.19 Comparison of the wall Nusselt number obtained for the packing of the CuO catalyst with literature correlations.

3.4 Heat transfer with chemical reaction

3.4.1 Introduction

In the pilot-scale wall-cooled tubular reactor, heat transfer experiments with chemical reaction were performed at reactor pressures of 3.8, 5 and 8 bara, inlet- and wall temperatures of 156, 170, 180 and 200 °C, CO concentrations between 0.05 and 2 vol% and gas loads from 0.45 to 4.5 kg m^{-2} s^{-1}. During all of the 600 experiments, the wall temperature was equal to the inlet temperature. In the following sections, the experimental data will first be compared to the two-dimensional pseudo-heterogeneous reactor model, in which uniform radial distributions of the porosity and the axial fluid velocity were assumed. This model will be referred to as the 'basic model' and is described in Chapter 1. The heat and mass balances of the model were solved numerically using the method of finite differences. In general, heat dispersion in axial direction was neglected. This assumption will be validated in sections 0 and 3.4.3.1. To be able to accurately describe the experiments over the whole range of conditions, the basic model was extended by introducing a radial variation of the bed porosity and fluid velocity.

3.4.2 First approach using the basic two-dimensional pseudo-heterogeneous model

3.4.2.1 Application of kinetics as measured in separate kinetic reactors

In Fig. 3.20, measured temperature and concentration profiles are compared to the predictions of the basic model, in which the heat transport parameters measured without reaction and the separately measured kinetics (see Chapter 2) were used. The used expression for the reaction rate is discussed in more detail in the next section. The Peclet number for radial mass transport was assumed to be the same as the Peclet number for radial heat transport. This assumption was validated by the results of mass transfer experiments in which the same catalyst was used as packing (see Appendix H). The graphs in Fig. 3.20 show the experiments performed at three different temperatures at flow rates close to the minimum and maximum values.

At reaction conditions at which the CO conversion is high, the agreement between the experiments and the basic model is far from disappointing. At the lowest inlet temperature and a fluid velocity corresponding to Re=150, the axial temperature profiles and the concentration at the wall are described very well. At Re=1400, the temperature rise is underestimated.

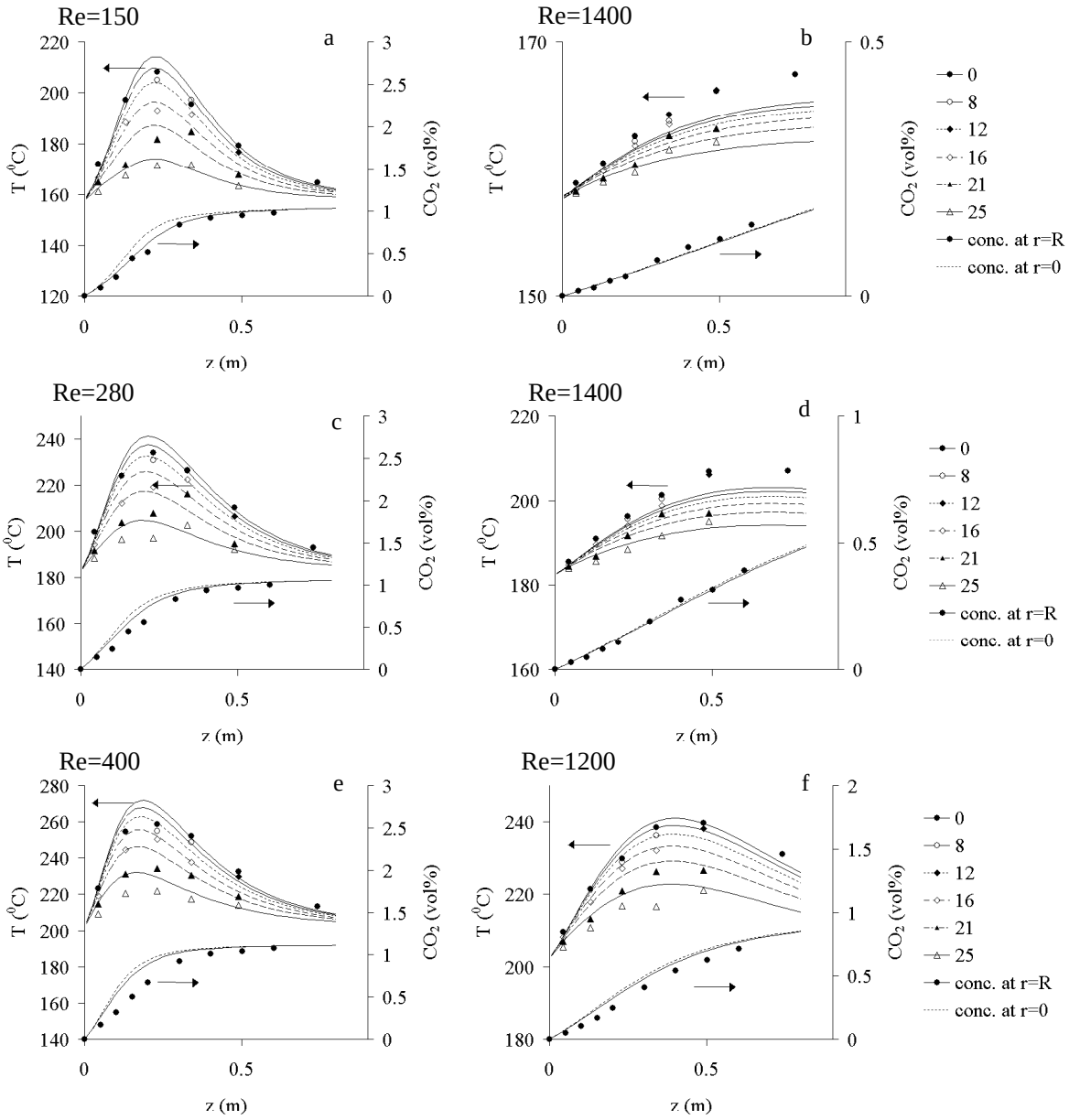

Fig. 3.20 Temperature and concentration profiles calculated using separately measured reaction kinetics and heat transfer parameters as measured without reaction. a and b: $T_{in}=T_w=156$ °C, P=3.8 bara, Re=150 and 1400; c and d: $T_{in}=T_w=180$ °C, P=3.8 bara, Re=280 and 1400; e and f: $T_{in}=T_w=200$ °C 8 bara, Re=400 and 1200. The CO inlet concentrations were approximately 1 vol% for all experiments.

At higher inlet temperatures, the model prediction of the temperature profiles measured at high fluid velocities tends to improve. At the highest wall and inlet temperatures, the calculated temperatures become higher than the measured ones if the flow rate is small. This trend was observed for all inlet concentrations and reactor pressures.

The particle-to-fluid heat and mass transfer coefficients were calculated according to the correlation proposed by *Gnielinski 1982* (see also Chapter 1).

$$\mathrm{Nu_p} = 1.6\left[2 + 0.644\mathrm{Pr}^{1/3}\left(\mathrm{Re}/\bar{\varepsilon}\right)^{1/2}\sqrt{1+\left(\frac{0.0557\left(\mathrm{Re}/\bar{\varepsilon}\right)^{0.3}\mathrm{Pr}^{2/3}}{1+2.443\left(\mathrm{Re}/\bar{\varepsilon}\right)^{-0.1}\left(\mathrm{Pr}^{2/3}-1\right)}\right)}\right] \tag{3.11}$$

The calculated solid temperatures agree with the experimental data, as is shown in Fig. 3.21 for two experiments at different flow rates. The profiles shown in this figure were calculated after optimization of the effective radial thermal conductivity and the wall heat transfer coefficient. During none of the experiments unexpected temperature differences between the solid and the fluid temperature, which would indicate the existence of local inhomogeneities in the packing, were observed.

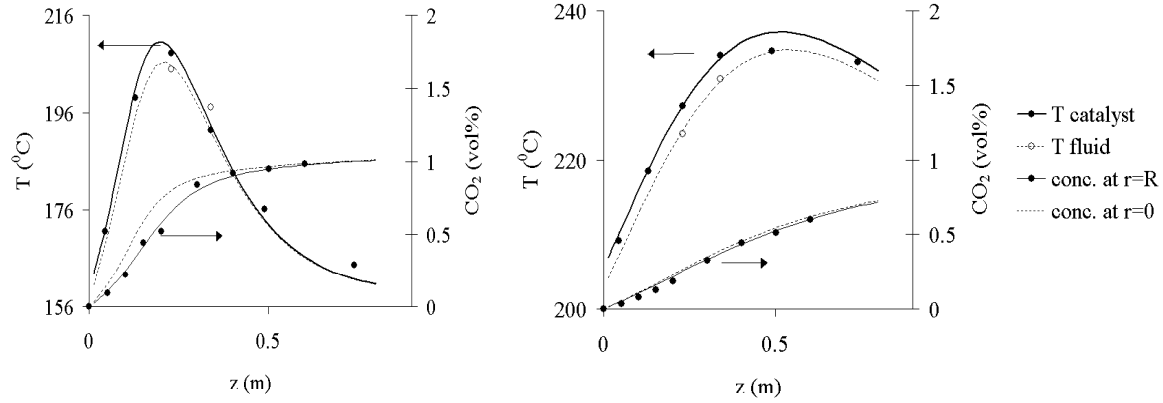

Fig. 3.21 Catalyst and fluid temperatures at 8 mm from the centerline for two experiments at Re=140 (left) and Re=1400 (right). The profiles were calculated after optimization of the effective heat transfer parameters to the measured fluid temperatures and concentration profile.

3.4.2.2 Fine tuning of the reaction rate in the pilot scale tubular reactor

In the previous section, it was shown that the agreement between the experiments and the predictions of the basic model, when using the separately measured reaction kinetics and the heat transfer parameters from experiments at non-reacting conditions, is fair. The heat transfer parameters that were obtained by fitting $\lambda_{e,r}$ and α_w to the measured temperature profiles, shown in Fig. 3.28, are consistent, though the effective radial conductivity at reacting conditions seems systematically lower than at non-reacting conditions. This difference between the heat transfer parameters will be discussed further in this section.

A typical feature of packed bed reactors is the sensitivity of the temperature field with respect to the reaction kinetics, in particular to the (apparent) activation energy. Thought the used kinetics expression could describe the reaction rates that were measured in an internal recycle reactor with an average error of 4% (Chapter 2), it would be daring to state that this same

accuracy applies to the reaction rate in the catalyst bed in the tubular reactor. The temperature history of the catalyst in both reactors was different, as was the ratio of the air load and the amount of catalyst. If the reaction rate used in the model is not highly accurate, discrimination between different reactor models is difficult, or even impossible. In this case, the difference between the model results and the experimental data cannot be entirely attributed to errors in the reaction kinetics. When varying the flow rate, the reactor pressure and the volume fraction of CO in the feed, the concentrations and the temperatures inside the bed during experiments at different inlet and wall temperatures and flow rates overlapped, allowing cross checking of the reaction kinetics. If the difference between the measured and the calculated profiles in Fig. 3.21 would be only due to the use of an incorrect reaction rate, it should be possible to obtain a perfect fit by optimizing the kinetic parameters. This, however, was not the case.

Applying of an incorrect reaction rate influences the effective heat transport parameters mainly due to the under- or overestimation of the total heat production inside the bed. The spatial distribution of this heat production, which is a function of the apparent activation energy and the reaction orders with respect to oxygen, carbon monoxide and carbon dioxide, is less important, provided that the errors in these parameters are not very large. These parameters are accurate and reliable, as is concluded from the experimental investigation of the reaction kinetics (see Chapter 2). Initially, kinetic experiments were performed using catalyst that had not been calcined. This catalyst was less active than the batch of catalyst used in the pilot-scale wall-cooled tubular reactor, which was subjected to such thermal treatment. When using dry air, the (calcined) catalyst was approximately four times more active than at the conditions used later. Although the catalyst activity exhibited large differences, the apparent values of the activation energies differed less than 7%. The effective orders with respect to CO and CO_2 deviated less than 10% from the apparent values corresponding to the finally obtained expression. The difference in activity is attributed to a change of the number of active sites that are available for reaction, which is contained in the frequency factor $k_{0,3}$ in eq. (3.13). This equation was used to calculate the intrinsic reaction rate. An analytical expression for the particle effectiveness factor, η, was used to correct for intra-particle diffusion limitation (see Appendix B).

$$R = \eta R_i \tag{3.12}$$

$$R_i = \frac{k_3\ [CO]}{1+\frac{k_3}{k_{-6}}[CO]+K_7[CO_2]+K_8[H_2O]} \tag{3.13}$$

$$k_j = k_{0,j}\ \exp\left(\frac{-E_a}{RT}\right)\ ;\ K_j = K_{0,j}\exp\left(\frac{-\Delta H_{ads}}{RT}\right)$$

Table 3.2: Values of the parameters in equation (3.13)

$k_{0,3}$	43	$kg^{-1}s^{-1}$
Ea_3	33	kJ $mole^{-1}$
$k_{0,3}/k_{-0,-6}$	$6.3 \cdot 10^{-6}$	$kg^{-1}s^{-1}$
Ea_{-6}-Ea_3	-49	kJ $mole^{-1}$
$K_{0,7}$	$2.0 \cdot 10^{-9}$	$kg^{-1}s^{-1}$
ΔH_7	-79	kJ $mole^{-1}$
$K_{0,8}$	$1.2 \cdot 10^{-6}$	$kg^{-1}s^{-1}$
ΔH_8	-60	kJ $mole^{-1}$
E_a apparent	50	kJ $mole^{-1}$

The effective diffusivities of CO and CO_2 were calculated as the weighed average of the contributions of pores of different size and could be approximated as the rate of molecular diffusion in pores with an average diameter of 190 nm and a porosity/tortuosity ratio of 0.27. The concentration of oxygen, which was always added in large excess, was found not to influence the reaction rate in the kinetic reactors.

To minimize the effect of a slightly different activity of the catalyst in the pilot scale packed bed reactor, frequency factor $k_{0,3}$ was optimized to make the calculated conversion match the measured CO conversion. In most cases, the CO_2 concentrations measured at the end of the bed were used. If the CO conversion at this position was above 90%, concentrations measured closer to the inlet were used. This restriction of the conversion was necessary, because $k_{0,3}$ is very sensitive to small errors in the measured CO_2 concentration if the conversion approaches 100%.

Another way of optimizing the reaction rate could be to multiply the overall reaction rate, ηR, by some fitting parameter. If $k_{0,3}$ is optimized, the apparent orders with respect to CO

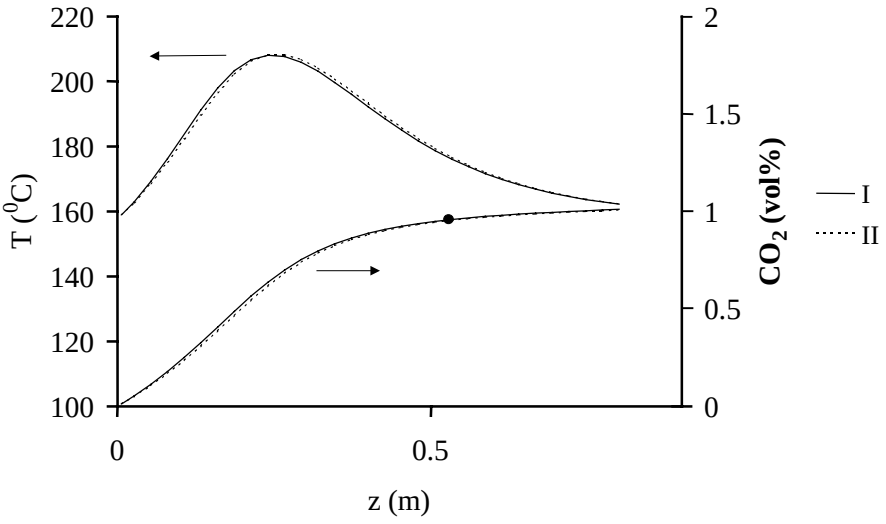

Fig. 3.22 Temperature at the centerline of the reactor and the CO_2 concentration at the wall calculated after optimization of the reaction rate to fit the measured CO_2 concentration (dot). I: profiles after optimization of $k_{0,3}$; II: profiles after multiplying the (overall) reaction rate by a constant. $T_{in}=T_w=156$ °C, P=3.8 bara, Re=140 and CO_{in}= 1.1 vol%.

and CO_2 and the apparent activation energy are changed due to a change of the particle effectiveness factor. When changing ηR, they remain constant. The shape of the temperature and concentration profiles will depend on the way in which the reaction rate is altered. The maximum difference that can be expected is very small, as is shown in Fig. 3.22. The temperatures at the centerline of the reactor shown in this graph were calculated by increasing the reaction rate using both methods. The increase of reaction rate corresponds with an increase of $k_{0.3}$ of 1.5, which was the maximum difference observed for all experiments. If it is assumed that the necessary change in reaction rate is due to the use of 'wrong' values of the parameters in eq. (3.13), the proper way to correct it would be to optimize the value of $k_{0,3}$. For each steady state experiment, $k_{0,3}$ was constant over the entire volume of the catalyst bed. It was also tried to use separate values of $k_{0,3}$ for different sections of the bed between each two gas sample locations. The thus obtained values did not indicate a change of $k_{0.3}$ over the length of the reactor.

To check whether the assumed dependence of the reaction rate on the CO_2 concentration is correct, experiments were performed during which CO_2 was added to the reactor feed. The influence of CO_2 on on the calculated temperature and concentration profiles is significant at low reactor temperatures, as is shown in Fig. 3.23. This graph shows the measured and the calculated temperatures at the centerline of the reactor at different CO_2 inlet concentrations. To be able to compare the experiments to the basic model, the heat transfer parameters and $k_{0,3}$ were optimized to match the first experiment, in which no extra CO_2 was present in the reactor feed. These values were subsequently used to calculate the axial temperature profiles

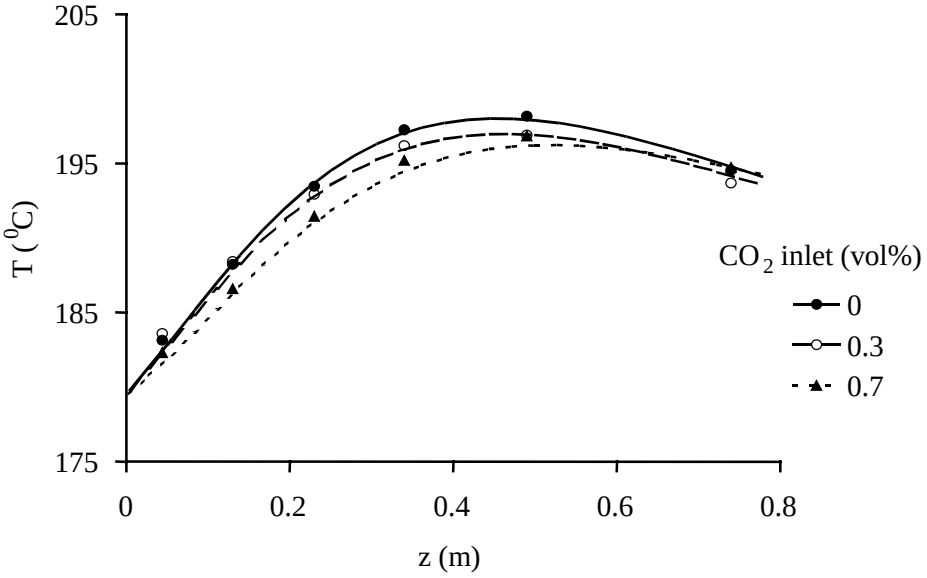

Fig. 3.23 Measured and calculated temperatures at the reactor center line for experiments at different CO_2 inlet concentrations at $T_{in}=T_w=156$ °C, P=3.8 bara, $CO_{in}=0.5$ vol%, Re=1100. The calculated profiles result after optimization of both $k_{0,3}$ and the effective radial heat transport parameters using the first experiment ($CO_{2,\ inlet}=0$).

for the remaining experiments. Fig. 3.24 shows the influence of product CO_2 at a low fluid velocity by comparison of two calculated temperature profiles. In this case, the temperature and location of the hot spot change appreciably if the influence of product CO_2 is neglected.

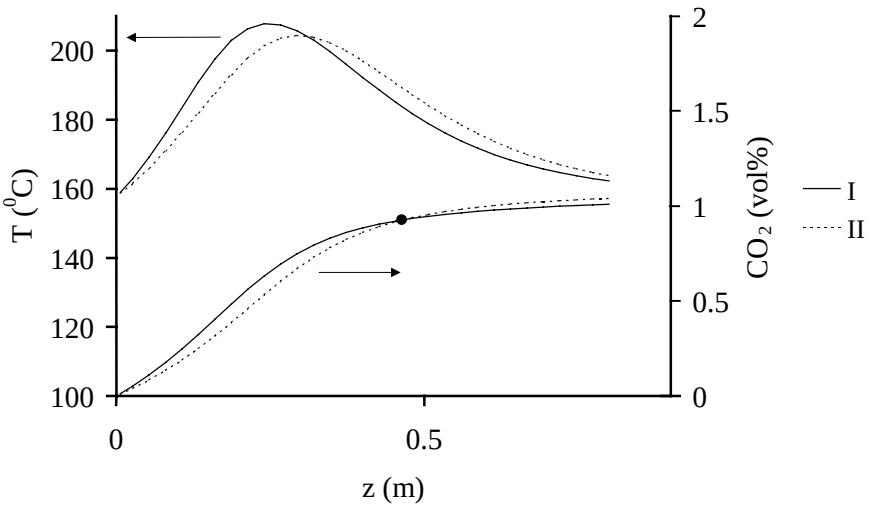

Fig. 3.24 Simulated influence of product CO_2 on the calculated temperature at the center line of the reactor and the CO_2 concentration at the wall at $T_{in}=T_w=156$ °C, P=3.8 bara, Re=140 and $CO_{in}=$ 1.1 vol%. $k_{0,3}$ was optimized to fit the measured conversion at 40 cm from the reactor inlet. I: reaction rate according to eq. 3.18; II: no influence of product CO_2 on the reaction rate.

Instead of fixing the CO conversions to the measured values, one could extend the target function (eq. (3.1)) with the difference between the measured and the calculated concentrations and optimize the parameters in the reaction rate expression together with the heat transfer parameters. Such approach was used by *Schwedock et al., 1989* and *Hofmann, 1979*. However, application of this method could conceal some of the heat transfer properties of the packing. Later in this chapter, it will be demonstrated that the existence of a non-uniform distribution of the axial fluid velocity over the radius can explain the difference between the effective heat transfer coefficients in the basic model that were obtained from experiments with and without reaction. A decreased fluid velocity at the core of the bed causes the initial temperature increase along the reactor axis to be faster, whilst the temperature after the hot spot becomes lower than predicted by the basic model. If the kinetic parameters would have been optimized to the measured temperature and concentration profiles, the neglecting of the velocity distribution would be compensated by change of the activation energy and the order with respect to CO_2. Another problem that arises when fitting the model to the concentrations, as well as the temperatures, is the choice of the weight factors that should be assigned to either one. It was found that the resulting kinetic parameters are rather sensitive to the ratio of the weight factors for temperature and concentration.

A disadvantage of the used experimental setup is that it was not possible to measure radial concentration profiles. Since the CO and CO_2 concentrations are known only at the wall of the reactor, the radial concentration profile at some axial position has to be calculated, so that

it depends on the radial mass dispersion coefficient. In our calculations, the flow-dependent contributions to the Peclet numbers for heat and mass dispersion in radial direction were assumed equal. Since this assumption was confirmed by mass transfer experiments (Appendix H), and the influence of the radial dispersion coefficient on the temperature field is small compared to the influence of the effective radial thermal conductivity, the lack of experimental data on the radial concentration distributions is considered not to be a serious problem.

In Fig. 3.25, the same experiments are shown as in Fig. 3.20, but after optimization of $k_{0,3}$ to match the measured CO_2 conversion for each individual experiment. As can be seen in the graphs, the basic model still fails to match the measured temperature profiles at the high fluid

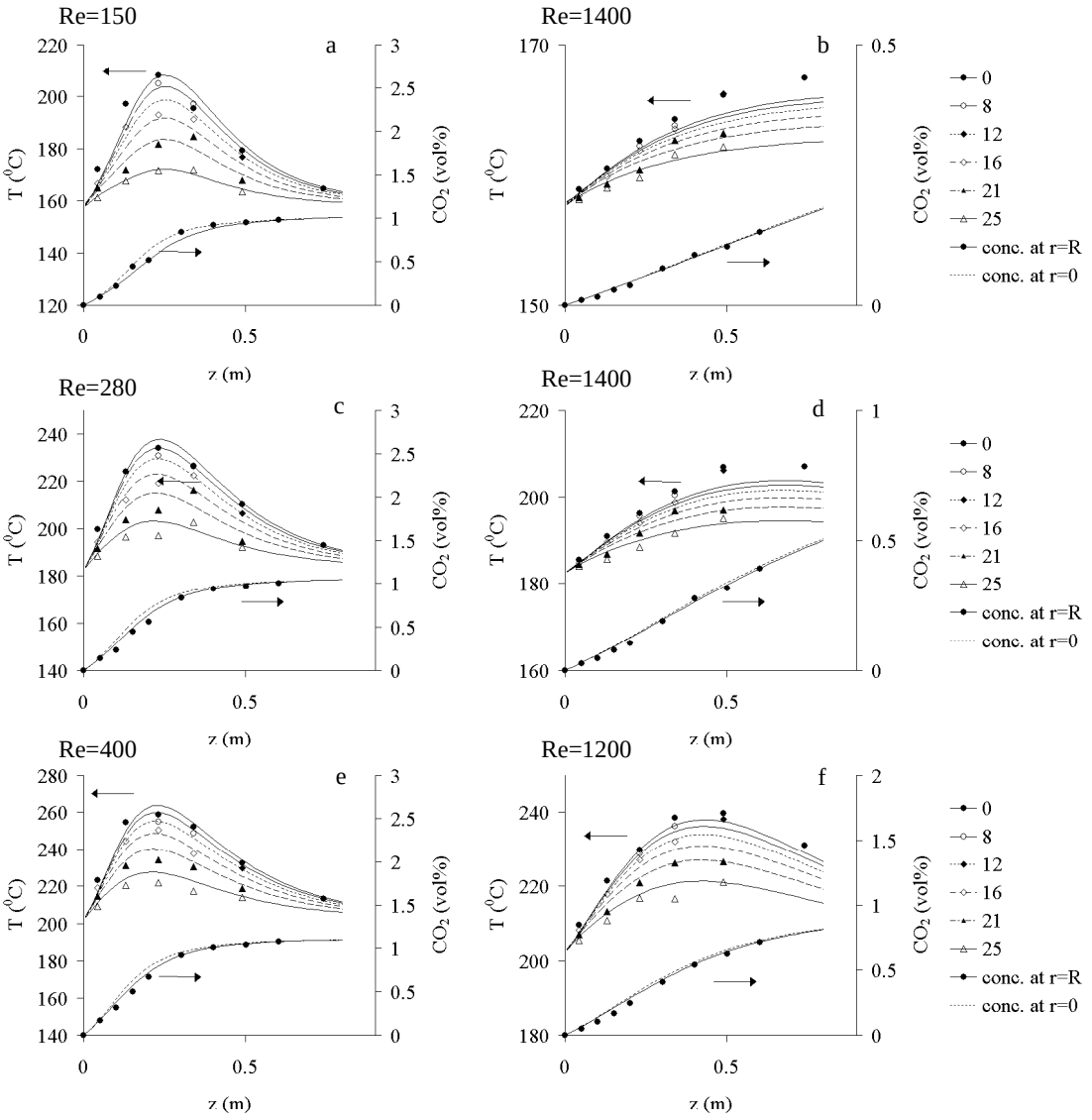

Fig. 3.25 Temperature and concentration profiles calculated using heat transfer parameters as measured without reaction after optimization of $k_{0,3}$ in reaction rate equation 3.19. a and b: $T_{in}=T_w=156$ °C, P=3.8 bara, Re=150 and 1400; c and d: $T_{in}=T_w=180$ °C, P=3.8 bara, Re=280 and 1400; e and f: $T_{in}=T_w=200$ °C 8 bara, Re=400 and 1200. Inlet concentrations approximately 1 vol% for all experiments.

velocities. The possibility that errors in the calibration of the used mass flow controllers causes the difference between model and experiments can be ruled out. The sum of the readings of the CO and the CO_2 analyzer was always constant over the length of the reactor. When using the originally measured kinetics, the hot spot temperature was overestimated, as was shown earlier in the graphs at the left-hand side of Fig. 3.20. At high fluid velocities, the opposite was the case for the experiments performed at wall- and inlet temperatures of 156 and 180 °C. When making the model comply with the measured CO conversion (Fig. 3.25), the maximum temperature at the hot spot of the reactor is estimated quite well if the flow rate is small. At the higher flow rates, as in the graphs at the right-hand of Fig. 3.25, the predicted temperature at the centerline of the reactor is too low. In all examples, the model seems to underestimate the axial temperature gradient near the reactor inlet, whilst, in most cases, the calculated CO_2 concentrations are a little higher than the concentrations measured at the wall.

3.4.2.3 Possible change of the catalyst activity over the reactor length

In order to be able to discriminate between different models, one should be sure that the differences between experiments and model as described above are not due to a change of the activity of the catalyst over the length of the reactor. This can be caused, for instance, by poisoning of the catalyst or by a dependency of the activity on the local temperature history. It is not likely that a length-dependence of the catalyst activity causes the difference between the measured and the calculated temperature profiles, shown in Fig. 3.25. Since the CO conversion at the end of the bed was fixed, the temperature near the inlet could only be increased if the catalyst near the inlet was assumed to be more active than in the remaining part of the reactor. When using such activity distribution, the initial increase of the calculated CO_2 concentration was distinctly faster than measured. More important evidence for a uniform activity of the catalyst was obtained from experiments in which the bed was repacked by fluidization.

All experiments with reaction that are used in this work were measured in one catalyst bed, which will be referred to as ‘main packing’. The same catalyst had been used already for considerable time when measuring the heat transfer parameters without reaction and during earlier experiments with reaction. The main packing was created by fluidization of the catalyst that was already present in the reactor. The catalyst was fluidized during a period that was three times as long as was necessary to obtain an even distribution of the dyed particles in the glass cold-flow setup (see section 3.2.4). Fig. 3.26 shows the axial temperature profiles at the centerline of the reactor, measured before and after creating the main packing. After compensating for a small difference of 0.5 K between the wall- and inlet temperatures, all temperatures are practically the same.

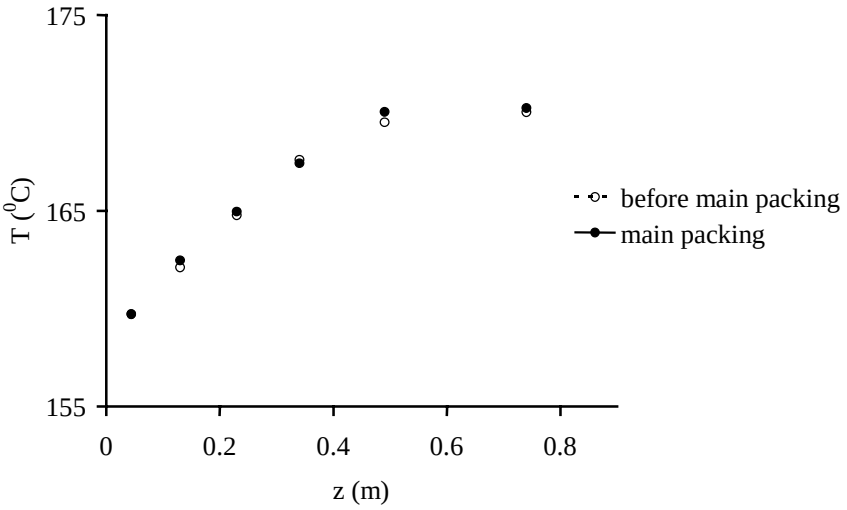

Fig. 3.26 Measured axial temperature profiles at the center line of the reactor before and after fluidizing the bed to obtain the main packing used in this chapter. Temperature profiles are compensated for a 0.5 K difference in inlet- and wall temperature. $T_{in}=T_w=156$ °C, P≈5 bara, CO_{in}≈1.1 vol%, Re=800.

After finishing the experiments with the main packing, the bed was repacked again by fluidization. Experiments using this packing were performed at pressures that were different from those used earlier, so that the temperature profiles can only be compared indirectly. Fig. 3.27 shows two axial temperature profiles at similar conditions, except for the pressure. The lines in this graph are the axial temperature profiles that were calculated after fitting $k_{0,3}$ and the heat transport parameters in the basic model to the temperature and concentration profiles

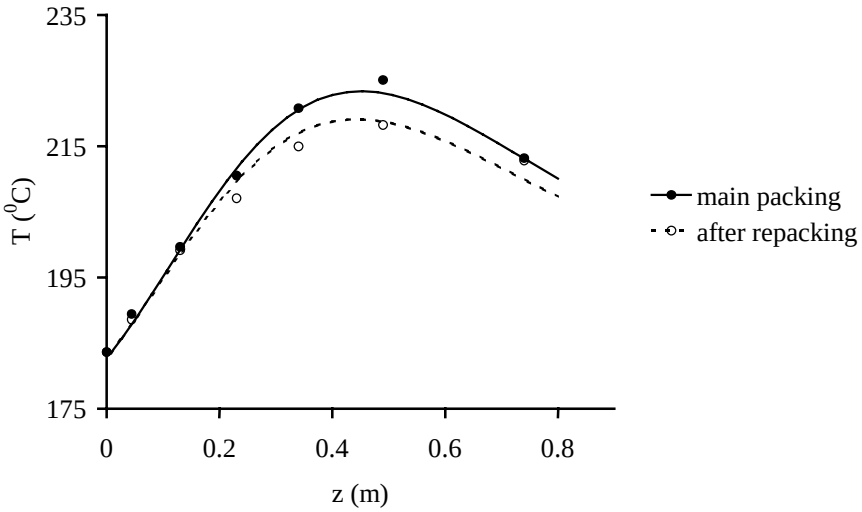

Fig. 3.27 Measured and calculated temperatures at the reactor center line of the reactor after repacking the catalyst bed used to obtained the experimental data presented in this chapter. Temperature profiles calculated after fitting $Pe_{h,r}$, Biot and $k_{0,3}$ to all temperatures measured in the main packing at $T_{in}=T_w=180$ °C, P≈5 bara, CO_{in}≈1.1 vol%, Re=800.

in the main packing. Both temperature profiles are described very well using identical heat transfer- and kinetic parameters, which would not be the case if the distribution of the catalyst activity was different in both packings.

3.4.2.4 Heat transport parameters derived from experiments at reacting conditions

for all experiments, the values of the effective radial thermal conductivity and wall heat transfer coefficient, in the form of $Pe_{h,r}$ and Biot, were optimized to minimize the difference between measured and calculated temperatures. The flow-dependent contribution to the Peclet number for radial mass transport, $Pe_{m,r}$ was assumed to be the equal to the value of $Pe_{h,r}$. The flow-independent contribution to $Pe_{m,r}$ was calculated from the molecular diffusivities of CO and CO_2, multiplied by the bed porosity/tortuosity ratio. The bed tortuosity was estimated to be 2. Since molecular diffusion is very slow compared to convective transport and the particles are practically impenetrable, the contribution of molecular diffusion to the overall mass transport is very small at the used flow rates.
The effective heat transfer parameters in the graphs at the left-hand side of Fig. 3.28 were calculated using the reaction rate that was measured independently in the kinetic reactors. In the graphs at the right-hand side, the value of $k_{0,3}$ was optimized to make the model comply with the measured CO conversion. In both cases, the effective radial thermal conductivity is less than the values that were obtained at non-reacting conditions. The same holds for the overall heat transfer coefficient in the one-dimensional model, which was calculated according to eq. 3.5. The wall Nusselt number shows a considerable spread, and is generally smaller than at non-reacting conditions. It was found that the effective heat transfer parameters do not depend on the CO inlet concentration, except if it was very small. In that case, $\lambda_{e,r}$ and α_w are very sensitive to small errors in the wall- and inlet temperature. The spread in Nu is larger than that in $\lambda_{e,r}$, which is caused by the fact that the model is less sensitive to α_w than it is to $\lambda_{e,r}$. In many cases, the model still fails to accurately predict the measured temperature profiles, especially at high fluid velocities, even if $k_{0,3}$ was optimized. In the next section, it will be demonstrated that the introduction of a radial distribution of the axial fluid velocity can explain the observed difference between the predictions of the basic model and the temperature and concentration fields measured inside the packing.
The velocity distribution is also able to explain the difference between the effective heat transport parameters obtained from experiments with and without reaction.

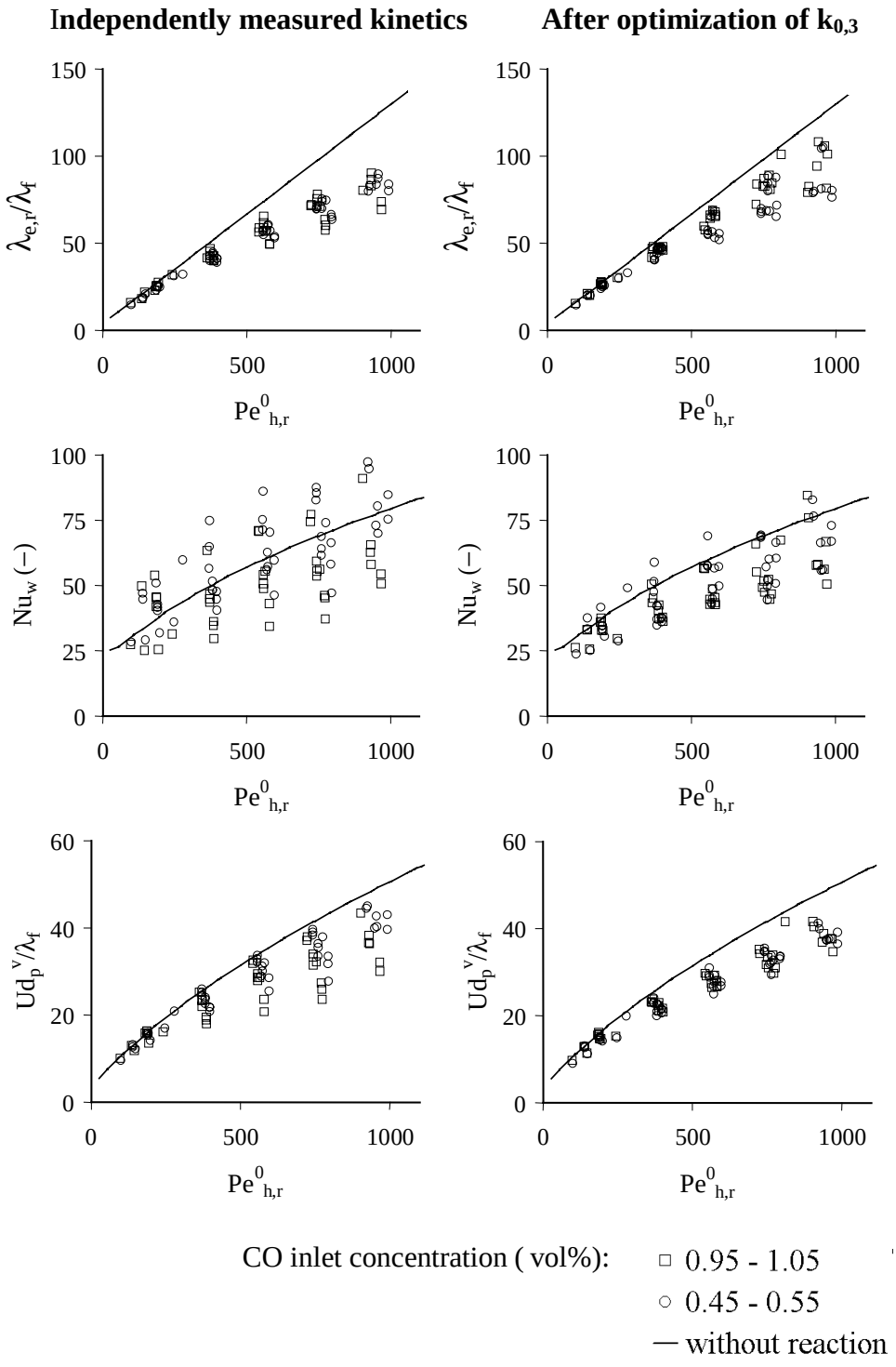

Fig. 3.28 Effective radial heat transfer parameters after minimizing the difference between the measured and the calculated temperatures inside the packing. To the left are the values when using the independently measured reaction kinetics; to the right the values obtained using optimization of $k_{0,3}$ to match the measured CO conversion.

3.4.3 Improvement of basic model

Two known phenomena, that were neglected in the basic model, are dispersion of heat and mass in axial direction and the existence of a non-uniform radial porosity distribution. Both phenomena will affect the calculated temperature and concentration profiles in different manners. Addition of heat and mass dispersion in axial direction to the model will lead to a smoothening of the temperature and concentration gradients. The maximum calculated temperature inside the packing does not necessarily decrease after introduction of these dispersion terms, since an increase of the temperature near the reactor inlet due to back mixing of heat will increase the reaction rate there. In the next section, it will be shown that axial dispersion of heat and mass cannot account for the observed difference between the measured temperature and concentration fields and the predictions of the basic model.

If the porosity is not constant, but a function of the radial position, this will significantly affect the temperature profiles in case chemical reaction takes place. In the first place, the source terms in the heat and mass balances will become a function radius, since the volume fraction of catalyst decreases near the reactor wall. Secondly, an increased porosity near the wall will cause an increase of the axial fluid velocity here, whereas the velocity at the core of the bed is decreased. A radial distribution of the axial fluid velocity affects the radial concentration and temperature gradients directly. Indirectly, the gradients in the packing are affected by a change of the effective heat and mass dispersion coefficients. If a uniform distribution of the fluid velocity is assumed, radial concentration gradients can often be neglected when modeling wall-cooled packed bed reactors. When assuming a uniform radial distribution of the axial velocity, the predicted concentrations of the reactants and reaction products usually does not vary significantly over the radius, except for very small flow rates and high reaction rates. Introduction of a non-uniform velocity distribution can cause pronounced radial concentration gradients at conditions at which they are negligible according to the basic model.

In most of the models of wall-cooled tubular reactors presented in literature, radial variations of the porosity and the axial gas velocity are neglected. Authors are aware that the porosity and the velocity increase near the wall, but they generally use this knowledge to explain why trends are observed in the values of the heat and mass transport parameters in the basic model. Well known are, for instance, correlations that describe the dependence of the effective radial thermal conductivity on the tube-to-particle diameter ratio. The local bed porosity is not a smooth function of the position in the bed and depends on the bed- and particle geometry. Because of this, the local fluid velocity will also fluctuate strongly over cross section of the bed. Prediction of the fluid velocity distribution over the radius on the basis of the porosity distribution is not a trivial procedure, since involves the use of averaged values of the velocity, which is rather questionable. At the same time, experimental investigation of the fluid velocity distribution is very difficult.

Until now, most investigators have measured only heat transfer without reaction (cold-flow experiments). In that case, the basic model generally predicts the experimental data very satisfactory. Assumption of a non-uniform velocity distribution does not result in an improved description of the measured temperature distribution (see e.g. *Borkink and Westerterp, 1994*). This, together with the additional question of how to define the dependence of the effective heat and mass dispersion coefficients on the radial porosity and velocity distribution, has caused that the radial non-uniformity of the bed is generally not accounted for.

The situation becomes different if a chemical reaction takes place in or at the catalyst particles (*Vortmeyer and Haidegger, 1991*, *Hein, 1999)*, when evaluating mass dispersion experiments (*Ziólkowski and Szustek, 1989*), or when attempting to reconcile the results of cold flow experiments obtained using reactors and packings of different geometries (*Winterberg et al., 2000a,b*). In these cases, discrimination between models with and without a radial distribution of the porosity and the fluid velocity on the basis of experiments is possible, but difficult. In case of chemical reaction, the uncertainty of the temperature and concentration profiles, caused by uncertainty of the kinetic parameters, easily outweighs the difference between the profiles predicted by the different reactor models. In case of tracer propagation experiments, the influence of the non-uniform radial velocity distribution is small, so that the measured radial concentration profiles should be very accurate.

A third phenomenon that was neglected in the basic model is the spread in the temperatures over a cross section of the bed in angular direction. Temperature fields inside a packed bed are not smooth, but exhibit large fluctuations in radial and angular direction. In the known reactor models, the reaction rate is calculated using the angulary averaged temperature. The actual average reaction rate should be higher, as will be discussed in section 3.4.3.2.

3.4.3.1 Influence of heat and mass dispersion in axial direction

It was concluded earlier (see section 0), that axial dispersion of heat could be neglected when treating the experiments performed at non-reacting conditions. At the conditions during experiments at reacting conditions, heat conduction and mass dispersion in axial direction should not have a great influence on the calculated temperature and concentration profiles either. During these experiments, the axial temperature gradients were smaller than those in the experiments without chemical reaction.

The maximum difference between the radial heat transfer parameters at reacting and non-reacting conditions was observed for high fluid velocities. At those conditions, heat and mass dispersion in axial direction have the least influence on the predicted temperature and concentration profiles. For this reason, axial dispersion alone cannot account for the observed difference.

To estimate the effect of neglecting of axial heat conduction and mass dispersion, calculations were made for 'worst case' situations, i.e. at operating conditions giving the highest temperature gradient near the reactor inlet. In the heat and mass balance, Danckwerts' boundary conditions were used at the reactor inlet and at the end of the bed (see Chapter 1).

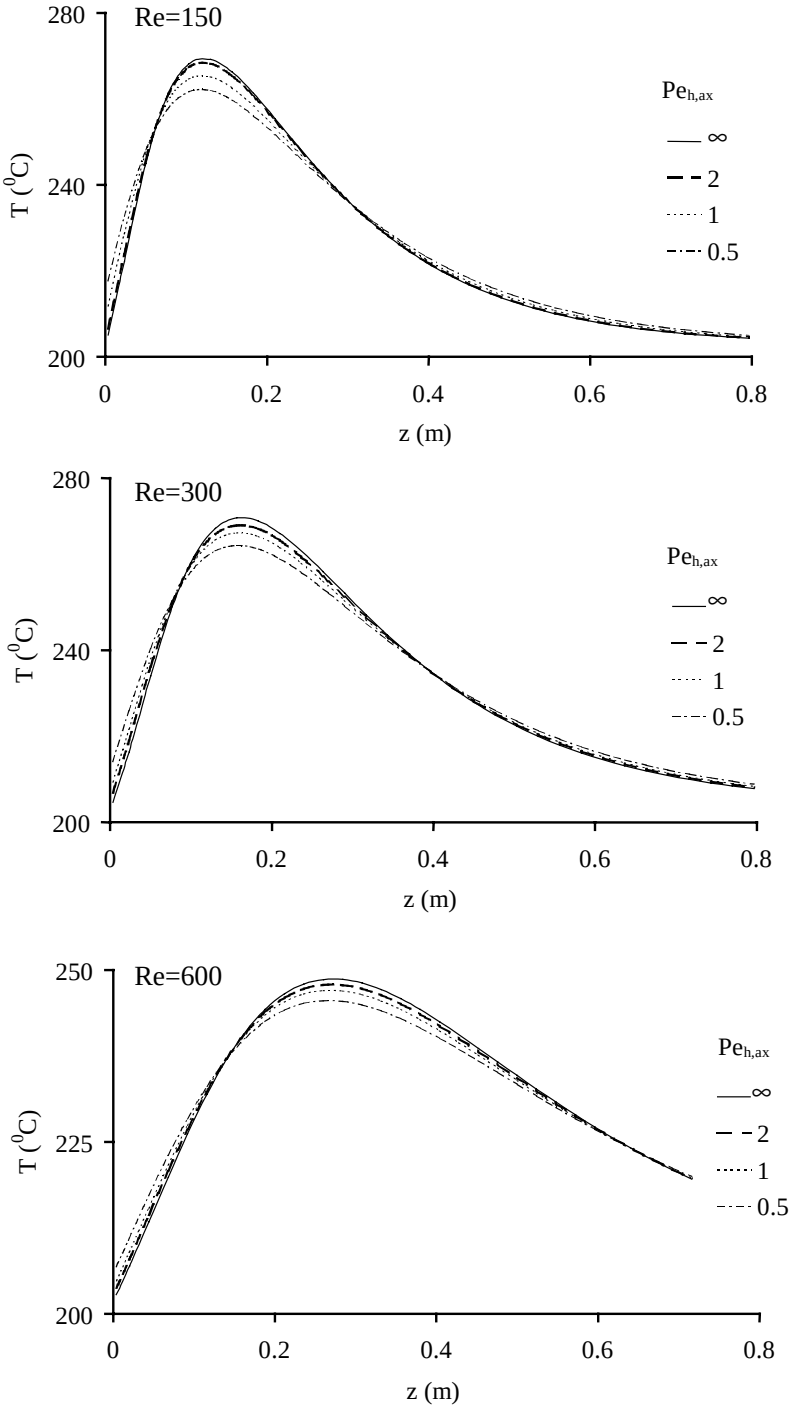

Fig. 3.29 Sensitivity of calculated axial temperature profiles at r=0 to Peclet number for axial thermal conductivity for experiments at Re=150, 300 and 600. $Pe_{m,ax}=Pe_{h,ax}$, CO inlet concentration 1 vol%, reactor pressure 3.8 bara. Peclet- and Biot number for radial heat transfer equal to values measured without chemical reaction.

The change of the temperature at the center line of the reactor if $Pe_{m,ax}=Pe_{h,ax}=2$ is very small (see Fig. 3.29); certainly if it is compared to the change in temperature due to wall channeling, which will be discussed in the next section.
The maximum change of the dimensionless temperature $\Theta=T/\Delta T_{ad}$ after introducing axial dispersion was found to be approximately 2 % at $Pe_{h,ax}=2$, Re=150, $T_{in}=T_w=200$ °C, $CO_{in}=1.2$ vol%. A significant change of the axial temperature profile, such as an increase in temperature close to the reactor inlet, is observed only if values of $\lambda_{e,ax}$ and $D_{e,ax}$ are used which are over twice as large as the values corresponding to $Pe_{ax}=2$, which is generally recommended in literature.
As concluded for experiments at non-reacting conditions, the influence of axial heat and mass dispersion can be safely neglected here.

3.4.3.2 Influence of angular temperature spread on reaction rate

In current models of wall-cooled tubular reactors, the reaction rate is calculated using the angular average temperature. However, the temperature fields over the cross-section of a packed bed show large fluctuations in radial and angular direction, which are proportional tot the heat fluxes in radial and axial direction (see Chapter 4). Due to the non-linear dependence of the reaction rate on temperature, the reaction rate at the angulary averaged temperature is smaller than angulary averaged reaction rate:

$$R\left(\overline{T}\right) \le \overline{R\left(T\right)} \tag{3.14}$$

Depending on the thermal conductivity of the catalyst particles and the scale of the temperature oscillations, temperature differences inside the particles are smaller than those inside the fluid phase. In some systems, however, this may not be true. In case of competitive adsorption of two or more of the reactants, for instance, a relatively small change of the fluid temperature may cause particles to travel from the lower to the higher steady-state. Such behavior was not observed for the reaction system used here, so that the maximum spread in the solid phases is taken equal to the maximum spread in the fluid temperatures. The quantitative data on the angular temperature spread, obtained from the cold flow experiments described in Chapter 4, were used to estimate whether the temperature spread has a significant influence on the rate of CO oxidation in the pilot-scale wall cooled tubular reactor. In appendix G, an analytical expression is derived which predicts the increase of the reaction rate as function of the temperature spread, which is assumed have a Gaussian distribution:

$$\Psi = \frac{\overline{R\left(T\right)}}{R\left(\overline{T}\right)} = \exp\left(\frac{1}{2}\left(\frac{\sigma E_a}{\overline{T}^2 R}\right)^2\right) \tag{3.15}$$

In eq. (3.15), E_a is the apparent activation energy and $\overline{T}$ is the average temperature at some position in the bed. σ is the standard deviation of the temperatures at this position, which was equal to (see Chapter 4):

$$\sigma = \frac{\tau}{1.6}\left(\frac{u_r}{\lambda_{e,r}} j_r + \frac{u_z}{\lambda_{e,ax}} j_z\right) = \frac{1}{\rho_f c_{p,f}}\left(\frac{j_r}{u_r} + \frac{j_z}{u_z}\right) \quad ; \quad \tau = \frac{9}{Pe_{h,r}} \frac{d_p^v}{u} \tag{3.16}$$

In eq. (3.16), j_r and j_z are the heat fluxes in radial and in axial direction; τ is the relaxation time and u_r and u_z are the fluctuation velocities in radial and in axial direction. By analyzing the temperature profiles measured above packings of the catalyst cylinders and two packings of glass spheres, it was found that u_r and u_z should be the same. The measured temperature spread in these packings could be described using $u/u_r=u/u_z=3.1$ for the catalyst cylinders and $u/u_r=u/u_z=1.8$ for the glass spheres.

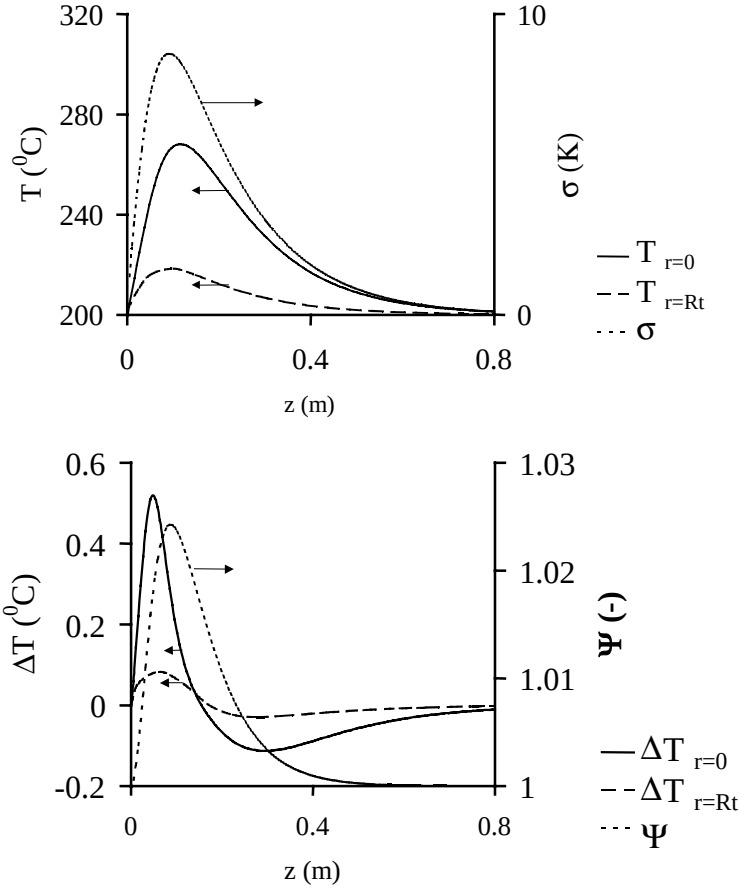

Fig. 3.30 Above: Axial fluid temperature profiles at r=0 and r=R_t and the standard deviation of the fluid temperature at r=R_t. Below: Change of the axial temperature profiles after accounting for the change of the reaction rate due to the temperature spread.
Re=200, CO_{in}=1.2 vol%, P=5.9 bara. Apparent activation energy E_a= 50 kJ mole^{-1}.

The apparent activation energy of the CO oxidation reaction over CuO/γ-alumina is 50 kJ mole^{-1}, which is relatively small. At the operating conditions at which the influence of the temperature spread was largest, the maximum change of the temperature inside the bed was predicted to be less than one degree Kelvin (see Fig. 3.30). As can be seen in the lower graph in this figure, the increase of the reaction rate that is caused by the temperature spread does not increase the temperature over the entire length of the bed. Since more CO is consumed close to the inlet, where the temperature is increased, the reaction rate further from the inlet is decreased, causing the temperature here to be below its original value.
The change of the heat transfer parameters, caused by neglecting of the temperature spread, is less than 0.8% for α_w and less than 0.5% for $\lambda_{e,r}$ at conditions as used in Fig. 3.30. Since, for all other experiments, the change of the reaction rate caused by the temperature spread is less, it was neglected when optimizing the heat transfer parameters.

3.4.3.3 Influence of a radial distribution of the porosity and the axial fluid velocity

In this section, it will be demonstrated that a non-uniform radial distribution of the porosity and the axial fluid velocity can explain the difference between the heat transfer parameters in the basic model, that were obtained from experiments with and without reaction. The importance of this phenomenon when treating experiments with chemical reaction has been stressed in numerous articles by the group of Vortmeyer. He and his coworkers have presented convincing arguments for the existence of a radial velocity distribution, based on experiments at particle Reynolds numbers up to 320 (*Haidegger and Vortmeyer, 1991, Hein, 1999*). Haidegger and Vortmeyer modified the standard dispersion model (basic model) to account for the radial non-uniformity of the bed. In the model proposed by Hein, the effective radial thermal conductivity of the bed is assumed to decrease within a small region near the reactor wall. This decrease of the thermal conductivity would cause the sharp temperature decrease near the wall, rather than a film resistance, as is assumed in the standard dispersion models. This model has been used by Winterberg (*Winterberg et al., 2000a,b*) to reconcile heat transfer parameters in literature that were obtained from cold-flow experiments. An abundant amount of literature data is available on radial porosity distributions in packed beds. In our work, the average radial porosity distribution was calculated as a smooth function of over the radius using the expression proposed by *Giese et al.,1998* and *Latifi et al. 1998*:

$$\varepsilon(r) = \varepsilon_\infty \left[1 + \left(\frac{\varepsilon_w}{\varepsilon_\infty} - 1 \right) \exp\left(-C \frac{(R_t - r)}{d_p^v} \right) \right] \tag{3.17}$$

This expression was used by Giese et al. to model the radial velocity distributions of fluid flowing through packings of spheres and cylinders that were measured using a laser-Doppler technique. The value of constant C in eq. (3.17) determines at what radial position the porosity starts to increase. When approximating eq. (3.17) by $\varepsilon(r)=k\ r^n$, the order n is approximately three times C. ε_w is value of the porosity at the wall after extrapolation of (3.17) to $r=R_t$. In reality, the porosity profile shows a sharp increase to become 1 at the reactor wall. For packings of cylindrical particles with the same height as the diameter, C=6 and ε_w=0.65 are recommended by *Giese et al., 1998* and *Winterberg et al., 2000b*. For packings of spheres, these values are 5 and 0.87 respectively. Fig. 3.31 shows the shape of the porosity distributions for different values of ε_w and an average porosity of the bed of 0.42.
A decrease of the bed porosity towards the reactor wall causes a radial distribution of the axial fluid velocity profile. In case of packed beds of high aspect ratio ($N=D_t/d_p^v$), the well known Ergun equation can be used to calculate the pressure drop as function of the average fluid velocity, since the fraction of the cross section with an increased velocity is small compared to the total cross-sectional area. This is not the case, however, for wall-cooled tubular reactors.
Experimental investigations of velocity profiles in packed beds are rather scarce compared to those of heat transfer. Measured velocity profiles exhibit large fluctuations, as one can expect for such a heterogeneous system. With increasing resolution of the experimental technique (*Ziólkowska and Ziólkowski 1993 and 2001, Giese et al. 1998*), the observed oscillations become more pronounced. Close to the reactor wall, the angular average porosity is an oscillating function of the radial coordinate. These oscillations are more distinct in case of well defined packings as those of spheres, than for less ordered packings such as those of

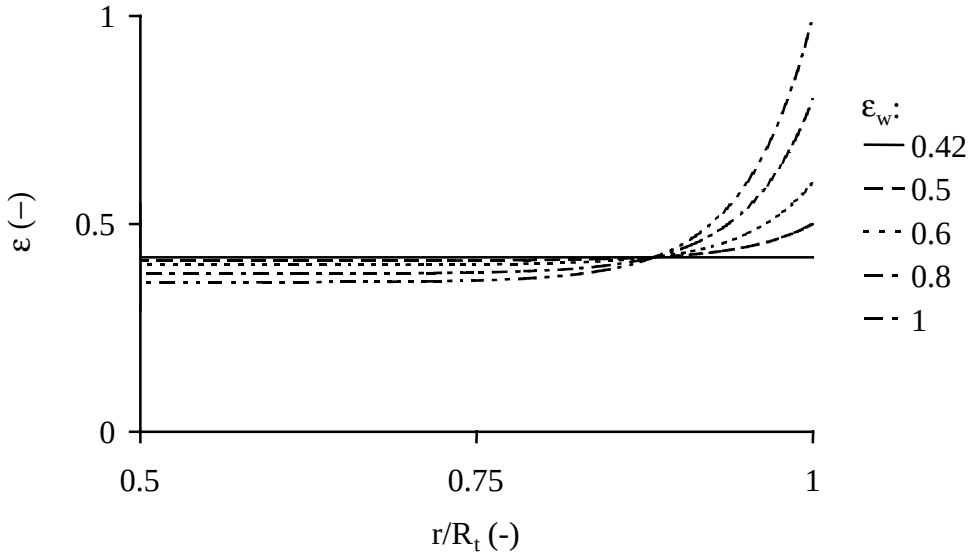

Fig. 3.31 Radial porosity distribution for C=6. The average porosity is the same as the porosity of the catalyst bed in the pilot-scale wall-cooled tubular reactor, which is 0.42.

cylindrical particles.
In this investigation, the velocity was assumed to be a smooth function of the radial position. To our opinion, the use of more complicated (oscillating) velocity distributions contradicts with the use of averaged values of the effective radial thermal conductivity in two-dimensional reactor models. The radial distribution of the axial fluid velocity was calculated by minimizing the radial difference of the pressure drop calculated according to:

$$\frac{\partial p}{\partial z} = -f_1 u(r) - f_2 u^2(r) + \frac{\eta_{eff}}{r}\frac{\partial}{\partial r}\left(r\frac{\partial u(r)}{\partial r}\right) \tag{3.18}$$

in which:

$$f_1 = 150\frac{(1-\varepsilon(r))^2}{\varepsilon^3(r)}\frac{\eta_f}{\left(d_p^v\right)^2} \;;\; f_2 = 1.75\frac{1-\varepsilon(r)}{\varepsilon^3(r)}\frac{\rho_f}{d_p^v} \tag{3.19}$$

The boundary conditions that apply to eq. (3.18) are:

$$\begin{aligned} r = 0: &\quad \frac{\partial u(r)}{\partial r} = 0 \\ r = R_t: &\quad u(r) = 0 \end{aligned} \tag{3.20}$$

If ε(r) is constant over the radius, eq. (3.18) is identical to the correlation proposed by Ergun. The velocity gradient near the wall, at which a non-slip boundary condition is applied, is a function of the effective viscosity η_{eff}, which depends of the fluid velocity. In case of packings of spheres, the velocity distributions measured by *Giese et al., 1998* could be described by eq. (3.18) if the following values of the effective viscosity were used:

$$\begin{aligned} \eta_{eff} &= 2\,\eta_f \exp\left(2\cdot 10^{-3}\,Re\right) \quad \text{(spheres)} \\ \eta_{eff} &= 2.6\,\eta_f \qquad\qquad\qquad\quad \text{(cylinders)} \end{aligned} \tag{3.21}$$

Fig. 3.32 shows the radial distribution of the axial fluid velocity at the minimum and maximum value of Re used in this investigation for different values of ε_w,. The radial porosity distribution was calculated according to eq.(3.18), with C equal to 6. At Re between 100 and 1400, the ratio of the velocity at the core of the bed and the average fluid velocity is almost independent of the flow rate. With increasing flow rate, the ‘wall region’ becomes narrower, but, at the same time, the maximum velocity increases.

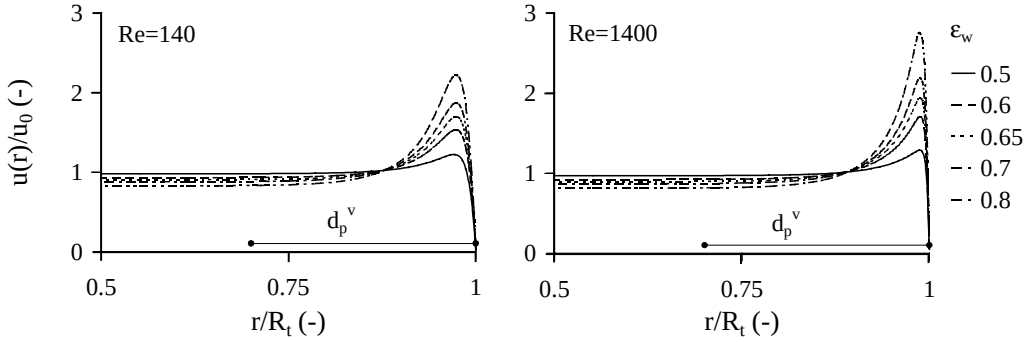

Fig. 3.32 Radial distribution of axial fluid velocity at lowest and highest flow rate. The average porosity of the bed is 0.42.

When applying the non-uniform porosity and velocity distributions, the dependence of the effective radial thermal conductivity of the radial position in the bed should be defined. The increased porosity near the wall results in an increased fluid velocity and in a decreased tortuosity of the fluid path in between the catalyst pellets. These two effects have an opposite influence on λ_f^r. It was assumed that the effects cancel each other, so that λ_r^f is constant over the radius (see *Borkink and Westerterp 1994, Hennecke and Schlünder 1973* and *Vortmeyer and Haidegger, 1991*).

As was observed by *Borkink and Westerterp 1994*, who investigated the influence of a radial porosity profile using a two-region model, the shape of the temperature profile was found not to be sensitive to the shape of the velocity distribution. A temperature profile that is calculated using the basic model can be perfectly described by the two-dimensionless pseudo-heterogeneous model with radial velocity distribution, which will be further referred to as the u(r)-model, if the effective radial thermal conductivity is decreased proportionally with the velocity at the core of the bed. By fitting the parameters in the u(r)-model to temperature profiles calculated using the basic model, it was found that the flow-dependent contribution to the effective radial thermal conductivity in the u(r) model, $\lambda_r^{f\,*}$, decreases with a factor u_c/u_0 with respect to its value in the basic model:

$$\lambda_r^{f\,*} = \frac{u_c}{u_0}\lambda_r^f \tag{3.22}$$

In (3.22), u_0 is the average fluid velocity and u_c is the fluid velocity at the centerline of the reactor. The flow-independent contribution to the effective radial thermal conductivity was calculated as function of the local porosity (eq. (3.8)), so that:

$$\lambda_{e,r}^{*} = \lambda_r^{0\,*}(\varepsilon) + \lambda_r^{f\,*} \tag{3.23}$$

The wall heat transfer coefficient did not change if a velocity distribution was used. Within the range of 140<Re<1400, as were the conditions during the experiments presented in this thesis, the values of the effective radial thermal conductivity predicted according to eq. (3.22) differed less than 3% from the values obtained by optimization of the parameters in the u(r)-model to temperature profiles that were calculated using the basic model (and vice versa) in case $0.42<\varepsilon_w<0.8$. At a constant ratio of u_0 and u_c, the model is not sensitive to the exact shape of the velocity distribution. Eq. (3.22) still holds if C in eq. (3.17) is varied between 4 and 8. Even assumption of full slip at the wall, which is the opposite extreme of the boundary condition at the wall in (3.20), hardly affects the calculated temperature profiles. Therefore, it was not necessary to fit the heat transport parameters for experiments at no-reacting conditions if the velocity distribution was changed. They could be predicted from eq. (3.22).
Earlier, the following expression by *Dixon, 1996* for the lumping of the heat transfer parameters was used:

$$\frac{1}{U} = \frac{1}{\alpha_w} + \frac{R_t}{3\lambda_{e,r}} \frac{Bi+3}{Bi+4} \tag{3.24}$$

Eq. (3.24) is still valid if a radial velocity distribution is assumed, provided that the value of $\lambda_{e,r}$ is used that corresponds to $\lambda_{e,r}^{*}$

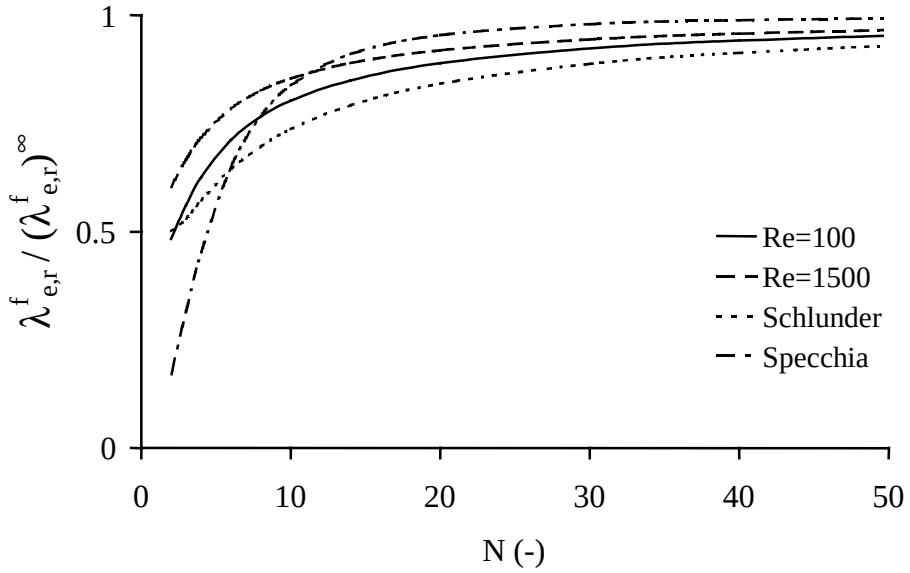

Fig. 3.33 Dependence of the effective radial thermal conductivity on the aspect ratio $N=D_t/d_p$ for packings of spheres. Values for Re=100 and Re=1500 calculated for velocity distributions according to eq. (3.22). $\varepsilon_c=0.37$, η_{eff} as in eq. (3.21).

According to eq. (3.22), $\lambda^{f}_{e,r}$ in the basic model should decrease with increasing flow maldistribution. This agrees with the relationships between $\lambda^{f}_{e,r}$ and the aspect ratio N that have been reported in literature. In Fig. 3.33, the values of $\lambda^{f}_{e,r}$ for packings of spheres according to (3.22) are compared to the following correlations:

$$\frac{\lambda_r^f}{\lambda_f} = \frac{Pe_h^0}{Pe_{h,r}^\infty} \tag{3.25}$$

with (*Bauer and Schlünder, 1978*):

$$Pe_{h,r}^\infty = 8\left[2 - \left(1 - \frac{2}{N}\right)^2\right] \tag{3.26}$$

or (*Specchia et al. 1980*):

$$Pe_{h,r}^\infty = 8.65\frac{d_p^e}{d_p^a}\left(1 + \frac{19.4}{N^2}\right) \quad \left(N = \frac{D_t}{d_p^a}\right) \tag{3.27}$$

The dependence of the thermal conductivity on N was calculated assuming a constant porosity of 0.37 and constant values of λ_r^{f*} and λ_r^{0*} at the core of the bed. The shapes of the

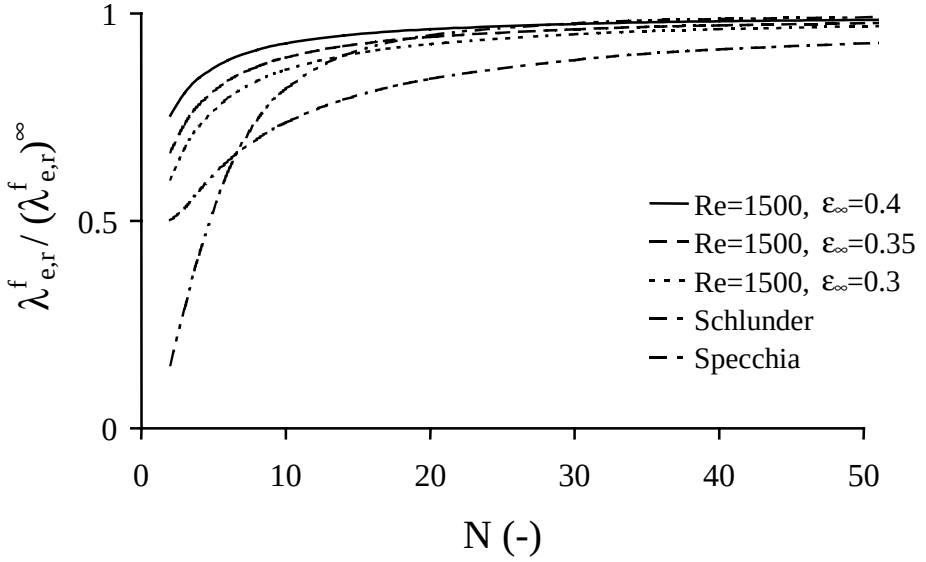

Fig. 3.34 Dependence of the effective radial thermal conductivity on the aspect ratio according to (3.22) for packings of cylindrical particles (h_p=d_p). ε_c=0.36, D_t=10 cm, η_{eff} according to (3.21).

curves for Re=100 and Re=1500 agree quite well with the correlations of *Bauer and Schlünder 1978* and *Specchia et al. 1980.* For packings of cylindrical particles, the decrease of $\lambda^{f}_{e,r}$ in the basic model is less than for packings of spheres. This is because, according to the used correlations, the porosity – and therefore the velocity – changes less over the radius. As a consequence, the dependence of λ_r^{f} for a packing of cylinders, shown in Fig. 3.34 is less strong.

The shape of the catalyst used in this investigation is different from the shape of the cylinders used by *Giese et al., 1998*. Because of this, the radial distribution of the bed porosity and the axial fluid velocity may differ from their predictions. When treating the experimental data, the radial velocity distribution was varied by changing the porosity at the wall, ε_w. This is the parameter that dominates the ratio of the average superficial velocity and the superficial fluid velocity at the core of the bed.

The heat and mass balance of the u(r) model are similar to those of the basic model, which were given in Chapter 1. In dimensionless form, the steady state balance equations and the boundary conditions are written as:

$$\frac{\partial \Theta_f}{\partial x} = \frac{1}{PE^{*}_{h,r}(r)} \frac{1}{y} \frac{\partial}{\partial y}\left(y \frac{\partial \Theta_f}{\partial y} \right) + St_h(r)(\Theta_s - \Theta_f) \tag{3.28}$$

$$St_h(r)(\Theta_s - \Theta_f) - Da(r)\Re(\mathbf{C}_s, \Theta_s) = 0 \tag{3.29}$$

$$\frac{\partial C_f^j}{\partial x} = \frac{1}{PE^{*j}_{m,r}} \frac{1}{y} \frac{\partial}{\partial y}\left(y \frac{\partial C_f^j}{\partial y} \right) + St_m^j(r)\left(C_s^j - C_f^j\right) \tag{3.30}$$

$$St_m^j(r)\left(C_s^j - C_f^j\right) + Da(r)\Re(\mathbf{C}_s, \Theta_s) = 0 \tag{3.31}$$

Boundary conditions:

$$x = 0: \qquad C_f^j = C_{in}^j \qquad \Theta_f = \Theta_{in} \tag{3.32}$$

$$y = 0: \qquad \frac{\partial C_f^j}{\partial y} = 0 \qquad -\frac{\partial \Theta_f^j}{\partial y} = 0 \tag{3.33}$$

$$y=1: \qquad \frac{\partial C_f^j}{\partial y}=0 \qquad\qquad -\frac{\partial \Theta_f^j}{\partial y}=Bi^*\left(\Theta_f^j-\Theta_w\right) \tag{3.34}$$

The dimensionless numbers and variables in the above equations are defined as:

$$\Theta=\frac{T-T_0}{\Delta T_{ad}} \qquad \text{or:} \qquad \Theta=\frac{T\text{-}T_w}{T_0-T_w} \qquad \text{(no reaction)}$$

$$\Delta T_{ad}=\frac{\left|\Delta H_r\right| c_0^i}{\rho_f c_{p,f}} \quad , \quad C^j=\frac{c^j}{c_0^j}$$

$$x=\frac{z}{R_t} \, , \qquad y=\frac{r}{R_t}$$

$$PE_{h,r}^*(r)=\frac{u(r)\rho_f c_{p,f} R_t}{\lambda_{e,r}^*(r)} \quad , \quad PE_{m,r}^{*\,j}=\frac{u(r)R_t}{D_{e,r}^{*\,j}(r)} \tag{3.35}$$

$$Bi^*=\frac{\alpha_w R_t}{\lambda_{e,r}^*} \quad , \quad St_h(r)=\frac{a\alpha_p(r)R_t}{u(r)\rho_f c_{p,f}} \, , \quad St_m^j(r)=\frac{ak_g^j(r)R_t}{u(r)}$$

$$Da(r)=\frac{R_t}{u(r)c_0}R\left(\mathbf{C}_{0,}\Theta_0\right) \quad , \quad \Re\left(\mathbf{C}_s,\Theta_s\right)=\frac{\varepsilon(r)}{\bar{\varepsilon}}\frac{R\left(\mathbf{C}_s,\Theta_s\right)}{R\left(\mathbf{C}_0,\Theta_0\right)}$$

Four of the terms in the heat and mass balance have been changed with respect to the basic model. The reaction rate has been corrected for the distribution of the catalyst over the radius by multiplying R(**C**,Θ), which is the reaction rate based on the average bed density, by a factor $\varepsilon(r)/\bar{\varepsilon}$. The ratio of the heat and mass production rate and the rate of the transport due to convection, Da(r), has become inversely proportional to the fluid velocity. The particle-to-fluid heat and mass transfer coefficients α_p and k_g^j depend on the local fluid velocity and bed porosity and are calculated from these local values according to *Gnielinski 1982* (eq. (3.11)).

The fourth difference is the change of the effective heat and mass dispersion coefficients. The flow-dependent contributions change proportionally with the ratio of the velocity at the core

of the bed and the average fluid velocity, whilst the flow-independent contributions depend on the local bed porosity. It is assumed that the flow-dependent contributions of the effective mass dispersion coefficient and the effective radial thermal conductivity are fully analogous. Fig. 3.35 shows the effect of the porosity and the velocity distribution on temperature for the mildest (left) and for the most severe operating conditions (right) applied in this investigation.

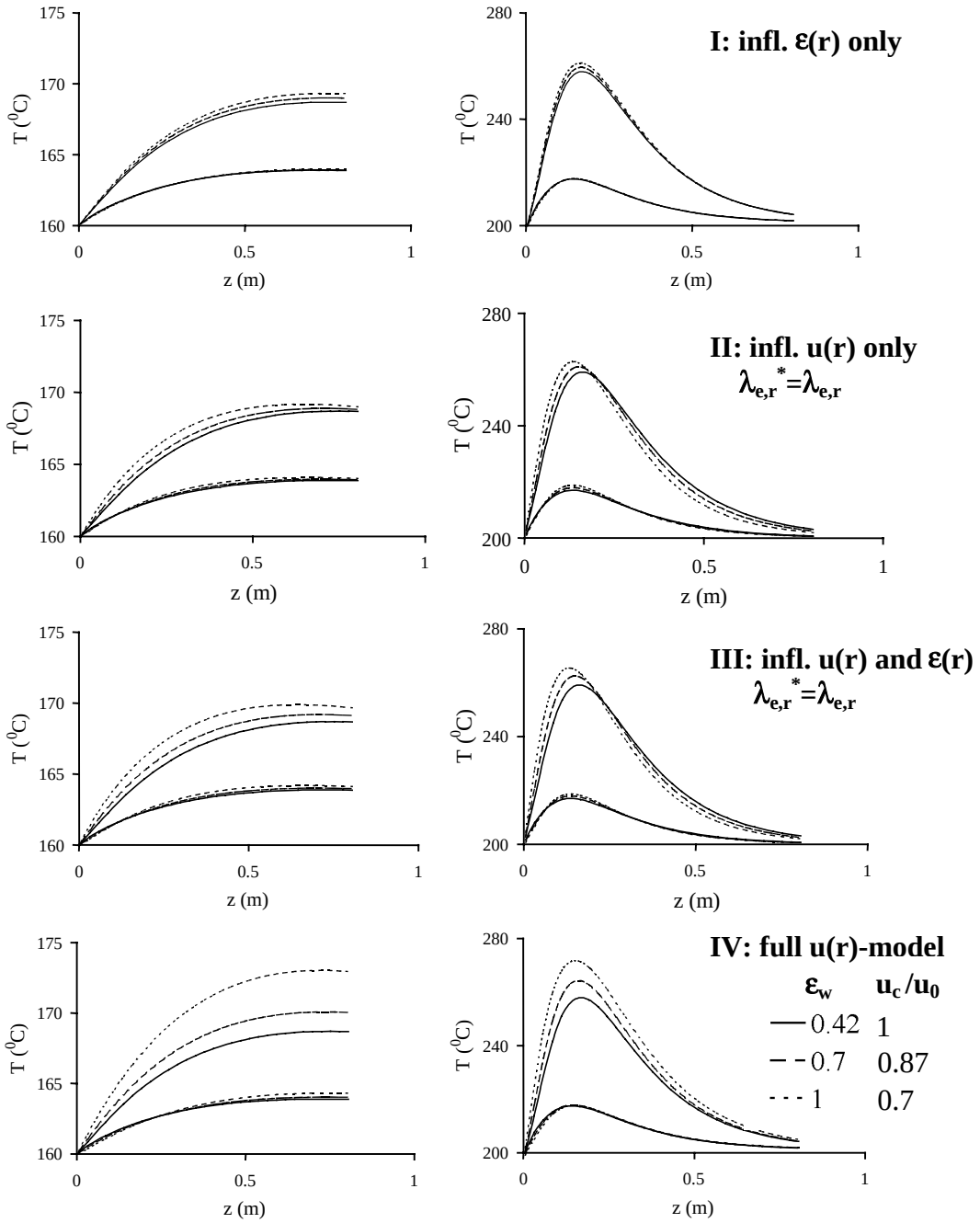

Fig. 3.35 Effect of the radial porosity and velocity distribution on the fluid temperatures at the centerline of the reactor and at the wall. I: influence of porosity distribution only; II: influence of non-uniform velocity profile only; III: Combined effect of porosity and velocity distribution; IV: Full u(r) model, including the change of the thermal conductivity and mass dispersion coefficients. Left: Re=1100, $Pe_{m,r}=Pe_{h,r}=27$, Bi=2.2; Right: Re=150, $Pe_{m,r}=Pe_{h,r}=25$, Bi=4.2. Further: CO_{in}=1 vol%, P=3.8 bara. Reaction rate calculated according to separately measured kinetics.

If ε_w is equal to the average porosity of the bed, the u(r) model is identical to the basic model. If only the change of the distribution of the catalyst is taken into account, the temperature profiles are not much different from those according to the basic model.
At the core of the bed, the reaction rate becomes higher due to the increase of the volume fraction of catalyst (graphs I). At the wall, the increased porosity causes a decrease of the reaction rate. The fluid temperature at the wall increases, however, which is due to an increase of the average reaction rate over the cross section of the bed.
More pronounced than the effect of the changed porosity distribution, is the effect of the velocity distribution it causes (graphs II). The radial velocity distribution causes Da, $PE_{h,r}$, $PE_{m,r}$, St_h and St_m to depend on the radial position. In graphs II, the change of the effective radial thermal conductivity and mass dispersion coefficient, as in eq. (3.22), has not been taken into account yet. Making these parameters dependent of the velocity profile does have a strong effect on the calculated temperature field.
At the used operating conditions, the models are not very sensitive to the particle-to-fluid heat and mass transfer coefficients. The sensitivity of the temperature field with respect to ε_w is mainly caused by a change of the ratio of the heat production rate and the heat removal rate (Da(r)). Graphs III show how the temperature is increased if both the radial porosity and velocity distribution are taken into account. Graphs IV (full u(r) model) show the axial temperature profiles if the effective radial thermal conductivity and the radial mass dispersion coefficient are decreased proportionally with u_c/u_0.
To some extent, the reaction rate is influenced by the existence of radial concentration gradients. At constant effective radial diffusivity, the difference between the concentration at the center of the bed and the concentration at the wall increases with increasing fluid maldistribution, as is shown in Fig. 3.36 for ε_w=0.65 (u_c/u_0=0.9). At conditions as used for the graphs at the left-hand side of this figure, the maximum concentration difference over the radius is 0.2% of the inlet concentration if the velocity is constant over the radius and 1% if the porosity and velocity distribution are accounted for.
At a higher inlet temperature and a smaller flow rate, the maximum radial concentration difference is increased from 5 to 15 % of the inlet concentration, which is shown in the graph at the right-hand side of Fig. 3.36.

The heat transfer parameters in the u(r)-model were optimized to the experiments with chemical reaction for different values of the ratio of u_c and u_0, which was varied by changing the value of the porosity at the wall, ε_w. As before, the model was made to match the CO conversion that was measured at the end of the bed by optimizing $k_{0,3}$. Optimal agreement between the heat transfer parameters, obtained from experiments with and without reaction, was obtained if ε_w=0.75 was used, which gives an (average) ratio u_c/u_0 of 0.85. In Fig. 3.37, the values of the heat transfer coefficients in the basic model and the u(r) model are compared.

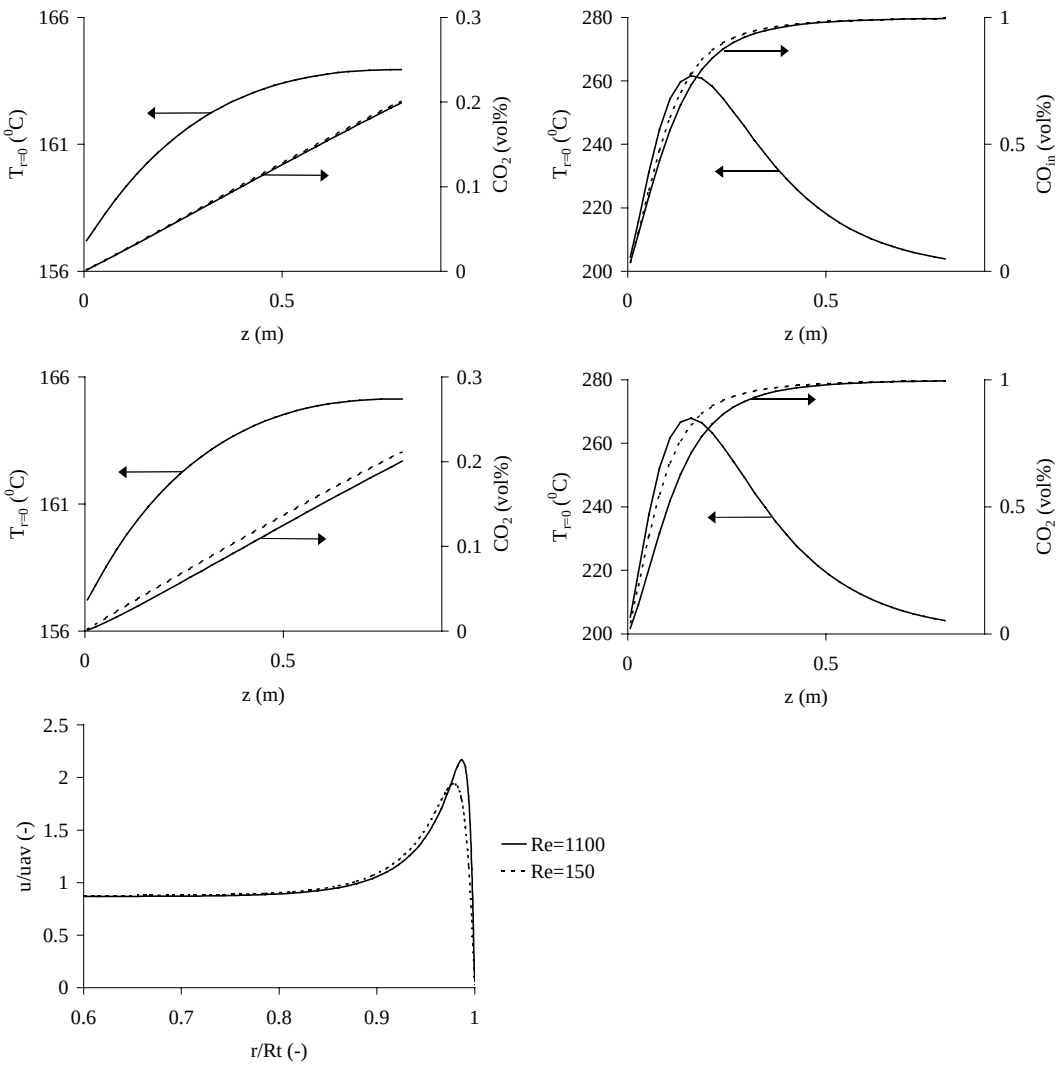

Fig. 3.36 Difference between CO_2 concentration at r=0 and r=R_t in case u(r)=u_c (top) and in case of a velocity as shown in the graph at the bottom (C=6, ε_w=0.65). $Pe_{m,r}$=$Pe_{h,r}$=25 Left: Re=1100, Bi=2.2, CO_{in}=1 vol%, P=3.8 bara; Right: Re=150, Bi=4.2, CO_{in}=1 vol%, P=3.8 bara. Reaction rate according to separately measured kinetics.

With the assumption of a radial velocity distribution, the difference between the heat transfer parameters disappears almost entirely. At small CO inlet concentrations, the
effective radial thermal conductivity seems to be a bit smaller than at non-reacting conditions. This difference is likely to be due to the rather small temperature increase of the bed, which causes the heat transfer parameters to be more sensitive to errors in the used wall and inlet temperature profiles. A further decrease of u_c/u_0 increases the effective thermal conductivity is obtained for high flow rates and small inlet concentrations, but at the same time causes the values at small flow rates to be higher than at non-reacting conditions. The wall heat transfer coefficients in the basic model show a large spread. This spread seems to be caused by the inability of the model to find a good match between the measured and the calculated temperatures, as will be
discussed later.

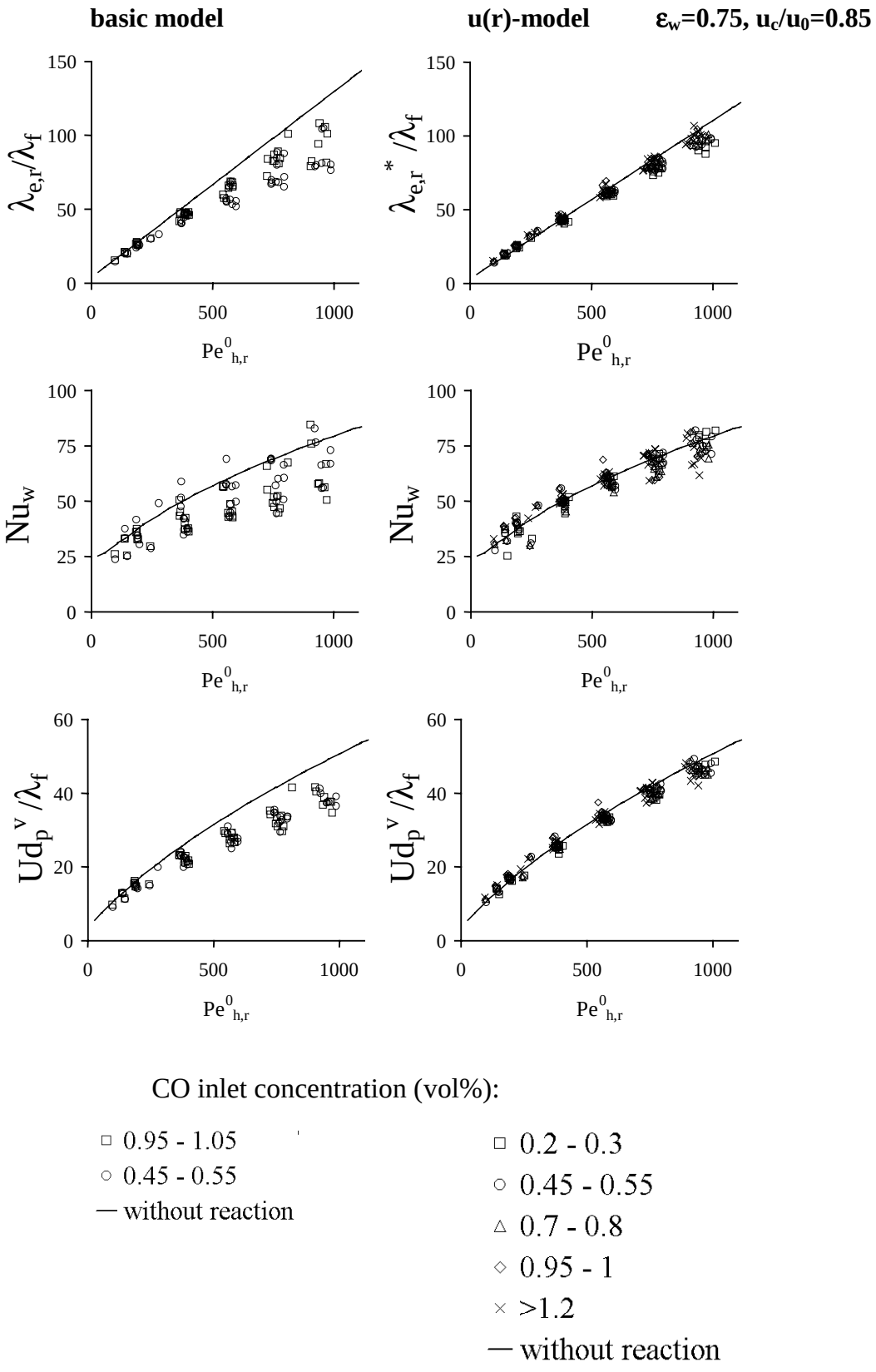

Fig. 3.37 Effective radial heat transfer parameters according to the basic model (left) and the u(r)-model. The graphs show the results of experiments at all flow rates, reactor pressures and inlet- and wall temperatures and a certain inlet concentration of CO.

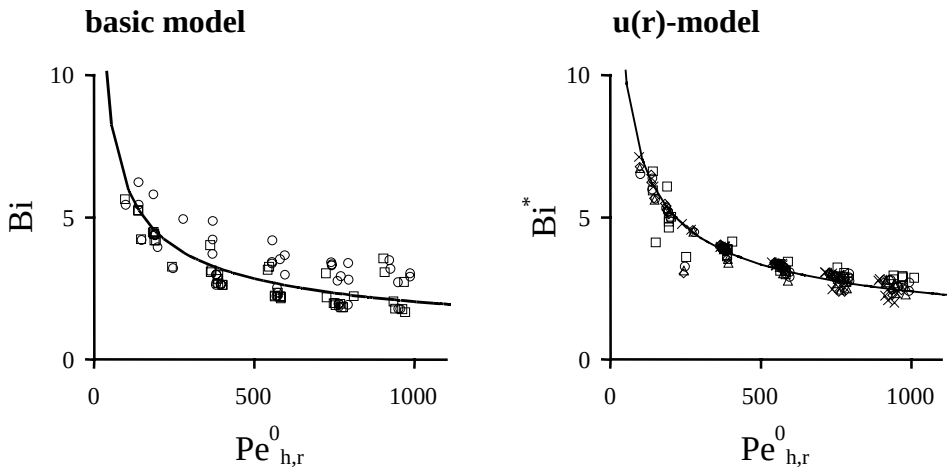

Fig. 3.38 Comparison of the Biot numbers according to the basic model and the u(r) obtained at reacting (dots) and non-reacting (lines) conditions. The legend is as shown in Fig. 3.37.

The spread in the wall Nusselt numbers is greatly reduced when applying the u(r) model. At the same time, the new values are close to those that were obtained at non-reacting conditions. This improved consistency becomes even clearer when comparing the Biot numbers, which are shown in Fig. 3.38. In case of the u(r) model, the Biot number is defined as:

$$Bi^{*} = \frac{\alpha_w R_t}{\lambda^{*}_{e,r}} \tag{3.36}$$

In Fig. 3.39, measured temperature and concentration profiles are compared to the predictions of the basic and the u(r) model. The profiles were calculated after optimization of the heat transfer parameters, so that the difference between the two models is small. However, it is clear that, besides giving a better agreement between the heat transport parameters at reacting and non-reacting conditions, the u(r) model gives a better description of the measured

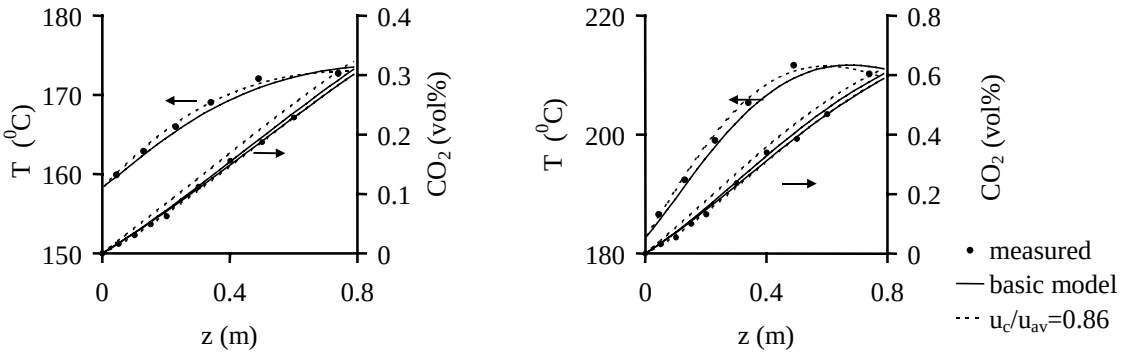

Fig. 3.39 Temperature at r=0 and CO_2 concentration at r=0 and r=1 for experiments at different wall- and inlet temperatures. Re=1100, P= 8 bara, CO_{in}= 1 vol%.

temperature profiles. In the basic model, the axial temperature gradients at z=0 are too small because the convective heat transport is overestimated. If the heat transfer parameters are optimized, the radial thermal conductivity is decreased with respect to its value at non-reacting conditions. This, in turn, causes an overestimation of the temperature after the hot spot.

3.5 Conclusions

Heat transfer experiments at non-reacting conditions were evaluated using a basic model, which is the pseudo-heterogeneous two-dimensional plug flow model without axial dispersion of heat and mass. The heat transport at reacting and non-reacting conditions was examined thoroughly over a wide range of operating conditions. The effective heat transport parameters, which were measured after fluidization and settling of the catalyst bed, were consistent. The values of the effective radial thermal conductivity and the wall heat transfer coefficient are close to those measured for packings of other cylindrical particles of similar size. The difference between the correlations obtained in this work and literature correlations is larger. However, this is not surprizing if the spread in the literature data is considered, together with the fact that the shape of the used particles differs from the shapes that are generally used in heat transfer investigations.

When the basic model was used to predict the temperature and concentration profiles measured at reacting conditions, it was found that, at high flow rates, this model underestimates the maximum bed temperature. The difference between the experimental data and the predictions of the model could not be attributed to the use of a inaccurate reaction rate expression. To minimize the influence of errors in the used reaction rate expression on the heat transfer parameters, the reaction rate was optimized to make the reactor model fit the measured CO conversion for each run.

After optimization of the radial heat transport parameters, the effective radial thermal conductivity reamained consistently lower than the values obtained from heat transfer experiments at non-reacting conditions. A similar behavior was observed for the wall heat transfer coefficient. The values of the wall heat transfer coefficient also exhibited a large spread, caused by the inability of the model to give a good description of the measured temperature profiles.

Different possible reasons for the discrepancy between the heat transfer parameters at reacting and non-reacting conditions were investigated, such as neglecting of dispersion of heat and mass in axial direction, neglecting of angular temperature fluctuations and the assumption of uniform radial porosity- and velocity distributions. The latter assumption was found to be the most important shortcoming of the basic model. After modification of the basic model by incorporating radial distributions of the porosity and the axial fluid velocity, the discrepancy between the effective radial heat transport parameters, obtained from

experiments at reacting and non-reacting conditions, disappeared. At the same time, the quality of the predicted temperature and concentration profiles was improved.

Notation

A, B	constants	-
C_f	shape factor	-
C^j	dimensionless concentration component j	-
c^j	concentration of component j	mole m^{-3}
c_p	heat capacity	J kg^{-1} K^{-1}
d_p^v	diameter of sphere with equal volume	m
d_p^v	diameter of sphere with equal surface area	m
ΔH_{ads}	adsorption enthalpy	J $mole^{-1}$
ΔH_r	reaction enthalpy	J $mole^{-1}$
E_a	activation energy	J $mole^{-1}$
F	target function	
j_r, j_z	heat flux in radial and axial direction	J m^{-2} s^{-1}
$k_{0,i}$	frequency factor reaction rate constant	s^{-1}
k, k_i	reaction rate constant	s^{-1}
$K_{0,i}$	frequency factor adsorption constant	-
K_i	adsorption constant	-
n_{exp}	number of experiments	-
n_Θ	number of measured temperatures	-
p	pressure	Pa
R	reaction rate	mole m^{-3} s^{-1}
	gas constant	J $mole^{-1}$ K^{-1}
R_t	tube radius	m
r	radial coordinate	m
T	temperature	K
ΔT_{ad}	adiabatic temperature rise	K
U	overall heat transfer coefficient	W m^{-2} K^{-1}
u_0	superficial fluid velocity	m s^{-1}
u_{ax}	axial fluctuation velocity	m s^{-1}
u_c	axial fluid velocity at the centerline	m s^{-1}
u_r	radial fluctuation velocity	m s^{-1}
u(r)	superficial fluid velocity as function of radius	m s^{-1}
x	dimensionless axial coordinate	z/R_t
y	dimensionless radial coordinate	r/R_t
z	axial coordinate	m

Greek

α_w	wall heat transfer coefficient	W m^{-2} K^{-1}
ε	porosity	-
ε_∞	porosity of an infinitely wide bed	-

ε_w	porosity at the wall		-
η_{eff}	effective viscosity of fluid flowing in packing		Pa s
η_f	fluid viscosity		Pa s
κ	ratio of thermal cond. of solid and fluid		-
λ_{ax}^{f}	fluid contribution to axial thermal conductivity		W m^{-1} K^{-1}
λ_f	thermal conductivity of fluid		W m^{-1} K^{-1}
λ_r^0	thermal cond. of bed in case of stagnant fluid		W m^{-1} K^{-1}
λ_r^f	fluid contribution to radial thermal conductivity		W m^{-1} K^{-1}
$\lambda_{e,r}$	effective radial thermal conductivity		W m^{-1} K^{-1}
$\lambda_{e,ax}$	effective axial thermal conductivity		W m^{-1} K^{-1}
σ	standard deviation of temperature		K
Θ	dimensionless temperature	with reaction:	$\frac{T-T_0}{\Delta T_{ad}}$
		without reaction:	$\frac{T-T_w}{T_0-T_w}$
ρ	density		kg m^{-3}
τ	relaxation time		s
ψ	ratio of reaction rates		-

Dimensionless groups

Bi	Biot number for heat transfer at the wall	$\frac{\alpha_w R_t}{\lambda_{e,r}}$
Da	Damkohler number	$\frac{R_t}{uc_0} R(c_0,T_0)$
N	aspect ratio	$\frac{D_t}{d_p^v}$
Nu_p	particle Nusselt number	$\frac{\alpha_{f-p} d_p^v}{\lambda_f}$
$PE_{h,r}$	Peclet number for radial heat conduction (model)	$\frac{u\rho_f c_{p,f} R_t}{\lambda_{e,r}}$
$Pe_{h,r}$	Peclet number for radial heat transfer	-
Pe_h^0	fluid Peclet number	$\frac{u_0 (\rho c_p)_f d_p^e}{\lambda_f} = Re_0 Pr$
$Pe_{h,ax}^{\infty}$	axial Peclet number at fully developed turb. flow	-
$Pe_{h,r}^{\infty}$	radial Peclet number at fully developed turb. flow	-
$PE_{m,r}$	Peclet number for radial mass dispersion (model)	$\frac{uR_t}{D_{e,r}}$
Pr	fluid Prandtl number	$\frac{\eta_f c_p}{\lambda_f}$

Re	particle Reynolds number	$\frac{u_0 \rho_f d_p^v}{\eta_f}$
$\Re$	dimensionless reaction rate	$\Re(c,T) = \frac{R(c,T)}{R(c_0,T_0)}$
St_h	Stanton number for particle-to-fluid heat transfer	$St_h = \frac{a \alpha_p R_t}{u \rho_f c_{p,f}}$
St_m	Stanton number for particle-to-fluid mass transfer	$St_h = \frac{a k_g^j R_t}{u}$

Super- and subscripts

*	value of parameter in u(r) model
0	at inlet (-conditions)
ax	axial
e, eff	effective
exp	experimental value
f	fluid
in	at inlet
j	component number
mod	model value
s	solid (catalyst)
w	wall

Chapter 4

Study of heat transfer at non-reacting conditions

ABSTRACT

In two reactors with different diameters, detailed temperature profiles were measured over packed beds of 14 mm glass spheres and the cylindrical catalyst that was used for the investigation of heat transfer at reacting and non-reacting conditions (see Chapter 3). The wave model, which has been recently developed at the University of Twente, was successfully applied to interpret the spread in the measured temperatures around the local angulary averaged temperature. In this model, heat transport is not driven directly by the radial and axial temperature gradients, but is a result of movement and mixing of fluid elements with different temperatures and velocities. By using the measured temperature spread, the apparent wall heat transfer coefficient in the two-dimensional reactor model could be divided into a real film resistance to heat transfer at the wall and an apparent resistance, which is caused by mixing of fluid elements moving towards and coming from the wall. The experiments showed that the film resistance accounts for more than 80% of the total resistance to heat transfer at the wall at Re> 500.

4.1 Introduction

Much experimental and theoretical work has been done over the past 50 years on heat transfer in packed beds without chemical reaction. In this work, close attention is paid to the influence of experimental errors on the effective heat transfer parameters, obtained from measured temperature profiles, such as non-uniformity of the wall- and inlet temperature, errors in the radial temperature profile due to the spread in local temperatures, and the distance between the bed and the thermocouples. According to the wave model for heat and mass transport in packed beds, the temperature spread should be related to the heat fluxes in radial and axial direction. To study the significance of heat dispersion in axial direction, experiments were performed in which the temperature profile changes from convex to concave due to a step change in the wall temperature.

Experiments were performed in two reactors with inner diameters of 100 and 64 mm. The packings consisted of 14 mm glass spheres or cylindrical catalyst particles with a diameter of

5.5 mm and an average height of 11.4 mm. The latter packing was only used in the 64 mm diameter reactor and the heat transport parameters obtained from these experiments were compared to those obtained in the pilot-scale wall-cooled tubular reactor. All the experiments discussed in this chapter were performed with air at ambient pressure.

4.2 Experimental setup and procedure

Figure 4.1 shows the setup including the 100 mm inner diameter reactor. The reactor consisted of three separate, independently cooled or heated sections, made of stainless steel. To reduce heat exchange between the different sections, they were separated by 3 mm layers of teflon packing rings and connected using nylon bolts. The first section, with a height of 140 mm, will be referred to as 'calming section' and was kept at the same temperature as the reactor feed. This section was used to obtain a uniform inlet temperature and to establish the flow pattern before the air entered the test sections. For that reason, the calming section was filled with the same packing material as the test sections. At the end of the calming section, radial temperature profiles were measured using thermocouples that were fixed to a course

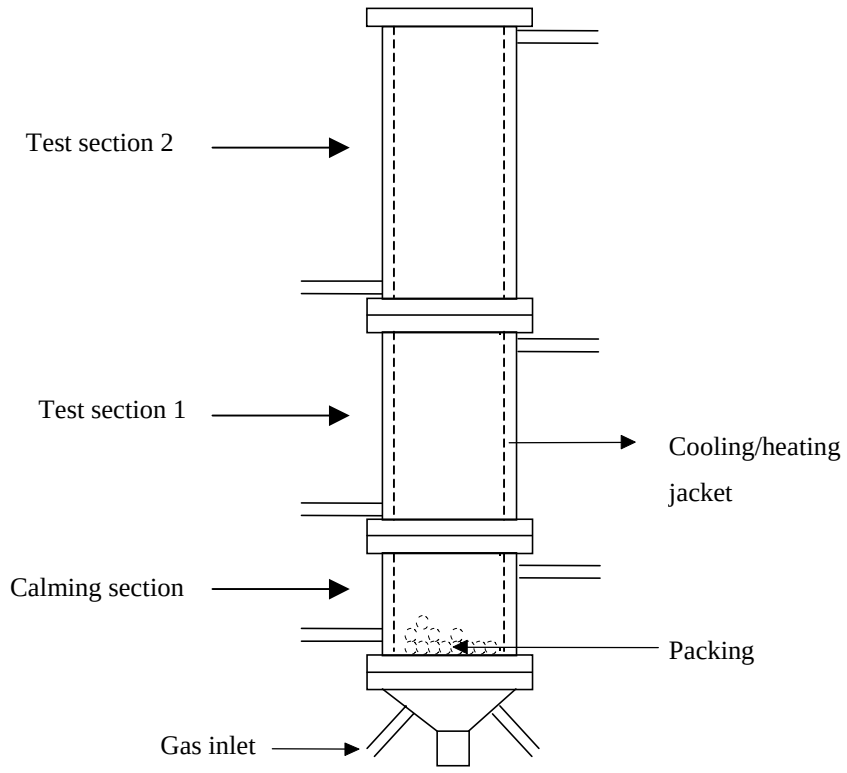

gauze.

Fig. 4.1 Setup used for heat transfer measurements without reaction.

The first test section has a height of 450 mm and its wall was kept at a temperature lower than that of the calming section. The second test section, with a height of 1000 mm, had the same wall temperature as the calming section. The walls of the calming section and the second test section were kept at a constant temperature of approximately 70 °C by circulation of water from a thermostat bath through the annular jackets surrounding the tubes. The velocity of the water in these jackets was approximately 0.1 m s^{-1}. The wall of the first test section was cooled by circulation of ethylene glycol from a cryostat through the cooling jacket. The glycol had a temperature of approximately 20 °C and was circulated at a velocity of 0.5 m s^{-1}. The flow rates in the cooling and heating jackets was more than sufficient to prevent a significant change of the temperature of the cooling medium over the length of the jackets.

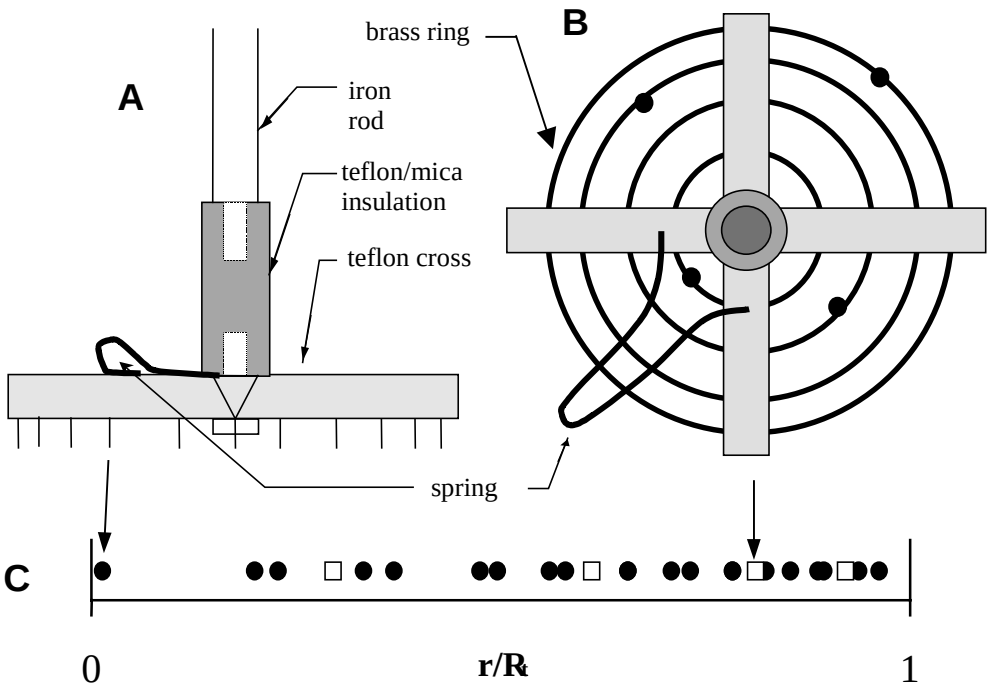

Fig. 4.2 Probes used for temperature measurement in 100 mm i.d. tubular reactor. A: Separate thermocouples, B: Brass rings, C: dimensionless radial positions of thermocouples in both probes.

Air was supplied by a blower and was preheated electrically to the desired inlet temperature. The flow rate was measured using a calibrated rotameter (Brooks).

Radial temperature profiles were measured at the outlet of the bed using 0.5 mm thermocouples (type K, Thermo-Electric) held by two different cross-shaped probes made of teflon. In one probe, shown in Fig. 4.2.A, the thermocouples were distributed over the four arms of the cross. To make sure that the distance between the thermocouples and the wall was always the same, two of the legs of the cross were pushed against the wall by a metal

spring. The thermocouples – 5 in each arm plus one in the center- protruded out of the arms over a distance of 3 mm. The radial positions of the thermocouples were measured after assembly and are shown in Fig. 4.2.C. A second probe holds 4 concentric brass rings with a thickness of 1 mm and a height of 3 mm. Thermocouples were welded to the rings in between the support arms, as shown in Fig. 4.2.B. It can be proven that their temperatures are uniform, in spite of the spread in the temperature of the fluid (see Appendix E). The wall temperature profile was measured at 0, 12, 23, 32 and 43 mm from the bottom of the test section by thermocouples that were fixed to the inner wall of the reactor and by a thermocouple that was pushed against the wall. This thermocouple was inserted into the reactor, which was then filled with the packing material. After the temperature profile inside the bed had become stable, the exact course of the wall temperature profile, especially near the flanges, was measured by slowly retracting the thermocouple, whilst pushing it against the reactor wall.

The setup including the reactor with an inner diameter of 64 mm was very similar to the one described above. This reactor consisted of two sections only. The calming section had a height of 157 mm and was heated by water from a thermostat bath. The particles in the calming section were glued together to separate them from the rest of the packing, which was later brought into the reactor. The velocity of the heating liquid in the jacket of the calming section was approximately 0.3 m s^{-1}. The test section was cooled by tap water that ran through the cooling jacket at approximately 2 m s^{-1}. The inlet temperature profile was measured by 5 thermocouples that were fixed to the packing inside the calming section. The wall temperature of the test section was measured at 2, 10, 40, 80 and 1000 mm from its bottom by thermocouples fixed to the wall. The temperature profiles above the packing were measured using a similar probe as that in Fig. 4.2, of which the radial positions of the thermocouples are shown in Fig. 4.3.A data acquisition unit (Hewlett Packard) was used collect the readings of the thermocouples.

The reactors were loaded by adding few particles at a time, after which the top layer was smoothened manually. After that, a 1 mm thick metal disk was put on top of the bed. The required axial position of the probe was determined by carefully lowering it until the thermocouples touch the disk, which was removed before performing the experiments. In this way, the risk of damaging the thermocouples was minimized. The measured bed porosity for

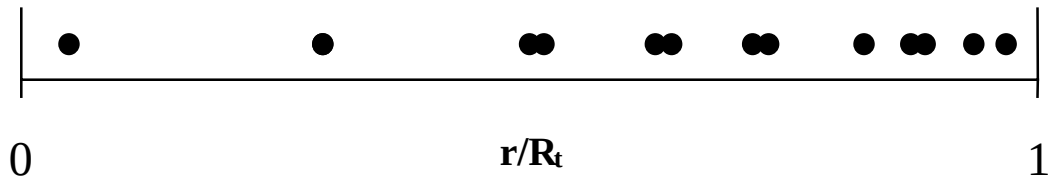

Fig. 4.3 Dimensionless radial positions of thermocouples in measuring probe in 64 mm i.d. test section.

the packings of glass spheres was 0.38 (D_t=100 mm) and 0.41 (D_t=64 mm). The average porosity of the beds of the cylindrical catalyst pellets was 0.34.

After changing the height of the bed, the fluid flow rate or the position of the temperature probe, measurements were started when no variation was observed in the temperatures measured above the packing at different radial positions.

4.3 Experimental results

4.3.1 Boundary conditions

Despite the use of a calming section in both setups, radial non-uniformities in the temperature profile at the inlet of the first test section could not be prevented. Therefore, it was necessary to use the measured radial temperature profile at this axialposition as boundary condition. The wall temperature of the calming section was influenced by heat exchange with the wall of the test section. The temperatures of the walls of the test sections were significantly increased due to heat transferred from the wall of the calming section. The rate of heat exchange between the cooling medium and the wall was insufficient to keep the wall at a constant temperature. Close to the flanges of both sections, the velocity of the cooling medium was be much smaller than the average velocity, causing poor heat transfer, whereas the heat flux from the packing is largest here.

Despite the use of 3 mm of teflon insulation between the sections, the temperatures of the adjacent flanges were almost identical due to the large contact area between the flanges,

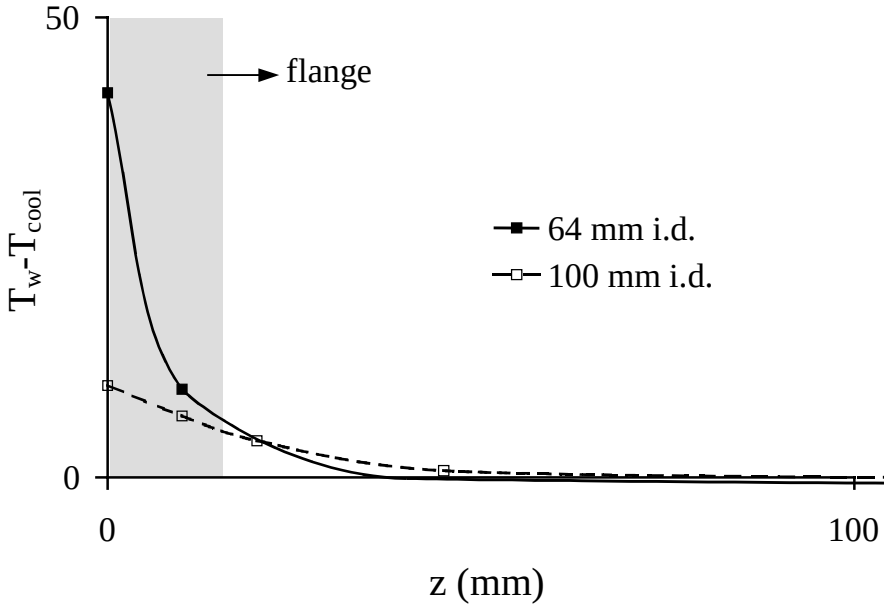

Fig. 4.4 Difference between the temperature of the wall and the temperature of the cooling medium near the entrance of the (first) test sections of both setups.

compared to the contact area between the flanges and the cooling jacket. Figure 4.4 shows typical wall temperature profiles measured in both reactors by thermocouples fixed to the reactor walls. The temperature profile measured by sliding a thermocouple along the wall of the 100 mm tube had the same shape. The wall temperatures used in the reactor model were calculated from a polynomial in z that was fitted to the measured wall temperature profiles.

4.3.2 Angular average temperature

A comparison was made between the angulary averaged temperature that was measured using the temperature probe with the brass rings (see Fig. 4.2.B) and the average of the temperatures measured along the circumference using the probe with the free thermocouples (see Fig. 4.2.A). The latter temperatures show a spread around the average. Such a spread is inevitable and is related to the heat flux, as will be discussed in section 4.3.4. As is shown in Fig. 4.5, the temperature of the rings may be used instead of the angular average temperature, measured by the free thermocouples. When the first probe was used, the cross was rotated stepwise with so small angular intervals as were necessary to obtain the average temperature for each experimental condition. It was found that local temperatures have to be measured at approximately 8, evenly distributed, angular positions to have less than 5 % difference between the thus obtained heat transfer parameters and those calculated using the temperatures measured at 22 angular positions.
The experimental effort can be greatly reduced when measuring the temperature fields over

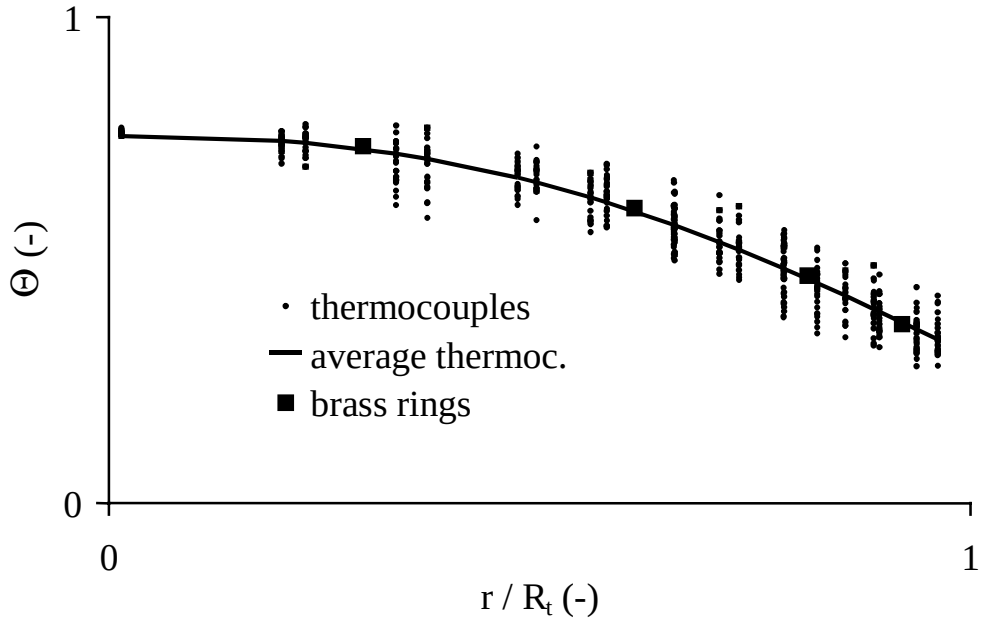

Fig. 4.5 Dimensionless radial temperature profiles obtained by averaging of temperatures measured at different angular positions and by direct measurement using brass rings.

the packing using the ring system. However, in this case the accuracy of the determined effective radial conductivity and the wall heat transfer coefficient decreases because of a decrease of the number of radial positions. The number of rings is limited, since a possible disturbance of the velocity profile inside the bed should be avoided. For this reason, the distance between the wall and the outer ring was rather large. As a result, the correlation between the effective radial thermal conductivity and the wall heat transfer coefficient was increased.

4.3.3 Heat transfer parameters

The effective radial thermal conductivity and wall heat transfer coefficient were estimated by minimizing the difference between the measured and the calculated temperatures as:

$$f\left(\lambda_{e,r},\alpha_w\right)=\sum_{i=1}^{n\Theta}\frac{\left(\Theta_i^{exp}-\Theta_i^{model}\right)^2}{\Theta_{r=0}-\Theta_{r=R_t}} \tag{4.1}$$

The temperatures Θ^{model} were calculated using the two-dimensional model described in Chapter 1. The Peclet number for heat conduction in axial direction, $Pe_{h,ax}$, was equal to 2 unless indicated otherwise. Different methods were applied for obtaining the relations between the effective heat transfer coefficients and the fluid velocity. $\lambda_{e,r}$ and α_w in eq. (4.1) were calculated using the individual experiments, performed at a single flow rate, as well as using all experiments simultaneously. In the latter case, $\lambda_{e,r}$ and α_w were assumed to comply with eqs. (4.2) and (4.3):

$$\frac{\lambda_{e,r}}{\lambda_f}=\frac{\lambda_r^0}{\lambda_f}+\frac{\lambda_r^f}{\lambda_f} \tag{4.2}$$

$$Bi=\frac{\alpha_w R_t}{\lambda_{e,r}}=a\ \ Re^{-b} \tag{4.3}$$

In (4.2), the first term at the right-hand side is the flow-independent radial thermal conductivity. According to *Bauer and Schlünder, 1978 b*:

$$\frac{\lambda_r^0}{\lambda_f}=\left(1-\sqrt{1-\varepsilon}\right)+\frac{2\sqrt{1-\varepsilon}}{1-B\frac{\lambda_f}{\lambda_s}}\left[\frac{B\left(1-\frac{\lambda_f}{\lambda_s}\right)}{\left(1-B\frac{\lambda_f}{\lambda_s}\right)^2}\ln\left(\frac{\lambda_s}{\lambda_f B}\right)-\frac{B-1}{1-B\frac{\lambda_f}{\lambda_s}}-\frac{B+1}{2}\right]\quad;\quad B=C_f\left(\frac{1-\varepsilon}{\varepsilon}\right)^{1.11} \tag{4.4}$$

The second term is the convective contribution

$$\frac{\lambda_r^f}{\lambda_f} = \frac{Pe_h^0}{Pe_{h,r}^\infty}, \tag{4.5}$$

in which $Pe_{h,r}^\infty$ is the fluid Peclet number at fully developed turbulent flow. The thermal conductivity of the 14 mm glass spheres of 1.1 W m^{-1} K^{-1} was measured according to the procedure described in Appendix C. The thermal conductivity of the catalyst material was found to depend on the temperature and has a value of about 0.25 W m^{-1} K^{-1} at the average temperature used in this investigation. The ratio of the heat transfer resistance of the bed and that of the near-wall region, known as the Biot number, is taken to be a function of Reynolds (see eq. (4.3)). According to *Dixon and Cresswell, 1979*, a=1.5 N b=–0.25.

Fig. 4.6 shows the effective heat transfer parameters obtained for the 14 mm glass spheres. At the lowest flow rate, the temperature profiles in the 100 mm diameter reactor were measured using the probe with brass rings. At all flow rates, all temperatures measured at minimum 5 different axial positions were used. Temperatures less than 3 K above the wall temperature were discarded since the model is rather sensitive to errors in temperatures close to the wall temperature. An experiment at Pe_h^0 = 340 in the 100 mm diameter reactor was repeated after repacking. The values of the effective heat transfer parameters changed less than 5%. The effective radial thermal conductivity, $\lambda_{e,r}$, decreases with decreasing aspect ratio $N=D_t/d_p^v$. The ratio of the slopes in Fig. 4.6 is 1.05, which is closer to the value of 1.13 predicted by *Bauer and Schlünder, 1978a* than to that predicted by *Fahien and Smith 1955*, which is 1.4. The difference between the values of the target function (4.1) after optimizing the heat transfer parameters per steady state experiment fluid velocity and after optimizing the correlations (4.2) and (4.3) to all experimental data is negligible. The flow-independent part of $\lambda_{e,r}$, λ_r^0, is higher than the values predicted by *Bauer and Schlünder, 1978 b* (eq. (4.4)). In the 100 mm and 64 mm diameter reactors, λ_r^0 is higher by a factor of 1.3 and 1.9 respectively. This, however, is not surprising, since the minimum flow rate that was used is rather high. Because of that, λ_r^0, which makes only a small contribution to the effective radial thermal conductivity, was calculated by extrapolation over a large interval of the horizon axis.

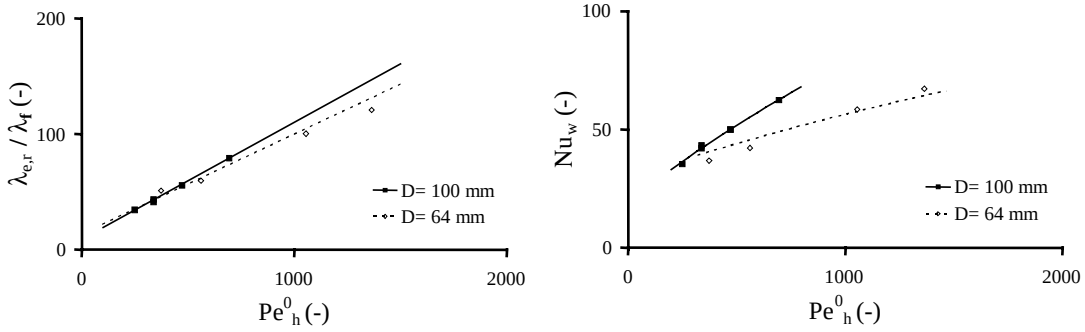

Fig. 4.6 Heat transfer parameters of the pseudo-homogeneous plug-flow model obtained by fitting experiments at different flow rates separately (dots) and those obtained by optimization of the parameters in correlations (4.2) and (4.4) to the experiments at different flow rates simultaneously (lines). Shown here are the values for packings of 14 mm glass spheres.

The wall heat transfer coefficient, here expressed in the form of the wall Nusselt number

$$Nu_w = \frac{\alpha_w d_p}{\lambda_f}, \tag{4.6}$$

was found to decrease with decreasing aspect ratio. In literature, the wall heat transfer coefficient is either taken to be independent (*Martin and Nilles, 1993, Borkink and Westerterp, 1992, Li and Finlayson, 1977, Dixon and Cresswell, 1979*) or dependent (*Tsotsas and Schlünder 1990, Dixon and Paterson, 1978*) on the aspect ratio. The observed difference in wall heat transfer coefficients is larger than follows from the predictions of the latter authors. An explanation of the observed difference is given in section 4.3.4, where it shown that the difference in wall roughness is a plausible cause.

In Fig. 4.8, the effective heat transfer parameters of the pseudo-homogeneous plug flow model measured for 11 x 5.5 mm cylindrical catalyst particles (CuO/γ-alumina) are compared to the values for the packing of glass spheres with a similar aspect ratio and to the values

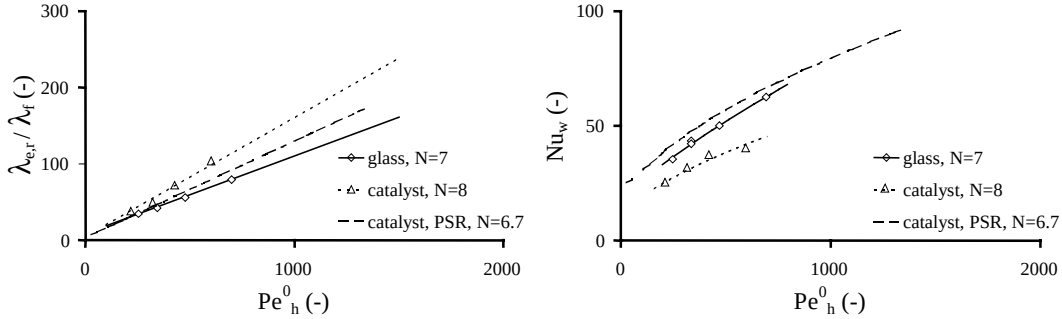

Fig. 4.8 Comparison of effective heat transfer parameters obtained for catalyst particles (D_t=64 mm. d_p^e= 8 mm), glass spheres (D_t=100 mm, d_p= 14 mm) and the values obtained For a packing of catalyst in the Pilot Scale wall-cooled tubular Reactor (PSR, D_t=53 mm); $Pe_{h,ax}$= 2.

measured for the same catalyst in the pilot-scale wall-cooled tubular reactor (see Chapter 3). The effective radial thermal conductivity for the packing of the cylindrical particles is higher than that of the packing of glass spheres. In literature, this increased conductivity of packings of cylinders is well known. *Bauer and Schlünder 1978a*, for instance, multiply the volume-equivalent particle diameter by a factor depending on the particle shape, which is 1.15 and 1.75 for cylinders and spheres respectively. This is exactly the difference between the values of $\lambda_{e,r}$ found here for the glass spheres and the catalyst cylinders. The wall heat transfer coefficient, obtained for the catalyst packing, is lower than that for the spherical glass particles.

The ratio $\lambda_{e,r} / \alpha_w$ for the catalyst in the cold-flow setup is different from the values obtained in the pilot-scale wall cooled tubular reactor. The wall heat transfer coefficient is lower, whilst the radial thermal conductivity is higher in the cold flow setup. The values of the overall heat transfer coefficient in the one-dimensional model that correspond to the calculated values of $\lambda_{e,r}$ and α_w do not differ much. The maximum difference is less than 10 %, with the overall coefficient obtained in the cold-flow setup being lower than the one obtained in the pilot-scale reactor. The higher value of the radial thermal conductivity measured in the cold flow setup can be explained through the radial distribution of the axial fluid velocity. As discussed in Chapter 3, the effective radial thermal conductivity is proportional to the velocity.

With decreasing reactor diameter, the ratio of the velocity at the core of the bed and the average superficial fluid velocity becomes smaller, which leads to smaller values of $\lambda_{e,r}$.

The higher value of α_w in the pilot-scale wall-cooled tubular reactor can be explained by considering that the inner wall of this reactor is very rough compared to the wall of the cold-flow setup, which results in a smaller resistance to heat transfer in the fluid film near the wall (see section 4.3.4).

α_w and $\lambda_{e,r}$ are strongly correlated. With increasing heat transfer resistance in the bed, compared to the heat transfer resistance at the wall, the model becomes insensitive with respect to α_w. In that case, small uncertainties in the boundary conditions significantly influence the value of Bi. In order to verify the reliability of $\lambda_{e,r}$ and α_w, both parameters were determined independently by avoiding the use of a heat flux-type boundary condition at the wall. Instead, the temperatures measured closest to the wall were used as boundary condition and only temperatures inside the new boundary were considered. An exponential function, fitted to the temperatures measured at 48 mm from the centerline of the 100 mm diameter reactor, was used as the new boundary condition of the test section. The wall heat transfer coefficient was calculated from the fluid temperature at the reactor wall using the obtained value of $\lambda_{e,r}$. When applying this procedure, the effective heat transfer parameters are very close to the values obtained by optimizing both parameters simultaneously, as is shown in Fig. 4.8.

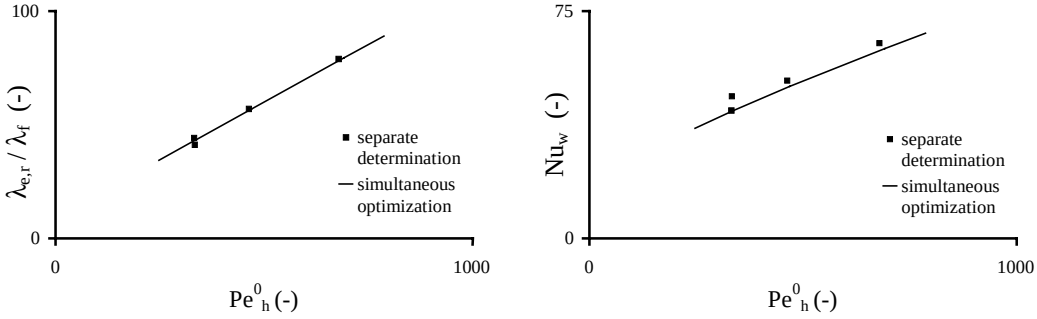

Fig. 4.8 Comparison of effective radial heat transfer parameters obtained by separate determination of $\lambda_{e,r}$ and α_w (dots) and values obtained by simultaneously optimization (lines, see also Fig. 4.6). $Pe_{h,ax}$=2.

In the present work, a possible length-dependency of the effective radial heat transfer parameters, as was observed by different authors (*Borkink, 1991, Dixon, 1985a and b, De Wasch and Froment, 1972, Li and Finlayson, 1977, Martin and Nilles, 1993, Winterberg et al, 2000 a, b*), was investigated by optimizing these parameters using only a part of the measured temperatures. One method was to use the temperature profile measured at a certain axial position as the 'inlet' temperature distribution, after which the model parameters were optimized to decribe the radial temperature profile(s) at the next axial position(s). Another method was to use the measured inlet temperature profile and to fit the model parameters to the temperatures measured after a certain minimum distance from the inlet of the test section. No dependency of the effective radial heat transfer parameters on the axial position was observed. The parameters showed a spread around an average, which increased when less data points were taken into account.

4.3.4 Angular temperature spread

As discussed in Chapter 1, the temperatures measured above or inside a packed bed show a spread around the angulary averaged local temperature. In literature, the nature and cause for this spread in temperature is often not recognized and is usually not accounted for by reactor models. Investigators have become accustomed to the well-known two-dimensional reactor models, which predict smooth temperature profiles and assume that the heat flux is proportional to the effective thermal conductivity and the temperature gradient. These models do not explicitly recognize the true mechanism of heat dispersion. At high Reynolds numbers, radial and axial dispersion of heat is caused mainly by movement of fluid elements with different temperatures and different radial and axial velocities, as discussed in Chapter 1. At high flow rates, molecular conduction of heat makes only a small contribution to the overall heat transport rate. The description of the radial and axial heat and mass fluxes using Fick's and Fourier's laws does not follow automatically from the mixing mechanism, but was

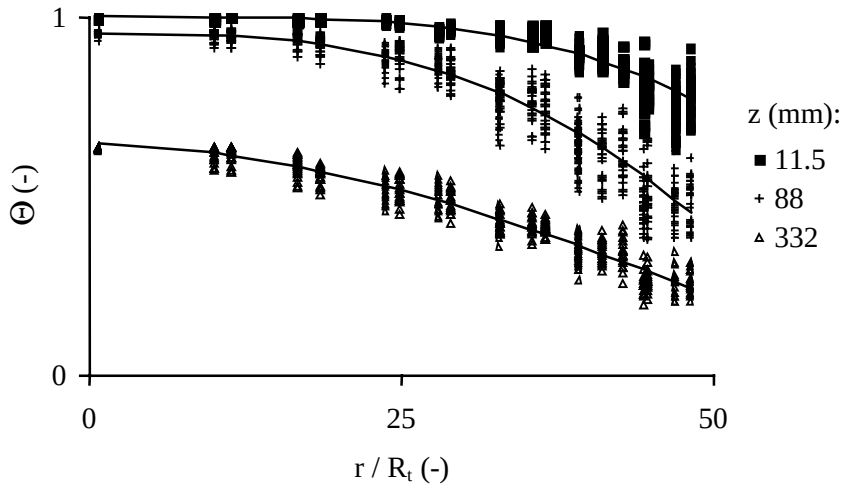

Fig. 4.9 Radial temperature profiles measured at various angular positions at different bed heights (z); R_t=5 cm, d_p=14 mm, Re=475.

developed empirically. For the conditions used in laboratory experiments and in industry, the justification of the use of these laws was given later, in the derivation of the wave model (*Kronberg and Westerterp, 1999*). The heat balance equations and the boundary conditions of this model are:

$$\rho_f c_{p,f}\left(\frac{\partial T}{\partial t}+u\frac{\partial T}{\partial z}\right)+\frac{1}{r}\frac{\partial\left(r j_{h,r}\right)}{\partial r}+\frac{\partial j_{h,z}}{\partial z}=0 \qquad (4.7)$$

$$j_{h,r}+\tau\frac{\partial j_{h,r}}{\partial t}+\tau u\frac{\partial j_{h,r}}{\partial z}=-\lambda_{e,r}\frac{\partial T}{\partial r} \qquad (4.8)$$

$$j_{h,z}+\tau\frac{\partial j_{h,z}}{\partial t}+\tau\left(u+u_a\right)\frac{\partial j_{h,z}}{\partial z}=-\lambda_{e,ax}\frac{\partial T}{\partial z} \qquad (4.9)$$

$$z=0: \qquad T=T_0 \quad ; \quad j_{h,r}=j_{h,r,0} \quad ; \quad j_{h,z}=j_{h,z,0} \qquad (4.10)$$

$$r=R_t: \qquad j_{h,r}=\alpha_w\left(T-T_w\right) \qquad (4.11)$$

in equations 4.7-4.11, τ is the 'relaxation time' and u_a is a parameter characterizing the asymmetry of the fluctuating velocities in axial direction. It is expected that the term u_a is of minor importance to the overall performance of the model and it is therefore neglected here (see *Kronberg et al., 1996*).

At some radial position r, the radial heat flux, caused by movement of the fluid elements, is a function of the fluctuating radial fluid velocity $u_r(\phi)$ and the temperature distribution $T(\phi)$ (see Fig. 4.10):

$$j_r = \frac{1}{2\pi}\int_0^{2\pi} \rho_f c_{p,f} \left(T(\varphi) - \overline{T}\right) u_r(\varphi)\, d\varphi \qquad (4.12)$$

An exact expression of (4.12) in terms of the average temperature $\overline{T}$ is not available, since the temperature- and velocity profiles are unknown. If T_1 and T_2 are the average temperatures of the fluid elements moving in positive and negative radial direction respectively and u_r is the average radial velocity of the fluid elements in positive or negative direction, eq. (4.12) can be simplified to:

$$j_{h,r} = \rho_f c_{p,f} u_r \left(T_1 - T_2\right) \qquad (4.13)$$

Figure 4.9 shows the spread in temperature measured at different angular positions in a 100 mm diameter reactor filled with 24 mm glass spheres. Close to the center of the reactor, near the bottom of the test section, both the axial and the radial temperature gradients are zero. The spread in temperature is negligible here. With increasing radial position, the temperature spread, and therefore the heat flux, increases. The temperature spread depends not only on the

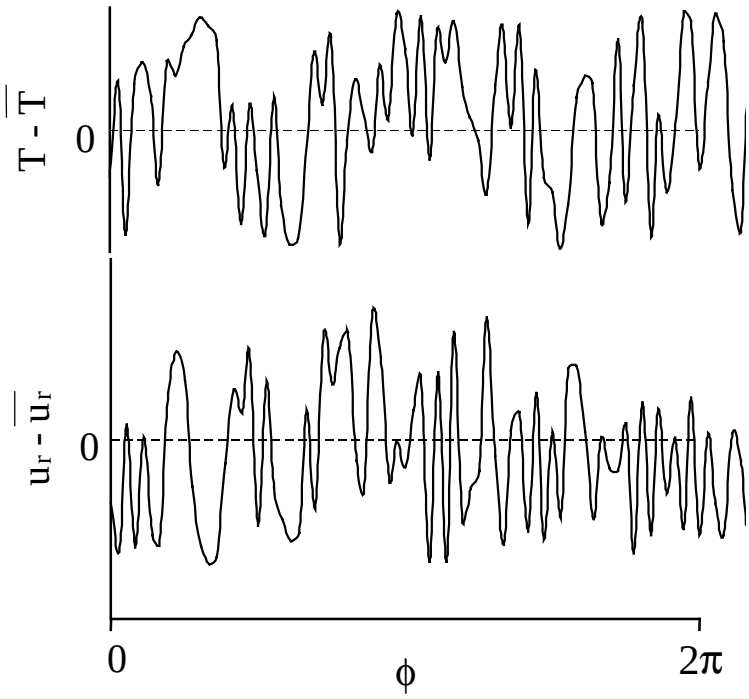

Fig. 4.10 Sketch of the spread in the temperature and the variation of the fluid velocity in angular direction.

radial, but also on the axial temperature gradient. In Fig. 4.9, it can be seen that, for the same radial temperature gradient, the temperature spread at z= 11.5 mm is smaller than at 88 mm.
In the 100 mm diameter reactor, the temperature was measured at 25 angular positions. In the reactor with the smaller diameter, the number of angular positions was 11. At each thermocouple position, the standard deviation was calculated, as well as the difference between the maximum and minimum measured temperatures. The measured temperature difference is approximately 3.3 times the standard deviation, which corresponds with the 90 % interval in case of a Gaussian distribution around the average temperature (see Fig. 4.11). Assuming this distribution, the average of the temperatures higher than the average value, T_1,

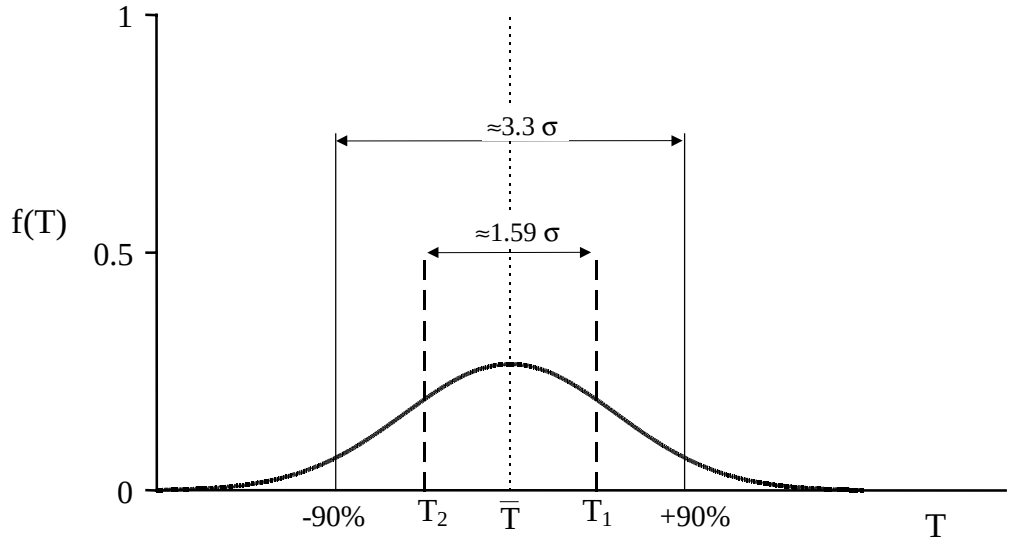

Fig. 4.11 Sketch of the Gaussian distribution of the angular temperature spread. The measured difference between the maximum and minimum temperatures were found to be equal to the limits of the 90% confidence interval. T_1 and T_2 are the average temperatures of the fluid streams with temperatures below or above the average temperature.

minus that of the temperatures lower than the average, T_2, is about 1.6 times the standard deviation σ. It is here assumed that all fluid elements moving in the same direction as that of the radial or axial heat flux have a temperature higher than the average temperature and vice versa. In the wave model of *Kronberg and Westerterp, 1999*, the equations relating the heat flux in axial and radial direction to the average temperature, in case of steady state conditions, are:

$$j_{h,r} + \tau u \frac{\partial j_{h,r}}{\partial z} = -\lambda_{e,r} \frac{\partial T}{\partial r}$$
$$j_{h,z} + \tau u \frac{\partial j_{h,z}}{\partial z} = -\lambda_{e,ax} \frac{\partial T}{\partial z} \qquad (4.14)$$

The heat fluxes are related to the temperature spread as:

$$T_1\text{-}T_2 = \tau\left(\frac{u_r}{\lambda_{e,r}} j_r + \frac{u_z}{\lambda_{e,ax}} j_z\right) = \frac{1}{\rho c_{p,f}}\left(\frac{j_r}{u_r} + \frac{j_z}{u_z}\right) \tag{4.15}$$

and:

$$T_1\text{-}T_2 = 1.6\sigma \tag{4.16}$$

The temperature gradients can be calculated using the reactor model. The derivatives of the heat fluxes can approximately be calculated from:

$$\frac{\partial j_{h,r}}{\partial z} \approx -\lambda_{e,r}\frac{\partial^2 T}{\partial z \partial r} \quad ; \quad \frac{\partial j_{h,z}}{\partial z} \approx -\lambda_{e,ax}\frac{\partial^2 T}{\partial z^2} \tag{4.17}$$

In case of convection-dominated dispersion, Kronberg and Westerterp proposed the following values of the relaxation time and the fluctuating fluid velocities:

$$u_r \approx \frac{u}{3}, \quad u_z \approx \sqrt{5}\frac{u}{3}, \quad \tau \approx \frac{9}{Pe_{h,r}}\frac{d_p^v}{u} \tag{4.18}$$

The above values were obtained from analysis of tracer profiles in a two-dimensional packed bed. In this work, the values of u_r and u_z were calculated from the measured heat fluxes and temperature spread.

De Wasch and Froment, 1972 stated that the temperature oscillations decreased when the temperature fields were not measured directly over the packing, but at a distance of approximately one particle diameter above it. The experiments in this work show that this is not true. The angular temperature spread measured at 5 and 10 mm distance from the packing was the same as that in the temperatures measured directly above it. Therefore, it is not likely that dependence of the heat transfer parameters on the distance between the packing and the thermocouples (see section 4.3.6) is caused by smoothening of the radial temperature profile due to mixing of the fluid after the packing. It seems that, after the bed, the temperature profile changes due to lateral displacement of the fluid. This redistribution of the fluid occurs very rapidly, since the effective viscosity of the fluid is many times larger than its molecular viscosity (*Dil'man and Kronberg, 1990*).

Fig. 4.12 shows the ratio of the measured standard deviation and the predictions of eqs. (4.15)-(4.17) for different bed heights. Close to z=0, the radial and axial temperature gradients are very small, so that even small errors in the measured standard deviation lead to

very large ratios of the measured and the predicted standard deviation. Therefore, data points for which the sum of the temperature gradients in axial and radial direction is less than 200 K m^{-1} have been omitted.

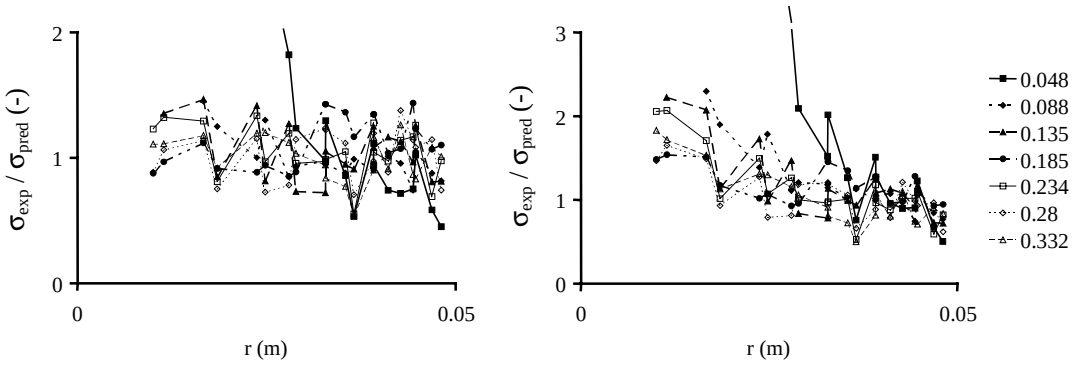

Fig. 4.12 Ratio of the measured and the predicted standard deviation in temperatures measured in angular direction as function of the radial position for different bed heights. Left: u/ u_z= u/ u_r=1.8; right: u/ u_r=2.5, spread due to heat flux in axial direction is neglected. D_t= 100 mm, d_p= 14 mm, Re= 920, $Pe_{h,r}$=7.8, Bi= 3.6.

At the right-hand-side of Fig. 4.12, the temperature spread was calculated only taking into account the radial temperature gradients, i.e. only the first term in eq. (4.15) was used. In this case, the predicted temperature spread is underestimated near the centerline of the reactor. This radial dependence largely disappears if both radial and axial temperature gradients are taken into account, as is shown in the graph at the left-hand side of Fig. 4.12. In this graph, the axial and radial fluctuating axial fluid velocities u_z and u_r are the same and u/1.8 was found to give the best agreement between the measured and the predicted values. This result contradicts the available knowledge. The fluctuation fluid velocities in eq. (4.18) were obtained assuming that the axial dispersion coefficient is five times as large as the radial dispersion coefficient. However, the local axial dispersion coefficient has never been measured. Cross-sectionally averaged values of the axial dispersion coefficient, as used in the one-dimensional model, are to a large extent determined by the radial distribution of the bed porosity and the axial fluid velocity. Equal radial and axial fluctuation velocities are very well plausible in a bed of spheres.

For experiments at different fluid velocities than applied in Fig. 4.12, the same values of the fluctuation velocities were obtained. It is to be expected that at low fluid velocities, the temperature spread will decrease due to the contribution of solid phase heat conduction. In Fig. 4.13, it can be seen that the standard deviation in the temperatures measured in the reactor with a smaller diameter using the same packing is similar. The spread in the data is somewhat larger, which is mainly caused by the smaller number of angular positions from which the standard deviation in the temperatures was calculated.

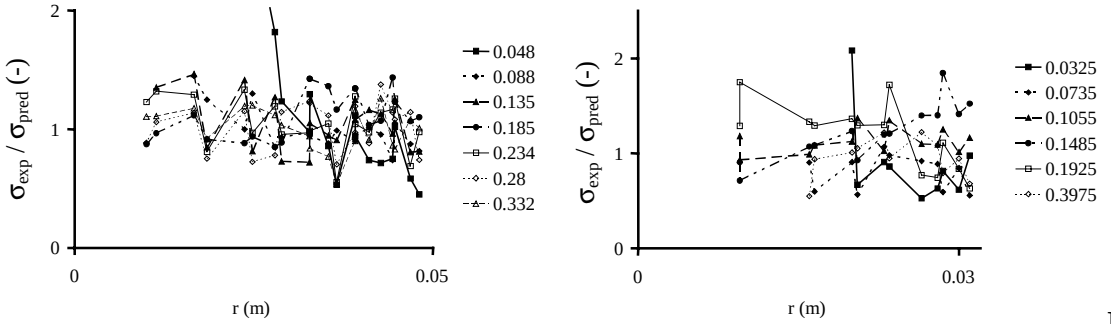

Fig. 4.13 Ratio of the measured and the predicted standard deviation in temperatures for different reactor diameters. d_p=14 mm, u/ u_z= u/ u_r=1.8. Left: D_t= 100 mm, Re=920, $Pe_{h,r}$=7.8, Bi= 3.6; right: D_t= 64 mm, Re=1050, $Pe_{h,r}$=10, Bi=1.5.

Since the number of particles across the beds is rather small, plots of the standard deviation as in the above figures cannot be smooth due to the stochastic nature of the packing. Removal of one layer of particles, for instance, will change the orientation of the thermocouples towards the particles at the top of the bed. After that, the local temperature spread may change.

Fig. 4.14 shows the temperature spread measured above a packing of the catalyst cylinders. The volume-equivalent particle diameter, d_p^v is used as characteristic size. The fluctuation velocities calculated from the measured standard deviations are smaller than in the case of spheres (u/u_r= u/u_z =3.1 instead of 1.8). The fluctuation velocities in the catalyst packing are 1.7 times smaller than in the packings of glass spheres. This difference can be explained by the formation of clusters of particles. Such clustering, i.e. particles lining-up in parallel, has been observed when filling a glass tube with the catalyst.

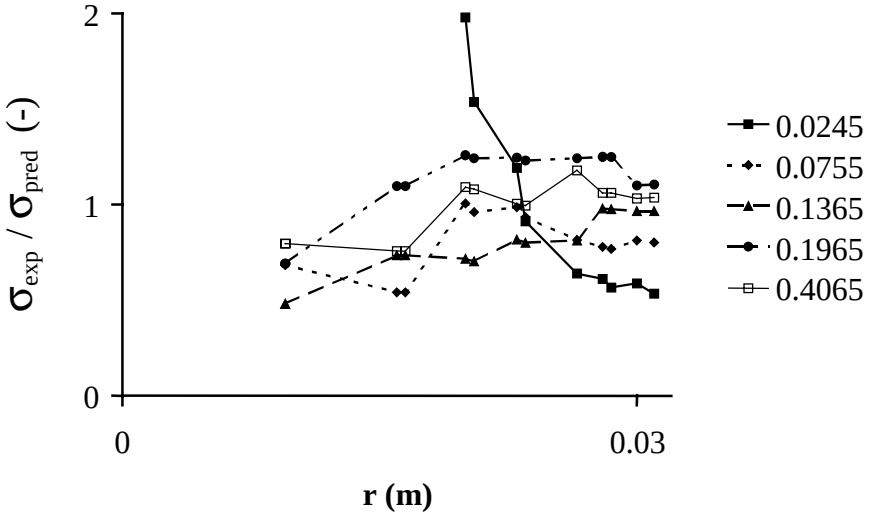

Fig. 4.14 Ratio of the measured and the predicted standard deviation in temperatures measured over a packing of catalyst cylinders. d_p^e= 8 mm, u/ u_z= u/ u_r=3.1. D_t= 64 mm, Re=500, $Pe_{h,r}$=6.5, Bi=3.1.

4.3.5 Meaning of the wall heat transfer coefficient

The measured temperature spread can be used to distinguish between the temperature jump at the wall that is caused by a true film resistance and the jump in the average temperature that is caused by the averaging of the temperature of fluid elements coming from and going to the wall (see Fig. 4.15):

$$\alpha_w = \left(\frac{1}{\alpha_{bed}} + \frac{1}{\alpha_{film}} \right)^{-1} \tag{4.19}$$

In eq. (4.19), $1/\alpha_{bed}$ is the apparent resistance due to mixing of the fluid elements and α_{film} is the film resistance to heat transfer. α_w is the overall heat transfer coefficient that is used in the boundary condition of the standard dispersion model (see Chapter 1) and the wave model. In case of cooling of the fluid, the temperature of the fluid film near the wall can never be higher than the minimum measured temperature T_2. This temperature can be taken directly from the available experimental data, or can be calculated from:

$$T_2 = \overline{T}_{r=R_t} - 1.65\sigma \tag{4.20}$$

with:

$$\overline{T}_{r=R_t} = \frac{T_1 + T_2}{2} \tag{4.21}$$

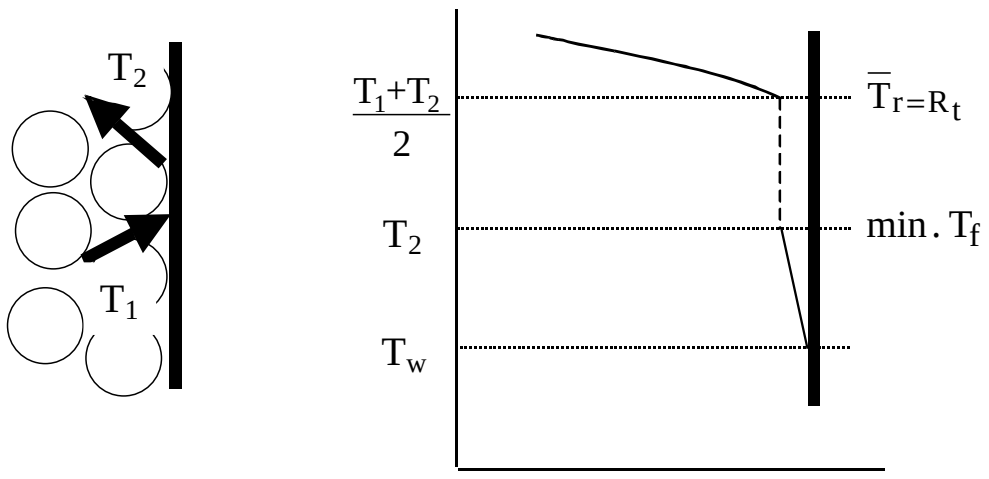

Fig. 4.15 Temperature jump near the wall caused by a true film resistance and by averaging of temperatures of fluid elements with different radial velocities. T_2=min. T_f is the minimum fluid temperature that is measured close to the reactor wall.

In eq. (4.20), the standard deviation is multiplied by 1.65, which is the ratio of the temperature spread and the standard deviation (see Fig. 4.11). Equation (4.20) agrees very well with the minimum temperatures that were measured by the thermocouples closest to the reactor wall.

The apparent heat transfer resistance caused by the temperature spread is (*Kronberg and Westerterp, 1999*):

$$\alpha_{bed} = \rho_f c_{p,f} u_r \tag{4.22}$$

In eq. (4.22), the contribution of the axial heat dispersion flux to the temperature spread is neglected. This is allowed if α_{bed} is calculated from radial temperature profiles measured far from the inlet, which was the case here.

Two different approaches were used to calculate α_{film}. From eqs (4.19) and (4.22), it follows that:

$$\alpha_{film}^{(1)} = \left(\frac{1}{\alpha_w} - \frac{1}{\rho_f c_{p,f} u_r} \right)^{-1} \tag{4.23}$$

α_{film} can also be calculated directly from the difference between the average and the minimum temperatures measured by the thermocouples closest to the reactor wall:

$$\alpha_{film}^{(2)} = \left(\frac{1}{\alpha_w} - \frac{\overline{T}_{r=R_t} - T_{min,\, r=R_t}}{j_r} \right)^{-1} \tag{4.24}$$

Fig. 4.16 is a parity plot of $\alpha_{film}^{(1)}$ and $\alpha_{film}^{(2)}$ for all experiments. The values of $\alpha_{film}^{(1)}$ and $\alpha_{film}^{(2)}$ shown in Fig. 4.16 are the averages of the values calculated from the radial temperature profiles measured after a distance of 20 cm from the inlet of the (first) test section. The fluctuation velocities u_r used in eq. (4.23) are the same as those calculated from the temperature spread measured above the packing (u/u_r= 1.8 for spheres and 3.1 for cylinders). For the packings of spheres, the agreement between $\alpha_{film}^{(1)}$ and $\alpha_{film}^{(2)}$ is excellent, which is an indication for the consistency of the theory and the experimental data. As illustration, the minimum near the wall, predicted using eq. (4.23), and the minimum measured temperature near the wall are shown in Fig. 4.17 for different axial positions. Closer to the inlet, the value of $\alpha^{(2)}$ decreased due to neglecting of the axial heat flux term in the derivation of eq. (4.22).

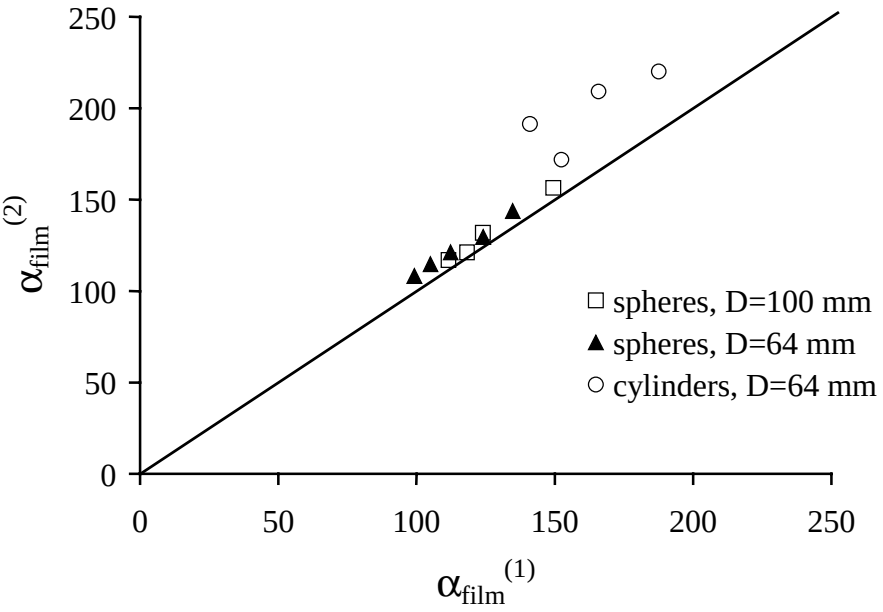

Fig. 4.16 Parity plot of $\alpha_{film}^{(1)}$ and $\alpha_{film}^{(2)}$ according to eqs. (4.23) and (4.24). Each point represents the average of the values obtained from the radial temperature profiles measured after a distance of 20 cm from the inlet of the test sections.

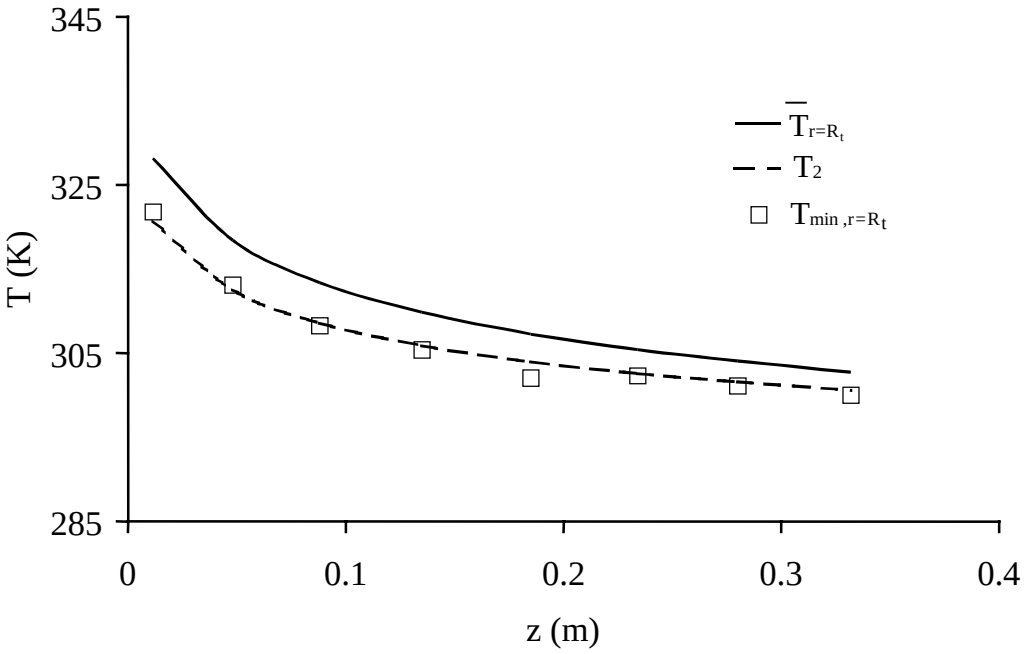

Fig. 4.17 Comparison of the minimum fluid temperature predicted by eq. (4.23), T_2, and the minimum measured fluid temperature, $T_{min,r=Rt}$, at different axial positions. The temperature profiles were measured over a packing of spheres at Re=660.

For the packing of catalyst cylinders, $\alpha_{film}^{(2)}$ is higher than $\alpha_{film}^{(1)}$, which is caused by the large uncertainty in u_r. Equations (4.23) and (4.24) give the same value if u_r=u/4 rather than u/3.1.

Fig. 4.18 shows the fraction of the total resistance to heat transfer at the wall that is located in the fluid film as function of the Reynolds number.

It is important to notice that the values of α_{bed} measured for the glass spheres in both setups is exactly the same. The difference in α_w, as was shown in Fig. 4.6, seems to be caused by a difference in the heat transfer resistance over the fluid film, α_{film}, rather than by a difference in the packing structure near the wall. The higher value of α_w, and therefore α_{film}, measured in the 100 mm diameter reactor can be explained by the fact that the wall of this reactor is not as smooth as that of the 64 mm diameter reactor.

Literature correlations for the wall heat transfer coefficient are far less consistent than those for the effective radial thermal conductivity. In Fig. 4.18, it is shown that, at Re>200, the apparent resistance to heat transfer is dominated by the resistance located in the fluid film near the wall. Though the influence of wall-roughness is a well-known issue in literature on heat transfer in heat exchangers, no attention has been paid to it by investigators doing research on tubular reactors. The neglecting of this influence could very well be responsible for part of the discrepancy between the available correlations.

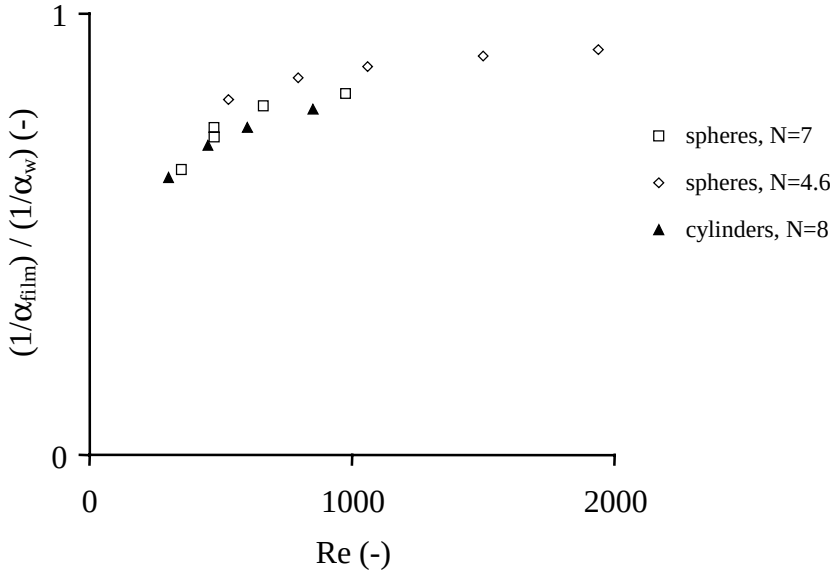

Fig. 4.18 Fluid-film resistance as fraction of the total apparent resistance to heat transfer at the wall according to (4.19) and (4.22).

Models for wall-cooled tubular reactors can be divided into two types: models that assume a temperature jump at the wall (α_w models) and models that assume that the fluid temperature decreases in radial direction till it reaches the temperature of the wall. A recent model of the latter type is the $\Lambda(r)$ model of Winterberg and Tsotsas (*Winterberg et al., 2000 a and b*), in

which the effective radial thermal conductivity strongly decreases near the reactor wall, where the axial fluid velocity is higher. The temperature profiles calculated by the two types of models are different only near the reactor wall. In the Λ(r) model, the region near the wall over which the fluid temperature sharply decreases to become equal to the wall temperature is significant compared to the particle size. This will affect the reaction rate near the wall, where the calculation of the temperature of the catalyst particles is not unambiguous. Particles here are exposed to strong radial gradients in temperature and axial fluid velocity.
The temperature profiles measured in this work do not support the continuum models. Near the wall, the minimum fluid temperature never approaches the wall temperature, but always is always closer to the bed temperature.

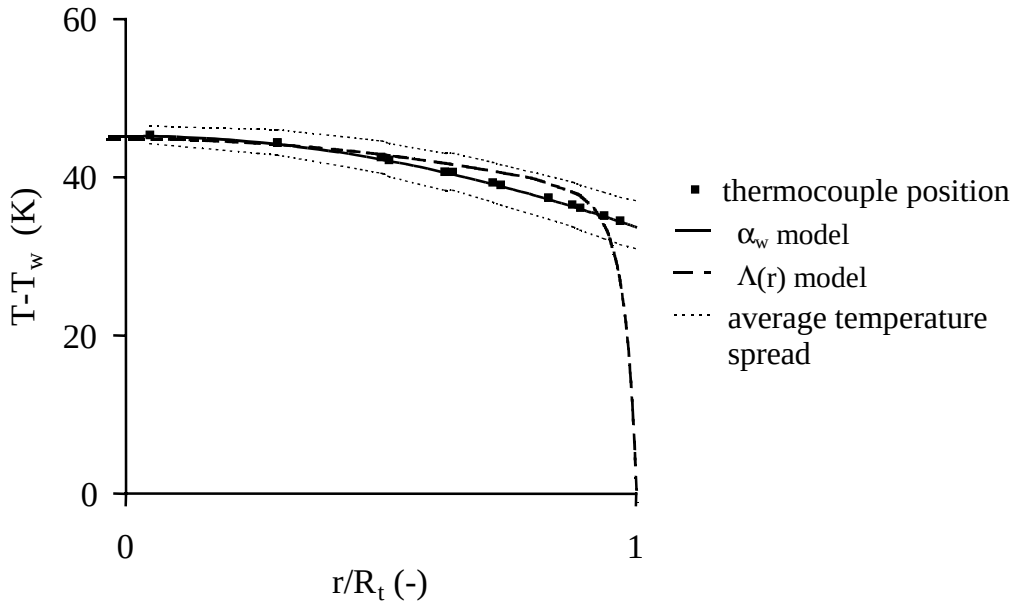

Fig. 19 Radial temperature profiles according to α_w and Λ(r) model with the same radial heat flux at the wall. Temperature spread calculated according to (4.15) and (4.20)

Figure 19 shows radial temperature profiles calculated according to the α_w and the Λ(r) model, in which the recommended values are used for the thermal conductivity and the radial distribution of the axial fluid velocity (*Winterberg et al. 2000a*). The effective heat transfer parameters in the α_w model were optimized to the give the closest match between both profiles, provided that the heat flux at r= R_t is the same.
Near the wall, the temperature predicted by the Λ(r) model is significantly lower than the minimum temperature of the fluid film, which is calculated according to eqs. (4.15) and (4.20).
When optimizing the parameters in the Λ(r) model to our experimental data, the region in which the steep temperature decrease occurs becomes narrower than according to the original

values of the model parameters. The original difference between both models disappears, except for the assumption of a radial distribution of the axial fluid velocity. Such velocity distribution has no effect on the 'goodness of fit' if no chemical reaction occurs and was therefore neglected here. The average reaction rate will be underestimated by the Λ(r) model, since the temperature of the relatively large fraction of catalyst, present near the wall, is too low.

4.3.6 Dependence of observed heat transfer parameters on the distance between the packing and the thermocouples

To study the reliability of the heat transfer parameters obtained from temperature profiles that are measured above a packed bed in a cold-flow setup, experiments were performed at different distances between the packing and the thermocouples. In Figure 20, it is shown that

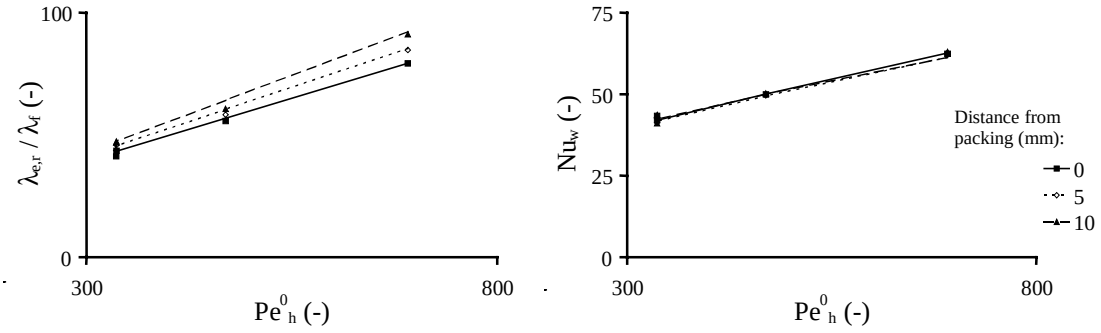

Fig. 20 Dependence of effective radial thermal conductivity and wall Nusselt number on the distance between the packing and the thermocouples. Dots: α_w and $\lambda_{e,r}$ fitted to separate experiments at different flow rates; lines: correlations of $\lambda_{e,r}$ and α_w (eqs (4.2) and (4.3)) optimized to all experiments at different flow rates; D_t=100 mm; d_p= 14 mm.

the effective radial thermal conductivity is a strong function of the distance between the thermocouples and the packing, whereas the wall heat transfer coefficient is hardly affected. The heat transfer parameters in this figure were calculated using radial temperature profiles that were measured at different axial positions. As discussed in section 4.3.4, the angular temperature spread did not depend on the distance between the bed and the temperature probe if this distance was less than 10 mm. If the change of the radial temperature profiles would only be due to movement of fluid elements after they leave the packing, the temperature profiles would change over the entire radius, causing an increase of the observed $\lambda_{e,r}$ and a decrease in the wall heat transfer coefficient α_w. The fact that the temperature at the wall (see Fig. 4.21) and α_w remain constant can be explained by the redistribution of the fluid flow over the cross section of the tube.

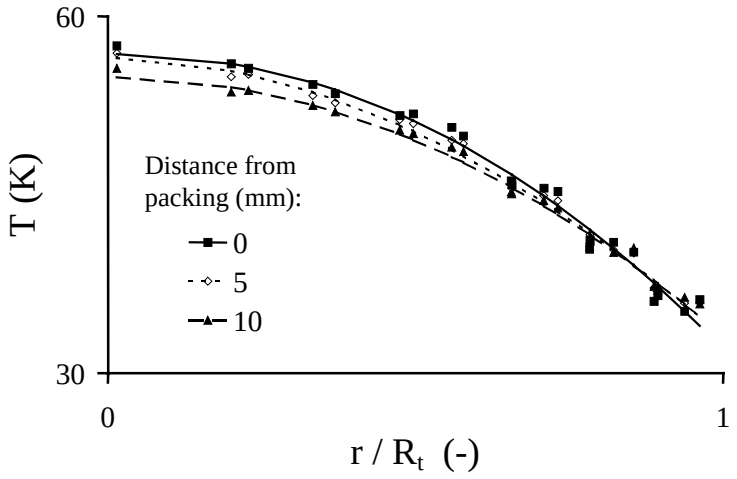

Fig. 4.21 Change of the radial temperature profile measured at 0.23 m from the bottom of the test section with increasing distance between the bed and the thermocouples. D=100 mm, d_p= 14 mm, Re= 450.

4.3.7 Complex developing temperature profiles

Radial temperature profiles with a different shape than those during 'simple' cooling experiments could be measured by increasing the wall temperature of the second test section, after a convex profile had been established in the first test section. One set of radial temperature profiles was measured using the temperature probe containing the bare thermocouples and three others using the probe containing the brass rings. Figure 4.22 shows

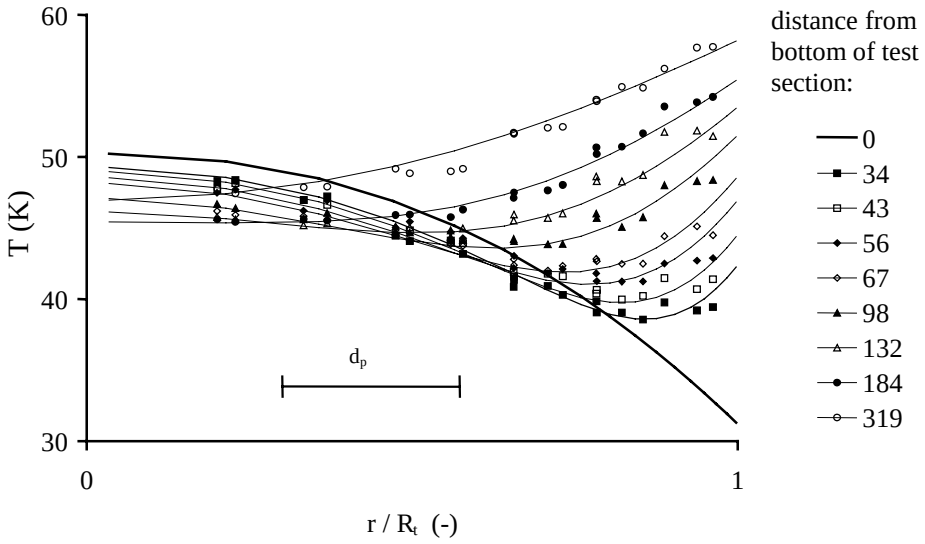

Fig. 4.22 Measured and calculated radial temperature profiles in the second test section with an increased wall temperature. Re= 1100, Dt= 100 mm, d_p= 14 mm. $Pe_{h,r}$= 10.8, Bi=3.4, no axial heat conduction.

the measured and the calculated temperature profiles in the second test section, were the wall temperature was increased from 24 to 65 °C. The points in Fig. 4.22 are the average of the temperatures measured at 15 angular positions. Heat conduction in axial direction was neglected when calculating the radial temperature profiles. Although the axial temperature gradients are quite large and the temperature profile changes shape over a distance less than a particle diameter, the 'simple' two-dimensional model without heat dispersion in axial direction still performs satisfactory. When using axial heat dispersion, assuming $Pe_{h,ax}= 2$, the description of the temperature profile shown in Fig. 4.22 does not improve.

4.4 Conclusions

Heat transport parameters have been measured for different packed beds at atmospheric pressure. The temperature spread in angular direction was measured in detail over packings of 14 mm glass spheres in reactors with inner diameters of 100 and 64 mm. The temperature spread measured at various axial and radial positions was found to depend on the radial and axial heat fluxes, as was assumed in the derivation of the wave model, if the axial and radial fluctuation velocities were the same and were equal to 0.56 times the superficial fluid velocity. The fluctuation velocities derived from the temperature spread that was measured using a packed bed of long catalyst cylinders (11.2 x 5.5 mm) were smaller. This was attributed to the formation of clusters of particles.

On the basis of the measured temperature spread in angular direction, the apparent resistance to heat transfer at the wall could be divided into a resistance, which is due to mixing of the fluid inside the packing near the wall, and a true film resistance. It was shown that this film resistance accounts for over 80% of the total resistance to heat transfer at the wall at Re>500. The difference between the wall heat transfer coefficients measured for packings of the 14 mm glass spheres in different columns could not be attributed to a radial distribution of the axial fluid velocity. The difference between the wall heat transfer coefficients was explained on the basis of a difference in wall-roughness. The wall of the reactor with a diameter of 100 mm was rougher than that of the reactor with the smaller diameter, causing the wall heat transfer coefficient to be higher. Similarly, the wall heat transfer coefficient obtained for packings of the catalyst cylinders in the 64 mm reactor was smaller than the value calculated from the temperature profiles in the pilot-scale wall-cooled tubular reactor, which had a very rough inner wall surface.

Though the influence of wall-roughness is a well-known issue in literature on heat transfer in heat exchangers, it has not been paid any attention to by investigators doing research on tubular reactors. The work presented in this chapter shows that this parameter may be of significant importance and that neglecting of the wall roughness contributes to the discrepancy between correlations for the wall heat transfer coefficient.

Notation

c_p	heat capacity	J kg^{-1} K^{-1}
D	reactor diameter	m
$j_{h,z}$, $j_{h,r}$	heat flux in axial and radial direction	W m^{-2}
n_Θ	number of measured temperatures	-
r	radial coordinate	m
R_t	bed radius	m
T	temperature	K or °C
u	superficial fluid velocity	m s^{-1}
u_z, u_r	axial and radial component of superficial fluid velocity	m s^{-1}
z	axial coordinate	m

Greek

α_w	wall heat transfer coefficient	W m^{-2} K^{-1}
α_{bed}, α_{film}	bed- and wall contribution to α_w	W m^{-2} K^{-1}
δ	thickness of fluid film at wall	m
ε	porosity	-
λ_r^0	thermal cond. of bed in case of stagnant fluid	W m^{-1} K^{-1}
λ_r^f	fluid contribution to radial thermal conductivity	W m^{-1} K^{-1}
$\lambda_{e,r}$	effective radial thermal conductivity	W m^{-1} K^{-1}
ρ	density	kg m^{-3}
σ	standard deviation in temperature	K
τ	relaxation time	s

Dimensionless groups

Nu_w	wall Nusselt number	$\frac{\alpha_w d_p^v}{\lambda_f}$
Pe_h^0	fluid Peclet number	$\frac{u_0 \left(\rho c_p\right)_f d_p^e}{\lambda_f} = Re\ Pr$
$Pe_{h,r}$	Peclet number for radial heat transfer	$\frac{u_0 \rho_f c_{p,f} d_p^v}{\lambda_{e,r}}$
$Pe_{h,r}^\infty$	Peclet number at fully developed turb. flow	-
Pr	fluid Prandtl number	$\frac{\eta_f c_p}{\lambda_f}$
Re	particle Reynolds number	$\frac{u_0 \rho_f d_p^v}{\eta_f}$

y	dimensionless radial coordinate	$\frac{r}{R_t}$
Θ	dimensionless temperature	$\frac{T - T_w}{T_0 - T_w}$

Super- and subscripts

ax	axial direction
cool	cooling fluid
f	fluid
h	heat
r	radial direction
s	solid

Chapter 5

Improved one-dimensional reactor model of a wall-cooled tubular reactor

ABSTRACT

The major drawback of one-dimensional models of wall-cooled tubular reactors, which are often used if the computational effort should be small, is the fact that the reaction rate is calculated using the radially averaged temperature. The difference between this reaction rate and the radially averaged reaction rate increases with increasing temperature difference over the radius of the reactor and with increasing activation energy of reaction. Improved one-dimensional models, such as the α-model model' (*Hagan, Herskowitz and Pirkles, 1988*), are available, which use an analytical approximation of the radial temperature profile to improve the prediction of the average reaction rate. However, application of these models involves solving of implicit equations. A new model is proposed as alternative to the existing one-dimensional models. This 'δ-model' has the same form as the conventional one-dimensional model and contains only explicit functions. It is demonstrated that, at conditions not too close to runaway, the new model performs better than the well-known αmodel.

5.1 Introduction

For a detailed reactor design, two-dimensional homogeneous or heterogeneous reactor models with or without heat and mass dispersion in direction of fluid flow are generally used. These models provide higher accuracy than one-dimensional models. The major disadvantage of the two-dimensional models is the required computational effort. For that reason, one-dimensional models are frequently applied in studies of reactor dynamics (flowsheeting software), in (kinetics-) parameter optimization and in process control software (*Froment and Bischof, 1979* , *Westerterp et al., 1987*). Generally, radial concentration differences in wall-cooled tubular reactors can be neglected. Since the high rate of heat removal is the main reason for the use of this type of reactor, this is not the case for the radial temperature distribution. In a one-dimensional model, the heat flux to the wall is proportional to the difference between the average temperature over the cross section and the wall, and an overall heat transfer coefficient U. If no heat is produced, the average axial temperature profile can be approximated rather well if the overall heat transfer coefficient is calculated from the effective radial heat transfer parameters $\lambda_{e,r}$ and α_w as:

$$\frac{1}{U}=\frac{1}{\alpha_w}+\frac{2R_t}{\beta\lambda_{e,r}} \qquad (\textit{Crider and Foss, 1965}) \tag{5.1}$$

or:

$$\frac{1}{U}=\frac{1}{\alpha_w}+\frac{R_t}{3\lambda_{e,r}}\frac{Bi+3}{Bi+4} \qquad (\textit{Dixon, 1996}) \tag{5.2}$$

The above approximations are valid if the radial temperature profiles are parabolic. If the temperature profile is flat, which is often the case near the inlet of the reactor, the overall heat transfer coefficient will be underestimated. For this reason, one should be careful to use the above correlations if the length-to-diameter ratio of the reactor is small. The value of β in eq. (5.1) can be derived from the analytical solution of the two-dimensional reactor model (see Chapter 1), which is available in case no reaction occurs:

$$\Theta=2\sum_{n=1}^{\infty}\frac{J_0(A_n y)\exp\left(-A_n^2 x\right)}{A_n J_1(A_n)\left[\left(\frac{A_n^2}{Bi}\right)+1\right]} \tag{5.3}$$

By equating the average temperature obtained from eq. (5.3) to the temperature that is predicted by the one-dimensional model, eq. (5.4) is obtained, from which U or β can be calculated:

$$\overline{\Theta}=4\sum_{n=1}^{\infty}\frac{\exp\left(-A_n^2 x\right)}{A_n^2\left[\left(\frac{A_n^2}{Bi}\right)+1\right]}=\exp\left(-U^* x\right) \quad ; \quad U^*=\frac{\beta Bi}{\beta/2+Bi} \tag{5.4}$$

Here, $\Theta=(T-T_w)/(T_0-T_w)$, $y=r/R_t$ and $x=z/(R_t PE_{h,r})$. A_n (n=1,2,…) are the eigenvalues of :

$$A_n J_1(A_n)=Bi J_0 A_n \tag{5.5}$$

in which J_0 and J_1 are the first and second order Bessel function. Equations (5.4) and (5.5) show that both U and β change along the reactor axis. If the inlet temperature is constant over the radius, the radial temperature gradient at the wall at the inlet is infinite, causing U to be infinite. From here, U decreases to a constant value that is a function of Bi. If chemical reaction occurs, the dependence of U on x and Bi becomes more complicated. In this case, U also depends on the reaction rate. In practice, the used overall heat transfer coefficient is

constant. Average values of β in the range 5.8-8 were proposed instead by *Beek, 1962* and *Crider and Foss, 1965*.
Another point of concern is that, in the one-dimensional models, the reaction rate at the average temperature is assumed equal to the average reaction rate:

$$R\left(\overline{T}\right) = \overline{R\left(T\right)} \tag{5.6}$$

Hagan, Herskowitz and Pirkles, 1988 proposed a significant modification of the conventional one-dimensional model to overcome this drawback. In their new model, called α-model, the influence of the radial temperature profiles is accounted for by correction of the effective heat transfer coefficient. The α-model produces very good results in many situations at which the conventional models fail. However, it is not convenient for use and it fails if no heat generation occurs.
In this chapter, a new, improved, pseudo-homogeneous one-dimensional model will be proposed, which does take into account the radial temperature and concentration distribution. This model will be compared to the standard one- and two-dimensional models, as well as to the α-model. The improved model uses different correction factors in the heat and mass balance, which can be calculated from the known activation energy and wall Biot number $Bi=\alpha_w R_t/\lambda_{e,r}$. Solving of the heat and mass balances therefore requires the same effort as when applying the conventional one-dimensional model and can be performed, for instance, using spreadsheet software.

5.2 Model equations

Both the α model and the improved one-dimensional model are based on the two-dimensional homogeneous plug flow model. Heat conduction in axial direction is neglected, as well as the differences in concentration and temperature between the fluid and the solid phase. Heat and mass dispersion in axial direction can easily be added to either model. However, the effect of these terms on the calculated temperature and concentration profiles is usually very small and much less than the difference between the 'exact' two-dimensional model and the one-dimensional models.
The heat and mass balances of the one-dimensional model have the following general form:

$$(\varepsilon\rho_f c_{p,f} + (1-\varepsilon)\rho_s c_{p,s})\frac{\partial\overline{T}}{\partial t} = -u\rho_f c_{p,f}\frac{\partial\overline{T}}{\partial z} - \frac{2U}{R_t}\left(\overline{T} - T_w\right) + \sum_{i=1}^{n}\left(-\Delta H_r^i\right)R_i\left(\overline{\mathbf{c}},\overline{T}\right) \tag{5.7}$$

$$\varepsilon\frac{\partial\overline{c^j}}{\partial t}=-u\frac{\partial\overline{c^j}}{\partial z}-\sum_{i=1}^{n}\nu_i^j\eta_i R_i\left(\overline{\mathbf{c}},\overline{T}\right) \tag{5.8}$$

The left-hand-side of eqs. (5.7) and (5.8) account for the accumulation of heat and mass. The first terms at the right-hand-side account for convective transport of heat and mass. The heat flux from the bed to the wall is proportional to the product of the overall heat transfer coefficient U, the specific wall area $2/R_t$ and the difference between the average bed temperature $\overline{T}$ and the temperature of the wall. The total heat production rate is the sum of the heat of reaction per mole of key component, multiplied by the reaction rate. Similarly, the production rate of component j is the sum of the production rates per reaction, multiplied by the stoichiometric coefficient ν_i^j. In the remainder of this chapter, steady-state operation will be assumed, so that the left hand side of eqs. (5.7) and (5.8) is zero. This does not mean, of course, that the effect of the difference between the models does not affect the models' response to perturbations, which can be more pronounced than the difference between steady-state predictions.

A single-reaction of order n will be considered first. The heat and mass balance can be written in the following dimensionless form:

$$\frac{\partial\overline{\Theta}}{\partial y}=-U^*\left(\overline{\Theta}-\Theta_w\right)+F_H\Lambda C^n e^{\frac{\gamma_0\overline{\Theta}\Delta\Theta_{ad}}{1+\overline{\Theta}\Delta\Theta_{ad}}} \tag{5.9}$$

$$\frac{\partial C}{\partial y}=-F_M\Lambda C^n e^{\frac{\gamma_0\overline{\Theta}\Delta\Theta_{ad}}{1+\overline{\Theta}\Delta\Theta_{ad}}} \tag{5.10}$$

with:

$$PE_{h,r}=\frac{u\rho_f c_{p,f}R_t}{\lambda_{e,r}} \qquad y=\frac{z}{R_t}PE_{h,r}^{-1} \qquad \overline{\Theta}=\frac{\overline{T}-T_0}{\Delta T_{ad}} \qquad C=\frac{c}{c_0}$$

$$\gamma_0=\frac{E_a}{RT_0} \qquad \Delta\Theta_{ad}=\frac{\Delta T_{ad}}{T_0} \tag{5.11}$$

$$\Lambda=PE_{h,r}\frac{R_t}{uc_0}(1-\varepsilon)\rho_s k_0 c_0^n e^{-\gamma_0} \tag{5.12}$$

When using eq. (5.2) for the overall heat transfer coefficient of U, then:

$$U^*=\frac{2U}{u\rho_f c_{p,f}}PE_{h,r}=\frac{6Bi(Bi+4)}{Bi^2+6Bi+12} \tag{5.13}$$

$PE_{h,r}$ is the Peclet number for radial heat transfer used in the two-dimensional reactor model, which is made dimensionless using the reactor radius as characteristic length. The dimensionless temperature $\overline{\Theta}$ is the difference between the local temperature and the inlet temperature T_0, divided by the adiabatic temperature rise ΔT_{ad}. The reaction rate is made dimensionless, using the reaction rate at inlet conditions, incorporated in Λ in (5.12). Since heat and mass dispersion in axial direction have been neglected, the boundary conditions at y=0 are $\overline{\Theta}$=0 and C=1.

The terms F_H and F_M in eqs. (5.9) and (5.10) appear in the one-dimensional model as factors correcting for the difference between the reaction rate at the average temperature and the average reaction rate. F_M and F_H could be different if the occurrence of chemical reaction influences the rate of heat removal. In the conventional model, $F_H=F_M=1$. In the new one-dimensional model, both correction factors depend on the activation energy and the wall Biot number.

Reactor models are often compared using bifurcation diagrams, in which the temperature at the hot spot of the reactor is shown as function of the concentrations. At the hot spot, the axial derivative of the radial average temperature is zero. This means that the convection term can be omitted from the heat balance, so that the heat removal rate is equal to the heat production rate:

$$F_H \Lambda C^n e^{\frac{\gamma_0 \overline{\Theta} \Delta\Theta_{ad}}{1+\overline{\Theta}\Delta\Theta_{ad}}} = U^* \left(\overline{\Theta} - \Theta_w \right) \tag{5.14}$$

For convenience, a new dimensionless reaction rate constant Λ^* is introduced, which is calculated using the average radial concentration at the hot spot, so that:

$$F_H \Lambda^* e^{\frac{\gamma_0 \overline{\Theta} \Delta\Theta_{ad}}{1+\overline{\Theta}\Delta\Theta_{ad}}} = U^* \left(\overline{\Theta} - \Theta_w \right) \tag{5.15}$$

For each Λ^*, Eq. (5.14) has two solutions, as is shown in Fig. 5.1. The lower line in this graph is a stable solution, meaning that after a temperature excursion, the system will return to this value. Around this point, the heat removal rate increases faster with temperature than the heat production rate.

The second solution of eq. (5.15) is an unstable solution. At the upper line in the figure, heat production and heat removal are at equilibrium. Below the line, heat removal prevails, causing the system to travel to the stable solution. Above the line, heat production prevails, so that the system temperature will continue to increase. The latter corresponds to an infinite slope when plotting the temperature as function of the axial coordinate and is generally referred to as ‘runaway’.

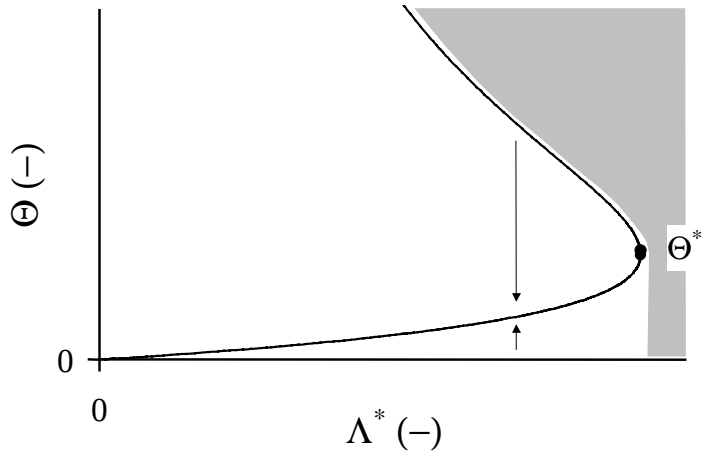

Fig. 5.1 Temperature at the hot spot as function of the dimensionless reaction rate constant. Runaway conditions shown as shaded area.

Above a certain maximum value of Λ^*, eq. (5.15) has no solution. The heat production rate exceeds the rate of heat removal, so that the system is always at runaway conditions. *Hagan, Herskowitz and Pirkles, 1988*, in their publication of the α-model, refer to the temperatures in the runaway region as 'unreasonably large temperatures' and limit the application of their model to temperatures lower than Θ^*. This is not necessarily true. Runaway may lead to reactor damage only if it causes temperatures at which either the catalyst or the reactor construction is damaged. In case of complete, catalytic combustion, for instance, the critical temperature Θ^* may well be exceeded without having an undesired situation.

5.3 α-model

The α-model was derived using an approximate expression of the radial temperature distribution at the hot spot of the reactor. This solution is available if heat transport by convection can be neglected and if the reaction rate is approximated by:

$$R(c,T) = k_0 e^{\frac{-E_a}{RT}} \approx k_0 e^{A(T-\bar{T})+B(T-\bar{T})^2} \qquad (5.16)$$

Hagan, Herskowitz and Pirkles, 1988 started their approximation by stating that the convection term can be neglected far from the inlet, where axial temperature and concentration gradients are generally small. This statement, however, is not necessarily correct. Far from the inlet, the reaction rate also decreases. Convective transport may be neglected only at the hot spot of the reactor. This explains why the α-model is well suited for the description of the radial temperature distribution at this position in the reactor. In the first

paper on the α-model by *Hagan, Herskowitz and Pirkles, 1988*, some inconsistencies were found. The authors mention a value of the ratio between the Peclet numbers for radial heat and mass transfer, whereas the one-dimensional model was derived assuming that the radial concentration distribution is uniform. In the bifurcation diagrams presented in the article, the line showing the average temperature at the hot spot as function of the dimensionless reaction rate does not return to the vertical axis as in Fig. 5.1, but continues to increase.

A distinction is made between an average temperature which is characteristic for heat transfer, and a characteristic temperature, T_r, for the radial average reaction rate ($R\left(\overline{T_r}\right) \equiv \overline{R(T)}$). The reaction- average temperature is used in the heat balance equations:

$$\frac{\partial \overline{\Theta}}{\partial y} = \Lambda C^n e^{\frac{\gamma_0 \overline{\Theta} \Delta\Theta_{ad}}{1+\overline{\Theta}\Delta\Theta_{ad}}} - 8\alpha \frac{\left(1+\overline{\Theta}\Delta\Theta_{ad}\right)^2}{\left(\gamma_0 \overline{\Theta} \Delta\Theta_{ad}\right)} \tag{5.17}$$

The mass balance of the α model is identical to that of the standard one-dimensional model (eq. (5.10), F_M=1). The difference between the reaction-average temperature and the true average temperature increases with increasing activation energy and temperature difference over the radius. The value of α is therefore a function of these parameters and is determined by:

$$\gamma_0 \Delta\Theta_{ad} \frac{\overline{\Theta}-\Theta_w}{\left(1+\overline{\Theta}\Delta\Theta_{ad}\right)^2} = \frac{4\alpha}{Bi} - \ln(1-\alpha) - \frac{\left(1+\overline{\Theta}\Delta\Theta_{ad}\right)}{3\gamma_0} \ln^2(1-\alpha) \tag{5.18}$$

In order to fulfill the criterion $\overline{\Theta} < \Theta^*$ imposed by the authors, α should be smaller than 0.5.

An important drawback of the α-model is the fact that the overall heat transfer coefficient, which is the last term at the right-hand side of eq. (5.17), contains the dimensionless activation energy. This means that the overall heat transfer coefficient cannot be calculated if no reaction occurs.

5.4 Improved one-dimensional model: δ-model

Since, generally, $\overline{\Theta}\Delta\Theta_{ad} << 1$, the reaction rate expression can be simplified using the Frank-Kamenetskii approximation:

$$\Lambda C^n e^{\frac{\gamma_0 \overline{\Theta}\Delta\Theta_{ad}}{1+\overline{\Theta}\Delta\Theta_{ad}}} \approx \Lambda C^n e^{\gamma_0 \overline{\Theta}\Delta\Theta_{ad}} \tag{5.19}$$

The radial temperature and concentration profiles are obtained from the two-dimensional balance equations by the method of successive approximation, starting from flat temperature and concentration distributions. After the first step, a parabolically shaped temperature profile is obtained:

$$\Theta(y) = \overline{\Theta} + \frac{Bi\left(\overline{\Theta}-\Theta_w\right)}{Bi+4}\left(1-2y^2\right), \tag{5.20}$$

whereas the radial concentration profile remains flat. Eq. (5.20) is already a fair approximation of the exact solution of the heat balance over the radius at the hot spot:

$$\begin{aligned} &\frac{\partial\Theta}{\partial x} = \frac{1}{y}\frac{\partial}{\partial y}\left(y\frac{\partial\Theta}{\partial y}\right) + \Lambda C^n e^{\gamma_0 \overline{\Theta}\Delta\Theta_{ad}} = 0 \\ &y = 0: \quad \frac{\partial\Theta}{\partial y} = 0 \qquad\qquad y=1: \quad -\frac{\partial\Theta}{\partial y} = Bi\left(\Theta-\Theta_w\right) \end{aligned} \tag{5.21}$$

Here y is the dimensionless radial coordinate r/R_t. From this temperature distribution, the reaction rate as a function of the radial position follows, assuming a constant reactant concentration. After substitution of this reaction rate into the two-dimensional heat balance, an improved approximation of the radial temperature profile is obtained. This procedure can be repeated once more without causing the analytical solution to become too complicated. This second solution predicts the difference between the average reaction rate and the reaction rate at the average temperature, which is used to calculate the correction factors F_H and F_M in the heat and mass balance of the one-dimensional model (eqs. (5.9) and (5.10)). In Appendix H, the derivation of the model is explained in more detail.
The obtained correction factors F_M and F_H are:

$$F_M = \frac{\sinh(\delta)}{\delta} \tag{5.22}$$

$$F_H = 3\frac{Bi+4}{12+6Bi+Bi^2}\left[\frac{\sinh(\delta)}{\delta}+\frac{Bi}{4\delta}\left(e^{\delta}-\frac{\sinh(\delta)}{\delta}\right)\right] \tag{5.23}$$

where:

$$\delta=\gamma_0\frac{Bi}{4+Bi}\frac{\overline{\Theta}\Delta\Theta_{ad}}{\left(1+\overline{\Theta}\Delta\Theta_{ad}\right)^2} \tag{5.24}$$

It is important to note that the correction factors do not account for the influence of radial concentration differences, but are solely based on the effect of the non-uniform radial temperature distribution on the average reaction rate over the radius. For convenience, the improved one-dimensional model will be further referred to as the 'δ-model'.

5.5 Model comparison

In Fig. 5.2, the different one-dimensional models are compared to the solution of the two-dimensional model. Shown here is the dimensionless temperature at the hot spot, which is most sensitive to the overall heat transfer coefficient. Fig. 5.3 shows the axial temperature profiles for the different models at conditions similar to those used in the experimental investigation of the effective heat transfer parameters, which are described in Chapter 3.

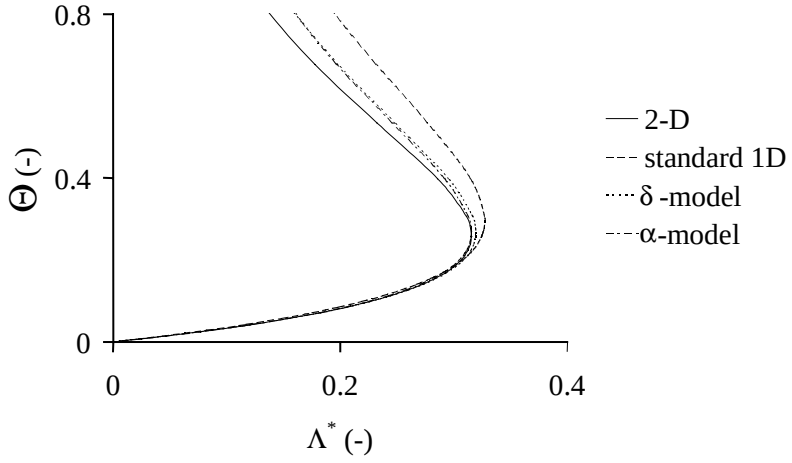

Fig. 5.2 Comparison of one-dimensional models with the numerical solution of the two-dimensional model in which the concentration is assumed constant over the radius ($Pe_{m,r}= \infty$). First order reaction, $\gamma_0= 15$, $\Delta\Theta_{ad}= 0.26$, $Bi= 3$.

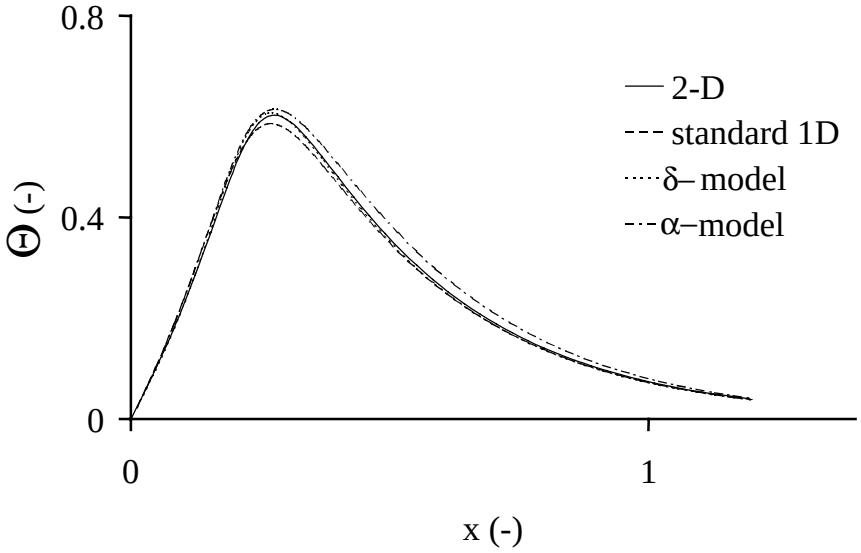

Fig. 5.3 Axial temperature profiles according to the different models for the same conditions as in Fig. 5.2, Λ= 0.12. The solution of the δ-model almost coincides with the solution of the 2-D model.

In the bifurcation diagram in Fig. 5.2, both α- and δ-model are equally close to the exact solution, whilst the standard one-dimensional model gives a much higher temperature at the hot spot of the reactor. Similar results are obtained for different values of γ_0 and Bi.

In general, the δ model should be preferred in case the reactor is operated at conditions not too close to runaway. Independent of the values of γ_0, Bi and the reaction order, the prediction of the δ-model is closer to the numerical solution of the two-dimensional model than that of the α-model. When approaching reactor runaway, any known one-dimensional model will exhibit more and more deviation from the exact solution. The reason for this, is that the shape of the radial temperature profile will deviate from the regular shape that is assumed in the

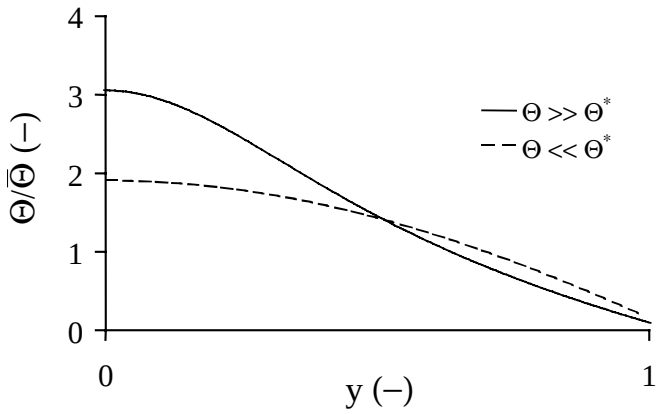

Fig. 5.4 Radial temperature profiles at average reactor temperatures below and above the critical temperature Θ^*. Bi= 3, γ_0= 15, $\Delta\Theta_{ad}$=0.15, n= 1.

derivation of the model.

Above temperature Θ^*, the sign of the second derivative of the temperature with respect to r changes at some distance from the centerline, as is shown in Fig. 5.4. Depending on the values of γ_0 and Bi, either one of the three one-dimensional models can give the best approximation, though better accuracy is usually achieved using the α- or the δ-model.
At conditions close to runaway, the application of a homogeneous model alone is questionable, since temperature difference will occur between the solid and the fluid phases.
In Fig. 5.5, the one-dimensional models are compared for different combinations of Bi, γ_0 and reaction order. The value of Λ was adapted to obtain a significant increase of the average temperature over the reactor length. In all examples, the δ-model performs very well

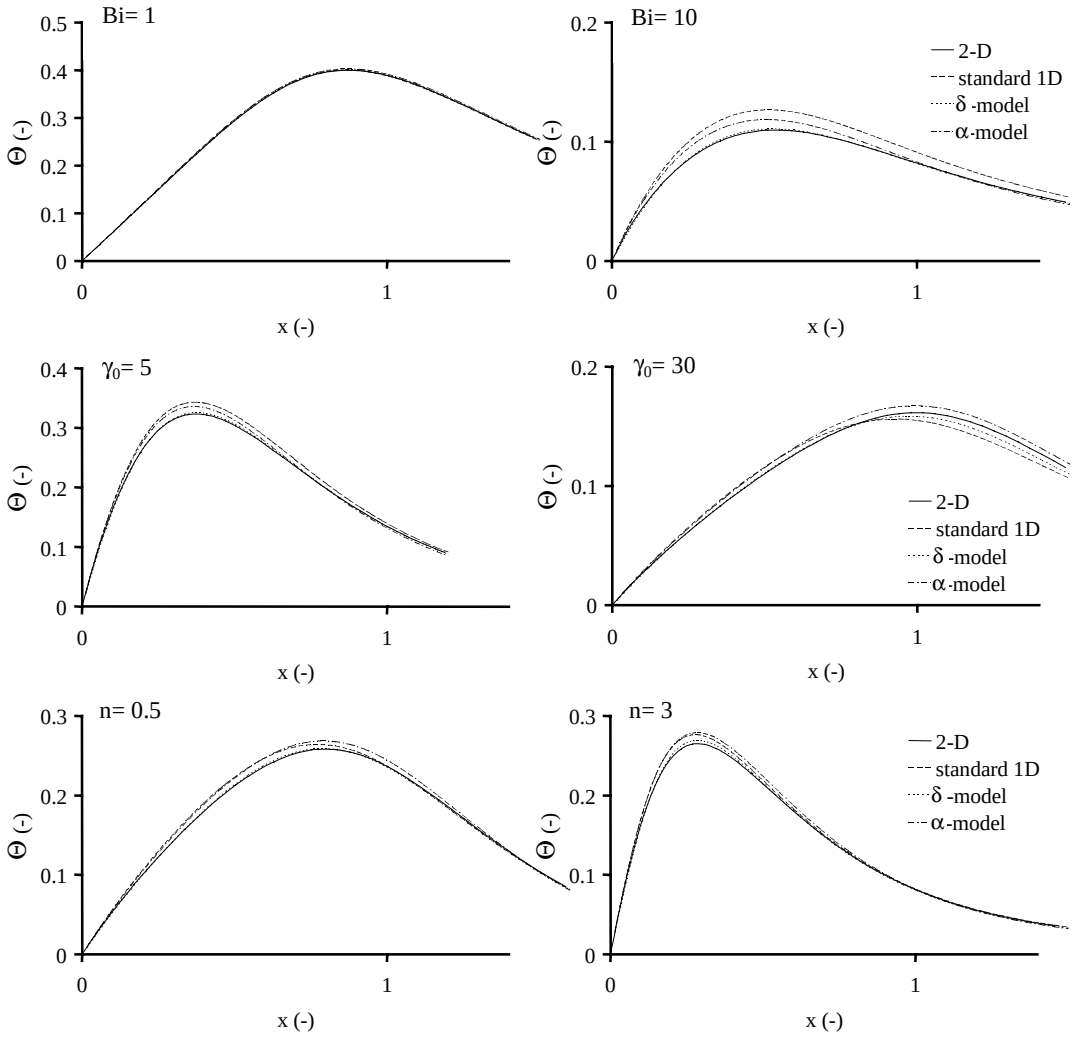

Fig. 5.5 Comparison of the one-dimensional models with the numerical solution of the two-dimensional model for different values of Bi, γ_0 and reaction order n. If not mentioned, the following values are used: Bi= 3, γ_0= 15 and n= 1. $\Delta\Theta_{ad}$= 0.25, Λ is varied to achieve similar temperature maxima. In some graphs, the solution of the δ model cannot be distinguished from the solution of the 2-D model.

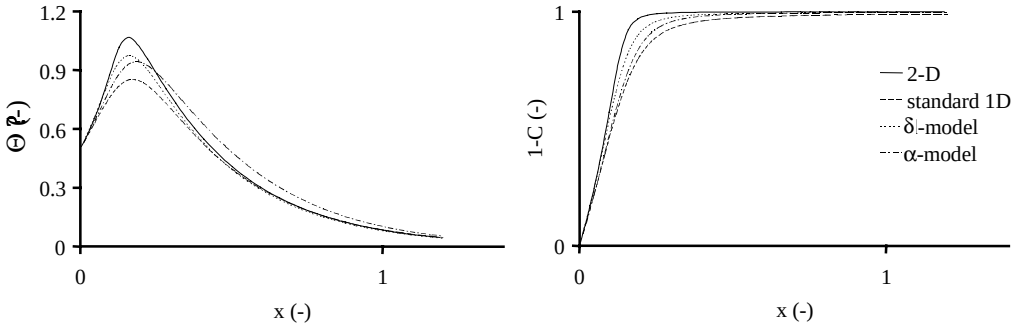

Fig. 5.6 Comparison of the one-dimensional models with the numerical solution of the two-dimensional homogeneous model (heterogeneous reaction). The radial temperature at z=0 is a parabola (eq. (5.20). Θ is made dimensionless with respect to T_w instead of T_0. Bi= 3, γ_0= 15, $\Delta\Theta_{ad}$=0.15, n= 1, Λ= 0.8. α has a maximum of 0.8 at the hot spot; F_H has a maximum of 1.3.

compared to the α- model and the standard one-dimensional model. The agreement between the axial concentration profiles is similar. The fact that the largest improvement is obtained at high values of the Biot number indicates that the new δ-model gives a very accurate prediction of the radial temperature profile. At high Bi, the radial temperature profiles are most pronounced.

As discussed earlier, *Hagan, Herskowitz and Pirkles, 1988* limit the use of the α-model to temperatures lower than the critical temperature Θ^*, for which $\alpha \leq 0.5$. At temperatures higher than Θ^*, the system is considered to be at runaway. Two cases will be considered here, for which this is not true. If the inlet temperature is higher than the wall temperature, it is possible that the temperature at z=0 may be higher than Θ^*, whilst the temperature decreases monotonically in axial direction.

The δ-model can be applied here successfully if the temperature distribution at z=0 is a parabola. If the initial radial temperature profile is uniform, any one-dimensional model will fail. In that case, the overall heat transfer coefficient at z=0 is underestimated, since it should be infinitely large. At the same time, the reaction rate is overestimated in the α- and the δ-model. Fig. 5.6 shows axial temperature and concentration profiles calculated for Θ= 0.5 at z=0. The δ-model does not match the exact solution, but is closer to it than the standard model and the α-model. The latter models overestimate the average temperature after the hot spot and underestimate the conversion at the hot spot.

If the reaction is endothermic, the rate of heat supply and that of heat consumption are at equilibrium only at one temperature. The unstable operating point (Fig. 5.1) does not exist and α may therefore take any value. Fig. 5.7 shows the temperature profiles calculated for an endothermic reaction. Θ is still positive, since ΔT_{ad} has changed sign. α and U^* now have a negative value.

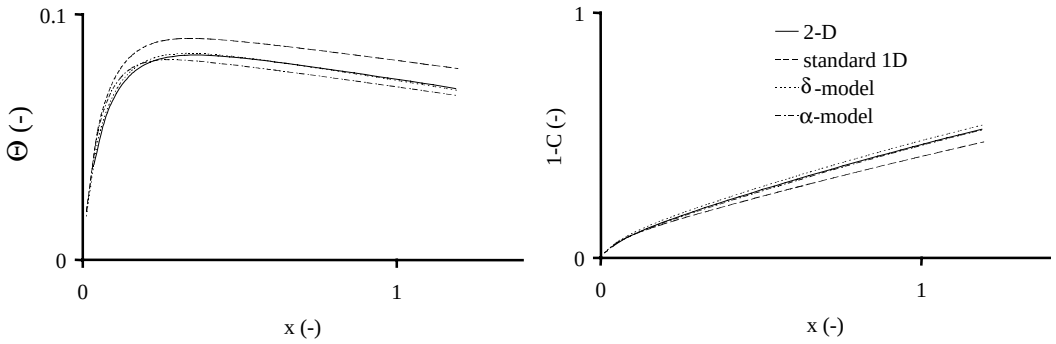

Fig. 5.7 Comparison of the one-dimensional models with the exact solution of the two-dimensional homogeneous model in case of an endothermic reaction. Bi= 5, γ_0= 15, $\Delta\Theta_{ad}$=1, n= 1, Λ= 2. α has a minimum of –0.96; F_H has a minimum of 0.86.

5.6 Non-Arrhenius type of kinetics

A well-known type of non-Arrhenius reaction rate equation is the Langmuir-Hinshelwood expression, which will be used here to demonstrate the derivation of the correction factors F_M and F_H in the heat and mass balance. The reaction rate is expressed as:

$$R(c,T)=\frac{k_r K_a c}{1+K_a c} \tag{5.25}$$

$$k_r=k_{r,0}e^{-\frac{E_a}{RT}} \quad ; \quad K_a=K_{a,0}e^{\frac{|\Delta H_a|}{RT}} \tag{5.26}$$

in which k_1 is the reaction constant and K_a the adsorption constant. The decrease of the adsorption equilibrium constant K_a with temperature is determined by the absolute adsorption enthalpy ΔH_a. It is convenient to write eq. (5.25) as:

$$R(c,T)=\frac{kc}{1+K_a c} \quad ; \quad k=k_{r,0}K_{a,0}e^{\frac{-(E_a-|\Delta H_a|)}{RT}} \tag{5.27}$$

In order to calculate the correction factors F_M and F_H in the heat- and mass balances, the temperature dependence of the reaction rate should be known, which is now a function of both concentration and temperature. For this purpose, the reaction rate is approximated by an Arrhenius type of equation, in which the frequency factor k_e and activation energy $E_{a,e}$ are effective values. Using the dimensionless temperature and concentration, this is:

$$R\left(C,\Theta\right)=\frac{f_1\left(\Theta\right)C}{1+f_2\left(\Theta\right)C}\approx f_e\left(\Theta\right)C\ , \tag{5.28}$$

in which:

$$f_1\left(\Theta\right)=k_{r,0}K_{a,0}c_0e^{\frac{-\gamma_1}{1+\Delta\Theta_{ad}\Theta}} \quad ; \quad \gamma_1=\frac{E_a-\left|\Delta H_a\right|}{RT_0} \tag{5.29}$$

$$f_2\left(\Theta\right)=K_{a,0}c_0e^{\frac{-\gamma_2}{1+\Delta\Theta_{ad}\Theta}} \quad ; \quad \gamma_2=\frac{\left|\Delta H_a\right|}{RT_0} \tag{5.30}$$

$$f_e\left(\Theta\right)=k_{e,0}c_0e^{\frac{-\gamma_e}{1+\Delta\Theta_{ad}\Theta}} \quad ; \quad \gamma_e=\frac{E_{a,e}}{RT_0} \tag{5.31}$$

γ_e and $k_{e,0}$ can be calculated after linearization of the reaction rate at the radial average temperature using:

$$\frac{1}{T}=\frac{1}{T_0\left(1+\Theta\Delta\Theta_{ad}\right)}\approx\frac{1}{T_0\left(1+\Theta\Delta\Theta_{ad}\right)}\left(1-\frac{\Delta\Theta_{ad}\left(\Theta-\overline{\Theta}\right)}{1+\overline{\Theta}\Delta\Theta_{ad}}\right) \tag{5.32}$$

After this, eq. (5.28) is written as:

$$\frac{f_1\left(\overline{\Theta}\right)e^{\Gamma_1\Delta\Theta_{ad}\left(\Theta-\overline{\Theta}\right)}C}{1+f_2\left(\overline{\Theta}\right)e^{\Gamma_2\Delta\Theta_{ad}\left(\Theta-\overline{\Theta}\right)}C}\approx f_e\left(\overline{\Theta}\right)e^{\Gamma_e\Delta\Theta_{ad}\left(\Theta-\overline{\Theta}\right)}C \tag{5.33}$$

$$\Gamma_i=\frac{\gamma_i}{\left(1+\overline{\Theta}\Delta\Theta_{ad}\right)^2} \tag{5.34}$$

At $\Theta=\overline{\Theta}$, the reaction rates in eq. (5.33) and their derivatives with respect to temperature should be equal, sot that:

$$f_e\left(\overline{\Theta}\right)=\frac{f_1\left(\overline{\Theta}\right)}{1+f_2\left(\overline{\Theta}\right)C} \quad ; \quad \gamma_e\left(\overline{\Theta}\right)=\frac{\gamma_1+f_2\left(\overline{\Theta}\right)(\gamma_1-\gamma_2)C}{1+f_2\left(\overline{\Theta}\right)C} \tag{5.35}$$

The correction factors F_M and F_H can be calculated by replacing γ_0 in eq. (5.24) by the effective activation energy γ_e.

Similar results are obtained if the reaction rate is a function of the concentrations of more than one species that react after adsorption or directly from the fluid phase. Generally, the adsorption enthalpy is (much) smaller than the activation energy of reaction. In this case, the performance of the δ-model is similar as in the case of Arrhenius type expressions for the reaction rate. If the sum of the adsorption enthalpies is close to the activation energy, the reaction rate may not be a continuously increasing or decreasing function of temperature. In that case, all of the one-dimensional models discussed here deviate from the solution of the two-dimensional model.

The occurrence of intra-particle mass transport limitations is often encountered in industrial processes. The change of the reaction rate that is caused by it is commonly expressed using an effectiveness factor, for which analytical approximations are available (see e.g. *Wijngaarden et al., 1999*, and Appendix B). These analytical approximations can be used to calculate the apparent activation energy in the expression of F_H in a similar way as is described in this paragraph.

5.7 Systems with multiple reactions

Application of the δ-model to systems in which multiple reactions occur simultaneously is very simple. A system with two consecutive reactions and a system with two parallel reactions will be considered here as an example. In both cases, the approach is the same. To be able to calculate the correction factor F_H in the heat balance, the activation energies of the set of reactions should be lumped into an effective activation energy in order to calculate the shape of the radial temperature distribution.

5.7.1 Consecutive reactions

For the following system of consecutive reactions which are first order in each component:

$$A+B\xrightarrow[\Delta H_1]{R_1}C+B\xrightarrow[\Delta H_2]{R_2}D\,, \tag{5.36}$$

the dimensionless heat and mass balances are:

$$\frac{\partial\overline{\Theta}}{\partial x}=-U^{*}\left(\overline{\Theta}-\Theta_{w}\right)+F_{H}\left(\overline{\Theta},\gamma_{e}\right)\left(R_{1}+\frac{\Delta H_{2}}{\Delta H_{1}}R_{2}\right) \tag{5.37}$$

$$\frac{\partial A}{\partial x}=-F_{M}\left(\overline{\Theta},\gamma_{1}\right)R_{1} \qquad \frac{\partial B}{\partial x}=-F_{M}\left(\overline{\Theta},\gamma_{1}\right)R_{1}-F_{M}\left(\overline{\Theta},\gamma_{2}\right)R_{2} \tag{5.38}$$

$$\frac{\partial C}{\partial x}=F_{M}\left(\overline{\Theta},\gamma_{1}\right)R_{1} \qquad \frac{\partial D}{\partial x}=F_{M}\left(\overline{\Theta},\gamma_{2}\right)R_{2} \tag{5.39}$$

$$R_{1}=\Lambda_{1}e^{\frac{\gamma_{1}\overline{\Theta}\Delta\Theta_{ad}}{1+\overline{\Theta}\Delta\Theta_{ad}}}C_{A}C_{B} \qquad \Lambda_{2}e^{\frac{\gamma_{2}\overline{\Theta}\Delta\Theta_{ad}}{1+\overline{\Theta}\Delta\Theta_{ad}}}C_{B}C_{C} \tag{5.40}$$

The dimensionless temperature and concentrations are defined with respect to the concentration of component A and the adiabatic temperature rise of the first reaction:

$$\Theta=\frac{T-T_{0}}{\Delta T_{ad}} \qquad \Delta T_{ad}=\frac{c_{0,A}\Delta H_{1}}{\rho_{f}c_{p,f}} \qquad C_{i}=\frac{c_{i}}{c_{0,A}} \qquad \gamma_{i}=\frac{E_{a,i}}{RT_{0}} \tag{5.41}$$

The value of F_H is calculated using eq. (5.23) after replacing γ_0 in eq. (5.24) by γ_e. This effective activation energy can be calculated in a similar way as was done in the previous section. The sum of the reaction rates is replaced by a single reaction rate of an Arrhenius type:

$$R\left(C,\Theta\right)\approx\lambda_{1}\left(\overline{\Theta}\right)e^{\Gamma_{1}\Delta\Theta_{ad}\left(\Theta-\overline{\Theta}\right)}C_{A}C_{B}+\lambda_{2}\left(\overline{\Theta}\right)e^{\Gamma_{2}\Delta\Theta_{ad}\left(\Theta-\overline{\Theta}\right)}C_{B}C_{C}\approx\lambda_{e}\left(\overline{\Theta}\right)e^{\Gamma_{e}\Delta\Theta_{ad}\left(\Theta-\overline{\Theta}\right)} \tag{5.42}$$

At the right hand side, concentrations are omitted, since they are assumed constant over the radius. For this particular case, γ_e is equal to:

$$\gamma_{e}\left(\overline{\Theta}\right)=\frac{f_{1}\left(\overline{\Theta}\right)C_{B}\gamma_{1}+f_{2}\left(\overline{\Theta}\right)C_{C}\gamma_{2}}{f_{1}\left(\overline{\Theta}\right)C_{B}+f_{2}\left(\overline{\Theta}\right)C_{C}} \tag{5.43}$$

with:

$$f_{1}\left(\Theta\right)=k_{1,0}c_{A,0}c_{B,0}e^{\frac{-\gamma_{1}}{1+\Delta\Theta_{ad}\Theta}} \qquad f_{2}\left(\Theta\right)=k_{2,0}c_{A,0}c_{C,0}e^{\frac{-\gamma_{2}}{1+\Delta\Theta_{ad}\Theta}} \tag{5.44}$$

The general expression for the effective activation energy for a system of n reactions involving m components is:

$$\gamma_e\left(\overline{\Theta}\right)=\frac{\sum_{i=1}^{n} f_i\left(\overline{\Theta}\right)\gamma_i\prod_{j=1}^{m}\left(C_j\right)^{n_{i,j}}}{\sum_{i=1}^{n} f_i\left(\overline{\Theta}\right)\prod_{j=1}^{m}\left(C_j\right)^{n_{i,j}}} \qquad f_i\left(\Theta\right)=k_{i,0}\left(c_0\right)e^{\frac{-\gamma_i}{1+\Delta\Theta_{ad}\Theta}} \tag{5.45}$$

$n_{i,j}$ is the order of reaction i with respect to component j. The factors F_M depend on the activation energy γ_i of the reaction rate for which they are calculated. F_M corrects each reaction source term for the radial temperature distribution; it is not important how the different reactions contribute to the total heat production rate.

Fig. 5.8 shows an example of a the temperature at the centerline of the reactor and the integral selectivity of component A to the desired product C in case the second reaction has a heat of reaction and an activation energy that are twice as large as those of the first reaction. The value of the Biot number for heat transfer at the wall is chosen rather high to make the test of the model more severe.

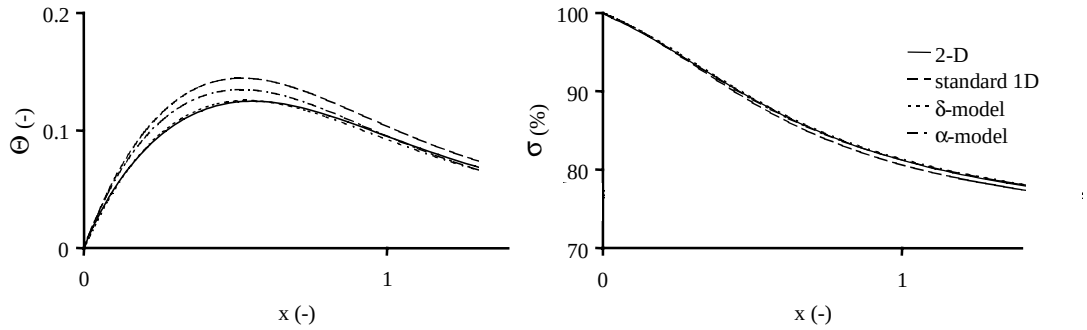

Fig. 5.8 Temperature at the centerline of the reactor and the integral selectivity of component A to the desired product C in case of two consecutive reactions. Λ_1= 0.7, Λ_2= 0.3, γ_1= 10. γ_2= 20, $\Delta\Theta_{ad}$= 0.3, ΔH_2= $2\Delta H_1$, Bi= 10.

5.7.2 Parallel reactions

In case of parallel reactions, the correction factors to be used in the δ-model are the same as those in case of consecutive reactions. F_M should be calculated using the apparent activation energy given by eq. (5.45).

As an example, the following reaction system is used:

$$\begin{aligned} &A+B \xrightarrow[\Delta H_1]{R_1} C \\ &A+B \xrightarrow[\Delta H_2]{R_2} D \end{aligned} \qquad (5.46)$$

The reaction enthalpy and activation energy of the second reaction are twice as large as those of the, desired, first reaction. Systems like this one are typical for partial oxidation reactions as that of ethylene, which are often carried out in wall-cooled tubular reactors. Fig. 5.9 shows the temperature profiles at the centerline of the reactor and the selectivity of component A towards C, calculated using the different models. The heat and mass balance are similar to those in case of consecutive reactions.

The δ-model performs very well compared to the other one-dimensional models. The temperature at the centerline of the reactor is overestimated by both the α- and the standard one-dimensional model. The integral selectivities predicted by the α- and the δ-model are equally close to the solution of the two-dimensional model.

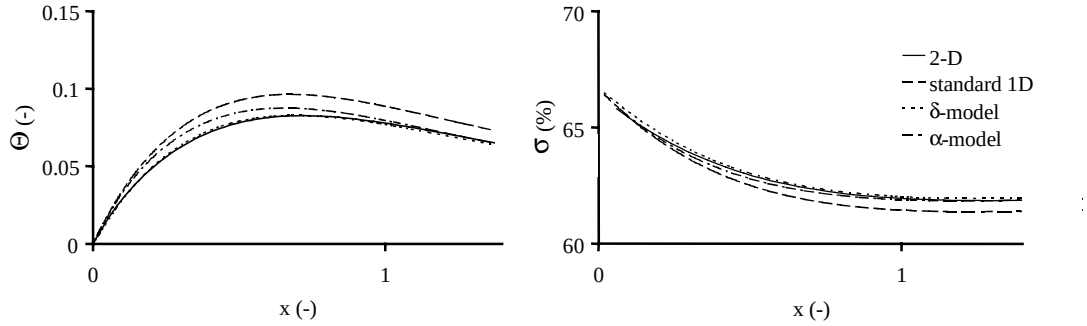

Fig. 5.9 Temperature at the centerline of the reactor and the integral selectivity of component A to the desired product C in case of two parallel reactions. Λ_1= 0.2, Λ_2= 0.1, γ_1= 10. γ_2= 20, $\Delta\Theta_{ad}$= 0.3, ΔH_2= $2\Delta H_1$, Bi= 10.

5.8 Conclusions

A new model has been derived as an alternative to the standard one-dimensional model. The model uses an analytical approximation of the radial temperature distribution for the calculation of the average reaction rate. This ‘δ-model’ can be easily adapted for different reaction systems. At conditions not too close to runaway, the δ-model should be preferred to the standard one-dimensional model and the α-model of *Hagan, Herskowitz and Pirkles, 1988*. The latter model uses an analytical solution of the temperature distribution at the hot spot to account for the non-linear dependence of the reaction rate on the radial average temperature. The predictions of the new model are very close to the numerical solution of the

two-dimensional model, whilst the correction factors used in the heat and mass balances are simple explicit functions of temperature, Biot number and activation energy. This makes the use of the model far easier than the α-model, in which a parameter α has to be obtained at each axial position.

Notation

A_n	eigenvalues of Bessel function	-
c	concentration	mole m^{-3}
c_p	heat capacity	J kg^{-1} K^{-1}
F_H	correction factor heat production term	-
F_M	correction factor heat removal term	-
ΔH_a	adsorption enthalpy	J $mole^{-1}$
ΔH_r	reaction enthalpy	J $mole^{-1}$
J_0, J_1	zeroth and first order Bessel function	
K_a	adsorption constant	-
$K_{a,0}$	adsorption rate constant	-
k	reaction rate constant	$mole^{1-n}$ m^{3n} kg^{-1} s^{-1}
k_0	frequency factor	$mole^{1-n}$ m^{3n} kg^{-1} s^{-1}
n	reaction order	-
R	gas constant	J $mole^{-1}$ K^{-1}
R_i	rate of reaction i	mole kg^{-1} s^{-1}
R_t	bed radius	m
T	temperature	K
ΔT_{ad}	adiabatic temperature rise	K
t	time	-
U	overall heat transfer coefficient	W m^{-2} K^{-1}
u	fluid velocity	m s^{-1}
z	axial coordinate	-

Greek

α	constant used in α-model	-
α_w	wall heat transfer coefficient	W m^{-2} K^{-1}
β	constant	-
δ	constant used in δ-model	-
ε	bed porosity	-
η	effectiveness factor	-
$\lambda_{e,r}$	effective radial thermal conductivity	W m^{-1} K^{-1}
ν	stoichiometric coefficient	-
ρ	density	kg m^{-3}
σ	selectivity	-

Dimensionless groups

Bi	Biot number for heat transfer at the wall		$Bi=\frac{\alpha_w R_t}{\lambda_{e,r}}$
C	dimensionless concentration		$\frac{c}{c_0}$
Γ_i	dimensionless activation energy at $\Theta=\overline{\Theta}$		$\frac{\gamma_i}{\left(1+\overline{\Theta}\Delta\Theta_{ad}\right)^2}$
Λ	dimensionless reaction rate at inl. cond.		$\Lambda=PE_{h,r}\frac{R_t}{uc_0}(1-\varepsilon)\rho_s k_0 c_0^n e^{-\gamma_0}$
$PE_{h,r}$	Peclet number for radial heat transfer		$PE_{h,r}=\frac{u\rho c_{p,f} R_t}{\lambda_{e,r}}$
U^*	dimensionless overall heat transfer coefficient		$U^*=\frac{2PE_{h,r}U}{u\rho c_p}$
x	dimensionless axial coordinate		$\frac{z}{R_t PE_{h,r}}$
y	dimensionless radial coordinate		$\frac{r}{R_t}$
γ_0, γ_i	dimensionless activation energy		$\frac{E_a}{RT_0}$, $\frac{E_{a,i}}{RT_0}$
Θ	dimensionless temperature	no reaction	$\frac{T-T_w}{T_0-T_w}$
		with reaction:	$\frac{T-T_w}{\Delta T_{ad}}$
$\Delta\Theta_{ad}$	dimensionless adiabatic temperature rise		$\frac{\Delta T_{ad}}{T_0}$

Sub- and superscripts

0	value at inlet conditions
f	fluid
i	reaction number
j	component number
s	solid
w	wall

Appendix A .

Catalyst Porosity and Permeability

To be able to calculate the effectiveness factor of the carbon monoxide oxidation reaction inside a porous catalyst consisting of copper oxide on γ-alumina (see Chapter 2), the intra-particle diffusivities of CO and CO_2 should be known. The effective diffusion coefficients depend on the porosity of the catalyst and of the diameter and the tortuosity of the pores. The porosity and the pore diameter distribution were obtained from mercury intrusion experiments. The pore tortuosity was calculated from helium permeation experiments, taking the broad pore size distribution into account.

A.1 Porosity and pore size distribution

Intra-particle mass transport is determined by the particle porosity and the size and shape (tortuosity) of the pores.

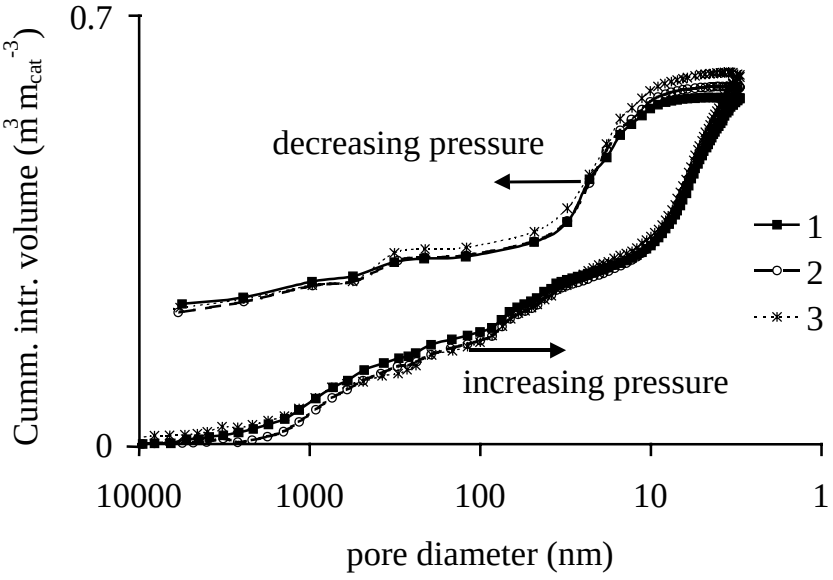

Fig. A.1 Cumulative intrusion volume as function of the pore diameter for 3 samples of fresh catalyst (entire particles).

The porosity was measured using by mercury intrusion experiments (Micrometrics). As can be seen in figures A.1 and A.2, the spread in the pore diameters is very large.
Since the catalyst is an extrudate, two peaks in the pore size distribution are to be expected.

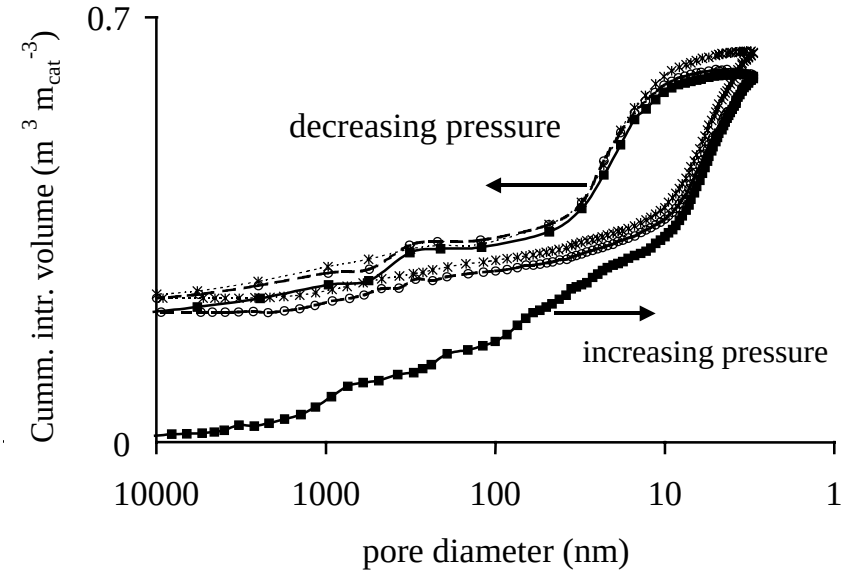

Fig. A.2 Cumulative intrusion volume as function if the pore diameter during 3 intrusion/extrusion cycles using a single catalyst sample

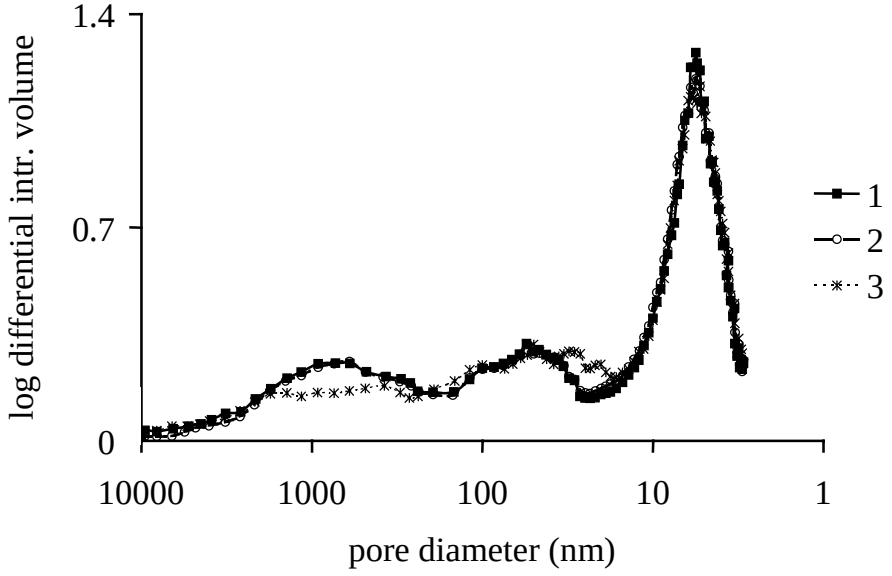

Fig. A.3 Log differential intrusion volume dV/d(log(dp)) as function of the pore diameter during 3 intrusion/extrusion cycles using a single catalyst sample.

Larger pores occur between the particles of the starting material, whilst smaller pores will be present inside it. Such a distribution in pore size is observed. There are two broad peaks at larger pore diameters, which are probably due to a non-uniform particle size of the starting material.As can be seen in Figures A.1 and A.3, there is a large difference between the cumulative intrusion volumes in case of intrusion and extrusion experiments. This indicates the occurrence of bottlenecks *(Webb and Orr 1997).* If a larger cavity is accessed through narrow pores, the intrusion volume is associated to the diameter of these smaller pores. During the extrusion cycle, mercury stays trapped within the cavity.

A.2 Permeability

In case the mean free path λ of the migrating species is much smaller than the pore diameter, molecules collide with the wall much more frequently than with each other.

$$\lambda = \frac{kT}{\sqrt{2}\pi d_c^2 P} \tag{A.1}$$

where k is the Bolzman constant and d_c the collision diameter of the molecule.
In this so-called Knudsen-regime the flux is independent of the gas composition and the absolute pressure and can be calculated using the well known equation:

$$D_k = \frac{4}{3} K_0 \bar{v}, \tag{A.2}$$

derived by Knudsen (*Knudsen, 1909):*
The average velocity $\bar{v}$ of the migrating molecules can be calculated using the kinetic theory of gases:

$$\bar{v} = \sqrt{\frac{8RT}{\pi M}} \tag{A.3}$$

The Knudsen diffusivity, D_k, is a function of only temperature, the mass of the molecules, M (kg $mole^{-1}$) and a structure parameter K_0:

$$K_0 = \frac{1}{4} \frac{\varepsilon}{\tau} d_p \tag{A.4}$$

where ε is the porosity of the solid and τ is the tortuosity of the pores, which is the ratio of the pore length and the distance between both ends of the pore.
If the mean free path λ is much smaller than the pore diameter, the flux is not influenced by the pore wall, but is determined by momentum exchange between the colliding molecules. In a gas mixture, the diffusion coefficient of each species slightly depends of the composition of the mixture. In case of a binary mixture of non-polar molecules, the diffusion coefficient D_{ij} can be estimated from *(Fuller et al. 1966)*:

$$D_{ij} = 1.013 \cdot 10^{-2} \frac{T^{1.75}}{P\left(v_i^{1/3} + v_j^{1/3}\right)^2} \sqrt{\frac{M_i + M_j}{M_i M_j}} \tag{A.5}$$

where v_i and v_j are the diffusion volumes of the species and M_i and M_j arethe molar mass in g mole^{-1}.

When a pressure drop is applied over a slab of a porous solid, the flux of a gas through the solid can be described by the following equation, in which Knudsen diffusion and convective (D'Arcy) flow are assumed to be additive:

$$J_{Mole} = -\frac{\Delta P}{RTs}\left(D_k + \frac{B_0}{\eta} P_{av}\right) \tag{A.6}$$

In (A.6), J_{Mole} is the mole flux, ΔP the pressure difference over the slab, P_{av} the average pressure, s the thickness of the slab, D_k the Knudsen diffusion coefficient (A.2), η the dynamic viscosity of the gas and B_0 the permeability of the material. B_0 is a function of material structure and is defined as:

$$B_0 = \frac{1}{32} \frac{\varepsilon}{\tau} d_p^2 \tag{A.7}$$

If migrating molecules adsorb at the walls of the pores, surface diffusion can occur. If oxygen is present in large excess, the effectiveness factor of CO oxidation reaction (see Chapter 2) is determined by the intra-particle diffusivities of CO and CO_2. Of these two components, CO_2 is most likely to migrate along the pore surface. *Benes, 2000* investigated the permeability of porous α-alumina (d_p=0.16 μm) using CO_2 and found that, at temperatures between 30 and 350 °C and pressures between 1 and 6 bars, the contribution of surface diffusion was less

than the experimental error. Since the operating conditions, applied in this work, were similar, surface diffusion was neglected.

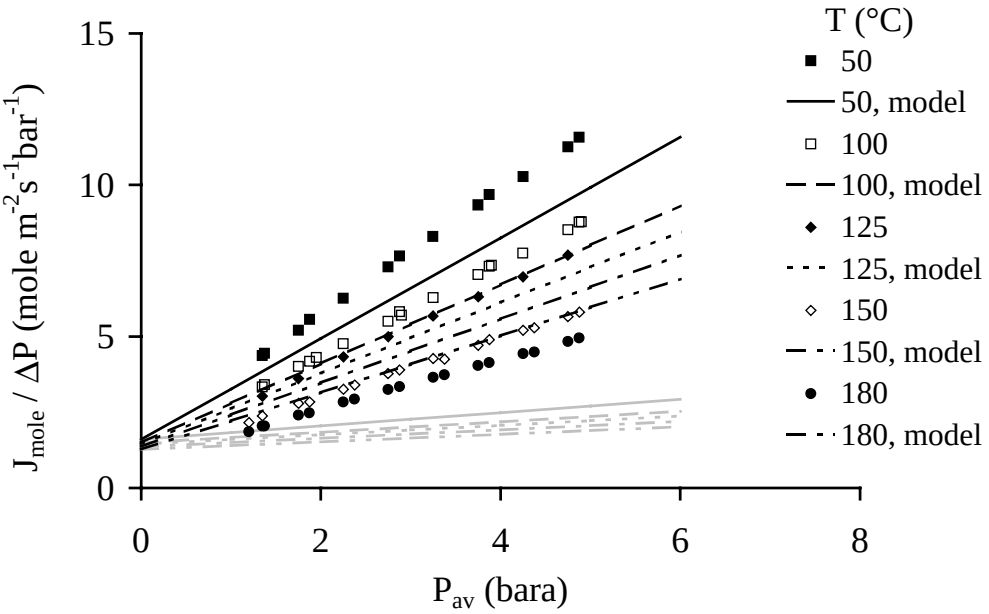

Fig. A.4 Permeation flux of Helium through a catalyst cross section with a thickness of 2 mm as function of the average pressure at ΔP=0.25 and 0.5 bar (no difference observed). Experimental data are represented by dots. Black lines represent the flux calculated using the parallel pore model; Grey lines represent the mole fluxes according to the average pore size $d_{p,av}$=400 nm. In all calculations, τ was equal to 1.25.

The permeability of the catalyst was measured using the experimental setup described by (*Benes 2000*). In all experiments, the used gas was helium. The barrier through which the helium flux was measured consisted of a disc of impermeable γ-alumina with a thickness of 2 mm, in which a slice of catalyst of the same thickness was sealed. The alumina disc was fixed in a stainless steel cylindrical reactor using rings of silicone rubber. The cell was heated uniformly using a tubular electrical oven. The pressure after the sample was controlled by an electronic mass flow controller (Brooks). The gas flow before the sample was adjusted by a second mass flow controller to maintain the desired pressure drop over the sample. Experiments were done at temperatures of 50, 100, 125, 150 and 180 °C. The pressure drop over the slice of catalyst was either 0.25 or 0.5 bar. In Fig. A.4, the measured permeation flux of helium is shown as function of the average pressure in the catalyst sample.

For each temperature, the average pore diameter and the ratio ε/τ can be calculated using eqs. (A.2)-(A.7). The obtained values are listed in Table A.1.

Table A.1. Flow-average pore diameter and porosity/tortuosity ratio (ε=0.6)

	ΔP=0.5 bar		ΔP=0.25 bar	
Temperature	d_p (μm)	ε/τ (-)	d_p (μm)	ε/τ (-)
50 °C	3.6	0.058	3.7	0.055
100 °C	3.9	0.045	4.1	0.043
125 °C	4.1	0.042	-	-
150 °C	3.5	0.044	4.0	0.036
180 °C	3.6	0.039	4.1	0.032
Average	3.8	0.046	3.9	0.042

These results should be considered with care. Eq. (A.6) is only justified for porous materials with a relatively uniform pore structure and when the mean free path differs from the average pore size. This is hardly the case for the used catalyst. The pore geometry is determined by the properties of the starting material, the method of processing (precipitation, dip-coating, extrusion) and further treatment, such as calcination. In case of preparation by dip-coating or extrusion, the pores will have a similar shape as the voidages between (spherical) particles in a random packing and they will be strongly interconnected. Sintering of this material will cause a smoothening of the pores and a decrease in porosity and connectivity. If pore size distribution is broad, the average values of d_p and ε/τ that are obtained from permeation experiments are apparent values. The obtained pore diameter may be very different from the true average pore diameter, which is obtained from mercury intrusion experiments. The pore diameters calculated from the permeation experiments are approximately 4 μm, which is ten times larger than the average pore diameter that is calculated from the mercury intrusion experiments. The apparent pore tortuosity is close to 14, which is extremely high (values are generally between 1.5 and 5). The high value of the apparent pore diameter can be explained from the fact that the relative contribution of the wide pores to the permeation flux is much larger than that of the smaller pores. The measured contribution of Knudsen diffusion is small, so that pore size calculated using eqs. (A.2)-(A.7) should be large. Since, in eq. (A.6), it assumed that these large pores constitute all of the pore volume, the permeation flux would be overestimated unless τ is taken very large.

It was tried to improve the model by using the measured pore size distribution. The pores with different diameters can be parallel, in series, or a combination of these. In the case of a distribution as shown in Fig. A.3., the overall transport is dominated by Knudsen diffusion through the narrow pores, if the pores are assumed to be connected in series:

$$J_{Mole} = \sum_i \frac{\Delta P_i}{RTsf\left(d_{p,i}\right)} \left(D_k\left(d_{p,i}\right) + \frac{B_0\left(d_{p,i}\right)}{\nu} \overline{P_i} \right) \tag{A.8}$$

In equation (A.8), the solid is regarded as a stack of slices with a pore diameter $d_{p,i}$, which thickness is proportional to the volume fraction of pores of this diameter. In case a parallel configuration is assumed, the flux is given by:

$$J_{Mole} = \sum_i f\left(d_{p,i}\right) \frac{\Delta P}{RTs} \left(D_k\left(d_{p,i}\right) + \frac{B_0\left(d_{p,i}\right)}{\eta} \overline{P} \right) \tag{A.9}$$

The permeation flux according to eq. (A.9) is determined by the larger pores down to 100 nm, through which 95 % of the transport occurs at pressures from 0 to 10 bara and temperatures between 50 and 180 °C. In Fig. A.4, black lines show the permeation flux according to eq. (A.9). The calculated permeation flux agrees reasonably well with the experimental data if τ is equal to 1.25. As a comparison, the mole fluxes calculated using the average pore diameter from the mercury intrusion experiments (400 nm) is shown (gray lines). It is clear that the use of this average pore diameter results in an underestimation of the permeation flux, even if the value of τ is increased to 5. The permeation flux according to eq. (A.8) is not shown in Fig. A.4, since these values are too small to be realistic.

The prediction on the basis of the measured pore size is close to the experimental data if the pores are assumed to be in parallel. The measured flux, however, do seem to be more sensitive to temperature than the calculated values. The assumption of a parallel connection of the pores seems realistic only for the larger pores formed during the extrusion of the starting material, but not for the smallest pores. These pores, however, contribute only little to the overall permeability.

A.3 Effective diffusivity

The effective diffusivity of the reactants and the products of the reaction system used in this investigation can be predicted by using the value of τ that was obtained from the permeability measurements. In case of equimolar diffusion in a binary gas mixture, the effective diffusion coefficient can be calculated as (*Pollard and Present 1948*):

$$D_{eff} = \frac{\varepsilon}{\tau}\left(\frac{1}{D_{ij}} + \frac{1}{D_k}\right) \qquad (A.10)$$

In (A.10), D_{ij} and D_k are the molecular and the Knudsen diffusion coefficient respectively. This correlation can be applied to diffusion of CO and CO_2 in air if the concentrations are small, as was the case during the kinetic experiments and the experiments performed in the wall-cooled tubular reactor.

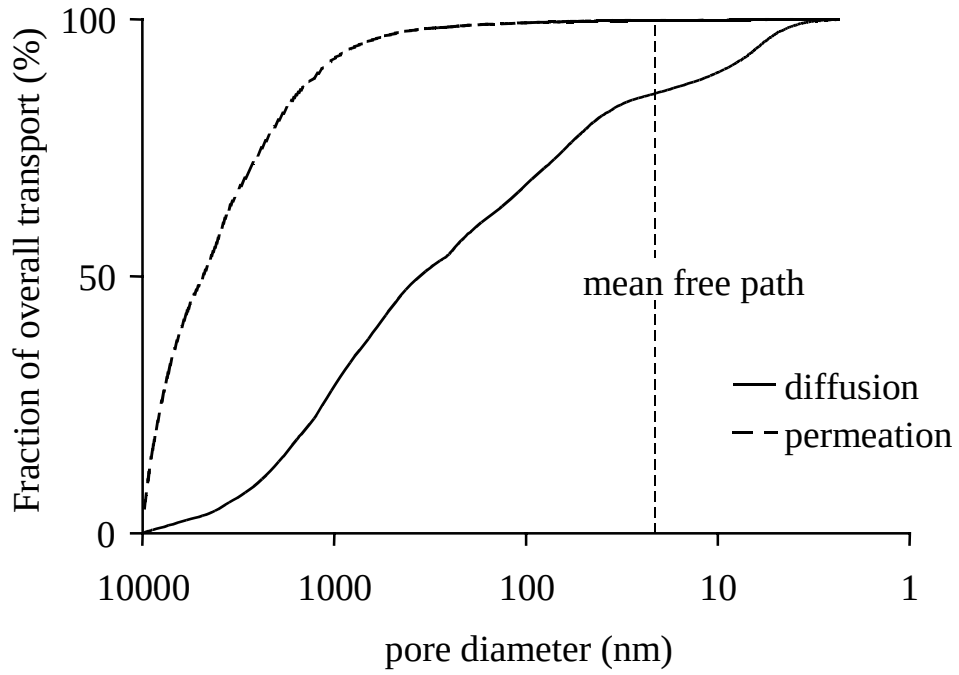

Fig. A.5 Distribution of the overall CO flux over the different pores at P=5 bara and T=200 °C. Shown here is the cumulative flux going from large to small pores. The value of τ is 1.25, as obtained from the permeation experiments.

The molecular diffusion coefficient is not affected by the pore size distribution; but the Knudsen diffusion coefficient is (eq. (A.2)). In case of a broad pore-size distribution, the apparent values of the pore diameter and the ratio ε/τ are different for permeation and diffusion. In both processes, the Knudsen diffusion term is the same. The rate of molecular diffusion does not dependent on the pore diameter, whereas the contribution of viscous flow quadratically increases with increasing pore diameter. The diffusion-average pore diameter will therefore be smaller than the flow-average diameter (see Table A.1). At the same time, the apparent value of ε/τ, which is obtained when assuming that all the pores have the same diameter, will be larger, since a larger fraction of pores will contribute to the overall mole flux. Analogous to eq. (A.9), the effective diffusivity was calculated assuming that pores of different diameter are connected in series:

$$D_{eff,i} = \frac{\varepsilon}{\tau} \sum_i f\left(d_{p,i}\right) \left(\frac{1}{D_{ij}} + \frac{1}{D_{k,i}} \right)^{-1} \qquad \text{(A.11)}$$

For the measured pore size distribution, intra-particle diffusion is governed by molecular diffusion, as is shown in Fig. A.5.

Fig. A.6 shows the values of D_{eff} for CO and CO_2 at pressures between 2 and 10 bara and temperatures between 100 and 250 °C. To minimize calculation time, the intra-particle diffusion constants used for the prediction of the particle effectiveness factor were calculated using apparent values of d_p and ε/τ. The predictions of eq. (A.11) are similar to the diffusion coefficients in case of a uniform pore size of 190 nm and a ratio ε/τ of 0.27.

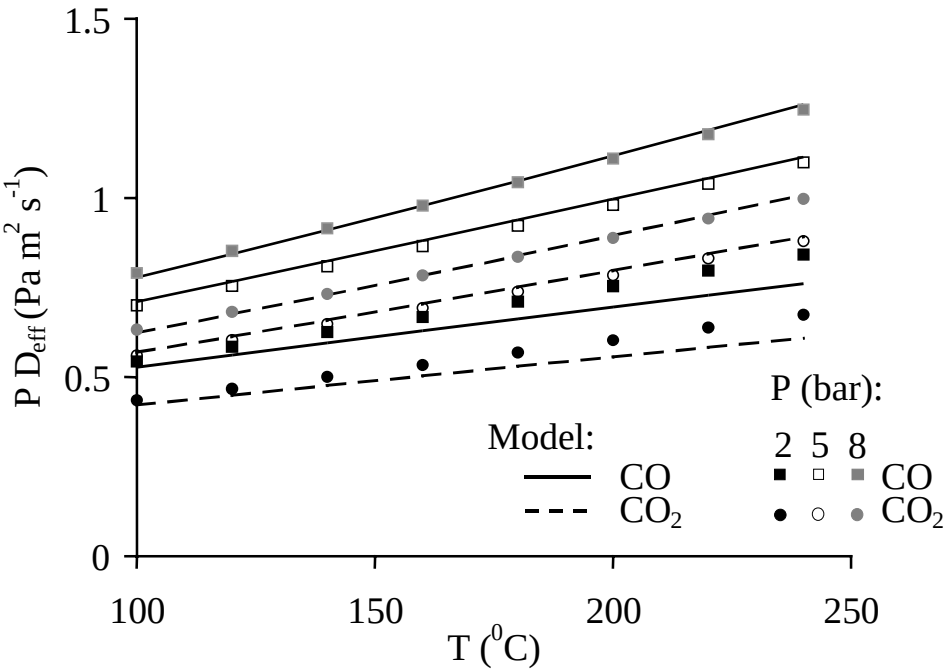

Fig. A.6 Effective diffusion coefficients for CO and CO_2, calculated using the measured pore size distribution (dots), compared to the values for an average pore diameter of 190 nm and ε/τ=0.27 (lines).

A.4 Summary

A very broad pore size distribution was obtained from mercury intrusion experiments. It was therefore not possible to predict the effective intra-particle diffusivity of the reactants and products of the CO oxidation reaction using the average pore diameter, as is generally proposed in engineering literature. If the pores are connected in parallel and the tortuosity, τ, is the same for all pores, a reasonable value of τ=1.25 was obtained from permeation

experiments. The intra-particle diffusion coefficients of CO and CO_2 were calculated for a parallel pore configuration, using the same value of τ. The contribution of Knudsen diffusion to the predicted overall diffusion coefficients was found to be negligible. When assuming a uniform pore size distribution, the apparent pore diameter for diffusion is 190 nm at a ratio ε/τ of 0.27.

Notation

B_0	permeability	m^2
d_c	collision diamter	m
d_p	pore diameter	m
D_k	Knudsen diffusion coefficient	$m^2\ s^{-1}$
D_{ij}	binary diffusion coefficient	$m^2\ s^{-1}$
D_{eff}	effective diffusion coefficient	$m^2 s^{-1}$
k	Bolzman constant	$1.380658 \cdot 10^{-23}$ J K^{-1}
J_{Mole}	mole flux	mole $m^{-2} s^{-1}$
K_0	structure parameter	m
M	molar mass	kg $mole^{-1}$
M_i, M_j	molar mas	g $mole^{-1}$
P	pressure	Pa
ΔP	pressure difference	Pa
R	gas constant	8.314 J $mole^{-1}$ K^{-1}
T	temperature	K
$\bar{v}$	mean molecular velocity	m s^{-1}
v_i, v_j	diffusion volume	m^3

Greek

ε	porosity	-
η	fluid viscosity	Pa s
λ	mean free path of molecule	-
τ	toruosity	-

Subscripts

i,j	component number
av	average

Appendix B .

Analytical approximation of the effectiveness factor

B.1 Summary

For the calculation of the overall reaction rate, an effectiveness factor is used to account for intra-particle transport limitations. An approximate analytical solution for the effectiveness factor for catalysts of various shapes and arbitrary reaction kinetics is described in this appendix. The presented analytical solution (eq. (B.10)) has a higher accuracy than the expressions in the usual textbooks, whereas it has a similar complexity. The effect of the particle shape is accounted for by a shape factor, which is given in eq. (B.25).

B.2 Problem

It is assumed that the concentration of reactant within a particle of any shape is described by the following differential equation:

$$D_e \nabla^2 c = R(c) \tag{B.1}$$

with the boundary condition $c=c_s$ at the surface of the particle. ∇^2 is the Laplacian operator, which is, in rectangular coordinates:

$$\nabla^2 = \frac{\partial^2}{\partial x^2} + \frac{\partial^2}{\partial y^2} + \frac{\partial^2}{\partial z^2} \tag{B.2}$$

In many cases, the temperature in side the catalyst particle can be related to the concentration. The approach described here for the calculation of the effectiveness factor can then also be applied to catalyst particles in which the intra-particle temperature gradients cannot be neglected. The effectiveness factor is defined as the ration between the reaction rate at the surface of the particle and the reaction rate averaged over the particle volume:

$$\eta = \frac{1}{V_p R(c_s)} \int_{V_p} R(c)\, dV = \frac{D_e}{V_p R(c_s)} \int_{A_p} \nabla c\, dA \quad , \tag{B.3}$$

where V_p and A_p are the particle volume and surface area
An exact analytical solution of eq. (B.1) and its boundary conditions is available only for linear reaction rates of the form $R(C)=k_1C+k_2$ and for 'simple' catalyst geometries as e.g. an infinite slab, an infinite cylinder or a sphere. In case of a slab and first order kinetics, the exact expression of η is:

$$\eta_{slab} = \frac{\tanh(\varphi)}{\varphi} \;;\; \varphi = \delta\sqrt{\frac{k}{D_e}} \tag{B.4}$$

The dimensionless group φ is defined as the Thiele modulus. The characteristic length δ is equal to half the thickness of the slab. In case of different types of reactions and particle shapes, the particle effectiveness factor η is approximated using the normalized Thiele modulus:

$$\varphi = \frac{V_p}{A_p} \frac{R(c_s)}{\sqrt{2D_e}} \left(\int_0^{c_s} R(c)\, dc \right)^{-1/2} \tag{B.5}$$

The normalized Thiele modulus can be used for particle shapes that are not too exotic, such as e.g. cylinders, raschig rings. The difference between the values of η, calculated using eq. (B.5), and the available exact solutions for a first order reaction is less than 15 %. The difference may be significantly larger, however, when the reaction rate is nonlinear. Problems can be expected in particular when the overall reaction order approaches zero, as can be the case for Langmuir Hinshelwood types of rate expressions. In this work, the effectiveness factor is calculated using a more advanced method, which uses the combination of two asymptotic analytical expressions for η, being:

$$\Lambda \to \infty \;\Rightarrow\; \eta = \eta_\infty \approx \frac{1}{\Lambda} \left(2 \int_0^1 f(C)\; dC \right)^{1/2} = \frac{1}{\sqrt{A_0}} \tag{B.6}$$

$$\Lambda \to 0 \Rightarrow\; \eta = \eta_0 \approx 1 - \frac{\Lambda^2 \Gamma}{2} \left. \frac{df(C)}{dC} \right|_{C=1} = 1 - \frac{A_1}{2} \tag{B.7}$$

where

$$f(C) = \frac{R(Cc_s)}{R(c_s)} \;;\; C = \frac{c}{c_s},$$

and: (B.8)

$$\Lambda^2 = \frac{a^2 R(c_s)}{D_e c_s} \qquad ; \qquad a = \frac{V_p}{A_p} \tag{B.9}$$

Λ is a generalized form of the Thiele modulus and is defined as the ratio between the diffusion time $t_D = a^2/D_e$ and the reaction time $t_R = c_s/R(c_s)$. If this ratio is high, the reactant(s) do not have the time to fully penetrate the particle before they react. At very high values of Λ, the reactants are consumed within a small surface layer with a thickness much smaller than a. At the other extreme, when $\Lambda << 1$, the concentration profile is almost uniform. $\sqrt{A_0}$ is the well known Thiele modulus, eq. (B.5), which can be found in the usual textbooks in which the effectiveness factor is calculated according to eq. (B.6)

The dimensionless groups A_0 and A_1, were introduced by *Wijngaarden et al., 1998* and are called the zeroth and first 'Aris number'. They will be explained in section B.4. Parameter Γ is a geometry factor depending only on the shape of the particle. The effectiveness over the whole range of Λ is given by the equation:

$$A_0 \neq A_1: \; \eta = \left(\frac{\sigma}{\gamma} \left(1 - \sqrt{1 - \frac{2\gamma}{\sigma^2}} \right) \right)^{1/2}$$

$$A_0 = A_1: \; \eta = \frac{1}{\sqrt{\sigma}} \tag{B.10}$$

where

$$\sigma = 1 + A_0 \;;\; \gamma = 2(A_0 - A_1) \tag{B.11}$$

The derivation of eq. (B.10), in which an interpolation is made between the limiting expressions of η, is explained in paragraph B.5.

B.3 Evaluation

Fig. B.1 shows the effectiveness factor for an infinite slab in case the reaction order approaches zero, as is the case when $k_2 C >> 1$ in the following Langmuir-Hinschelwood type of reaction rate expression:

$$R(C) = \frac{k_1 C}{1 + k_2 C} \tag{B.12}$$

The new expression is almost identical to the exact numerical solution, whilst the use of the traditional approaches causes an error up to 21 %. If $k_2 C = 0$ (first order reaction), equations (B.4) and (B.10) give identical results in case of an infinite slab.

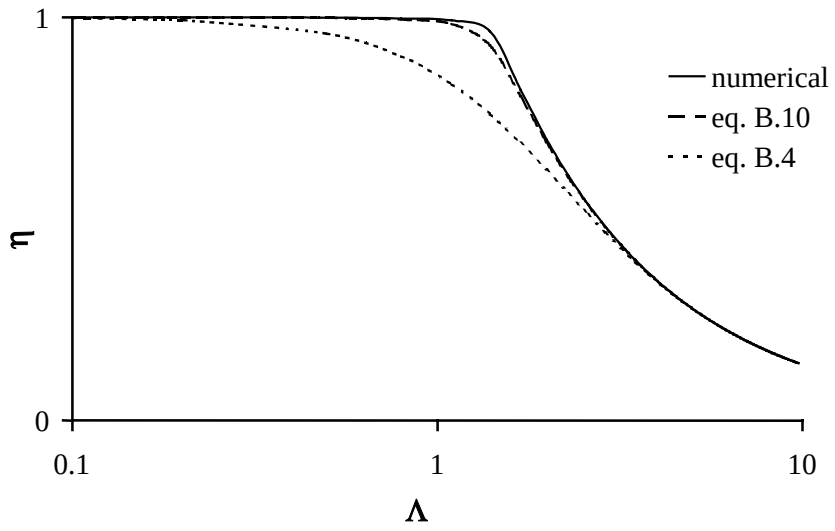

Fig. B.1 Effectiveness factor for an infinite slab according to the new (eq. B.11) and the old (eq. B.4) analytical approximation, compared to the numerical solution; $k_2 C = 100$.

If the particle is not spherical, the effectiveness factor calculated using the traditional equation will be an overestimation of the actual value, since not all of the solid does equally profit from the increase of the external surface area for a given particle volume. The new model takes the latter into account through the use of the shape factor Γ. Fig. B.2 shows the results of the different methods for a first order reaction in a Raschig-ring with a ratio of the internal and external diameter of 0.3.

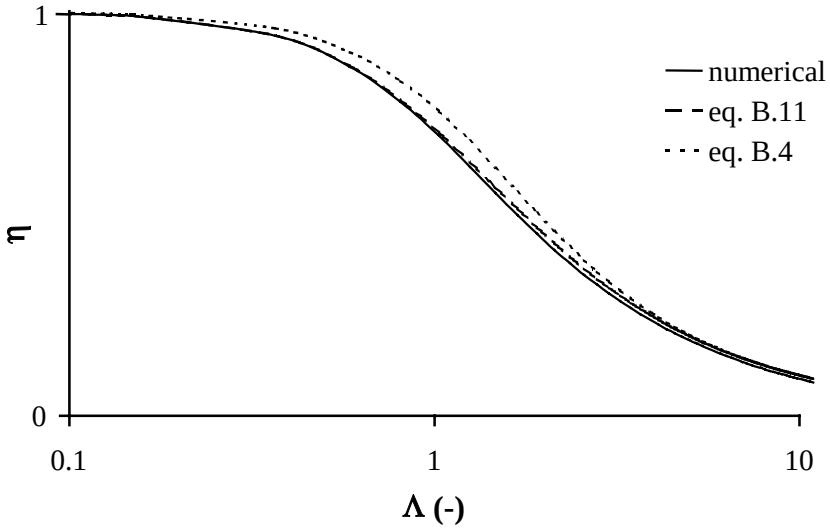

Fig. B.2 Comparison of effectiveness factors for a first order reaction in a Raschig ring with a height equal to the external diameter. The internal diameter is 0.3 times the external diameter.

The improvement of the analytical approximation of the effectiveness factor is significant. The difference between eqs. (B.4) and (B.10) increases if the order of reaction deviates from one.The expression for the rate of CO oxidation over the copper oxide catalyst used in the experimental work of this investigation depends on the concentrations of CO, CO_2 and water:

$$R = \frac{k_3 [CO]}{1 + \frac{k_3}{k_{-6}}[CO] + K_7[CO_2] + K_8[H_2O]}$$
$$k_j = k_{0,j} \exp\left(\frac{-E_a}{RT}\right) \quad ; \quad K_j = K_{0,j}\exp\left(\frac{-\Delta H_{ads}}{RT}\right) \tag{B.13}$$

Since water is inert and the local CO_2 concentration in the particles can be related to the external CO_2 concentration and the CO conversion, f(C) can be written as:

$$f(C) = \frac{k_3 C [CO]_s}{A + BC[CO]_s}, \tag{B.14}$$

where:

$$A = K_7\left([CO_s]_s + [CO]_s\right) + K_8[H_2O] \qquad ; \qquad B = \frac{k_3}{k_{-6}} - K_7 \tag{B.15}$$

B.4 Shape factor

Equation (B.1) can be written as:

$$\nabla^2 C = \frac{\Lambda^2}{a^2} f(C) \tag{B.16}$$

The boundary condition at the particle's surface is C=1. If Thiele modulus Λ approaches zero, the concentration C approaches 1 over the volume of the particle, so that eq. (B.16) becomes:

$$\Lambda \to 0 \quad \Rightarrow \quad C \to 1 \; ; \; f(C) \to 1 \quad \Rightarrow \quad \nabla^2 C = \frac{\Lambda^2}{a^2} \tag{B.17}$$

To calculate the deviation of the effectiveness factor from unity, the small variation of the reaction rate over the particle volume should be taken into account. A first order Taylor series expansion of f(C) gives:

$$\begin{aligned} f(C) &\approx f(1) - f'(1)(1-C) = 1 - f'(1)(1-C) \\ f'(C) &= \frac{df(C)}{dC} \end{aligned} \tag{B.18}$$

The effectiveness factor can be written as:

$$\eta = \frac{1}{V_p} \int_{V_p} f(C)\, dV \tag{B.19}$$

After inserting eq. (B.18), eq. (B.19) becomes:

$$\eta = 1 - \frac{f'(1)}{V_p} \int_{V_p} (1-C)\, dV \tag{B.20}$$

When designating:

$$g = \frac{(1-C)a^2}{\Lambda^2}, \tag{B.21}$$

eq. (B.20) becomes:

$$\eta = 1 - f'(1)\frac{\Lambda^2}{V_p a^2}\int_{V_p} g\,dV \equiv 1 - \frac{\Lambda^2}{2}\left(2\frac{A_p^2}{V_p^3}\int_{V_p} g\,dV\right)\left.\frac{df(C)}{dC}\right|_{C=1} \tag{B.22}$$

By introducing a dimensionless number Γ:

$$\Gamma = 2\frac{A_p^2}{V_p^3}\int_{V_p} g\,dV, \tag{B.23}$$

eq. (B.7) is obtained. The equation for g follows after combination of eqs. (B.17) and (B.21):

$$\nabla g + 1 = 0 \tag{B.24}$$

From eq. (B.21), it follows that g=0 at the surface of the particle. For simple geometries (infinite slab, cylinder or sphere), the value of the shape factor can also be obtained from the exact solution of the effectiveness factor in case $\Lambda \to \infty$. For an infinite slab and infinite cylinder and a sphere, these values are 2/3, 1 and 6/5 respectively. Catalysts are commonly available as spheres, cylinders and Raschig rings. For the ring-shaped pellets, the exact expression of the geometrical factor is given by *Wijngaarden et al., 1998*. Without noticeable loss of accuracy, this expression can be simplified to:

$$\Gamma = \frac{2}{3}\frac{I(\alpha)\left[\lambda^2 + 2\kappa(1-\alpha) + (1-\alpha)^2\right]}{\left(I(\alpha) + \frac{\lambda^2}{3}\right)(1-\alpha)^2} \tag{B.25}$$

where:

$$I(\alpha) = \alpha^2 + \frac{(1-\alpha)}{2}\left(1 + \frac{1}{\ln(\alpha)}\right) \tag{B.26}$$

α is the ratio of the internal and the external radius of the hollow cylinder and λ is the ratio of the height of the particle and the external radius. Eq. (B.25) was obtained by the method of weighed residuals (*Finlayson, 1972*). Additional corrections were made to make the solution agree with known limiting values of the effectiveness factor, from which it follows that $\kappa \approx 0.6114$. In practice, α is larger than 0.1. In this case, eq. (B.25) can be approximated by:

$$\Gamma = \frac{2}{3}\frac{\lambda^2 + 2\kappa\lambda(1-\alpha) + (1-\alpha)^2}{(1-\alpha)^2 + \lambda^2} \tag{B.27}$$

For solid cylinders, α= 0 and I(α)= 0.5, so that the shape factor is equal to:

$$\Gamma = \frac{\lambda^2 + 2\kappa\lambda + 1}{\frac{3}{2} + \lambda^2} \tag{B.28}$$

B.5 Derivation of equation (B.10)

Eq. (B.10) interpolates between the asymptotic values of the effectiveness factor η:

$$\Lambda \to 0: \qquad \eta \approx 1 - \frac{A_1}{2} \tag{B.29}$$

$$\Lambda \to \infty: \qquad \eta \approx \frac{1}{\sqrt{A_0}} \tag{B.30}$$

which are valid for arbitrary reaction kinetics and particle shapes. Its derivation is based on the assumption that the dependence of η on its two asymptotic solutions (B.29) and (B.30) does not strongly depend on the reaction kinetics and the shape of the catalyst. This assumption was proven for other systems involving simultaneous heat and mass transfer and reaction (*Polyanin et al., 1992*). Independent of the validity of this assumption, the simplified form, eq. (B.30), has been proven to be sufficient at most practical conditions. Taking into account the approximate solution for the case of $\Lambda \to 0$, for which the conventional solution may be no longer valid, should always lead to an improvement of the accuracy of η.

In case of a first order reaction, analytical expressions for the effectiveness factor are available for the following catalyst geometries:

Infinite slab:
$$\eta = \frac{\tanh(\Lambda)}{\Lambda} = \begin{cases} \Lambda \to 0: & \eta = 1 - \frac{1}{3}\Lambda^2 \\ \Lambda \to \infty: & \eta = \frac{1}{\Lambda} \end{cases} \tag{B.31}$$

Infinite cylinder: $$\eta = \frac{I_1(2\Lambda)}{\Lambda I_0(2\Lambda)} = \begin{cases} \Lambda \to 0: \quad \eta = 1 - \frac{1}{2}\Lambda^2 \\ \Lambda \to \infty: \quad \eta = \frac{1}{\Lambda} \end{cases} \tag{B.32}$$

Sphere: $$\eta = \frac{3\Lambda \coth(3\Lambda) - 1}{3\Lambda^2} = \begin{cases} \Lambda \to 0: \quad \eta = 1 - \frac{3}{5}\Lambda^2 \\ \Lambda \to \infty: \quad \eta = \frac{1}{\Lambda} \end{cases} \tag{B.33}$$

where:

$$R(C) = kC \quad ; \quad \Lambda = \frac{V_p^2}{A_p^2}\frac{k}{D_e} \tag{B.34}$$

The above expressions can be written as eqs. (B.29) and (B.30), since, for first order kinetics, $A_0 = \Lambda^2$ and $A_1 = \Lambda^2\Gamma$ (Γ= 2/3, 1 and 6/5 for the different particle shapes in this order). The predictions of eqs. (B.31)-(B.33) for the same value of Λ are rather similar and can be approximated as:

$$\eta = \frac{1}{\sqrt{1+\Lambda^2}} = \frac{1}{\sqrt{1+A_0^2}} \tag{B.35}$$

Equation (B.35) is a good approximation of the effectiveness factor for any catalyst shape when $\Lambda \to \infty$ and of (B.32) over the entire range of Λ. The maximum difference between this approximation and the exact solution for an infinite cylinder, eq. (B.32), is 4%. For $\Lambda \to 0$, eq. (B.35) gives:

$$\Lambda \to 0: \quad \eta = \frac{1}{\sqrt{1+A_0}} \approx 1 - \frac{A_0}{2}, \tag{B.36}$$

whereas the exact asymptotic expression is given by eq. (B.29). For an infinite cylinder, $A_0 = A_1$ and the asymptotic and the approximate solution are identical. For the other shapes mentioned above, the asymptotic value of (B.35) for $\Lambda \to 0$ differs from the exact solution. This difference is not pronounced in case of a first order reaction, since the difference between A_0 and A_1 is small. For other types of kinetics or particle shapes, the difference may not be neglected. To improve the predicted effectiveness factor for an infinite slab or a sphere when $\Lambda \to 0$, eq. (B.35) is modified to:

$$\eta = \frac{1}{\sqrt{1+\phi_0 A_0 + \phi_1 A_1}} \tag{B.37}$$

This expression should be valid for arbitrary values of Λ. ϕ_0 and ϕ_1, which are functions of Λ and/or η should meet the following criteria:

$$\begin{aligned} &\Lambda \to 0: \quad \phi_0 \to 0 \quad ; \quad \phi_1 \to 1 \\ &\Lambda \to \infty: \quad \phi_0 \to 1 \quad ; \quad \phi_1 \to 0 \end{aligned} \tag{B.38}$$

ϕ_0 and ϕ_1 are obtained by applying eq. (B.37) to two problems that have a known solution of η.

First-order reaction in an infinite cylinder:
In this case, $A_0 = A_1$ and the effectiveness factor is given by eq. (B.35):

$$\frac{1}{\sqrt{1+(\phi_0+\phi_1)A_0}} = \frac{1}{\sqrt{1+A_0}} \quad \Rightarrow \quad \phi_0 + \phi_1 = 1 \tag{B.39}$$

Zeroth-order reaction in an infinite slab:
In this case, $A_1=0$, since $\partial f(C)/\partial C=0$. Eq. (B.37) gives:

$$\eta = \frac{1}{\sqrt{1+\phi_0 A_0}} \quad \Rightarrow \quad \phi_0 A_0 = \frac{1}{\eta^2} - 1 \tag{B.40}$$

The exact effectiveness factor is:

$$\eta == \begin{cases} A_0 < 1: & \eta = 1 \\ A_0 > 1: & \eta = \dfrac{1}{\sqrt{A_0}} \end{cases} \tag{B.41}$$

Equation (B.40) is the exact solution if:

$$\phi_0 = 1 - \eta^2 \tag{B.42}$$

η is obtained by combing eqs. (B.37), (B.39) and (B.42):

$$\eta = \frac{1}{\sqrt{1+\left(1-\eta^2\right)A_0+\eta^2 A_1}} \tag{B.43}$$

or:

$$\eta = \left(\frac{\sigma}{\gamma}\left(1-\sqrt{1-\frac{2\gamma}{\sigma^2}}\right)\right)^{1/2} \tag{B.44}$$

with:

$$\sigma=1+A_0 \;\; ; \;\; \gamma=2\left(A_0-A_1\right) \tag{B.45}$$

If $A_1=A_0$, then:

$$\eta=\frac{1}{\sqrt{\sigma}} \tag{B.46}$$

Notation

A_0, A_1	Aris numbers	-
A_p	particle surface	m^2
a	specific surface area	$m^2\ m^{-3}$
C	dimensionless concentration	-
c	concentration	mole m^{-3}
D_e	effective diffusion coefficient	$m^2\ s^{-1}$
E_a	activation energy	J $mole^{-1}$
ΔH_{ads}	adsorption enthalpy	J $mole^{-1}$
$k_{0,i}$	frequency factor reaction rate constant	s^{-1}
k, k_i	reaction rate constant	s^{-1}
$K_{0,i}$	frequency factor adsorption constant	-
K_i	adsorption constant	-
R	reaction rate	mole $m^{-3}\ s^{-1}$
	gas constant	J $mole^{-1}\ K^{-1}$
t_D	diffusion time	s
V_p	particle volume	m^3

Greek

α	ratio of internal and external diameter of Raschig ring	-
δ	characteristic length	m
Γ	geometry factor	-
η	effectiveness factor	-
η_0	asymptotic value of η in case $\Lambda \rightarrow 0$	-
η_∞	asymptotic value of η in case $\Lambda \rightarrow \infty$	-
φ	Thiele modulus	-
Λ	normalized Thiele modulus	-
λ	ratio of height and radius of a Raschig ring or pellet	-

sub- and superscripts

p	particle
s	surface

Appendix C.

Measurement of thermal conductivity of Catalyst

The thermal conductivity of the catalyst is used to calculate the contribution of the solid phase to the overall effective thermal conductivity and to estimate whether or not intra-particle temperature profiles can be neglected or not. The thermal conductivity was measured using a step-response method. A particle with a known uniform initial temperature was heated in a fluidized bed of fine sand, together with an alumina particle of the same size and shape. The particle-to-bed heat transfer coefficient is calculated from the temperature curve measured for the aluminum particle, of which the temperature can be assumed to be uniform during the experiment ($\lambda_{Al} \approx$ 270 W m^{-1} K^{-1}). The thermal conductivity of the particle, λ_p was calculated by minimizing the difference between the measured and calculated temperature at the center of the particle. The temperature dependence of the heat capacity of the used aluminum and the catalyst are calculated from data given in *Lide et al. 1999.* For the catalyst, the heat capacity was calculated as the average of that of aluminum oxide (71 wt%) and Cu(I) oxide (29 wt%)

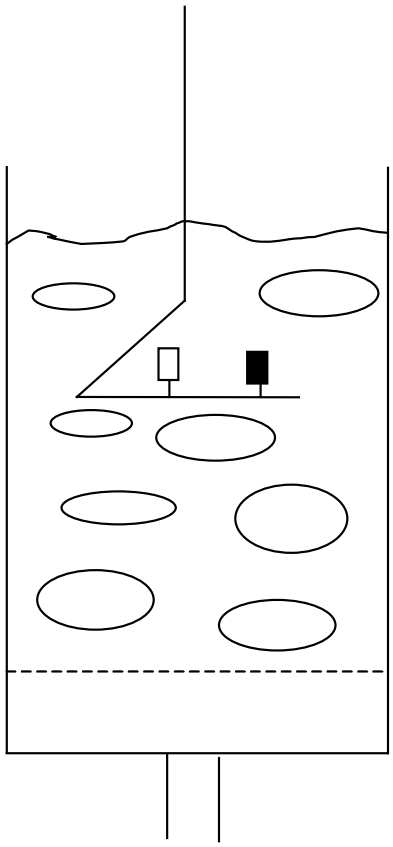

Fig. C.1 Setup used for hermal conductivity measurement.

The temperature at the center of the particles was measured by 0.5 mm Type-K thermocouples that were inserted from the top. In between experiments, the particles were buried in desiccant material to avoid adsorption of water from the air. If this was omitted, the energy necessary to desorb the water during the heating of the particle was found to have a significant influence on the heating rate.

The experimental procedure is quite simple: the probe containing the two particles was dropped into the hot fluidized bed as rapidly as possible. The fluidized bed was operated at the maximum flow rate at ambient pressure, at which the sand remained in the reactor. The

used flow rate was the same for all experiments. The position of the sample in the fluidized bed and the orientation of the particles with respect to the probe did not have a noticeable effect on the measured particle-to-bed heat transfer coefficient, which was 560 W m^{-2} K^{-1} at a bed temperature of 80 °C. The difference over 5 experiments was less than 5 %. The value of the heat transfer coefficient linearly increased with the bed temperature up to 700 $Wm^{-2}K^{-1}$ at 240 °C. This temperature dependence is mainly due to an increase of the superficial gas velocity with increasing temperature. Experiments have been performed at bed temperatures of 80, 155 and 233 °C using two catalyst particles (D_p=5.5, H_p=11.5 and 12.5 mm). The temperature profiles measured at three different temperatures using catalyst sample 1 (H_p=11.5 mm) are shown in Fig. C.2

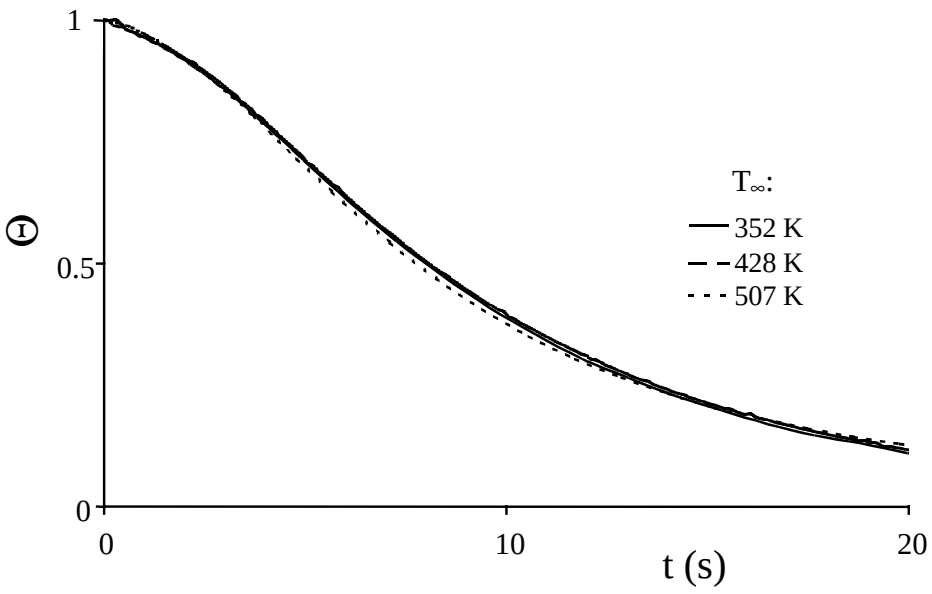

Fig. C.2 Dimensionless temperature as function of time during experiments at different bed temperatures (sample 1), $\Theta=(T-T_\infty)/(T_0-T_\infty)$

The temperature at the tip of the thermocouple as function of time was calculated by solving the following differential equation:

$$\rho\frac{\partial\left(c_pT\right)}{\partial t}=\frac{\partial}{\partial z}\left(\lambda_p\frac{\partial T}{\partial z}\right)+\frac{1}{r}\frac{\partial}{\partial r}\left(r\lambda_p\frac{\partial T}{\partial r}\right) \qquad \text{(C.1)}$$

When taking the coordinates r and z relative to the center of the particle, the following boundary conditions apply:

$$r=0:\ \frac{\partial T_p}{\partial r}=0 \quad r=\frac{D_p}{2}:\ -\lambda_p \frac{\partial T_p}{\partial r}=\alpha\left(T_p-T_b\right)$$
$$z=0:\ \frac{\partial T_p}{\partial z}=0 \quad r=\frac{H_p}{2}:\ -\lambda_p \frac{\partial T_p}{\partial z}=\alpha\left(T_p-T_b\right) \qquad \text{(C.2)}$$

The temperature distributions in the particles were calculated numerically using the method of finite differences. For simple particle shapes, e.g. a sphere or a cylinder, analytical solutions are available (*Carlslaw and Jaeger, 1959*).

When it is assumed the catalyst thermal conductivity is constant during each experiment, the value of λ_p increases when increasing the bed temperature, as is shown in Fig. C.3. When a linear dependence of the effective particle thermal conductivity on temperature is assumed, the following expression is obtained after optimizing λ_p for the experiments at all temperatures simultaneously:

$$\lambda_p=0.21+1.5\times10^{-4}T \quad Wm^{-1}K^{-1} \qquad \text{(C.3)}$$

Since the temperature profiles shown in Fig. C.2 are very similar, the increase of the thermal conductivity is compensated by the increase of the heat capacity c_p with temperature.

In case of a porous medium, the effective thermal conductivity can either increase or decrease with temperature, depending on the solid structure (pore size distribution, porosity) and the medium which is present within the pores, see *Litovski et al. 1995*. The effective thermal conductivity is determined by the sum of the contributions of conduction in the solid and the gas phase and radiation between the pore walls. The thermal conductivity of solids generally

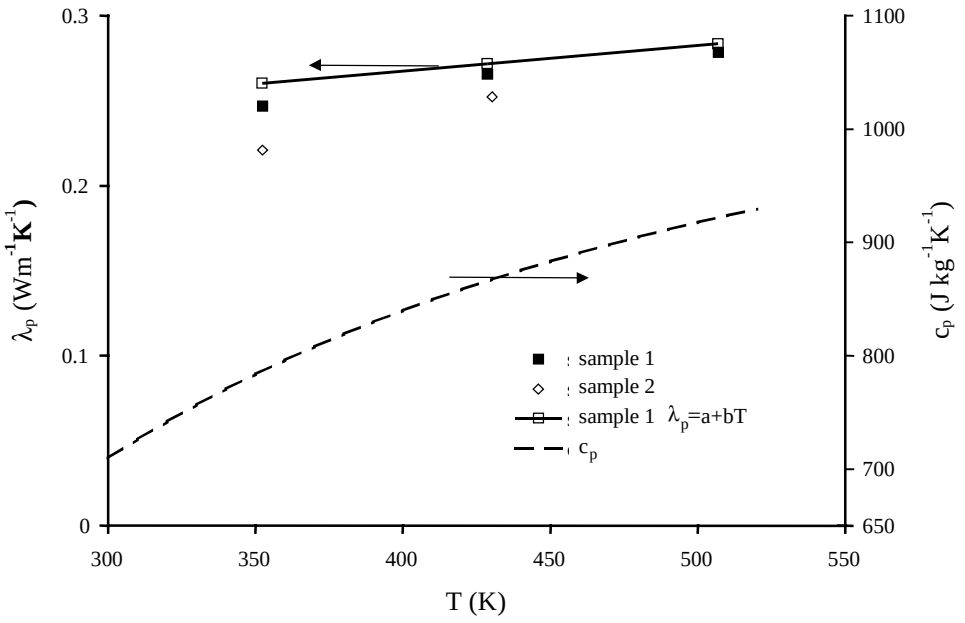

Fig. C.3 Effective thermal conductivity of a catalyst particle as function of temperature.

decreases with temperature, whilst that of the gas phase increases, as does the heat transport due to radiation.

The influence of pressure on the effective thermal conductivity has not been tested experimentally. The pressure dependence of the thermal conductivity due to the contribution of the gas phase depends on the pore size. In the case of pore sizes much larger than the mean free path of the gas molecules, the thermal conductivity will be influenced only little, since the thermal conductivity of gases is only weakly pressure dependent. For pore diameters comparable to the mean free path of the molecules, the effective thermal conductivity will increase with pressure due to an increase of the frequency of the collision between the gas molecules and the pore wall.

Notation

c_p	heat capacity	J kg^{-1} K^{-1}
D_p	diameter of cylindrical particle	m
H_p	height of cylindrical particle	m
r	radial coordinate	m
T	temperature	K
t	time	s
z	axial coordinate	m

Greek

λ	thermal conductivity	W m^{-1} K^{-1}
ρ	density	kg m^{-3}

sub- and superscripts

b	bed
p	particle

Appendix D

Derivation the δ-model

In this appendix, correction factors are calculated, which should be used in a one-dimensional reactor model in order to account for the influence of non-uniform radial temperature and concentration profiles. These radial distributions are determined by the following heat- and mass balance equations of the two-dimensional homogeneous reactor model:

$$(\varepsilon\rho_f c_{p,f} + (1-\varepsilon)\rho_s c_{p,s})\frac{\partial T}{\partial t} + u\rho_f c_{p,f}\frac{\partial T}{\partial z} - (-\Delta H_r)R(c,T) = \lambda_{e,r}\frac{1}{r}\frac{\partial}{\partial r}\left(r\frac{\partial T}{\partial r}\right) \tag{D.1}$$

$$(\varepsilon + (1-\varepsilon)\varepsilon_s)\frac{\partial c}{\partial t} + u\frac{\partial c}{\partial z} + R(c,T) = D_{e,r}\frac{1}{r}\frac{\partial}{\partial r}\left(r\frac{\partial c}{\partial r}\right) \tag{D.2}$$

$$r=0 \qquad \frac{\partial T}{\partial r} = 0 \qquad \frac{\partial c}{\partial r} = 0 \tag{D.3}$$

$$r=R_t \qquad -\lambda_{e,r}\frac{\partial T}{\partial r} = \alpha_w (T-T_w) \qquad \frac{\partial c}{\partial r} = 0 \tag{D.4}$$

Here, a single-reaction is considered. The model can be easily extended for systems with parallel and consecutive reactions, as is shown in Chapter 5.

For convenience, the following dimensionless variables are introduced, which may differ from those used in previous chapters.

$$\tau = \frac{tu}{R_t} \qquad x = \frac{z}{R_t} \qquad y = \frac{r}{R_t} \qquad \Theta = \frac{T-T_0}{T_0} \qquad C = \frac{c}{c_0} \tag{D.5}$$

T_0 and c_0 are some temperature and concentration characteristic for the system, e.g. the conditions at the reactor inlet. Using these dimensionless variables, the balances (D.1) and (D.2) can be rewritten as:

$$PE_{h,r}\left[(\varepsilon + (1-\varepsilon)\frac{\rho_s c_{p,s}}{\rho_f c_{p,f}})\frac{\partial\Theta}{\partial\tau} + \frac{\partial\Theta}{\partial x}\right] - q(C,\Theta) = \frac{1}{y}\frac{\partial}{\partial y}\left(y\frac{\partial\Theta}{\partial y}\right) \tag{D.6}$$

$$PE_{m,r}\left[(\varepsilon+(1-\varepsilon)\varepsilon_s)\frac{\partial C}{\partial \tau}+\frac{\partial C}{\partial x}\right]+p(C,\Theta)=\frac{1}{y}\frac{\partial}{\partial y}\left(y\frac{\partial C}{\partial y}\right) \tag{D.7}$$

$$y=0 \qquad \frac{\partial \Theta}{\partial y}=0 \qquad \frac{\partial C}{\partial y}=0 \tag{D.8}$$

$$y=1 \qquad -\frac{\partial \Theta}{\partial y}=Bi(\Theta-\Theta_w) \qquad \frac{\partial C}{\partial y}=0 \tag{D.9}$$

where:

$$PE_{h,r}=\frac{R_t u \rho_f c_{p,f}}{\lambda_{e,r}}=Pe_{h,r}\frac{R_t}{d_p} \qquad PE_{m,r}=\frac{R_t u}{D_{e,r}}=Pe_{m,r}\frac{R_t}{d_p} \tag{D.10}$$

$$p(C,\Theta)=\frac{R_t R(C,\Theta)}{u c_0}PE_{m,r} \qquad q(C,\Theta)=\Delta\Theta_{ad}\ p(C,\Theta)\frac{PE_{h,r}}{PE_{m,r}} \tag{D.11}$$

$$Bi=\frac{\alpha_w R_t}{\lambda_{e,r}} \qquad \Theta_w=\frac{T_w-T_0}{T_0} \qquad \Delta\Theta_{ad}=\frac{\Delta T_{ad}}{T_0}=\frac{-\Delta H_r c_0}{\rho_f c_{p,f} T_0} \tag{D.12}$$

Here, the definition of the dimensionless temperature differs from that used elsewhere in this thesis.

Eqs. (D.6) and (D.7) can be abbreviated by introduction of the following differential operators:

$$L_h=PE_{h,r}\left[\left(\varepsilon+(1-\varepsilon)\frac{\rho_s c_{p,s}}{\rho_f c_{p,f}}\right)\frac{\partial}{\partial \tau}+\frac{\partial}{\partial x}\right] \tag{D.13}$$

$$L_m=PE_{m,r}\left[\left(\varepsilon+(1-\varepsilon)\varepsilon_s\right)\frac{\partial}{\partial \tau}+\frac{\partial}{\partial x}\right], \tag{D.14}$$

After substitution, the heat- and mass balance can be written as:

$$L_h\Theta-q(C,\Theta)=\frac{1}{y}\frac{\partial}{\partial y}\left(y\frac{\partial \Theta}{\partial y}\right) \tag{D.15}$$

$$L_m C + p(C,\Theta) = \frac{1}{y}\frac{\partial}{\partial y}\left(y \frac{\partial C}{\partial y} \right) \tag{D.16}$$

To obtain the equations for the one-dimensional model, eqs. (D.15) and (D.16) have to be averaged over the cross-section of the bed to obtain:

$$L_h \bar{\Theta} - \bar{q}(C,\Theta) = -2Bi\left(\Theta\big|_{y=1} - \Theta_w \right) \tag{D.17}$$

$$L_m \bar{C} + \bar{p}(C,\Theta) = 0 \tag{D.18}$$

where an overbar on a quantity denotes its cross-sectionally averaged value, as defined for an axisymmetrical problem by:

$$\bar{\Psi} = 2\int_0^1 y\Psi(y)\,dy \tag{D.19}$$

The right-hand side of (D.17) is the result of integration of the right-hand side of eq. (D.15) over the cross section and using boundary condition (D.9).
In order to use eqs. (D.17) and (D.18) it is necessary to relate the averaged production terms $\bar{q}(C,\Theta)$ and $\bar{p}(C,\Theta)$ and $\Theta\big|_{y=1}$ to the average concentration and temperature. The result depends on the shape of the radial concentration and temperature profiles. Here, the method of successive approximation, similar to that used by *Westerterp et al., 1995* will be applied.

Successive approximation of radial temperature profile

The idea behind the following derivation is that the shape of the radial profiles is much more important for the correct calculation of the right hand sides of the two-dimensional balance equations (D.15) and (D.16) than of the left hand side.

Zeroth approximation

The one-dimensional model follows immediately from eqs. (D.17)and (D.18) if the radial distributions of temperature and concentration can be considered as uniform:

$$\Theta^{(0)}(\tau,x) = \bar{\Theta} \quad ; \quad C^{(0)}(\tau,x) = \bar{C} \tag{D.20}$$

In this case, $\bar{q} = q\left(\bar{C}, \bar{\Theta}\right)$, $\bar{p} = p\left(\bar{C}, \bar{\Theta}\right)$ and $\Theta\big|_{y=1} = \bar{\Theta}$. The model equations are:

$$L_h \bar{\Theta} - \bar{q} = -2Bi\left(\bar{\Theta} - \Theta_w\right) \tag{D.21}$$

$$L_m \bar{C} + \bar{p} = 0 \tag{D.22}$$

These equations represent the conventional one-dimensional model when Bi→ 0 and can be considered as a zeroth approximation of the one-dimensional model.

First approximation

The first approximation is found by substitution of the left-hand side of eqs. (D.15) and (D.16). The radial temperature and concentration profiles can be obtained by substitution of (D.20) into the left-hand side of eqs. (D.15) and (D.16):

$$L_h \Theta^{(0)} - q\left(C^{(0)}, \Theta^{(0)}\right) = A_h(\tau, x) = \frac{1}{y}\frac{\partial}{\partial y}\left(y\frac{\partial \Theta^{(1)}}{\partial y}\right) \tag{D.23}$$

$$L_m C^{(0)} - p\left(C^{(0)}, \Theta^{(0)}\right) = A_m(\tau, x) = \frac{1}{y}\frac{\partial}{\partial y}\left(y\frac{\partial C^{(1)}}{\partial y}\right) \tag{D.24}$$

Equation (D.23) has the analytical solution:

$$\Theta^{(1)} = A_h\frac{y^2}{4} + k_1 \ln(y) + k_2 = A_h\frac{y^2}{4} + k_2, \tag{D.25}$$

in which k_1 and k_2 are integration constants. k1 is zero, since $\Theta^{(1)}$ cannot be minus infinity at y=0. k_2 can be expressed through the average temperature:

$$k_2 = \overline{\Theta^{(1)}} - \frac{1}{8}A_h \tag{D.26}$$

and:

$$\Theta^{(1)} = \bar{\Theta}^{(1)} + A_h\left(\frac{y^2}{4} - \frac{1}{8}\right) \tag{D.27}$$

From the boundary conditions at y=1, eq. (D.9), it follows that:

$$A_h = -\frac{8Bi}{Bi+4}\left(\overline{\Theta}^{(1)} - \Theta_w\right) \tag{D.28}$$

By assuming that the average temperatures of the zeroth and the first approximation are equal, $\overline{\Theta}^{(0)} = \overline{\Theta}^{(1)}$, we get the equation for the average temperature in the first approximation from eq. (D.28):

$$L_h \overline{\Theta}^{(1)} - q\left(\overline{C}^{(1)}, \overline{\Theta}^{(1)}\right) = -\frac{8Bi}{Bi+4}\left(\overline{\Theta}^{(1)} - \Theta_w\right) \tag{D.29}$$

The first approximation of the radial temperature profile, (D.27), can now be expressed as function of the radial average temperature:

$$\Theta^{(1)}(\tau,x,y) = \overline{\Theta}^{(1)}(\tau,x) + \Delta\Theta(\tau,x)\left(1-2y^2\right) \quad ; \quad \Delta\Theta(\tau,x) = \frac{Bi\left(\overline{\Theta} - \Theta_w\right)}{Bi+4} \tag{D.30}$$

After applying the same procedure to the mass balance, the following balance equation is obtained:

$$L_m \overline{C}^{(1)} - p\left(\overline{C}^{(1)}, \overline{\Theta}^{(1)}\right) = 0 \tag{D.31}$$

Second Approximation

The next, second approximation is found from the equations:

$$L_h \Theta^{(1)} - q\left(C^{(1)}, \Theta^{(1)}\right) = 4\frac{\partial}{\partial\xi}\left(\xi\frac{\partial\Theta^{(2)}}{\partial\xi}\right) \tag{D.32}$$

$$L_m C^{(1)} + p\left(C^{(1)}, \Theta^{(1)}\right) = 4\frac{\partial}{\partial\xi}\left(\xi\frac{\partial C^{(2)}}{\partial\xi}\right) \tag{D.33}$$

$$\varphi = 0 \qquad \frac{\partial\Theta}{\partial\xi} = 0 \qquad \frac{\partial C}{\partial\xi} = 0 \tag{D.34}$$

$$\varphi=1 \qquad -2\frac{\partial\Theta}{\partial\xi}=\mathrm{Bi}\left(\Theta-\Theta_w\right) \qquad \frac{\partial C}{\partial\xi}=0 \tag{D.35}$$

$$C^{(1)}\left(\tau,x\right)=\overline{C}\left(\tau,x\right) \tag{D.36}$$

$$\Theta^{(1)}\left(\tau,x,\varphi\right)=\overline{\Theta}\left(\tau,x\right)+\Delta\Theta\left(\tau,x\right)\left(1-2\xi\right) \tag{D.37}$$

For convenience, y has been replaced by $\xi = y^2$. Integration of (D.32) over ξ between 0 and ξ, taking into account the boundary conditions at $\xi = 0$, gives:

$$\xi L_h\Theta^{(1)}+\left(\xi-\xi^2\right)L_h\Delta\Theta-\int_0^{\xi}q\left(C^{(1)},\overline{\Theta}^{(1)}\right)d\xi=4\xi\frac{\partial\Theta^{(2)}}{\partial\xi} \tag{D.38}$$

In order to calculate the integral in the above equation, we assume that the reaction rate can be presented as an exponential function of temperature. In many cases, the dependence of the reaction rate on concentration and temperature can be presented as:

$$R\left(c,T\right)=f\left(c\right)\exp\left(-\frac{E_a}{RT}\right) \tag{D.39}$$

Further, we will use the Frank-Kamenetski approximation of eq. (D.39) around the average temperature over the cross-section, $\overline{T}$:

$$\frac{1}{T}=\frac{1}{T_0\left(1+\Theta\right)}=\frac{1}{T_0\left(1+\overline{\Theta}\right)\left(1+\frac{\Theta-\overline{\Theta}}{1+\overline{\Theta}}\right)}\approx\frac{1}{T_0\left(1+\overline{\Theta}\right)}\left(1-\frac{\Theta-\overline{\Theta}}{1+\overline{\Theta}}\right) \tag{D.40}$$

and:

$$R\left(c,T\right)=R\left(c,\overline{T}\right)\exp\left(\gamma_0\frac{\Theta-\overline{\Theta}}{\left(1+\overline{\Theta}\right)^2}\right)=R\left(c,\overline{T}\right)\exp\left(\gamma\left(\overline{\Theta}\right)\left(\Theta-\overline{\Theta}\right)\right) \tag{D.41}$$

γ is the dimensionless activation energy at the average temperature:

$$\gamma\left(\Theta\right)=\gamma_0\left(\frac{T_0}{\overline{T}}\right)^2=\gamma_0\frac{1}{\left(1+\overline{\Theta}\right)^2}\qquad;\qquad\gamma_0=\frac{E_a}{RT_0}\tag{D.42}$$

Using eq. (D.41) and after omitting subscript (1), eq. (D.38) can be written as:

$$\xi L_h\overline{\Theta}+\left(\xi-\xi^2\right)L_h\Delta\Theta-Q\left(\overline{C},\overline{\Theta}\right)\int_0^\xi e^{-2\delta\xi}d\xi=4\xi\frac{\partial\Theta^{(2)}}{\partial\xi}\tag{D.43}$$

or:

$$\varphi L_h\overline{\Theta}+\left(\xi-\xi^2\right)L_h\Delta\Theta+\frac{Q\left(\overline{C},\overline{\Theta}\right)}{2\delta}\left(e^{-2\delta\xi}-1\right)=4\xi\frac{\partial\Theta^{(2)}}{\partial\xi}\tag{D.44}$$

where:

$$P\left(\overline{C}^{(1)},\overline{\Theta}^{(1)}\right)=p\left(C^{(1)},\overline{\Theta}^{(1)}\right)\exp\left(\delta\right)\quad;\quad Q\left(\overline{C}^{(1)},\overline{\Theta}^{(1)}\right)=q\left(C^{(1)},\overline{\Theta}^{(1)}\right)\exp\left(\delta\right)\tag{D.45}$$

and:

$$\delta=\gamma\Delta\Theta=\gamma\frac{Bi\left(\Theta-\Theta_w\right)}{Bi+4}\tag{D.46}$$

Similarly, the mass balance gives:

$$\xi L_m\overline{C}-\frac{P\left(\overline{C},\overline{\Theta}\right)}{2\delta}\left(e^{-2\delta\xi}-1\right)=4\xi\frac{\partial C^{(2)}}{\partial\xi}\tag{D.47}$$

After a second indefinite integration, we obtain:

$$\xi L_h\overline{\Theta}+\left(\varphi-\frac{\xi^2}{2}\right)L_h\Delta\Theta+\frac{Q\left(\overline{C},\overline{\Theta}\right)}{2\delta}\int_0^\xi\frac{e^{-2\delta\xi}-1}{\xi}d\xi=4\Theta^{(2)}\tag{D.48}$$

and:

$$\xi L_m\overline{C}-\frac{P\left(\overline{C},\overline{\Theta}\right)}{2\delta}\int_0^\xi\frac{e^{-2\delta\xi}-1}{\xi}d\xi=4C^{(2)}\tag{D.49}$$

The integral in eqs. (D.48) and (D.49) can be evaluated after Taylor series expansion:

$$I(x)=\int\frac{e^{-x}-1}{x}dx=\int\frac{\left[\sum_{n=0}^{\infty}(-1)^n\frac{x^n}{n!}\right]-1}{x}dx=\int\sum_{n=1}^{\infty}(-1)^n\frac{x^{n-1}}{n!}dx=\sum_{n=1}^{\infty}(-1)^n\frac{x^n}{nn!} \tag{D.50}$$

So that:

$$\xi L_h\overline{\Theta}+\left(\xi-\frac{\xi^2}{2}\right)L_h\Delta\Theta+\frac{Q\left(\overline{C},\overline{\Theta}\right)}{2\delta}\sum_{n=1}^{\infty}(-1)^n\frac{(2\delta\xi)^n}{nn!}+k_h=4\Theta^{(2)} \tag{D.51}$$

and:

$$\xi L_m\overline{C}-\frac{P\left(\overline{C},\overline{\Theta}\right)}{2\delta}\sum_{n=1}^{\infty}(-1)^n\frac{(2\delta\xi)^n}{nn!}+k_m=4C^{(2)} \tag{D.52}$$

Just as was done to obtain the profiles of the first approximation, the integration constants k_h and k_m are obtained by integration of eqs. (D.51) and (D.52):

$$k_h=4\overline{\Theta}-\frac{1}{2}L_h\overline{\Theta}-\left(\frac{1}{2}-\frac{1}{6}\right)L_h\Delta\Theta-\frac{Q\left(\overline{C},\overline{\Theta}\right)}{2\delta}\sum_{n=1}^{\infty}(-1)^n\frac{(2\delta)^n}{nn!(n+1)} \tag{D.53}$$

$$k_m=4\overline{C}-\frac{1}{2}L_m\overline{C}+\frac{P\left(\overline{C},\overline{\Theta}\right)}{2\delta}\sum_{n=0}^{\infty}(-1)^n\frac{(2\delta)^n}{nn!(n+1)} \tag{D.54}$$

After this, the radial distributions of temperature and concentration are:

$$\Theta^{(2)}=\overline{\Theta}+\frac{1}{4}\left[L_h(\xi-2)+L_h\Delta\Theta\left(\xi-\frac{\xi^2}{2}-\frac{1}{3}\right)+\frac{Q\left(\overline{C},\overline{\Theta}\right)}{2\delta}\sum_{n=1}^{\infty}(-1)^n\frac{(2\delta)^n}{nn!}\left(\xi^n-\frac{1}{n+1}\right)\right] \tag{D.55}$$

and:

$$C^{(2)}=\overline{C}+\frac{1}{4}\left[L_m\overline{C}-\frac{P\left(\overline{C},\overline{\Theta}\right)}{2\delta}\sum_{n=1}^{\infty}(-1)^n\frac{(2\delta)^n}{nn!}\left(\xi^n-\frac{1}{n+1}\right)\right] \tag{D.56}$$

The equations for the average temperature and concentration are obtained by substituting eqs. (D.51)and (D.52) into the boundary conditions at $\xi=1$:

$$\frac{1}{2}L_h\overline{\Theta}+\frac{1}{2}\frac{Q\left(\overline{C},\overline{\Theta}\right)}{2\delta}\sum_{n=1}^{\infty}(-1)^n\frac{(2\delta)^n}{n!}$$
$$+Bi\left(\overline{\Theta}-\Theta_w+\frac{1}{8}L_h\overline{\Theta}+\frac{1}{24}L_h\Delta\Theta+\frac{q\left(\overline{C},\overline{\Theta}\right)}{8\delta}\sum_{n=1}^{\infty}(-1)^n\frac{(2\delta)^n}{(n+1)n!}\right)=0 \qquad (D.57)$$

$$L_m\overline{C}-\frac{P\left(\overline{C},\overline{\Theta}\right)}{2\delta}\sum_{n=1}^{\infty}(-1)^n\frac{(2\delta)^n}{n!}=0 \qquad (D.58)$$

After replacing the series by exponents, these equations can be rewritten as:

$$\frac{1}{2}L_h\overline{\Theta}+\frac{1}{2}Q\left(\overline{C},\overline{\Theta}\right)\frac{e^{-2\delta}-1}{2\delta}+Bi\left(\overline{\Theta}-\Theta_w+\frac{1}{8}L_h\overline{\Theta}+\frac{1}{24}L_h\Delta\Theta-\frac{Q\left(\overline{C},\overline{\Theta}\right)}{8\delta}\frac{e^{-2\delta}-1+2\delta}{2\delta}\right)=0 \qquad (D.59)$$

$$L_m\overline{C}-P\left(\overline{C},\overline{\Theta}\right)\frac{e^{-2\delta}-1}{2\delta}=0 \qquad (D.60)$$

Using eqs. (D.45) and (D.46) and:

$$L_h\Delta\Theta(\tau,x)=\frac{Bi}{Bi+4}\left(L_h\overline{\Theta}-L_h\Theta_w\right), \qquad (D.61)$$

the one-dimensional equations in case of constant wall temperature become:

$$L_h\overline{\Theta}-q\left(\overline{C},\overline{\Theta}\right)\frac{3(Bi+4)}{12+6Bi+Bi^2}\left(\frac{\sinh(\delta)}{\delta}+\frac{Bi}{4\delta}\left(e^{\delta}-\frac{\sinh(\delta)}{\delta}\right)\right)+\frac{6Bi(Bi+4)}{12+6Bi+Bi^2}\left(\overline{\Theta}-\Theta_w\right)=0 \qquad (D.62)$$

$$L_m\overline{C}+p\left(\overline{C},\overline{\Theta}\right)\frac{\sinh(\delta)}{\delta}=0 \qquad (D.63)$$

The 'correction factors' F_M and F_H used in Chapter 5 are equal to the terms with which the production terms are multiplied. In that chapter, the definition of parameter δ looks somewhat different, which is only due to the use of a different dimensionless temperature.
According to the given derivation, the average heat production rate and the average mass consumption rate are:

$$\bar{q}=2\int_0^1 y\,q(\Theta)\,dy=\int_0^1 q(\varphi)\,d\varphi=\int_{\bar{\Theta}+\Delta\Theta}^{\bar{\Theta}-\Delta\Theta}\frac{q(\Theta)}{\frac{\partial\Theta}{\partial y}}d\Theta=\frac{1}{2\Delta\Theta}\int_{\bar{\Theta}-\Delta\Theta}^{\bar{\Theta}+\Delta\Theta} q(\Theta)\,d\Theta \tag{D.64}$$

and:

$$\bar{p}=\frac{1}{2\Delta\Theta}\int_{\bar{\Theta}-\Delta\Theta}^{\bar{\Theta}+\Delta\Theta} p(\Theta)\,d\Theta \tag{D.65}$$

It is easy to show that these relations hold true for arbitrary radial temperature profiles.
It is worth noting that, in case of no reaction, eq. (D.62) coincides with the heat balance equation derived by *Dixon, 1996*, who derived an improved equation for the overall heat transfer coefficient. The derivation given in this appendix shows that, in contrast to Dixon, the overall heat transfer coefficient is influenced by chemical reaction. This can be seen from eq. (D.62), taking into account that the average reaction rate is:

$$\bar{q}\left(\bar{C},\Theta\right)=q\left(\bar{C},\bar{\Theta}\right)\frac{\sinh(\delta)}{\delta} \tag{D.66}$$

Notation

A_h, A_m	sum of source- and accum. and axial transport	
C	dimensionless concentration	-
c	concentration	mole m^{-3}
c_p	heat capacity	J kg^{-1} K^{-1}
$D_{e,r}$	effective radial diffusion coefficient	m^2 s^{-1}
d_p	particle diameter	m
ΔH_r	reaction enthalpy	J $mole^{-1}$
I	integral	
k_1, k_2	integration constants	-
L_h, L_m	differential operators in heat and mass balance	-
P	p at radial average temperature	mole m^{-3} s^{-1}
p	p' PE_m	mole m^{-3} s^{-1}
p'	source term mass balance	mole m^{-3} s^{-1}
Q	q at radial average temperature	W m^{-3}
q	q' PE_h	W m^{-3}
q'	source term heat balance	W m^{-3}
R	reaction rate	mole m^{-3} s^{-1}
R_t	bed radius	m
r	radial coordinate	m
T	temperature	K
ΔT_{ad}	adiabatic temperature rise	K
t	time	s
U	overall heat transfer coefficient	W m^{-2} K^{-1}
u	superficial fluid velocity	m s^{-1}
z	axial coordinate	m

Greek

α_w	wall heat transfer coefficient	W m^{-2} K^{-1}
β	constant	-
ε	bed porosity	-
ε_s	solid porosity	-
ξ	square of dimensionless radial coordinate	-
$\lambda_{e,r}$	effective radial thermal conductivity	W m^{-1} K^{-1}
ρ	density	kg m^{-3}
Ψ	radial average of arbitrary parameter	

Dimensionless groups

Bi	Biot number heat transfer at reactor wall	$\frac{\alpha_w R_t}{\lambda_{e,r}}$
$PE_{h,r}$	Peclet number radial heat transfer	$\frac{u\rho_f c_{p,f} R_t}{\lambda_{e,r}}$
$PE_{h,r}$	Peclet number radial mass transfer	$\frac{uR_t}{D_{e,r}}$
x	dimensionless axial coordinate	$\frac{z}{R_t}$
y	dimensionless radial coordinate	$\frac{r}{R_t}$
δ	weighed temperature difference	$\gamma\Delta\Theta$
γ	dimensionless activation energy at average temp.	$\gamma_0\left(\frac{T_0}{\overline{T}}\right)^2$
γ_0	dimensionless activation energy	$\frac{E_a}{RT_0}$
Θ	dimensionless temperature	$\frac{T-T_0}{T_0}$
$\Delta\Theta_{ad}$	dimensionless adiabatic temperature rise	$\frac{\Delta T_{ad}}{T_0}$
τ	dimensionless time	$\frac{tu}{R_t}$

Sub- and superscripts

0	value at reference conditions
(1)	first solution
(2)	second solution
f	fluid
s	solid
w	wall

Appendix E

Averaging angular temperature variations using brass rings

Temperature profiles measured inside and over a packed bed are not smooth and monotonic, but exhibit strong oscillations on the scale of a particle diameter. The oscillations become stronger with increasing radial and axial temperature gradients. The average radial temperature profile can be obtained by either averaging the temperatures measured at various angular positions, or by measuring the temperature of a ring-shaped sensor with a sufficiently high thermal conductivity. This method has been discussed by *Giudici and do Nascimento, 1994*. The authors calculated temperature oscillations inside their 2 mm copper rings for a given temperature distribution in the fluid phase by numerical integration. If the temperature oscillations in the fluid phase in angular direction are described by a sinusoidal function, the steady state heat balance over the ring is:

$$\lambda_r \frac{\partial^2 T_r}{\partial x^2} = \alpha_{f-r} \frac{4}{d_r}\left(T_r - T_f\right) \tag{E.1}$$

$$T_f = \overline{T} + A\sin\left(fx\right)$$

where x is the distance along the ring, λ_r is the thermal conductivity of the ring material, $\alpha_{f\text{-}r}$ is the heat transfer coefficient between the fluid and the ring, d_r is the thickness of the ring and A and f are the amplitude and wave number of the oscillation in the fluid temperature along the ring. Since the temperature of the ring should be continuous, the temperature at fx= 0 is equal to that at fx= 2π. (E.1) can be solved analytically. At the maximum difference between the local ring temperature and the average ring temperature, the derivative of the temperature T_r with respect to x is zero. This maximum can be calculated analytically as:

$$S=\left(\frac{T_r - \overline{T}}{T_f - \overline{T}}\right)_{max} = \left(1+\frac{\Phi^2 d_r \lambda_r}{\left(\pi D_r\right)^2 \alpha_{f-r}}\right)^{-1} \tag{E.2}$$

Here, Φ is the dimensionless wave number of the temperature oscillations in the ring and the fluid. If the oscillations (one maximum and one minimum) are assumed to occur on the scale of n particle diameters:

$$\Phi = \frac{2\pi^2 D_r}{n d_p}, \tag{E.3}$$

so that:

$$S = \left(1 + \frac{\pi^2 d_r \lambda_r}{\left(n d_p\right)^2 \alpha_{f-r}} \right)^{-1} \tag{E.4}$$

The difference between the minimum and maximum ring temperature will be twice the dimensionless amplitude according to (E.4). α_w can be estimated from the Nusselt number for a cylinder perpendicular to the fluid stream:

$$Nu_r = \frac{\alpha_{f-r} d_r}{\lambda_f} = 0.42 Pr^{0.2} + 0.7 Re^{0.5} Pr^{0.33} \tag{E.5}$$

Fig. E.1 shows the relative spread in the ring temperature compared to the spread in the fluid temperature in angular direction for two values of n. Since n should be smaller than 2, the temperature variations in the brass rings used in this work (1 mm wide and 3 mm high) should be less than 3 % of the temperature spread in the fluid phase.

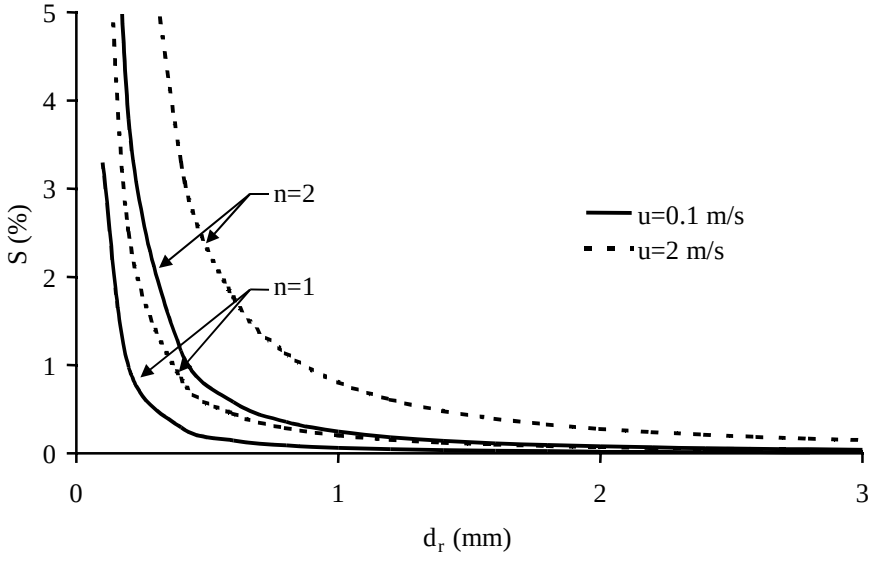

Fig. E.1 Spread in the temperature measured by a brass ring ($\lambda_r \approx 390$ W m^{-1}K^{-1}) relative to the spread in fluid temperature at two fluid velocities. d_p=10 mm, D_r= 5 cm

Notation

A	amplitude temperature oscillations fluid phase	K
D_r	ring diameter	m
d_p	particle diameter	m
d_r	ring thickness	m
f	wave number temperature oscillations	m^{-1}
n	wavelength temperature oscillations relative to particle diameter	-
S	dimensionless amplitude of temperature oscillations in ring	-
T_f, T_r	temperature of fluid and ring	K
u	superficial fluid velocity	m s^{-1}
x	spatial coordinate along ring	m

Greek

$\alpha_{f\text{-}r}$	fluid-to-ring heat transfer coefficient	W m^{-2}
Φ	dimensionless wave number	-
η_f	fluid viscosity	Pa s
λ_p, λ_r	thermal conductivity of fluid and ring	W m^{-1} K^{-1}

Dimensionless groups

Nu	ring Nusselt number	see eq. (E.5)
Pr	fluid Prandtl number	$Pr = \frac{\eta_f c_{p,f}}{\lambda_f}$
Re_r	Reynolds number for flow across ring	$Re_r = \frac{u \rho_f d_r}{\eta_f}$

Appendix F

Influence of heat conduction through the temperature probe on measured radial temperature profiles

F.1 Heat conduction through the thermocouples and their support

Temperature profiles used in this investigation have been measured by thermocouples that were fixed to a cross-shaped support. At the right hand side of Fig. F.1 the cross-shaped probe used for the measurement of temperature profiles over a packing in a 'cold flow' setup is shown. The support used in the pilot-scale wall cooled tubular reactor, fixed to two 1 mm

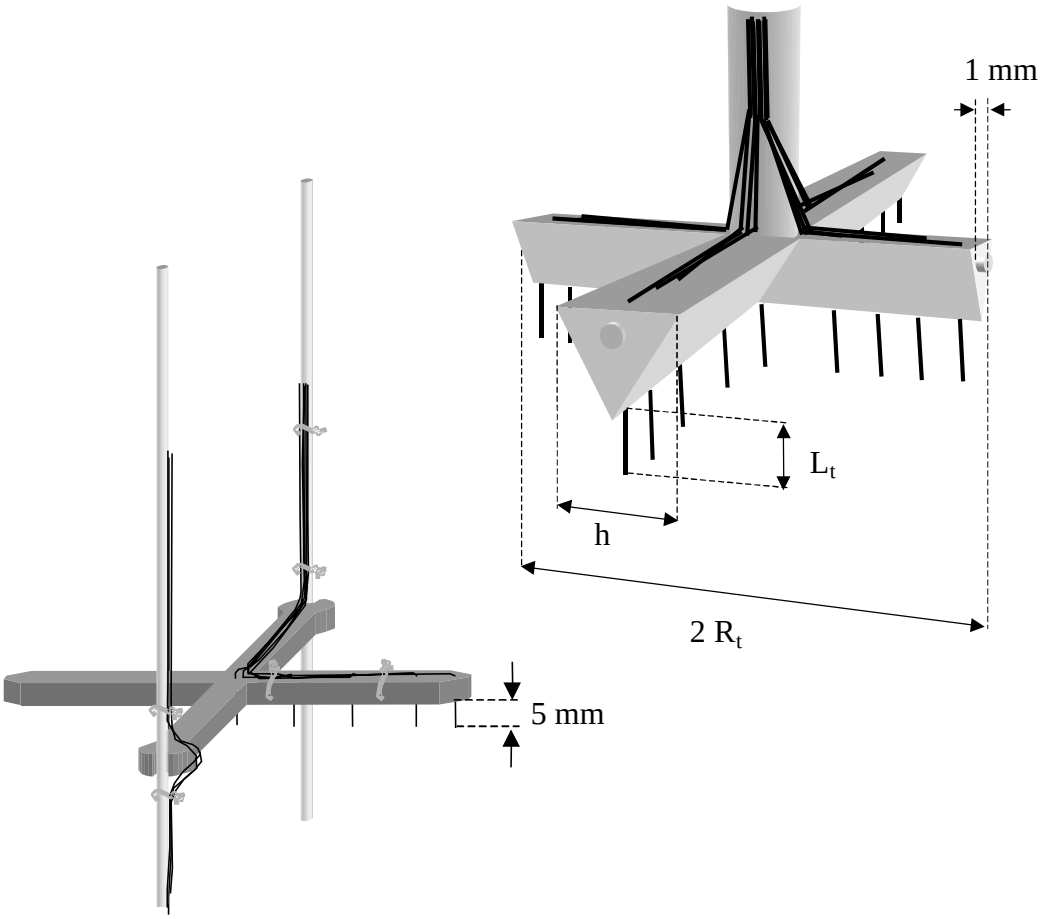

Fig. F.1 Scheme of the thermocouple supports used for measurement of temperature fields. Left: support used in the pilot-scale cooled tubular reactor; right: support used for measurements above packings.

wires, is shown at the left. To ensure that the temperature measured by these thermocouples correspond to the true fluid temperature, the thermal conductivity of the support should be low, whilst a minimum distance between the tip of a thermocouple and the support is required.

Two limiting cases will be considered here. In the first case, there is no heat exchange between the reactor wall and the thermocouple support; in the second case, the probe is in perfect contact with the wall, so that the temperature at the end of the support arms is equal to the wall temperature. Fig. F.2 shows a schematic of the temperature profiles to be expected for both cases. In the case of the experiments without chemical reaction, in which the temperature field is measured above the packing, the support is insulated from the wall by two small teflon plugs, so that heat transfer between the wall and the support is minimized. In the pilot-scale tubular reactor, the arms containing the thermocouples have sharp ends to minimize the contact area with the wall. The arms have better contact with the wires holding the supports in place, but the wires are far away from the thermocouples.

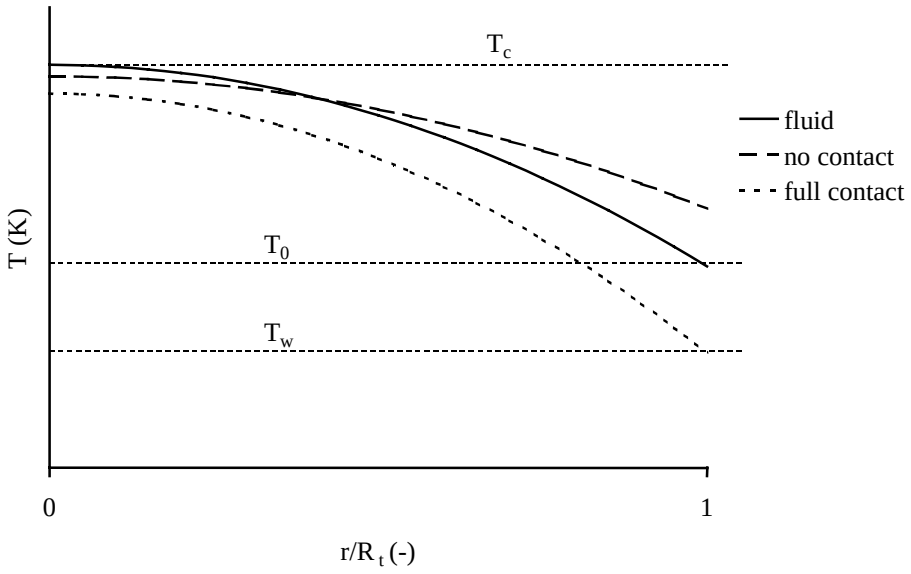

Fig. F.2 Expected temperature profiles along the arm of the thermocouple support.

The temperature along the length of a thermocouple protruding from the probe, T_t, can be calculated from:

$$\lambda_t \frac{\partial^2 T_t}{\partial x^2} = \alpha_{f-t} \frac{4}{d_t}(T_t - T_f) \qquad \text{(F.1)}$$

Here x is the distance from the probe, T_f is the local fluid temperature, d_t is the diameter of the thermocouple and $\alpha_{f\text{-}t}$ is the heat transfer coefficient between the thermocouple and the surrounding fluid. The latter is assumed to be constant along the length of the thermocouple, which is orientated in the direction of flow. At x= 0, the temperature of the thermocouple and that of the support are assumed to be equal. It is assumed that, at the tips of the thermocouples, the heat flux is zero, so that the first derivative of the temperature of the thermocouple with respect to x is zero. Equation (F.1) can be solved analytically to obtain:

$$\Theta_t = \frac{T_t - T_f}{T_s - T_f} = \frac{2\ \exp\left(\sqrt{k_1}\right)}{1+\exp\left(2\sqrt{k_1}\right)} = \cosh^{-1}\left(\sqrt{k_1}\right)\ ;\ k_1 = \frac{4\alpha_{f-t}L_t^2}{d_t\lambda_t}, \qquad \text{(F.2)}$$

in which T_s is the temperature of the support, L_t is the distance over which the thermocouple protrudes from the support and λ_t is the thermal conductivity of the thermocouple.

The temperature profile along the probe, as shown in Fig. F.2, is described by the following differential equation:

$$\lambda_s \frac{\partial^2 T_s}{\partial r^2} = \alpha_{f-s} a_s \left(T_s - T_f(r)\right), \qquad \text{(F.3)}$$

were which a_s is the specific surface area in $m^{2\ m\text{-}3}$ and $\alpha_{f\text{-}s}$ is the heat transfer coefficient between the fluid and the cross. Equation (F.3) is similar to eq. (F.1), except for the fact that the fluid temperature now varies along the length of the support rod. At r= 0, the derivative of T_s with respect to r is zero. The boundary conditions at the reactor wall are:

$$\begin{aligned} &r = R_t:\ \frac{\partial T_s}{\partial r} = 0 \quad \text{(no contact)} \\ &T_s = T_w \qquad\qquad \text{(full contact)} \end{aligned} \qquad \text{(F.4)}$$

Equation (F.3) can be solved analytically if the fluid temperature is assumed to be a quadratic function of the radial position, which is valid for axial positions not too close to the inlet of the reactor:

$$T_f(r) = T_0 + (T_c - T_0)\left(1 - \left(\frac{r}{R_t}\right)^2\right) \qquad \text{(F.5)}$$

In eq. (F.5), T_c and T_0 are the temperature of the fluid at the center of the reactor and at the wall. The fluid temperature at the wall can be expressed as function of the temperature at the center and the wall temperature by introduction of the dimensionless Biot number $Bi = \alpha_w R_t / \lambda_{e,r}$:

$$\Theta_f(\rho) = \frac{T_f - T_w}{T_c - T_w} = 1 - \frac{Bi}{Bi + 2}\rho^2 \qquad \text{(F.6)}$$

In (F.6), the radial coordinate r has been replaced by the dimensionless coordinate $\rho = /R_t$.

For cases I and II, the analytical solutions of (F.3) and (F.6) are:

$$\Theta_s^I(\rho) = \frac{T_s - T_f}{T_c - T_w} = -\frac{2}{k_2}\frac{Bi}{Bi + 2}\left[1 - \sqrt{k_2}\frac{\cosh\left(\sqrt{k_2}\rho\right)}{\sinh\left(\sqrt{k_2}\right)}\right] \quad \text{(no contact)} \qquad \text{(F.7)}$$

$$\Theta_s^{II}(\rho) = -\frac{2}{k_2}\frac{Bi}{Bi + 2}\left[1 + \left(\frac{k_2}{Bi} - 1\right)\frac{\cosh\left(\sqrt{k_2}\rho\right)}{\cosh\left(\sqrt{k_2}\right)}\right] \quad \text{(full contact)} \qquad \text{(F.8)}$$

with:

$$k_2 = \frac{\alpha_{f-s} a_s R_t^2}{\lambda_s} \qquad \text{(F.9)}$$

The difference between the actual fluid temperature and the temperature at the tip of the thermocouple can be calculated by combining equations (F.2), (F.7) or (F.8):

$$\frac{T_t - T_f}{T_c - T_w} = \Theta_t \Theta_s(\rho) \qquad \text{(F.10)}$$

The difference between the temperature indicated by the thermocouple and the fluid temperature is a function of the Biot number for radial heat transfer inside the packed bed and the constants k_1 and k_2 that depend on the geometry and the thermal conductivities of the thermocouple and the cross-shaped probe holding it.

The cross section of the arms of the thermocouple supports used in the cold-flow heat transfer measurements is an equilateral triangle. The heat transfer coefficient between the fluid and the support can be estimated using the following correlation for flow perpendicular to a bar with hydraulic diameter d_h (*Beek and Muttzal, 1975*):

$$Nu_p = \frac{\alpha_{f-s} d_h}{\lambda_f} = 0.42\,Pr^{0.2} + 0.57\,Re_s^{0.5} Pr^{0.33} \qquad (F.11)$$

in which, for a cross arm with height h, the hydraulic diameter d_h is taken equal to the diameter of a rod with a circular cross section having the same surface area. The thermal conductivity of the support material, teflon, is approximately 0.3 W $m^{-1}K^{-1}$ (*Lide, 1999*) at the temperature at which the experiments were performed. The thermal conductivity of the used thermocouples (0.5 mm, Thermo-Electric) is not known. It is estimated as the sum of parallel heat conduction through the sheath material (Inconel, 0.076 mm, λ= 15 W m^{-1} K^{-1}) and the insulating material (MgO powder, estimated thermal conductivity 5 W m^{-1} K^{-1}), which is 10 W m^{-1} K^{-1}.

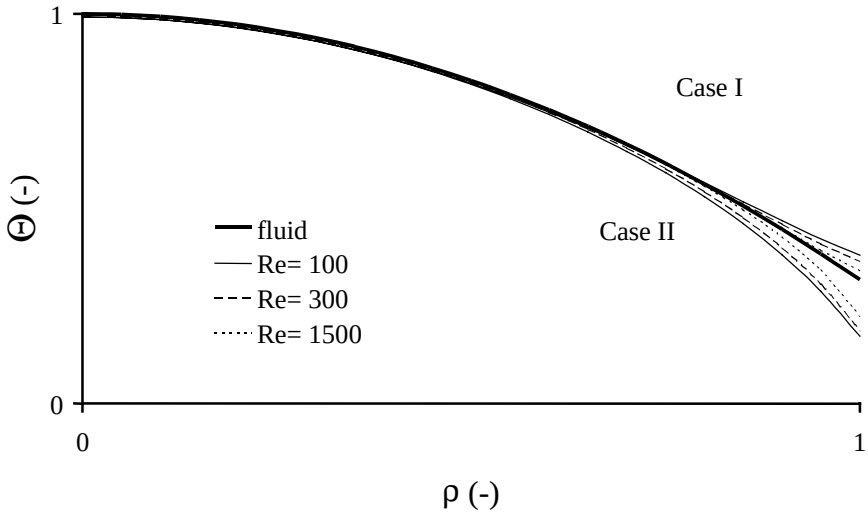

Fig. F.3 Radial temperature profiles in the cold-flow heat transfer setup (100 mm i.d.) in case of no (I) or full (II) contact between the support and the reactor wall. Bi= 3, L_t= 4.5 mm, Re calculated using the particle diameter of the packing (14 mm).

The Nusselt number for heat transfer between the fluid leaving the packing and the thermocouples is calculated as the value for a long cylinder orientated in parallel to fluid (*Beek and Muttzal, 1975):*

$$\frac{\alpha_{f-t} d_t}{\lambda_f} = 2 + 0.22 \mathrm{Re}_t^{0.62} \mathrm{Pr}^{0.33} \qquad \text{(F.12)}$$

In Fig. F.3, the temperature profiles, as they would be measured in the 100 mm diameter cold-flow setup, are compared to the actual fluid temperature. It is clear that contact between the thermocouple support and the wall (case II) should be avoided to minimize the difference between the measured and the actual fluid temperature. The difference between the actual and the measured temperature as function of the distance between the tip of the thermocouple and its support is shown in Fig. F.4. In case of a thermal conductivity of the thermocouple of 10 W m^{-1} K^{-1}, a distance of about 10 mm is required to have a temperature difference between the fluid and the tip of the thermocouple less than 5% of the characteristic temperature difference T_c-T_w. Such distance is impractical, since the thermocouples would be easily damaged or bent when placing the temperature probe above the bed. It is therefore important to use a thermocouple support that has a thermal conductivity as low as possible and which makes minimal contact with the reactor wall. For the temperatures measured above the bed in the cold-flow setups, the maximum difference between the measured and the actual fluid temperature near the wall of the reactor (ρ=0.95) at Re= 300 and Bi= 4.2 is approximately 4% of the difference between T_c and T_w.

The error in the temperatures measured by the thermocouples in the pilot-scale wall cooled tubular reactor is far less due to the shape of the support crosses (see Fig. F.1). The height

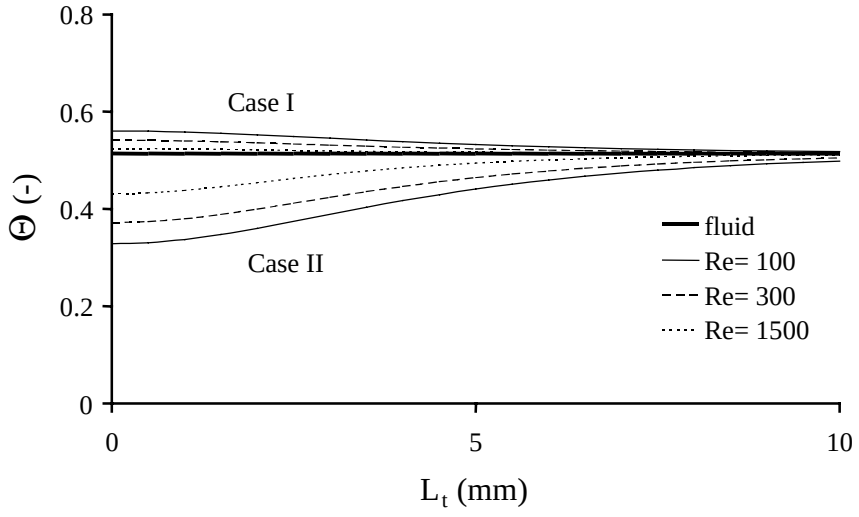

Fig. F.4 Comparison of the measured and the actual temperature above the packing in the 100 mm i.d. cold-flow setup at ρ=0.9 as function of the distance between the tip of the thermocouple and the support. Bi= 3, Re calculated using the particle diameter of the packing (14 mm).

and diameter of the arms containing the thermocouples are 1 and 3 mm respectively, giving a large specific surface area a_s. Using an effective thermal conductivity of the poly-ether-ether-keton (PEEK) of 0.4 W m^{-1} K^{-1}, the maximum temperature difference caused by heat conduction along the support is 0.2 % or 2 % of T_c-T_w in case of no or full contact between the support and the wall. It is assumed that heat conduction through the contact between the sharp thermocouple arms and the wall is negligible, and that the temperatures measured in this setup are not influenced by heat conduction along the thermocouple support.

F.2 Length-dependency of the radial heat transfer parameters due to heat conduction along the thermocouples and cross

Heat conduction along the thermocouples and their support may cause a length dependency in the effective heat transport parameters, due to the change in shape of the radial temperature profile. Here it will be shown that the length dependence of the heat transfer parametrs, as reported by *Li and Finlayson, 1977* and *De Wasch and Froment, 1972*, can be the result of distortion of the measured radial temperature profiles due to heat conduction along the support.

Fig. F.5 shows the influence of heat conduction along the temperature probe on the radial

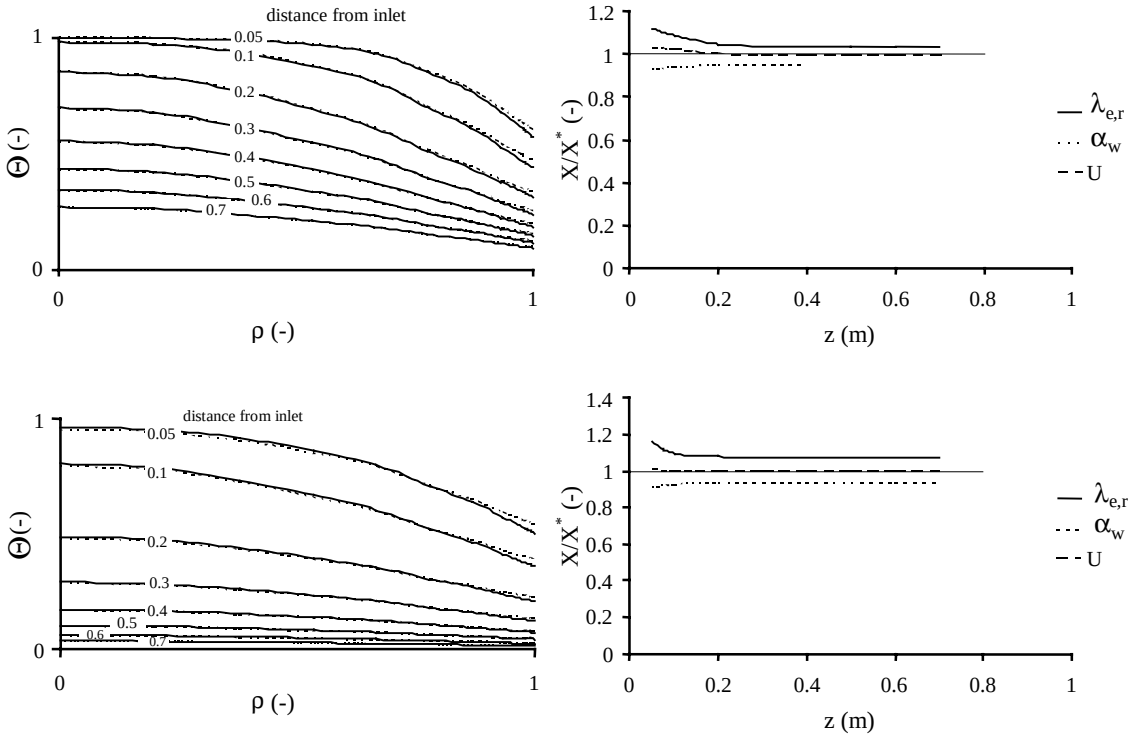

Fig. F.5 Change of effective radial heat transfer coefficients, caused by heat conduction through the temperature probe for the 100 mm (top) and 64 mm (bottom) cold flow setups which are described in Chapter 4. No contact between support and wall, L_t is 3 mm for both reactors. k_1= 1.06, k_2= 110 (top) and 45 (bottom). U is the overall heat transfer coefficient calculated from $\lambda_{e,r}$ and α_w.

temperature profiles, as they would be measured in both heat transfer coefficients described in Chapter 4. The fluid flow rates correspond to Re=300 for a particle diameter of the packing of 14 mm. In both simulations, the effective radial thermal conductivity $\lambda_{e,r}$ and the wall heat transfer coefficient α_w were set to 0.75 W m^{-1} K^{-1} and 65 W m^{-2} K^{-1} respectively. The hydraulic diameter of the arms of both supports was taken the same and the distance between the tips of the thermocouples and the support, L_t, was taken equal to the smallest distance of 4.5 mm used for the 100 i.d. reactor.

Though the change of the temperature profiles is rather small and is observed mainly in a region close to the reactor wall, the effect of heat conduction along the probe on the transport parameters is quite strong, as is shown in Fig. F.5. The distortion of the actual temperature profiles larger with decreasing reactor diameter, since the value of k_2 (eq. (F.9)) is proportional to the square of the radius. The length over which the effective heat transport parameters change decreases with the decreasing reactor diameter. This is because the final shape of the radial temperature profile is approached at shorter distances from the inlet.

The difference between the limit- and the original values of $\lambda_{e,r}$ and α_w is higher for smaller reactor diameters. The reason for this, is that in smaller reactors, the distortion of the temperature profiles is larger (the value of k_2 is smaller). The overall heat transfer coefficient U:

$$\frac{1}{U} = \frac{1}{\alpha_w} + \frac{R_t}{3\lambda_{e,r}} \frac{Bi+3}{Bi+4} \qquad (F.13)$$

is rather insensitive to the distortion of the fluid temperature. This is not unexpected, since the radial average fluid temperature is not strongly affected.

Notation

Bi	Biot number for heat transfer between bed and wall	$\frac{\alpha_w R_t}{\lambda_{e,r}}$
$c_{p,f}$	heat capacity of fluid	J kg^{-1} K^{-1}
d_h	hydraulic diameter of support arm	m
D_t	reactor diameter	m
d_t	diameter thermocouple	m
h	diameter support arm	m
k_1	dimensionless heat transfer constant thermocouple-to-fluid	-
k_2	dimensionless heat transfer constant support-to-fluid	-
L_t	distance between tip of thermocouple and support	m
Pr	fluid Prandtl number	$\frac{\eta_f c_{p,f}}{\lambda_f}$
r	radial coordinate	m
R_t	reactor radius	m
Re	Reynolds number for fluid flow in side packing	$\frac{u\rho_f d_p}{\eta_f}$
Re_t	Reynolds flow for fluid flow along thermocouple	$\frac{u\rho_f d_t}{\eta_f}$
Re_s	Reynolds number for fluid flow across support arm	$\frac{u\rho_f d_h}{\eta_f}$
r	radial coordinate	m
T	temperature	K
T_0	temperature of fluid at the reactor wall	K
T_c	temperature at centerline of reactor	K
x	coordinate along thermocouple	m

Greek

$\alpha_{f\text{-}t}$	thermocouple-to-fluid heat transfer coeff	W m^{-2} K^{-1}
$\alpha_{f\text{-}s}$	support-to-fluid heat transfer coeff	W m^{-2} K-1
η_f	fluid viscosity	Pa s
λ	thermal conductivity	W m^{-1} K^{-1}
ρ	dimensionless radial coordinate	-
ρ_f	fluid density	kg m^{-3}
Θ_f	dimensionless temperature of fluid	$(T_f - T_w)/(T_c - T_w)$
Θ_t	dimensionless temperature of thermocouple	$(T_t - T_f)/(T_s - T_f)$
Θ_s	dimensionless temperature of support	$(T_s - T_f)/(T_c - T_w)$

Subscripts

f	fluid
w	wall
s	support

Appendix G

Influence of angular temperature spread on reaction rate

In models of wall-cooled tubular packed bed reactors, it is assumed that the temperature field over a cross section of the bed is a smooth function of the radial position. In reality, large oscillations around this average temperature, which are proportional to the heat fluxes in radial and axial direction (see Chapter 4). In this work, the temperature spread is referred to as 'angular temperature spread', because is was measurered by rotating the used temperature probes. In this appendix, the influence of the temperature on the reaction rate will be estimated. The reaction rate depends on the spread in the temperatures of the of the catalyst particles, which were not measured. However, the maximum difference between the average reaction rate and the reaction rate at the average temperature (see eq. (G.1)) can be estimated by assuming that the spread in the catalyst temperatures is the same as the measured spread in the fluid temperatures.

$$R\left(\overline{T(z,r)}\right) \neq \overline{R\left(T\left(z,r\right)\right)} \tag{G.1}$$

The fluid temperatures are assume to be distributed around the average temperature according to a a gaussian distribution:

$$P\left(T\right) = \frac{1}{a\sqrt{2\pi}} \exp\left[-\frac{1}{2}\left(\frac{T-\overline{T}}{a} \right)^2 \right] \tag{G.2}$$

After substitution of T by 1/x, followed by linearization around $\overline{T}$:

$$\frac{T-\overline{T}}{a} = \frac{x-\overline{T}x^2}{ax^2} \approx \frac{\overline{T}\left(x\overline{T}-1\right)}{a}, \tag{G.3}$$

eq. (G.2) can be approximated by:

$$P\left(x\right) = \frac{\overline{T}^2}{a\sqrt{2\pi}} \exp\left[-\frac{1}{2}\left(\frac{\overline{T}\left(x\overline{T}-1\right)}{a} \right)^2 \right] \tag{G.4}$$

The constant a in the above expressions is approximately equal to the standard deviation σ in the temperatures measured in angular direction.
The ratio of the average reaction rate and the reaction rate at the angular average temperature is equal to:

$$\frac{\overline{R(T)}}{R(\overline{T})} = \frac{\int_{-\infty}^{\infty} P(x) \exp\left(-\frac{E_a x}{R}\right) dx}{\exp\left(-\frac{E_a}{R\overline{T}}\right)} \tag{G.5}$$

Here E_a is the (apparent) activation energy of reaction. Eq. (G.5) can be solved analytically to obtain, with a=σ:

$$\Psi = \frac{\overline{R(T)}}{R(\overline{T})} = \exp\left(\frac{1}{2}\left(\frac{\sigma E_a}{\overline{T}^2 R}\right)^2\right) \tag{G.6}$$

Fig. G.1 shows the relative increase in the reaction rate as function of the standard deviation and activation for an average temperature of 250 °C.
The standard deviation in the temperatures measured in angular direction is a function of the (effective) particle diameter and the heat fluxes in radial and axial direction. In Chapter 4, the angular temperature spread was investigated experimentally in two cold-flow setups in which packings of glass spheres and of cylindrical catalyst pellets were used. The following

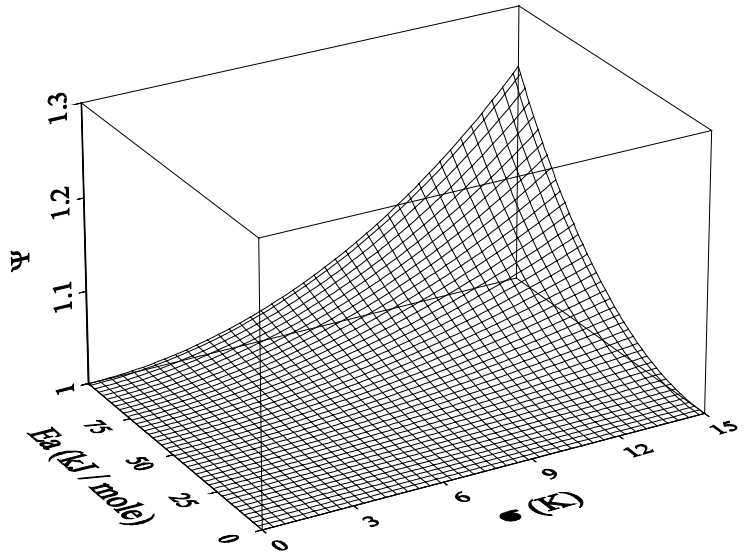

Fig. G.1 Relative increase of the reaction rate due to the angular temperature spread as function of activation energy of the reaction and the standard deviation in temperature. $\overline{T}$ = 250 °C.

relationship was derived to predict the temperature spread:

$$\sigma_{pred} = \frac{\tau}{1.6}\left(\frac{u_r}{\lambda_{e,r}} j_r + \frac{u_z}{\lambda_{e,ax}} j_z\right) = \frac{1}{\rho c_{p,f}}\left(\frac{j_r}{u_r} + \frac{j_z}{u_z}\right) \qquad (G.7)$$

The experimentally observed temperature spread, σ_{exp} was roughly 62 % and 110 % of the predicted temperature spread in case of spherical and cylindrical particles respectively. To estimate whether the increase in reaction rate could influence the effective heat transfer parameters measured with reaction, calculations were made for a worst case scenario. The maximum increase in reaction rate occurs when using a heterogeneous reactor model to calculate temperature profiles measured at the highest reactor temperature and CO inlet concentration. The angular temperature variations will automatically be largest at these conditions.

Fig. G.2 shows the increase in reaction rate after introduction of the factor Ψ to correct for the angular temperature variation. The chosen conditions correspond to the measured temperature profile having the largest axial and radial temperature gradients (see Chapter 3). The maximum increase in the reaction rate is found near the reactor wall and is about 2.5 %. The temperature of the fluid at the centerline and close to the wall of the reactor increase less than half a degree centigrade. The effective heat transfer parameters are only little affected by the change in the temperature profiles. The values of $\lambda_{e,r}$ and α_w are change with 0.5 and -0.8 % respectively when they are optimized to a simulated temperature field as shown in Fig. G.1. As model input, temperatures calculated for the axial and radial positions as in the experimental setup (Chapter 3) were used.

The small influence of the angular temperature spread on the temperature profiles measured in this investigation is merely due to the limited difference between the temperature at the centerline of the reactor and the wall temperature. An increase in the activation energy causes

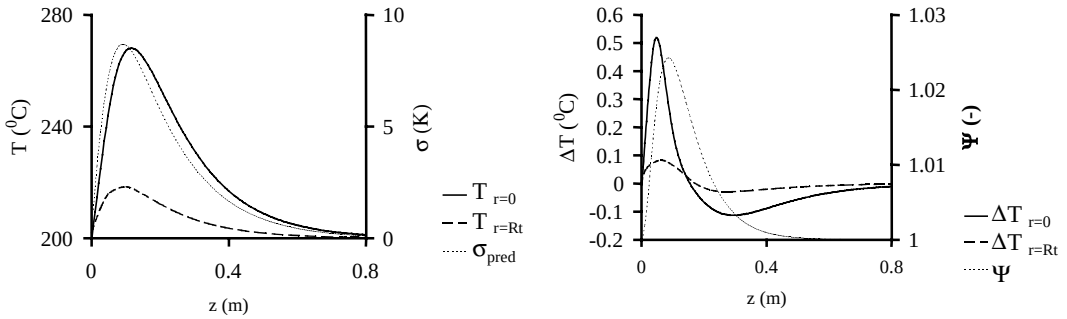

Fig. G.2 Left: Axial fluid temperature profiles and standard deviation in temperature at tube wall. Right: Increase in temperature due to an in crease in Ψ (at r= R_t), caused by the temperature spread. Re=200 CO_{in}=1.2 vol%, P=5.9 bara. Apparent activation energy E_a= 50 kJ $mole^{-1}$. Conditions corresponding to maximum radial and axial temperature gradients occurring during experiments with reaction.

an increase in Ψ, but at the same time lowers the maximum reactor temperature at which runaway occurs. Fig. G.3 shows the increase in temperature at the centerline of the reactor in case the maximum temperature difference between the fluid and the wall is 150 °C.

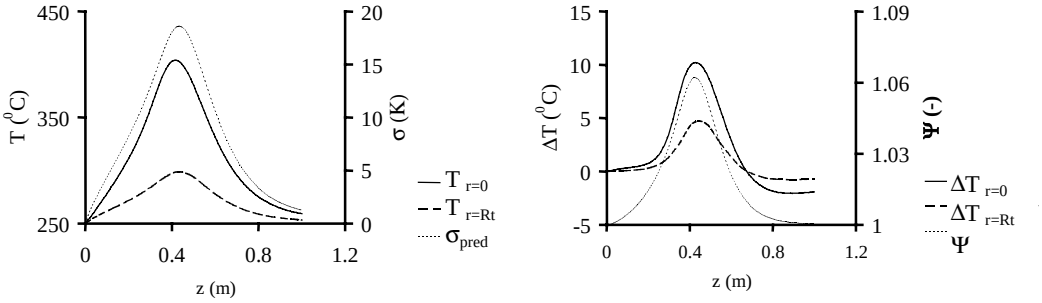

Fig. G.3 Left: Axial fluid temperature profiles and standard deviation in temperature at tube wall. Right: Increase in temperature due to an in crease in Ψ (at r= R_t), caused by the temperature spread. Re=350 CO_{in}=3 vol%, P=6 bara. R_t= 53 mm, d_p=14 mm. First order reaction, E_a= 50 kJ $mole^{-1}$. $Pe_{h,r}$= 8, Bi= 3.

Notation

a	degree of temperature spread	-
c_p	heat capacity	J kg^{-1} K^{-1}
d_p^v	volume-equivalent particle diameter	m
E_a	activation energy	J $mole^{-1}$
P(T)	probability density	-
r	radial coordinate	m
T	temperature	K
u_0	superficial fluid velocity	m s^{-1}
z	axial coordinate	m

Greek

$\lambda_{e,r}$, $\lambda_{e,ax}$	effective radial and axial thermal conductivity	W m^{-1} K^{-1}
σ	standard deviation in temperature	K
τ	relaxation time	s
ψ	ratio of reaction rates, see eq. (G.6)	

Dimensionless groups

$Pe_{h,r}$	Peclet number for radial heat transfer	$\frac{u_0 \rho c_p d_p^v}{\lambda_{e,r}}$
$Pe_{h,ax}$	Peclet number for axial heat transfer	$\frac{u_0 \rho c_p d_p^v}{\lambda_{e,ax}}$

sub- and superscripts

ax	axial
pred	predicted
r	radial

Appendix H

Mass dispersion experiments

H.1 Introduction

Tracer dispersion experiments were performed in the 100 mm reactor also used for measurement of detailed temperature profiles over several packings (see Chapter 4). Experiments with tracer injection at the centerline of the reactor were performed using packings of the same catalyst as was used for the investigation of heat and mass transfer in the pilot-scale wall-cooled tubular reactor at reacting and non-reacting conditions (see Chapter 3). The results of the mass dispersion experiments described in this appendix were used to validate the assumption that the flow-dependent contributions to Peclet number for radial mass dispersion and radial heat dispersion are the same. The effective radial thermal conductivity was determined simultaneously with the wall heat transfer coefficient by matching of the model predictions to the measured temperature profiles. The thus obtained values are subject to errors caused by the correlation of the effective radial thermal conductivity and the wall heat transfer coefficient (see Chapter 1). In Chapter 4, a method is discussed to avoid simultaneous determination of both parameters, but this approach only works if the axial temperature profile near the wall is known very accurately, which is usually not the case. The above mentioned problems are absent when measuring the effective radial dispersion coefficient, since the reactor wall is impermeable to the tracer. In case of fully developed turbulent flow, the flow-dependent contributions to the effective radial thermal conductivity and dispersion coefficient are the result of the same mechanism, which is mixing of the fluid elements moving in between the particles with different radial velocities. In that case:

$$\frac{\lambda_e^f}{\rho_f c_{p,f}} \approx D_e^f \tag{H.1}$$

As discussed in Chapter 1, the effective radial dispersion is assumed to be the sum of the flow-dependent contribution, given by eq. (H.1), and a flow-independent contribution, D_r^0, which is equal to:

$$D_r^0 = \frac{\varepsilon}{\tau} D_m \tag{H.2}$$

In equation (H.2), ε and τ are the porosity and the tortuosity of the bed and D_m is the molecular diffusion coefficient. Correlations for the effective radial dispersion coefficient are usually written in the dimensionless form:

$$\frac{D_{e,r}}{D_m} = \frac{D_r^0}{D_m} + \frac{Pe_f^0}{Pe_{m,r}^\infty}, \tag{H.3}$$

where Pe_f^0 is the fluid Peclet number:

H.2 Experimental

The used setup is described in detail in Chapter 4. At the interface of the calming section and the first test section, CO_2 was injected through a tube at the centerline of the reactor with an inner diameter of 4 mm, as shown in Fig. H.1. It was also possible to add tracer at the wall via a porous glass ring, but the results of such experiments are not discussed here. An infrared CO_2 analyzer (Mayhak UNOR) was used for measurement of the concentration of tracer in the gas samples taken using a crossed shaped probe, similar to that used for measurement of the temperature profiles over a packing, but now containing steel capillaries instead of thermocouples.

Two opposite arms of the probe contained 11 capillaries at 1, 13, 25, 33, 40 and 45 mm from the centerline of the reactor. The distance between the tips of the capillaries and the cross was approximately 3 cm to avoid disturbance of the flow pattern inside the packing. Teflon tubes were used to connect the capillaries to the infrared analyzer. The concentrations were recorded using a data acquisition unit to facilitate averaging. After changing the operating conditions, steady-state concentration profiles were recorded when the concentration at the centerline of the reactor was constant. Since the concentration of CO_2 in the room slowly

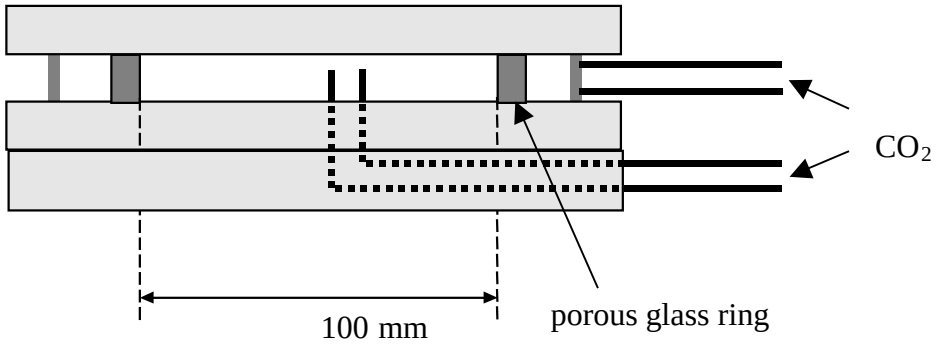

Fig. H.1 Scheme of the system used for injection of the CO_2 tracer.

increased over time, zero-calibration of the CO_2 analyzer was performed repeatedly. The span of the analyzer was calibrated by measuring the CO_2 concentration in the reactor effluent when it was injected in the air intake of the blower that was used for air supply.

H.3 Used model and results

Due to the fact that measurement of concentration profiles using a single analyzer is far more labor-intensive than measurement of temperature profiles, the set of experimental data is more restricted. At each bed height, the radial concentration profiles were measured rotating the cross three times, so that the resulting radial concentratoin distributions are an average over 6, evenly spaced angular positions. When measuring relatively far from the reactor inlet, the radial concentration distributions were rather smooth. Closer to the inlet, oscillations were observed, which are caused by the stochastic nature of the mixing process. A possible contribution of free convection to the overall dispersion process was examined by varying the CO_2 flux by a factor 5. This was done at the minimum fluid velocity using a packing of the large 25 mm spheres. In accordance with the criterion of *Benneker, 1997*, no change of the dimensionless profiles was observed. The effective radial dispersion coefficient was calculated by minimizing the difference between the measured and the calculated concentrations using the following target function:

$$F=\sum_{i=1}^{n}\frac{\left(C_i^{exp}-C_i^{mod}\right)^2}{C_{y=0}-C_{y=1}} \tag{H.4}$$

The dimensionless mass balance is (see also Chapter 1):

$$\frac{\partial C}{\partial x}=\frac{1}{PE_{m,r}}\frac{1}{y}\frac{\partial}{\partial y}\left(y\frac{\partial C}{\partial y}\right)+\frac{1}{PE_{m,ax}}\frac{\partial^2 C}{\partial x^2}, \tag{H.5}$$

to which the following boundary conditions apply:

$$y=0: \qquad \frac{\partial^2 C}{\partial y^2}=0 \tag{H.6}$$

$$y=1: \qquad \frac{\partial C}{\partial y}=0 \tag{H.7}$$

$$x = 0: \qquad C - 1 = \frac{1}{PE_{m,ax}} \frac{\partial C}{\partial x} \tag{H.8}$$

$$x = \frac{L}{R_t}: \qquad \frac{\partial^2 C}{\partial x^2} = 0 \tag{H.9}$$

The dimensionless groups and parameters are defined as:

$$x = \frac{z}{R_t} \qquad y = \frac{r}{R_t} \qquad C = \frac{c}{\overline{c_{MC}}} \tag{H.10}$$

$$PE_{m,r} = \frac{u_0 R_t}{D_{e,r}} = Pe_{m,r} \frac{R_t}{d_p^v} \qquad PE_{m,ax} = \frac{u_0 R_t}{D_{e,ax}} = Pe_{m,ax} \frac{R_t}{d_p^v} \tag{H.11}$$

$\overline{c_{MC}}$ is the mixed-cup concentration, defined as the ratio of the mole flow of the tracer and the mole flow of air. In case of a radial distribution of the axial fluid velocity, the mixed cup concentration may differ from the average concentration over the cross section, c_0. The mass balance equation was solved numerically using the method of finite-differences. Since axial and radial concentration gradients are extreme near the injection point, grid refining was applied there.

Mass dispersion in packings of the catalyst cylinders with an average length of 11.2 mm and a diameter of 5.5 mm were performed by injecting the CO_2 tracer at the centerline of the bed at ambient pressure at fluid velocities corresponding to Re= 206, 300 and 390. The average CO_2 concentration in the effluent of the reactor was approximately 1 vol%. At Re= 206, the profiles were measured at 4 axial positions; at the other velocities only at one axial position, close to maximum bed length of 40 cm. In Fig. H.2, the Peclet numbers for mass transfer calculated from the concentration profiles measured at 40 cm from the inlet are compared to the values of the Peclet number for radial heat transfer measured in the pilot-scale wall cooled tubular reactor. In both cases, the axial fluid velocity was assumed constant over the radius. Heat and mass dispersion in axial direction (parallel to the net direction of the fluid flow) was neglected. Since the profiles were measured rather far (40 cm) from the reactor inlet, the contribution of axial dispersion is very small. The radial dispersion coefficient is changed less than 1% if axial dispersion is taken into account using $Pe_{m,ax}$= 2.
The values of Pe^{∞} depend on the aspect ratio N= D_t/d_p^v (e.g. *Bauer and Schlünder 1978a, Specchia et al. 1980*). In case of pure heat transfer in packings of spheres, the relationships proposed by these investigators correspond well with the dependencies obtained when

attributing the dependence of Pe^{∞} on the aspect ratio to a non-uniform radial distribution of the axial fluid velocity (Chapter 3). In the case of packings of cylindrical particles, the radial distribution of the bed porosity is less pronounced and is limited to a smaller region near the wall. The Peclet numbers for radial heat and mass transfer is therefore less sensitive to the value of the aspect ratio. According to the correlation of *Bauer and Sclünder, 1978*, Pe^{∞} should be a factor 1.17 smaller in the 100 mm reactor used in this investigation. Here, this ratio is 1.05, which does seem very reasonable. The results of the tracer injection experiments affirm the results of the heat transport measurements in the pilot-scale wall-cooled tubular reactor.

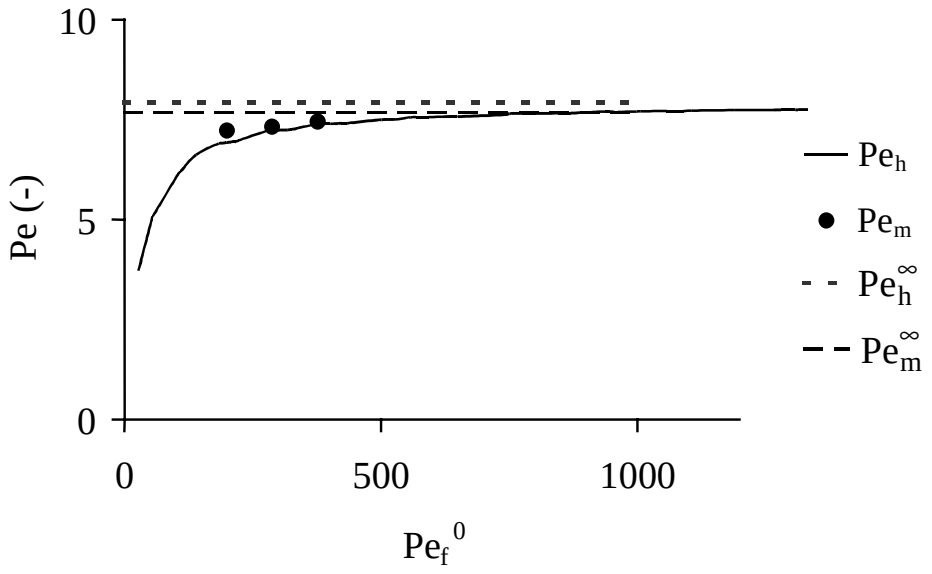

Fig. H.2 Comparison of Peclet number for radial heat transfer measured in the pilot scale wall-cooled tubular reactor (D_t= 53.1 mm) and the Peclet number for radial mass transfer measured in the cold-flow setup (D_t= 100 mm). Horizontal lines show the flow-dependent contribution to the effective heat transfer coefficient and mass dispersion coefficient. Axial dispersion of mass is neglected and the axial fluid velocity is assumed constant over the radius.

Notation

C	dimensionless concentration	C/C_0
$\overline{c}_{MC}$	mixed cup concentration	mole m^{-3}
$c_{p,f}$	heat capacity of fluid	J kg^{-1} K^{-1}
$D_{e,r}$	effective radial diffusion coefficient	m^2 s^{-1}
D_m	molecular diffusion coefficient	m^2 s^{-1}
d_p^v	volume-equivalent particle diameter	m
D_r^f	flow-dependent contr. to $D_{e,r}$	m^2 s^{-1}
D_r^0	effective diffusion coefficient in case of stagnant fluid	m^2 s^{-1}
D_t	reactor diameter	m
F	target function	-
L	bed lenth	m
$Pe_{h,r}^{\infty}$	Peclet number for heat disp. at fully dev. turb. flow	-
$Pe_{m,r}^{\infty}$	Peclet number for mass disp. at fully dev. turb. flow	-
r	radial coordinate	m
R_t	tube radius	m
u_0	superficial fluid velocity	m s^{-1}
x	dimensionless axial coordinate	-
y	dimensionless radial coordinate	-
z	axial coordinate	-

Greek

ε	bed porosity	-
η_f	fluid viscosity	Pa s
$\lambda_{e,r}$	effective radial thermal conductivity	W $m^{-1}K^{-1}$
λ_r^f	flow-dependent contr. to $\lambda_{e,r}$	W $m^{-1}K^{-1}$
ρ_f	fluid density	kg m^{-3}
τ	bed tortuosity	-

Dimensionless groups and variables:

$Pe_{h,r}$	Peclet number for radial heat conduction	$\frac{u_0 \rho_f c_{p,f} d_p^v}{\lambda_{e,r}}$
Pe_f^0	fluid Peclet number for mass dispersion	$\frac{u_0 d_p^v}{D_m}$ or $\frac{u_0 \rho_f c_{p,f} d_p^v}{\lambda_f}$
$Pe_{m,ax}$	Peclet number for axial mass dispersion	$\frac{u_0 d_p^v}{D_{e,ax}}$

$PE_{m,ax}$	Peclet number for axial mass dispersion (model)	$\frac{u_0 R_t}{D_{e,ax}}$
$PE_{m,r}$	Peclet number for radial mass dispersion (model)	$\frac{u_0 R_t}{D_{e,r}}$
Re	Reynolds number	$\frac{u_0 \rho_f d_p^v}{\eta_f}$
Sc	Schmidt number	$\frac{\eta_f}{\rho_f D_m}$

super- and subscripts

exp	experimental
f	fluid
mod	model

Epilogue

As has been discussed in the general introduction to this work, the purpose of the development of models for wall-cooled tubular packed bed reactors is not only to obtain a better understanding of the physical and chemical processes occurring in such reactor. The ultimate goal of these efforts is to be able to make a reactor design on the basis of separately measured reaction kinetics and known correlations for heat transport parameters and to skip the time-consuming and expensive stage of pilot-plant testing. Our expectations with respect to this are not very optimistic, which is based on the experience gained during the work that is presented in this thesis. Pilot-scale research can hardly be skipped completely, but the amount of tests can be reduced. The necessity of pilot-scale investigations is not only due to the inaccuracy of the available models, but due to the uncertainty of the reaction kinetics. It is not a very serious problem that correlations for the radial heat transfer parameters often do not agree. The values of the effective radial thermal conductivity of the bed, $\lambda_{e,r}$, and the wall heat transfer coefficient, α_w, obtained by different investigators may differ. However, the predictions of the reactor models are more sensitive to the value of the combined overall heat transfer rate between the bed and the wall, which is far more consistent.

Often, the rate and the selectivity of the chemical reaction are an important source of uncertainty. Slight differences in the preparation, the pretreatment and (inevitable) exposure to air can have large consequences. Long-term exposure to different reaction conditions may lead to either a more activated or more deactivated catalyst. This can even produce a profile of the specific catalytic activities in the wall-cooled packed bed reactor. Moreover, catalyst development does not stop after a reactor has been built. It is not unlikely that the activity of the catalyst will be increased during the lifetime of the reactor (change of active species or addition of other metals as promoters, change of the shape of the catalyst or a change of internal pore structure). After improvement of the catalyst, the activity can be easily increased by a factor two or more. The uncertainty in the reaction kinetics due to the reasons discussed above is likely to have more impact on the reactor design than the differences between the predictions of the available reactor models and the difference between the heat transport parameters that are used.

Initially, the reaction rates measured in the kinetic reactors and in the pilot-scale wall-cooled tubular reactor differed by a factor of approximately four. The inaccuracy of the predicted temperature and concentration profiles, caused by such a large uncertainty of the reaction rate, is of course far greater than the inaccuracy that is caused by the difference between correlations for the effective transport parameters. In the course of this investigation, the difference between the activities of the catalyst in both reactors could be attributed to the presence of water in the reactor feed and to the thermal treatment of the catalyst. It is likely

that the deactivation of the catalyst by small traces of water would not have been detected if no pilot-scale experiments had been performed. Therefore, testing of the performance of the catalyst in a pilot plant with a single tube, at conditions close to those in the industrial reactor, remain important. Even if the reaction kinetics are measured using a feed that has the same composition as that of the process for which the reactor is designed, the accuracy of the kinetic data will hardly be perfect.

The diameter of a pilot-scale reactor should be the same as that of the industrial-size reactor, whereas the length of it can be kept much smaller. For the measurement of the effective heat transport parameters, a length of approximately 1 meter is often enough. It is very well possible to have process conditions in such reactor, that are similar to those in different parts of the industrial-size reactor, in which the length of the tubes may be over 10 meters. The use of a pilot-scale reactor with a different diameter is not advised. Even at non-reacting conditions, the dependence of the effective heat transport parameters on the radial distributions of the bed porosity and the axial fluid velocity is very complex. These radial distributions cause the effective transport parameters to depend on the tube-to-particle diameter ratio. No literature correlations are available that give a very precise prediction of the dependence of the heat transport parameters on the reactor diameter, especially if the particles are not ideal spheres or cylinders. In this work, it was observed that the effective heat transfer parameters, obtained from experiments at reacting conditions, differ from those at non-reacting conditions if the correct radial distribution of the axial fluid velocity is not taken into account. Since literature data on the radial velocity distribution are scarce, scaling-up is dangerous if the diameter of the reactor tubes is increased.

Whereas the more complex models can be very helpful when interpreting the data obtained in a pilot-scale or an industrial reactor, the more simple one-dimensional models will often suffice.

References

Agnew, J.B., Potter, O.E., 1970, 'Heat transfer properties of packed tubes of small diameter', *Trans, Instn.Chem.Engs.*, **48**, T15

Agudo, L., Palacios, J.M., Fierro, J.L., Laine, G., Severino, F., 1992, 'Activity and structural changes of alumina-supported CuO and $CuCr_2O_4$ catalysts during carbon monoxide oxidation in the presence of water', *Appl. Catalysis A:General*, **91**, 43

Annamalai, J., Liauw, M.A., Luss, D., 1999, 'Temperature patterns on a hollow cylindrical catalytic pellet'. *Chaos* **9**, 36

Anderson, J.B., 1963, 'A criterion for isothermal behaviour of a catalyst pellet',*Chem. Eng. Sc.* **20**, 147

Barkelew, C.H., 1955, 'Stability of chemical reactors', *Chem. Engng. Prog. Symp. Ser.* **55**, 37

Bauer, R., Schlünder, E.U., 1978 a, 'Effective radial thermal conductivity of packings in gas flow. Part I. Convective transport coefficient', *Int. Chem. Eng*. **18**, 181

Bauer, R., Schlünder, E.U., 1978b, 'Effective radial thermal conductivity of packings in gas flow. Part II. Thermal conductivity of the packing fraction without gas flow', *Int. Chem. Eng*. **18**, 189

Benes, N.E., 2000, 'Mass transport in thin supported silica membranes', Doctoral Thesis, Twente University, Enschede, the Netherlands

Azevedo, S.F. de, Romero-Ogawa, M.A., Wardle, A.P., 1990, 'modeling of tubular fixed-bed catalytic reactors: a brief review', *Trans. IchemE* **68**, part A, 483

Baumann, E.G., Varma, A., 1990, 'Parametric sensitivity and runaway in catalytic reactors: experiments and theory using carbon monoxide oxidation as an example', *Chem. Eng. Sc.*, **45**, 2133

Beek, W.J., Drinkenburg, A.A.H., 1967, *Proc. Int. Symp. Fluidization*, Neth. Univ. Press, Amsterdam, 507

Beek, W.J., Mutzall, K.M.K., 1975, 'Transport phenomena', Wiley and Sons, Chichester, UK

Benneker, A.H., 1997, 'Hydrodynamical dispersion in packed beds. Influence of free convection and modeling', Doctoral Thesis, University of Twente, Enschede, the Netherlands

Benneker, A.H., Kronberg, A.E., Post, J.W., van der Ham, A.G.J., Westerterp, K.R., 1996, 'axial dispersion in gases flowing though a packed bed at elevated temperatures', *Chem. Eng. Sci*., **51**, 2099

Benneker, A.H., Kronberg, A.E., Lansbergen, I.C., Westerterp, K.R., 2002, 'Mass dispersion in liquid flow through packed beds', *Ind. Eng. Chem. Res.* **41**, 1716

Berty, J.M., 1974, 'Reactor for vapour-phase catalytic studies', *Chem. Eng. Prog.*, **70**, 78

Bey, O., Eigenberger, G., 1997, 'Fluid flow through catalyst filled tubes', *Chem. Eng. Sc.* **52**, 1365

Borkink, J.G.H., 1991, 'Heat transport in wall-cooled packed beds of low tube-to-particle ratio', Doctoral Thesis, Twente University, Enschede, the Netherlands

Borkink, J.G.H., van de Watering, C.G., Westerterp, K.R., 1992, 'The statistical character of bed-scale effective heat transport coefficients for packed beds', *Trans. IchemE*, **70**(A)

Borkink, J.G.H., Westerterp, K.R., 1992, 'Influence of tube and particle diameter on heat transport in packed beds', *AIChE J.* **38**, 703

Borkink, J.G.H., Borman, P.C., Westerterp, K.R., 1993, 'Modeling of radial heat transport in wall-cooled packed beds. Confidence intervals of estimated parameters and choice of boundary conditions', *Chem. Eng. Comm.* **121**, 135

Borkink, J.G.H., Westerterp, K.R., 1994, 'Significance of radial porosity profile for de description of heat transport in wall-cooled packed beds', *Chem. Eng. Sc.* **49**, 863

Borman, P.C., 1993, 'The selective oxidation of ethene in a wall-cooled tubular packed bed reactor', Doctoral Thesis, Twente University, Enschede, the Netherlands

Borman, P.C., Bos, A.N.R., Westerterp, K.R., 1994, 'A novel reactor for determination of kinetics for solid catalyzed gas reactions', *AIChE Journal* **40**, 862

Carberry, J.J., 1964, 'Designing laboratory catalytic reactors', *Ind. Eng. Chem.* **56**, 39

Carlslaw, H.S., Jaeger, J.C., 1959, 'Conduction of heat in solids', Second Edition, Clarendon Press, Oxford

Crider, J.E., Foss, A.S., 1965, 'Effective wall heat transfer coefficients and thermal resistances in mathematical models of packed beds', *AIChE J.* **11**, 1012

Cybulski, A., Eigenberger, G., Stankiewicz, A., 1997, 'operational and structural nonidalities in modelling and design of multitubular reactors', *Ind. Eng. Chem. Res.*, **36**, 3140

Damköhler, G., 1938, 'Einflüsse der Strömung, Diffusion und des Wärmeüberganges auf die Leistung von Reaktionsöfen, I. Allegmeine Gesichtspunkte für die Übertragung enes chemischen Prozesses aus dem Kleinen ins Große', *Zeischrift für Elektrochemie* **42**, 846

Deen, R., Scheltus, P.I.Th., de Vries, G.,1976, 'Electron paramagnetic resonance of supported copper oxide catalyst in the reduction to nitric oxide', *Journal of. Catalysis*. **41** 218

Dekker, F.H.M., Hoorn, J.A.A. Stegenga, S., Kapteijn, F., Moulijn, J.A., 1992, 'Kinetics of the CO oxidation by O_2 and N_2O over Cu-Cr/Al_2O_3', *AIChE Journal*, **38**, 385

Dekker, F.H.M., Klopper, G., Bliek, A., Kapteijn, F., Moulijn, J.A., 1994 **(I),** 'Modelling the transient kinetics of heterogeneous catalysts. CO-oxidation over supported Cr and Cu', *Chem. Eng. Science* **49**, 4375

Dekker, F.H.M., Klopper, G., Bliek, A., Kapteijn, F., Moulijn, J.A., 1994 **(II)**, 'A transient kinetic study of carbon monoxide oxidation over copper-based catalysts for automotive pollution control', *Catalysis today* **20**, 409

Dil'man, V.V., Kroberg, A.E., 1990, 'Additional stress tensor for fluid flow in stationary granular bed', *Theoretical Foundation of Chemical Engineering*, **24**, 483

Dixon, A.G.. Paterson, W.R., Cresswell, D.L., 1978, 'Heat transfer in packed beds of low tube/particle diameter ratio', *Chem. React. Eng. ACS Symp. Ser.* **65**, 238

Dixon, A.G., Cresswell, D.L., 1979, 'theoretical prediction of effective heat transfer parameters in packed beds', *AIChE J*. **25**, 663

Dixon, A.G., Dicostanzo, M.A., Soucy, B.A., 1984, 'Fluid-phase radial transport in packed beds of low tube-to-particle diameter ratio', *Int. J. Heat and Mass Transfer* **27**, 1701

Dixon, A.G., Labua, L.A., 1985a, 'wall-to-fluid coefficients for paced bed heat and mass transfer', int. j. heat and mass transfer **28**, 879

Dixon, A.G., 1985, 'The length effect on packed bed effective heat transfer parameters', *Chem. Eng. J*. **31**, 163

Dixon, A.G., 1988, 'Wall and particle shape effects on heat transfer in packed beds', *Chem. Eng. Comm.* **71**, 217

Dixon, A.G., 1996, 'An improved equation for the overall heat transfer coefficient in packed beds', *Chem. Eng. and Proc.* **35**, 323

Dercks, O.R., Dixon, A.G., 1997, 'Effect of the wall Nusselt number on the simulation of catalytic fixed bed reactors', *Cat. Today*, **35**, 435

Pereira Duarte, S.I., Ferretti, O.A., Lemcoff, N.O., 1984, 'A heterogeneous one-dimensional model for non-adiabatic fixed-bed catalytic reactors', *Chem. Eng. Sc.*, **39**, 1025

Eckert, E., Hlavaček, V., Marek, M., 1973, 'Catalytic oxidation of CO on CuO/Al_2O_3. I. Reaction rate model discrimination', *Chem. Eng. Comm*. **1**, 89

Edwards, M.F., Richardson, J.F., 1968, 'Gas dispersion in packed beds', *Chem. Eng. Sc*. **23**, 109

Eigenberger, G., 1972, 'On the dynamic behavior of the catalytic fixed-bed reactor in the reaction of multiple steady states – I. The influence of heat conduction in two phase models', *Chem. Eng. Sc.* **27**, 2909

Eisfeld, B., Schnitzlein, K., 2001, 'The influence of confining walls on the pressure drop in packed beds', *Chem. Eng. Sc.* **56**, 4321

Fahien, R.W., Smith, J.M., 1955, 'Mass transfer in packed beds', *AIChE J.*, **1**, 28

Finlayson, B.A., 1972, The method of weighed residuals and variational principles', Academic Press, New York

Friedman, R.M., Freeman, J.J., 1978, 'Characterization of Cu/Al_2O_3 catalysts', *Journal of Catalysis* **55**, 10

Froment, G.F., Bischoff, K.B., 1979, 'Chemical Reactor Analysis and Design', Wiley, New York

Fuller, E.N., Schettler, P.D., Giddings, J.C., 1966, 'A new method for prediction of binary gas-phase diffusion coefficients', *Ind. Eng. Chem*., **58**, 19

Giese, M., Rottschäfer, K/, Vortmeyer, D., 1998, 'Measured and modeled superficial flow profiles in packed beds with liquid flow', *AIChE J.* **44**, 484

Gmelins Handbuch der Anorganischen Chemie, 8. Auflage, Kupfer, Teil B-Lieferung 2, Verlag Chemie GmbH, Weinheim (Ger.), 1961

Gnielinksi, V., 1982, 'Berechnung des Wärme- und Stoffaustauschs durchströmten Schüttungen', *Verfahrenstechnik* **16**, 36

Guidici, R., do Nascimento, C.A.O., 1994, 'Analysis of a ring-shaped sensor for use in packed-bed heat transfer studies', *Can. J. of Chem. Eng.* **72**, 43-49

Gunn, D.J., 1969, 'Theory of axial and radial dispersion in packed beds', *Trans. Instn. Chem. Eng.* **47**, T135

Gunn, D.J., 1987, 'Axial and radial dispersion in packed beds', *Chem. Eng. Sc.* **42**, 363

Gupta, A.S., Thodos, G., 1963, 'Direct analogy between mass and heat transfer to beds of spheres', *AIChE* **9**, 751

Hagan, P.S., Herskowitz, M., Pirkles, C., 1988, 'A simple approach to highly sensitive tubular reactors', *SIAM J. Appl. Math*. **48**, 1083

Hall, R.E., Smith, J.M., 1949, 'Design of gas-solid reactors', *Chemical Engineering Progress* **45**, 459

Hein , St., Vortmeyer, D., 1995, 'Wandgekühlte chemische Festbettreaktoren und deren Modellierung mit Ein- und Zweiphasenmodellen', *Zeitschrift für Naturforschung* **50**, 568

Hennecke, F.W., Schlünder, E.U., 1973, 'Wärmeübergang in beheizten oder gekühlten Rohren mit Schüttungen aus Kugeln, Zylindern un Raschig-Ringen', *Chem. Ing. Techn*. **45**, 277

Hiby, J.W., 1963, 'Longitudinal and transverse mixing during single-phase flow through granular beds', *Interaction Between Fluids and Particles*, Institute of Chemical Engineers, London, 312

Hlavaček, V., Vortruba, J., 1974, 'Experimental study of Multiple Steady States in Adiabatic Catalytic Systems' in *Chemical Reaction Engineering-II: proceedings of the Third International Symposium on Chemical Reaction Engineering, Evanston, IL (US)*, American Chemical Society, Washington, (DC) ISBN 0-8412-0200-1

Hlavacek, V., Vortruba, J., 1977, 'Steady-state operation of fixed-bed reactors and monolithic structures', in: 'Chemical reactor theory – a review, chapter 6. Ed. by Lapidus, L., Amundsen, N.R., Prentice-Hall Inc., Inglewood Cliffs, NJ, USA.

Hoffman, H., 1979, 'Fortschritte bei der Modellierung von Festbettreaktoren', *Chem. – Ing. Techn.*. **51**, p. 257

Jernigan, G.G., Somorjai, G.A., 1994 'Carbon monoxide oxidation over three different oxidation states of copper: metallic copper, copper (I) oxide, and copper (II) oxide – A surface science and kinetics study', *Journal of Catalysis* **147,** 567

Kalthoff, O., Vortmeyer, D., 1979, 'Ignition/Extinction phenomena in a wall cooled fixed bed reactor, experiments and model calculation including radial porosity and velocity distributions', *Chem. Eng. Sc.* **35**, 1637

Kakhniashvili, G.N., Mashakova, E.N., Mischenko, Yu.A., 1989, 'Mechanism of oxidation of carbon monoxide on applied catalysts', *Kinetics and Catalysis* **29**, 712

Knudsen, M., 1909, 'Die Gesetze der Molekularströmung und der Inneren Reibungsströmung der Gase durch Röhren', *Ann. Phys.*, **28**, 75

Kronberg, A.E., Benneker, A.H., Westerterp, K.R.W., 1996, 'Wave model for longitudinal dispersion. Application to the laminar-flow tubular reactor', *AIChE J.*, **42**, 3133

Kronberg, A.E., Westerterp, K.R., 1999, 'Nonequilibrium effects in fixed-bed interstitial fluid dispersion', *Chem. Eng. Sc*. **54**, 3977

Kulkarni, B.D., Doraiswamy, L.K., 1990, 'Estimation of Effective Transport Properties in packed bed reactors', *Catal. Rev. –Sci. Eng.* **22**, 431

Kunii, F., Smith, J.M., 1960, 'Heat Transfer Characteristics of Porous Rocks, *AIChE J.* **6**, 71

Kuo, S.M., Tien, C.L., 1989, 'Transverse Dispersion in Packed-Sphere Beds', *ASME Proceedings of the 1988 heat transfer conference* I, 629

Laine, J., Brito, J., Severino, F., Castro, G., 1990, 'Surface copper enrichment by reduction of copper-chromyte catalysts employed for carbon monoxide oxidation', *Catal. Lett.* **5**, 45

Latifi, M.A., Lesage, F., Midoux, N., 1998, 'A two-zone model for liquid-to-wall mass transfer in a packed bed reactor with single phase liquid flow', *Computers Chem. Engng.* **22**, S905

Legawiec, B., Ziólkowski, D., 1995, 'Mathematical simulation of heat transfer within tubular flow apparatus with packed bed by a model considering system inhomogeneity', *Chem. Eng. Sc.* **50,** 673

Lemcoff., N.O., Pereira Duarte, S.I., Martinez, O.M., 1990, 'Heat Transfer in Packed Beds', *Reviews in Chem.l Eng.* **6**, 229

Lesage, F., Latifi, M.A., Midoux, N., 1999, 'Boundary element method in modeling of momentum transport and liquid-to-wall mass transfer in a packed-bed reactor', *Chem. Eng. Sc.* **55**, 455

Li, C-H, Finlayson, B.A., 1977, 'Heat transfer in packed beds- a reevaluation', *Chem. Eng. Sc.* **32**, 1055

Lide, D.R., 1999, 'Handbook of chemistry and physics', 80th edition', CRC Press, Florida, ISBN 0-8493-0480-6

Litovski, E. Shapiro, M., Shavit, A., 1995, 'Gas pressure and temperature dependencies of thermal conductivity of porous ceramic materials: Part 2, Refractories and ceramics with porosity exceeding 30%', *J. Am. Cer. Soc.* **79**(5), 1366

Logtenberg, S.A., Dixon, A.G., 1998, 'Computational fluid dynamics studies of fixed -bed heat transfer', *Chem. Eng. and Proc.* **37**, 7

Logtenberg, S.A., Nijemeisland, M., Dixon, A.G., 1999, 'Computational fluid dynamics simulations of fluid flow and heat transfer at the wall-particle contact points in a fixed bed reactor', *Chem. Eng. Sc.* **54**, 2433

Lund, K.O., Nguyen, H., Lord, S.M., Thompson, C., 1999, 'Numerical correlation for thermal conduction in packed beds', *Can. J. of Chem. Eng.* **77**, 769

Mardanova, N.M., Akhverdiev, R.B., Talyshinskii, R.M., 1996, 'Oxidation of carbon monoxide on Cu-Cr-Mn/γ-alumina catalysts from various sources', *Kinetics and Catalysis* **37**, 84

Martin, H., 1978, 'low peclet number particle-to-fluid heat and mass transfer in packed beds', *Chem. Eng. Sc.* **33**, 913

Martin, H., Nilles, M., 1993, 'Radiale Wärmeleitung in durchströmten Schüttungsrohren', *Chem. –Ing. –Techn.* **65,** 1468

Melanson, M.M., Dixon, A.G., 1985, 'Solid conduction in low d_t/d_p beds of spheres, pellets and rings', *Int. J, of Heat and Mass Transfer* 28, 383

Olbrich, W.E., Potter, O.E., 'Heat transfer in small-diameter packed beds', *Chem. Eng. Sci.*, **27**, 1723

Perry, R.H., Green, D.W., 1997, 'Perry's Chemical Engineers' Handbook', Seventh edition, McGraw-Hill, New York, ISBN 0-07-049841-5

Pollard, W.G., Present, R.D., 1948, 'On Gaseous Self-Diffusion in Long Capillary Tubes', *Phys. Rev.*, **73**, 762

Polyanin, A.D., Kordyumov, V.N., Dil'man, V.V., 1992, 'Asymptotic correction method in chemical engineering problems', *Theoretical foundations of chemical engineering* **26**, 404

Press, W.H., Teukolsky, S.A., 1986, 'Numerical recipies in Fortran', Second edition, Cambridge university Press, Cambridge, ISBN-0-521-43064-X

Prokopowicz, R.A., Silveston, P.L., Hudgins, R.R., 1988, 'Oxidation of carbon monoxide over a copper(II) oxide catalyst', *React. Kinet. Catal. Lett.*, **37**, 63

Rexwinkel, G., Heesink, A.B.M., van Swaaij, W.P.M., 1997, 'Mass transfer in packed beds at low Peclet numbers – wrong experiments or wrong interpretations?', *Chem. Eng. Sc.*, **52**, 3995

Schlünder, E.U, 1966, 'Wärme- und Stoffübertragung zwischen Durchströmten Schüttungen und darin Eingebetteten Einzelkörpern', *Chem. –Ing. –Techn.* **38**, *967*

Schlünder, E.U., Bauer, R., 1978, 'Effective radial thermal conductivity of packings in gas flow. Part I. Convective transport coefficient', *Int. Chem. Eng.* **18**, 181

Schlünder, E.U., Tsotsas, E., 1988, 'Wärmeübertragung in Festbetten, Durchmischten Schüttgütern und Wirbedlschichten', Georg Thieme Verlag, Stuttgart (Germany) 1988

Schouten, E.P.S., Borman, P.C., Westerterp, K.R., 1994, 'Oxidation of ethylene in a wall-cooled packed-bed reactor', *Chem. Eng. Sc.* **49**, 4725

Schouten, E.P.S., 1995, 'Verification of models for wall-cooled packed-bed reactors', Doctoral Thesis, Twente University, Enschede, the Netherlands

Schwedock, M.J., Windes, L.C., Ray, W.H., 1989, 'Steady state and dynamic modeling of packed bed reactor for the partial oxidation of methanol to formaldehyde, II. Experimental results compared with model predictions', *Chem. Eng. Comm.* **78**, 45

Severino, F., Laine, J., 1983, 'Effect of composition and pretreatment on the activity of copper-chromium-based catalysts for the oxidation of carbon monoxide', *Ind. Eng. Prod. Res. Dev.* **22**, 396

Singer, E., Wilhelm, R.H., 1950, 'Heat transfer in packed beds, analytical solution and design method', *Chem. Eng. Progress* **46**, 343

Specchia, V. Baldi, G., Sicardi, S., 1980, 'Heat transfer in packed bed reactors with one phase flow', *Chem. Eng. Comm.* **4**, 361

Stanckiewicz, A., 1989 Advances in modeling and design of multitubular fixed-bed reactors', *Chem. Eng. Technol.* **12**, 113

Stephenson, J.L., Stewart, W.E., 1986, 'Optical measurements of porosity and fluid motion in packed beds', *Chem. Eng. Sc.* **41**, 2161

Stewart, W.E., 1965, 'Transport phenomena in fixed-bed reactors', *AIChE Symp. Ser*, **58**, 61

Stewart, W.E., Villadsen, J.V.,1969,'Graphical calculation of multiple steady states and effectiveness factors for porous catalysts', *AIChe J*. **15**, 28

Subbotin, A.N., Gudkov, B.S., Yakerson, V.I., 1993, 'Catalysts on the basis of activated aluminium allows: II. Study of carbon monoxide oxidation on copper-containing catalysts by the transient response method', *Kinetics and Catalysis* **36**, 263

Sundaresan, S., Amundson, N.R., Aris, R., 1980, 'Observations on fixed-bed dispersion models: the role of the interstitial fluid', AIChE J. **26**, 529

Thoenes, D., Kramers, H., 1958, Mass transfer from spheres in various regular packings to a flowing fluid', Chem. Eng. Sc. **6**, 271

Thomas, N.T., Caretto, L.S., Nobe, K., 1969, 'Catalytic combustion of carbon monoxide on copper oxide', *Ind. Eng. Comm. Proc. Des. and Dev.* **8**, 282

Tsang, T.H., Edgar, T.F., Hougen, J.O., 1976, 'Estimation of heat transfer parameters in a packed bed', *Chem. Eng. J*. **11**, 57

Tsotsas, E., Schlünder, E.-U., 1990, 'Heat transfer in packed beds with fluid flow: remarks on the meaning and calculation of a heat transfer coefficient at the wall', *Chem. Eng. Sc.* **45**, 819

Vortmeyer, D., Schuster, J., 1983, 'Evaluation of steady flow profiles in rectangular and circular packed beds by a variational method', *Chem. Eng. Sc.* **38**, 1691

Vortmeyer, D., Haidegger, E., 1991, Discrimination of three approaches to evaluate heat fluxes for wall-cooled fixed bed chemical reactors', *Chem. Eng. Sc.* **46**, 2651

Vortmeyer, D., 1996, Preface to the Proceedings of the 14th International Symposium on Chemical Reaction Engineering, *Chem. Eng. Sc.* **51**, ix-x

Vortmeyer, D., 1987, 'Die Mathematische Modellierung von Reaktions- und Austasch prozessen in durchströmten festbetten unter Berücksichtigun von ungleichmäßigen Strömungs verteilungen', *Wärme- und Stoffübertragung* **21**, 247

Votruba, J., Hlavacek, J., Marek, M., 1972, **'**Packed bed axial thermal conductivity', *Chem. Eng. Sci.* **27**, 1845

Wakao, N., Kaguei, S., Funazkri, T., (1979), *Chem. Eng. Sci.* **34**, 325

de Wasch, A.P., Froment, G.F., 1972, 'Heat transfer in packed beds', *Chem. Eng. Sc.* **27**, 567

Webb, P.A., Orr, C., 1997, 'Analytical methods in fine particle technology', Micrometrix Instruments Corp., Norcross., U.S.A., ISBN 0-9656783-0-X

Wedel, S., Villadsen, J., 1983, 'Falsification of kinetic parameters by incorrect treatment of recirculation reactor data', Chem. Eng. Sci. **38**, 1346

Werner, K., 1994, 'Heat transfer with reaction in monoliths', *Chem. Eng. and Processing* **33**, 227

Westerink, E.J., Koster, N., Westerterp, K.R., 1990, 'The Choice between Cooled Tubular Reactor Models: Analysis of the Hot Spot', *Chem. Eng. Sc.* **45**, 3443

Westerink, E.J., Gerner, J.W., van der Wal, S., Westerterp, K.R., 1993, 'The lumping of heat transfer parameters in cooled packed beds: effect of the bed entry', *Chem. Eng. and Proc.* **32**, 83

Westerterp, K.R., van Swaaij, W.P.M., Beenackers, A.A.C.M., 1984, 'Chemical reactor design and operation', John Wiley & Sons, ISBN 0-471-91730-3

Westerterp, K.R., Dil'man, V.V., Kronberg, A.E., 1995a, 'Wave model for longitudinal dispersion: development of the model', *AIChE J.* **41**, 2013

Westerterp, K.R., Dil'man, V.V., Kronberg, A.E., Benneker, A.H., 1995b, 'Wave model for longitudinal dispersion: analysis and applications', *AIChE J.* **41**, 2029

White, S.M., Tien, C.L., 1987, 'Analysis of flow channeling near the wall in packed beds', *Wärme- und Stoffübertragung* **21**, 291

Wijngaarden, R.J.W., 1988, 'The scaling-up of cooled tubular reactors', Doctoral Thesis, Twente University, Enschede, the Netherlands

Wijngaarden, R.J., Kronberg, A., Westerterp, K.R., 1999, 'Industrial catalysis, optimizing catalysts and processes', Wiley-VCH, Weinheim (Germany), ISBN 3-527428581-4

Willhite, G.F., Kunii, D., Smith, J.M., 1962, 'Heat transfer in beds of fine particles (heat transfer perpendicular to flow)' *AIChE Journal* **8**, 340

Winterberg, M., Tsotsas, E., Krischke, A., Vortmeyer, D., 2000a, 'A simple and coherent set of coefficients for modeling of heat and mass transport with and without chemical reaction in tubes filled with spheres', *Chem. Eng. Sc.* **55**, 967

Winterberg, M., Tsotsas, E., 2000b, 'Correlations for effective heat transport coefficients in beds packed with cylindrical particles', *Chem. Eng. Sc*. **55**, 5937

Winterberg, M., Tsotsas, E., 2000c, 'Impact of tube-to-particle-diameter ration on pressure drop in packed beds', *AIChE J.* **46**, 1084

Yagi, S., Kunii, D., 1957, 'Studies on effective thermal conductivities in packed beds', *AIChE J.* **3**, 373

Yao, Y., Fang, Y., 1975, 'The oxidation of CO and C_2H_4 over metal oxides', *Journal of Catalysis* **39**, 104

Yao, Y.F.Y., Kummer, J.T., 'A study of high temperature treated supported metal oxide catalysts', *Journal of Catalysis* **46**, 388

Zehner, P, Schlünder, E.U., 1970, 'Wärmeleitfähigkeit von Schüttungen bei mäßigen Temperaturen', *Chemie- Ing. Techn.* **42**, 933

Ziólkowska, I., Ziólkowski, D., 1993, 'Modeling of gas interstitial velocity radial distribution over a cross-section of a tube packed with a granular catalyst bed', *Chem. Eng. Sc*. **48**(18), 3283

Ziólkowska, I., Ziólkowski, D., 2001, 'Experimental Analysis of isothermal gas flow field in tubes packed with spheres', *Chem. Eng. and Processing* **40**, 221

Ziólkowski, D., Szustek, S., 1989, 'Effect of fluid velocity radial profile on the radial mass dispersion in a fluid stream in a packed bed tubular apparatus', *Chem. Eng. Sc.* **44**, 1195

Dankwoord

Van de velen die, direct of indirect, aan de totstandkoming van dit proefschrift hebben meegewerkt wil ik hier, zonder de overigen tekort te willen doen, een aantal mensen met name bedanken.

Allereerst wil ik mijn begeleiders, prof. van Swaaij, prof. Westerterp en dr. Kronberg bedanken voor het vertrouwen dat zij de afgelopen jaren in mij hebben gesteld. Mede dankzij hun kennis en stimulering is dit proefschrift uiteindelijk tot stand gekomen.
Dit onderzoek is financieel mogelijk gemaakt door de Nederlandse Stichting voor wetenschappelijk Onderzoek, NWO. Ik ben de leden van de NWO-gebruikerscommissie zeer erkentelijk voor de belangstelling die zij hebben getoond voor dit werk.

Een belangrijk deel van dit proefschrift bestaat uit experimenteel werk. Ik wil de HDL-ers Gert Banis, Arie Pleiter, Geert Monnink, Fred Terborg en Karst van Bree niet alleen bedanken voor hun technische en organisatorische ondersteuning, maar evenzeer voor de prettige samenwerking, het lenen van hun gereedschap en de koffiepraat. Het onderhoud en de reparatie van de gekochte, geleende of gevonden onderdelen van de opstellingen werd verzorgd door Bert Kamp en Harry Olde Veldhuis. Wim Platvoet, Nelly Vos, Benny Hövels en Andries Groenink hebben ervoor gezorgd dat de benodigde apparaten en chemicaliën altijd gisteren bezorgd en betaald werden. Jan Heezen en Joachim Olde Bolhaar hebben kunnen voorkomen dat ik off-line raakte.
Uiteindelijk waren het de afstudeerders, van maar liefst 4 nationaliteiten, die een zeer belangrijk deel van de metingen moesten verrichten: Sherman de Lima, Thilo Klingel, Mario Iamarino, Nathalie Niessen, Nicolette Nieuwenhuizen, Manuel Puerto, Armin Pohlman, Herman van Staalduinen, Jeroen Vernooy, Ana Perez, Juan Padilla en Hugo Satink. Een aantal experimenten is uitgevoerd bij de vakgroep anorganische chemie, waarvoor ik hen zeer erkentelijk ben.
Yvonne Bruggert, Wies Elfers, Gery Stratingh en Ria Hofs dank ik voor hun administratieve en morele ondersteuning. Het is mij een genoegen geweest om samen te mogen werken met de staf, de AIO's en de studenten van de vakgroep IPP. In het bijzonder noem ik de kamergenoot die het het langst met mij heeft kunnen uithouden: Arthur. Hij was niet alleen zeer goed gezelschap, maar zorgde ook voor de nodige wiskundige input voor mijn fitterij. Essentieel was de steun van Sacha Kronberg, bij wie ik altijd mocht binnenvallen. Na een discussie met hem waren zelfs de meest ontmoedigende meetresultaten opeens interessant. Sacha is zowel een goede vriend als een uitstekende mentor.
Menige vrijdagmiddag heb ik mogen doorbrengen bij de bewoners van het Vlughterlab. Uit mijn toekomstige terugkeer naar deze plek mag worden geconcludeerd dat het er niet slecht toeven was.

Uiteraard ben ik de bovenstaande personen bijzonder dankbaar voor hun in- en ontspanning tijdens mijn promotieproject. Nog meer dank ben ik verschuldigd aan mijn ouders, zus, vrienden en huisgenoten, die mij altijd onvoorwaardelijk hebben gesteund.